

Effects of pressure on a sequential cascade system for electrochemical CO₂ reduction

A mathematical model and preliminary design



High pressure electrochemical sequential reduction of CO₂ to CO and CO to C₂₊ products

by

S.M.A. Buisman

to obtain the degree of Master of Science
at the Delft University of Technology

Student number: 4397541
Project duration: February 1, 2021 - November 17, 2021
Thesis committee: Dr. R. Kortlever, TU Delft, supervisor
Prof. Dr. ir. W. de Jong, TU Delft
Dr. ir. D. A. Vermaas, TU Delft
Dr. ir. J. W. Haverkort, TU Delft

An electronic version of this thesis is available at <http://repository.tudelft.nl/>.

Abstract

Within the electricity driven conversion methods, electrocatalysis has been assessed to be the closest to commercialisation. This can only be realised, if the system efficiency is increased in terms of the reaction rate, onset potential and/or selectivity. Current research has shown that, apart from the more widely investigated routes to improve these factors (GDEs, catalyst, etc.), cascade electrode systems and high pressure reactors could prove to be effective for increasing the system efficiency. By splitting the CO_2 reduction into two separate steps, CO_2 reduction to CO and the sequential reduction to C_{2+} products, both steps can be optimised in terms of operating conditions. Applying a cascade system has, therefore, shown to increase the selectivity and reaction rates in the system. Additionally, the advantage of the high pressure reactor originates from the fact that increasing the pressure, will result in an increase in the solubility of the reactant. By increasing the solubility, the mass transport to the electrode surface will subsequently be enhanced. The low solubility of reactants is often identified as a main limiting factor in system efficiency, therefore, increasing solubility has proven to increase reactant transport (current density) and selectivity in high pressure systems. Even though both of these advancements have shown promising results, techno-economic studies indicate that their feasibility is still too low to become commercially attractive at this point. Therefore, this research proposes to combine both technologies to increase the overall system efficiency in terms of: increasing the current density, increasing the Faradaic efficiency and decreasing the overpotential losses for the production of C_{2+} products.

Since this combination has not been investigated before, and both technologies are still rather new, there will be a lot to investigate in order to demonstrate the potential of this new combination. Therefore, in addition to an extensive literature study to uncover the relevant unanswered research questions regarding this field of research, a mathematical model was developed. A model is a valuable resource in determining the potential for a novel system, as it enables instantaneous control over system parameters and, therefore, can provide a lot of insight into its relations and limitations. However, as the accuracy of a model strongly depends on the quality of its input data, this research will also provide a design approach leading to a novel high pressure cascade reactor design. Eventually, the model can, therefore, provide the insight required for extensive experimental research, while the design can simultaneously aid in the improvement of the model.

The results evaluated by the model demonstrate both sequential reduction steps are positively affected by increasing the pressure. In addition, the otherwise poor CO solubility, can be dramatically increased by applying the combined system. The reaction rates are also evaluated to increase with the higher reactant concentration of CO and CO_2 . In addition, since the hydrogen evolution reaction is not affected by the pressure, as it does not present mass transfer limitations, the selectivity has been shown to also increase with increasing the system pressures. Additionally, the presence of the high CO concentration in the reduction towards C_{2+} products affects the selectivity of the system as well. The CO reduction reactions possess different behaviour from the CO_2 reduction reactions. Therefore, by indicating the share of both separate reduction reactions in the generated products, operating conditions for the maximum C_{2+} selectivity can be identified. This way, the combination of high pressure on a cascade system, has been demonstrated to possess a lot of potential for increasing the system efficiency towards C_{2+} products.

Contents

1	Introduction	1
1.1	Scope and goals	4
2	Literature study	7
2.1	Theory	7
2.1.1	The electrochemical cell	7
2.1.2	CO ₂ /CO reduction	11
2.1.3	Mass transport	17
2.1.4	High pressure effects	19
2.2	Modelling	27
2.2.1	Existing models and limitations	27
2.2.2	The electrode surface	32
2.2.3	Cascade modelling	34
2.2.4	Valid assumptions	36
2.2.5	Cascade high pressure model	38
2.3	Design procedure	38
2.3.1	The 2020 high pressure reactor	38
2.3.2	The new design	43
2.4	Conclusion: Research questions	46
2.4.1	Literature study summery	46
2.4.2	Discussion	48
2.4.3	Conclusion: research questions	50
3	The reactor design	53
3.1	The SolidWorks model	53
3.1.1	Design criteria	55
3.2	Strength calculations: the reactor stack	58
3.2.1	Stress originating from the clamp	58
3.2.2	Stress originating from internal pressure	59
3.3	Production	61
3.4	Design validation	64
3.4.1	Methodology	64
3.4.2	Results & Discussion	66
3.4.3	Conclusion	71
4	The high pressure cascade model	73
4.1	Mathematics	73
4.2	Strategy	76
4.3	Assumptions and limitations	78
4.4	Modelling structure	85
4.4.1	Parameters, constants and conditions	85
4.4.2	Bulk concentrations	87
4.4.3	Kinetic parameters	89
4.4.4	Solution parameters	92
4.4.5	Numerical solver conditions	93
4.4.6	Potential dependent: transport equations step 1	94
4.4.7	Potential dependent: transport equations step 2	96
4.4.8	Pressure dependent bulk concentrations	98
4.4.9	Pressure dependent: transport equations step 1	98
4.4.10	Pressure dependent: transport equations step 2	100
4.4.11	Plotting	102

4.5	Model validation	103
4.5.1	First reduction step	103
4.5.2	Second reduction step CO ₂ R	105
4.5.3	Second reduction step COR	108
4.5.4	High pressure effects	109
4.6	Sensitivity and conversion analysis	112
4.7	Conclusion validity model	113
5	Results & Discussion	115
5.1	Modelling results	115
5.1.1	Reaction rates	115
5.1.2	Product selectivity	119
5.1.3	Onset potential	124
6	Conclusion & Recommendations	127
6.1	Conclusion	127
6.2	Recommendations	129
6.2.1	General	129
6.2.2	The model	129
6.2.3	The design	131
A	Theory	133
A.1	Equilibrium and reaction rate constants	133
B	Design	137
B.1	Illustrations of the design.	137
B.2	Strength calculations in MATLAB	140
B.3	Construction drawings	141
B.4	Production	145
B.4.1	3D printing	145
B.4.2	Laser cutting	145
B.4.3	Machining processes	145
B.5	Production supplementary	148
B.5.1	Milling machine parts	148
B.5.2	Design validation set-up and results	148
C	Model	153
C.1	Classification of PDEs	153
C.2	Examples of methods for numerical mathematics	154
C.3	Standard equilibrium potentials	154
C.3.1	Convert between scales	155
C.3.2	Temperature correction factor	156
C.3.3	pH correction factor	157
C.3.4	Reference electrode correction factor	158
C.3.5	Supplementing the available information	158
C.4	Experimental input-data	159
C.5	Input data for the model	160

Nomenclature

Physics Constants

b	Tafel constant	[-]
e_0	Elementary charge electron	$1.602176634 \cdot 10^{-19}$ [C]
F	Faraday's constant	96 485.3 [sA/mol]
g	Gravitational Constant	[-]
h	Plank constant	$6.62607004 \cdot 10^{-34}$ [m ² kg/s]
H^{cp}	Henry's constant	[M/bar]
K	Equilibrium constant	[-]
K_B	Boltzmann constant	$1.3806 \cdot 10^{-23}$ [J/K]
k_i^0	Electron-transfer kinetic rate constant	[-]
$k_{f/r}$	Reaction rate constant (forward/backward)	[-]
R	Molar gas constant	8.31 [m ² kgs ⁻² K ⁻¹ mol ⁻¹]

Symbols

α	Charge transfer coefficient	[-]
ΔG	Change in Gibbs free energy	[J]
ΔH	Enthalpy of reaction	[kJ/mol]
δ	Diffusion layer length	[m]
η	Overpotential	[V]
γ	Activity coefficient	[-]
κ	Conductivity	[S/m]
κ_t	Transmission coefficient	[-]
μ	Chemical potential	[J/mol]
$\nabla\phi$	Electric field	[V/m]
ϕ	Electrolytic potential	[V]
ϕ_i	Fugacity coefficient species i	[-]
ρ	Density	[kg/m ³]
A	Surface area	[m ²]
C_0	Concentration in the bulk	[mol/L]
C_i	Concentration of species i	[mol/L]
$C_{O/R}$	Concentration at reductive/oxidation electrode surface	[mol/L]

D	Diffusivity	$[\text{m}^2/\text{s}]$
E	Cell voltage	$[\text{V}]$
F	Electric force	$[\text{N}]$
I	Current	$[\text{A}]$
j	Current density	$[\text{A}/\text{m}^2]$
j_*	Exchange current density	$[\text{A}/\text{m}^2]$
j_{lim}	Limiting current density	$[\text{A}/\text{m}^3]$
k_s	Salting out parameter	$[-]$
m_i	Number of moles of species i	$[-]$
N	Flux	$[\text{mol}/\text{m}^2/\text{s}]$
n	Number of electrons	$[-]$
P	Pressure	$[\text{bar}]$
p_i	Partial pressure species i	bar
Q	Reaction quotient	$[-]$
q	Electric charge	$[\text{C}]$
R	Electrical resistance	$[\Omega]$
S	Entropy	$[\text{J}/(\text{Kg})]$
S_i	Solubility of species i	$[-]$
t_i	Transport number	$[-]$
u_m	Mobility	$[\text{A}/\text{m}^2]$
V	Volume	$[\text{m}^3]$
v	Reaction rate	$[\text{M}/\text{s}]$
v_d	Drift velocity	$[\text{m}/\text{s}]$
v_i	Stoichiometric number	$[-]$
$V_i(x, t)$	Net rate of formation	$[\text{mol}/\text{m}^2/\text{s}]$
z_i	Ionic charge of ion i	$[-]$
\mathbf{u}	Velocity vector	$[\text{m}/\text{s}]$

List of Figures

1.1	Representation of the outline of the literature study. Arrows indicate connections between the chapters.	6
2.1	A simple schematic representation of a standard electrochemical cell.	7
2.2	Representation of sequential catalysis for the reduction of CO ₂ to C ₂₊ products. Derived from: [38].	8
2.3	Showing the difference between the SHE and RHE scales over different system pH for a temperature of 298 K. Derived from [49].	13
2.4	Tafel plot from experimental results by [115]. HCOOH at 5 atm (■), 40 atm (•) CO at 5 atm (□), at 40 atm (◦).	19
2.5	Comparison of the concentration profiles of CO ₂ and CO throughout the channel (Q=2 cm ³ /min) and with J _{Ag} =3 mA/cm ² , in the set-up from [38].	24
2.6	Reaction mechanism for CO ₂ reduction on Au, producing CO. Derived from: [98].	25
2.7	Two types of surface reactions: a) Langmuir-Hinshelwood LH. b) Eley-Rideal. Derived from: [96].	26
2.8	Possible reaction pathways for CO ₂ reduction (with CO as intermediate) to form: a) formate, methane and methanol, b) ethylene and ethanol, c) formate. Derived from: [54].	26
2.9	Schematic representation of the three sections considered in the model: the bulk solution, the diffusion layer and the electrode surface. The travelling species are also indicated per layer. Only diffusion is taken into account in this model. Derived from: [72].	29
2.10	Schematic representation of the set-up of the 2020 high pressure reactor. Derived from: [123].	40
2.11	An illustration of the designed reaction chamber piece (including the electrode fit), as designed in SolidWorks. Derived from: [123].	41
2.12	A 3D simulation of the global flow throughout the reaction chamber, modelled in COMSOL. The location of the electrodes is indicated with the circles on the sides. Derived from: [123].	42
2.13	Designs of the new reaction stack made in SolidWorks 2019.	45
2.14	Designs for the back plate, the spring contact for the electrical connection to the electrodes and the ring terminal connection to lead the wires to the top/bottom of the stack. Designs are made in SolidWorks.	45
3.1	The SolidWorks 3D model, rendered in Fusion 360.	54
3.2	Designs are made in SolidWorks and subsequently rendered in Fusion 360.	56
3.3	Representation of the stress on the reactor stack originating from the clamp.	58
3.4	Derived from [114]	59
3.5	Calculated stress [Pa] in the thick walled cylinder as a function of the radius r [m].	60
3.6	Images of the produced parts of the reactor stack including the lasercut and 3D printed parts.	61
3.7	A Nyquist plot representing an EIS measurement. Here R _{ct} represents the charge transfer resistance and R _s the solution resistance. C _{dl} , indicates the double layer change at the electrode surface and Z _w , the Warburg element (i.e. diffusion of the ions in the solution). Image is derived from [88].	65
3.8	QR code directing the reader to a short recording showing a successful 35 bar pressure test. Same file can be accessed via: https://youtu.be/m8fC6NrQG0M	68
3.9	Measurements completed with EC-Lab software.	68
3.10	Comparison between the results for an OCP measurement, conducted before and after a high pressure experiment.	69
3.11	Chronoamperometry measurement result.	70

3.12	Corrosion on the electrodes after different experiments.	70
4.1	Schematic representation of the iteration scheme. More detailed information on this subject can be found in section 11.3.2 of the Handbook of electrochemistry [127].	75
4.2	A schematic representation of the different sections and transport of species within the model.	78
4.3	The flow profile inside the reactor. Here the dotted line indicates the height of the diffusion layer.	80
4.4	Illustration of the comparison of the transport of particle c, by convective or diffusive transport.	81
4.5	Flowchart describing the main sections of the high pressure cascade model. The grey dashed square indicates the sections where the model follows the approach of the Soeteman [102] model. The Black dashed squares indicate the sections that required a new approach.	86
4.6	An example of the standard shape of a Tafel plot. The different regimes are indicated in the plot.	96
4.7	Comparison of the CO ₂ reduction rate on the Ag electrode, between the experimental results (left) and the modelled outcome (right).	104
4.8	Tafel plots, demonstrating the logarithmic partial current densities of the involved species against the applied potential.	104
4.9	Faradaic efficiency plots, showing the selectivity for a product for a specific potential.	105
4.10	Tafel plots, demonstrating the logarithmic partial current densities of the involved species against the applied potential.	106
4.11	Faradaic efficiency plots, showing the selectivity for a product for a specific potential.	107
4.12	Tafel plots, demonstrating the logarithmic partial current densities of the involved species against the applied potential.	108
4.13	Faradaic efficiency plots, showing the selectivity for a product for a specific potential.	109
4.14	Comparison of the kinetic trends at different gas pressures.	110
4.15	Indication of the pressure behaviour for the CO ₂ reduction on Cu as returned by the model.	111
4.16	Comparison of the modelled and experimental effects of pressure on the kinetics regarding COR on Cu electrodes.	111
4.17	Sensitivity analysis of the reduction rate of CO ₂ on Ag on the variation in diffusion coefficient values.	112
4.18	Showing the convergence profiles for the discretises and time variables.	113
5.1	Analysis of the effects of a cascade system and pressure on the solubility of the reactants, CO and CO ₂	116
5.2	Comparison between the modelled reduction rates at low pressure (1 bar) and high pressure (30 bar).	117
5.3	The modelled reduction rates, illustrating the maximum reduction and the accompanying potential.	117
5.4	Tafel plots, displaying the relation between the reaction rate (i.e the current density) and the applied potential.	118
5.5	pH profiles in the diffusion layer, showing low pH values at low absolute potentials and high values at high absolute potentials.	119
5.6	Comparison regarding the profiles for the Current Efficiency to the applied potential.	120
5.7	Comparison between the pressure Current Efficiency profiles and their relation with pressure at different potentials.	121
5.8	Formation rates for products originating from CO and CO ₂ reduction shown separately, at p=1 and p=30 bar.	122
5.9	A comparison of the different C ₂₊ , C ₂ and hydrogen distributions for three different potentials, evaluated at two different pressures.	123
5.10	Comparison of the changing onset potentials when operating with a tandem electrode instead of direct CO ₂ reduction on a Cu catalyst. Derived from [71].	124
B.1	An illustration of the clamp pressurising the reactor stack. Derived from: [123].	137
B.2	An illustration of the correction bolt pressurising the reactor stack. Derived from: [123].	137

B.3	An illustration of the female fittings used to connect the tubing to the reactor stack. Derived from: [123].	138
B.4	An illustration of the design being built up with the longitudinal placement bolts.	138
B.5	The 3D printed cathode reaction chamber part, to fit the new BASI reference electrode.	138
B.6	The construction drawing featuring the back cathode endplate.	141
B.7	The construction drawing featuring the connection rod.	142
B.8	The construction drawing featuring the cathode front endplate.	142
B.9	The construction drawing featuring the electrode holder.	143
B.10	The construction drawing featuring the cathode reaction chamber.	143
B.11	The construction drawing featuring the anode reaction chamber.	144
B.12	The construction drawing featuring the conductive endplate	144
B.13	Images of the produced parts of the reactor stack including the lasercut and 3D printed parts.	145
B.14	Schematic representation of a: (a). lathe, (b). milling machine. The axis are indicated in red in the figure. Original image derived from [7]	146
B.15	Construction drawings from the endplates and a reaction chamber.	147
B.16	A visual representation of the digital readout machine on the milling machine.	149
B.17	A visual representation of the process of tapping a thread into a hole. Derived from: [7].	149
B.18	An illustration of the connection of the stack to the potentiostat.	150
B.19	An illustration of the connections and set-up of the OCP testing of the reference electrode (right) against the master reference electrode (left).	150
B.20	The gold layer on the protrusion of the steel endplate to prevent corrosion as a result of the connection between the Nickel anode and the steel endplate.	151
C.1	Showing the difference between the SHE and RHE scales over different system pH for a temperature of 298 K. Derived from [49].	155
C.2	Representing the changing Tafel slope behaviour.	160
C.3	The Tafel slopes that were used as input for the modelling of the kinetic behaviour.	161

Introduction

Led by the Paris Agreement goals defined in 2015, recent focus has been on transitioning from a fossil fuel based energy system to a renewable based energy system. As a result, the share of renewable energy in the total global energy generation increased to 27% in 2019 [4]. In addition, many systems focusing on carbon capture, utilisation and storage (CCUS) are being developed, to mitigate the CO₂ emissions [3]. However, there are still many problems with deploying renewable energy as an alternative for fossil fuels. Arguably, the biggest problem is the intermittency of renewable energy generation. This issue makes it challenging to ensure the energy security level instated by fossil fuels. On top of that, the rise in electricity use is resulting in electricity transportation problems, emphasising the need for large scale storage systems [44]. At the same time, electricity generation related CO₂ emission levels are still four times higher than they should be for reaching the Paris Agreement goals [5].

A promising way to handle both the renewable energy storage and the CO₂ abundance problems, is the development of electricity driven CO₂ conversion methods. Here, the CO₂ can be converted into fuels or chemicals, effectively storing the renewable electricity while generating valuable products, in a carbon neutral way. Methods for converting CO₂ include:

- Thermal catalysis
- Photocatalytic reactions
- Electrocatalysis
- Photoelectrochemical (PEC) reactions

A promising area within these CO₂ conversion methods, is electrocatalysis. An economical feasibility study regarding these methods for catalytic conversion of CO₂, performed in 2018 by Bushuyev et al., concluded that of these different pathways, electrocatalysis is closest to commercialisation [19]. Electrocatalysis is a carbon neutral process where CO₂ can be converted into a multitude of products, including hydrocarbons and oxygenates. The reaction is driven by means of electricity powered redox reactions at low temperatures. However promising, at the moment these conversion processes cannot yet compete with fossil fuel based processes [23]. Reasons for this are the high overpotential / low energetic efficiency, low current densities / slow kinetics and low selectivity [107].

One of the largest problems with electrochemical CO₂ conversion is indeed the fact that it is hard to create sufficient selectivity for one single product [63]. In other words, the Faradaic efficiency (FE), a value used to indicate the ratio of actual product against the theoretical product formed, for one specific product, is too low. Most research is aimed at producing products with two or more carbons (C₂₊), such as ethanol, on the grounds that it is a valuable fuel/chemical. The advantage of C₂₊ products over, for example, hydrogen, is that they have a higher volumetric energy density. For ethanol the energy density is 24 MJ/L, which is not only higher than hydrogen, but also higher than advance battery technologies [112]. One of the challenges in the field of electrocatalysis is therefore to develop a system with increased selectivity towards C₂₊ products. Another parameter influencing the performance of the

system is the current density. The current density equals the rate of charge transfer per electrode area and is therefore related to the rate of reaction. Hence, increasing the reaction rate, increases system efficiency. The last important parameter mentioned regarding the system potential, is the overpotential. The overpotential is related to the voltage losses in the system. It can be explained as the extra voltage required, apart from the theoretical amount required, to drive the reaction. This parameter depends on operating conditions and cell geometry. In conclusion, to be more competitive, the performance of the system needs to be increased in terms of the Faradaic efficiency, the current density and the overpotential.

A widely studied approach to increase the performance of these parameters, is in the development of better catalysts. The high overpotentials and poor selectivity are related to the binding energy of the intermediates formed. At the same time, the Faradaic efficiencies are low because of competition with the hydrogen evolution reaction [54]. Engaging new catalysts with better adsorption behaviour and which repress the hydrogen evolution reaction could therefore increase efficiency. But developing suitable catalysts to ensure sufficient selectivity and energy efficiency is a major challenge, due to the complexity of the overall reaction [119]. So far, Cu based catalysts have proven to be the only catalysts able to produce significant amounts of C_{2+} products [57] [119] [92]. But as stated above, these reactions still are accompanied with too large overpotentials, and with low single product selectivity. Research indicates that the production of C_{2+} products and C_1 have mechanistic differences [119], indicating there is a possibility for optimisation through a selected pathway towards a specific product type. Some control on the reaction pathway - and therefore the selectivity - can be instated by tuning the intermediate binding energy. This can be achieved by increasing the activity of the catalyst, by changing the geometrical features (increasing edges and grain boundaries) or by changing the electronic structure by means of, for example, synthesising [6]. Putting this in practice, in 2016 Ma et al. reported a shift of 400 mV in overpotential for CO production from CO_2 , by synthesising their Ag catalyst to form oxide-derived Ag [64]. Likewise, oxygen-derived Cu (OD-Cu) has also shown to increase oxygenate production from CO at lower overpotentials. The 2015 study by Verdaguer-Casadevall et al., indeed links the increased activity of the OD-Cu to the presence of strong binding sites / grain boundaries [116]. This demonstrates that a lot of research is already being performed focused on increasing catalytic performance. Therefore, this will not be researched further in this report. A collaborative approach including catalyst optimisation will, however, be taken into account when looking at possibilities to further optimise electrocatalytic technology.

Another very interesting possibility for increasing the system performance, is to split the conversion steps and optimise the conditions for each individual step, in a cascade system. This makes sense, since most of the C_{2+} products (with the exception of formate) are produced with CO as key intermediate anyway [119]. Therefore, splitting up the overall reaction into two steps: 1) CO formation from CO_2 and 2) C_{2+} formation from CO, could greatly contribute to the overall cell efficiency. Furthermore, studies show that CO reduction has a higher C_{2+} selectivity and a higher activity than CO_2 reduction [51]. This makes the two-step system an interesting new approach to increase overall cell efficiency, making it a topic of interest in recent research.

For instance, in 2017 Somorjai and co-workers showed that they could reach a Faradaic efficiency of 60% for C_2 - C_4 products by deploying a two-step tandem process with optimised catalysts for each individual step [124]. Subsequently, the 2018 study by Jouny et al. compared the CO reduction (COR), as used in the cascade approach, to the more standard CO_2 reduction (CO_2R), to provide proof of how promising this new cascade approach can be [52]. They found a FE for COR of 80%, which was much higher than the CO_2R FE of only 55% for C_{2+} products. In addition, they found that the production rate for C_{2+} products of COR was more than double that of CO_2R , further emphasising the potential of the two-step system. Even more encouraging were the results of a 2018 study by Lum and Ager, who showed that by operating their sequential catalysis system they could create a local non-equilibrium state around the Cu electrode, allowing for a CO concentration above the solubility limit. This greatly impacts the reaction rates of the reduction, as the solubility of CO is normally rather low, resulting in mass transport limitations. This approach led to better results than they claim can be reached with a mixed CO/ CO_2 gas feed mixture [63]. In 2019, Gurudayal et al. further investigated these results and had similar findings indicating an increased local CO concentration. They also investigated the

influence of convection on top of diffusion on the cascade process, aiming to instate control on the selectivity by changing the configuration (distances) and flow conditions. Their results show that the cascade system can realise an increase in oxygenate to hydrocarbon ratio (1.95 at Ag: -1.0 V vs RHE; and Cu: -0.8 V vs RHE), tuning the selectivity towards specific products [38].

However, even with this new sequential approach, in a 2018 techno-economic study by Spurgeinon and Kumar, the feasibility of this electrocatalysis technique was found to be still too low to be commercially competitive [106]. This study relates the low overall efficiency to the second step of the system, the creation of C_{2+} products from CO (ethanol in particular). Other research on cascade systems had similar findings [112]. The first step, the creation of CO from CO_2 on Ag electrodes has already seen very good results in the past [94] [32] [23]. So in order to increase the overall cell efficiency, Spurgeinon and Kumar advise to focus on increasing the FE for C_{2+} products and the current density of the second step. The current density, related to the reaction rate of the system [87], is therefore an important property to boost the overall system performance. Since CO_2 and CO have poor solubility in aqueous electrolyte, the reaction rate can be dramatically increased by increasing the CO transport to the electrode surface.

A number of studies tried to solve this problem by increasing the active surface area of the electrodes [17] [62]. Often this is realised by deploying porous electrodes instead of the more general planar electrode. The porous electrode has a much larger surface area, effectively increasing the reaction rate of the system. However, even in these optimised systems there is evidence of mass transport limitations at higher overpotentials [84], indicating that the low solubility of the reactant still poses a problem for the system efficiency.

Another possibility for increasing the solubility, and therefore the mass transport of the reactants to the electrode surface, is increasing the pressure in the system. This idea has been executed and researched successfully before in CO_2 reduction systems and models [87] [115] [12] [84]. In a 2018 modelling study on high pressure CO_2 electrochemical conversion, performed by Morrison et al. [72], results showed an increase in obtainable partial current density (i.e. reactant transport). The article shows the clearly positive effects of pressure on the formate and carbon monoxide partial current densities. At the same time, the hydrogen partial current density seems to be unaffected by the increased pressure, because the hydrogen evolution reaction never was limited by mass transport in the first place. This means that by increasing reactant transport, apart from the current density, the FE will increase as well. This behaviour was confirmed by an experimental study by Hara et al. in 1995, who found results which suggest lower potentials are required when elevating the pressure (30 atm) [39]. A 2012 study by Dufek et al., investigating the effects of pressure on CO production on an Ag based cathode, reported the CO production at high pressures (18.5 atm) to be five times higher compared to using atmospheric pressures [29]. They also reached Faradaic efficiencies up to 92% at a current density of 350 mA/cm². Results that are similar to those of Gabardo et al. in 2018, investigating the effect of high pressure in CO_2 to CO electrolyzers. In this study they found exceptionally high energetic efficiencies of 80%, along with current densities of 300 mA/cm² [33]. Clear proof that the principle of increasing the pressure can have a positive effect on the CO_2 solubility and therefore its mass transport. However, to the best of the author's knowledge, no research has been done on the effects of high pressure on the CO reduction reaction. Some studies like Wang et al. (2018) [119] and Li et al. (2014) [57], do provide promising findings indicating increased mass transport behaviour under slightly higher pressures (1-2.4 atm), but no experimental results exist for higher pressures.

According to all of this prior research, the main challenges right now for increasing overall efficiency for electrocatalytic systems in order for them to compete with commercially available systems, are in: increasing the current density, the selectivity, while reducing the overpotentials. The current systems are limited by mass transfer and do not possess sufficiently high selectivity for a single product. Research has shown how promising COR can be compared to CO_2R , because of its higher activity and higher C_{2+} selectivity. Cascade systems have, therefore, been reported to increase cell performance, while adding control to the tuning of the selectivity for a specific product. In addition, by sequentially producing CO from CO_2 before reducing it at the second electrode, a high local CO concentration can be reached, even well above the solubility limit [38]. This will effectively help in solving the mass transport problem originating from the low CO solubility. However, another optimisation step is required for

these systems to become economically competitive. This could possibly be accomplished by another technological advancement: high pressure systems. Increasing the pressure could supposedly result in increased reactant solubility for both steps, reducing the overall mass transport limitations even further. Combining these technologies could therefore, hypothetically, reduce the overpotentials, while the current density and selectivity for a single product are increased.

The hypothesis in this study is therefore that increasing the pressure of the electrocatalytic system can increase mass transfer properties by increasing the reactant solubility for both sequential steps, and thus greatly increasing the overall cell efficiency. Hence, this study is dedicated to finding the effects of pressure on a cascade electrochemical cell.

1.1. Scope and goals

As stated above, this research focuses on uncovering the effects of pressure on each sequential step of a cascade system. Something that has not been investigated so far, but which possibly could have a positive effect on the campaign for electrocatalytic systems to become competitive with existing industrial systems. This research will, therefore, aim to provide an indication of the potential for this new research direction.

A means for uncovering the potential of a system, while enabling instantaneous control over system parameters, is the creation of a simulating model. Modelling will provide insight into relations between parameters and the possible limitations of a new system. Therefore, it is a good instrument to determine the possible capabilities of the system, without the need to build and test with an experimental set-up for each possible addition and idea. A number of models regarding high pressure CO_2R already exist, however, the connection with a second high pressure reduction step was never made before. Consequently, this study will focus on the generation of a model, simulating electrocatalytic behaviour for each step, and indicating the potential of the high pressure cascade reactor. From the simulated results, optimal operating conditions can be determined to further investigate and validate with experimental research.

However, at the moment there are no experimental results available for high pressure cascade systems, as this is a concept that has not been investigated yet. Therefore, it would be an important contribution to the campaign for electrocatalytic systems to become competitive, to provide the means for experimental research, so the modelled results can be validated, updated and investigated experimentally, in the future. Hence, this research will also regard the development of a new reactor design, for experimentally testing the high pressure cascade system.

Consequently, this research will be divided into the following elements:

- The construction of an adaptable high pressure cascade reactor, capable of facilitating all intended experiments
- The creation of a mathematical model, capable of accurately simulating each reduction step, based on existing models in literature and known theoretical principles
- The execution of validation experiments, directed to provide validation for the new reactor design and to create some early insights into the underlying principles taking place in this new system

The intended objective of this research therefore, to create insight into the effects of pressure on this proposed cascade system, for the creation of C_{2+} products from CO_2 . For this purpose, simple replaceable Ag and Cu electrodes will be used, along with a 0.1 M KHCO_3 electrolyte solution containing dissolved CO_2 gas. The Ag electrode will be used for the first step, creating CO and H_2 from CO_2 . Thereafter, the Cu electrode will be deployed for the second step, producing C_{2+} products from the CO produced in the first reduction step. The reactor set-up, used in this research, will be based on the set-up as described in the 2020 thesis report by Q. Wolls [123]. This set-up will be optimised and adapted so it can facilitate high pressure cascade experiments as well as single step experiments. The mathematical model will be based on the available models in literature, simulating the first step of the

system (CO₂ reduction on an Ag electrode) under high pressures [102] [72]. This modelling approach for this first step will be revised and updated to agree with the relevant reactions and operating conditions. Afterwards, the connection between the steps, along with the second reduction step, will be constructed.

To clarify, the aim of the research is to confirm or deny the potential of this new potential high pressure cascade pathway. A next step, afterwards, could be to use the insights originating from this research to aim for an optimised highly efficient electrocatalytic system, with the option to combine this new technology with newly discovered catalysts, electrode configurations (such as: GDEs or porous electrodes) and optimised cell configurations. However, in this research, aiming for the most optimal cell efficiency is not one of the intended goals, and is therefore outside the scope of this study.

There is still a lot to investigate regarding this subject. However, as stated above, a lot of important separate research has already been directed at cascade or high pressure systems. The first step in defining the ensuing research questions for this investigation – is therefore, to outline to which extent information is already available in literature, in order to find out what elements still need to be investigated further.

The following chapter, 'Literature study', consequently, is directed towards identifying all available relevant information in literature, regarding this subject. This will aid in formulating the research questions for this research, in order to investigate what is yet to be discovered regarding high pressure cascade systems. The first section, 'Theory', will be elaborating on derivations of common equations within the field of electrochemistry, so these can be used to explain the principles raised in the following chapters. It will also include the applicable current research reports on the theory of these topics, with a focus on experimental results, to indicate which experiments are most valuable to investigate as a next step. The emphasis of this section will be on the available theory behind the effects of high pressure on the solubility behaviour and kinetics of the reaction. The collected theory on solubility, mass transport and high pressure effects, will subsequently be used to set up a modelling approach in the section 'Modelling'. This section will compare the most relevant models available in literature on their modelling approach, limitations and adopted assumptions. From this comparison, a modelling structure can be adopted for the model to be used in this study. In the section 'Design procedure', reactor designs in literature relevant for the high pressure cascade reactor will be analysed. Next, the design criteria for the design improvements required to enable the intended experiments will be defined. These will be based on the design improvements required after reviewing the current high pressure design, on which the design in this study will be based.

From each section the information gaps regarding the available research in literature will emerge. From these gaps, it will become clear which segments require further investigation – and to what extent. This analysis will eventually lead to the research questions on which the resulting study in this research will be based. This structure is represented schematically in figure 1.1.

Consequently, the subsequent chapters will be directed at answering these research questions. They will include a description of the development of the model and the accompanying reactor design, their results and validation. This will lead to an overall conclusion and recommendation regarding the high pressure cascade system and the potential for this technology in future research. After answering the respective research questions, the potential for this new technology will be indicated, in accordance with the predetermined research objectives.

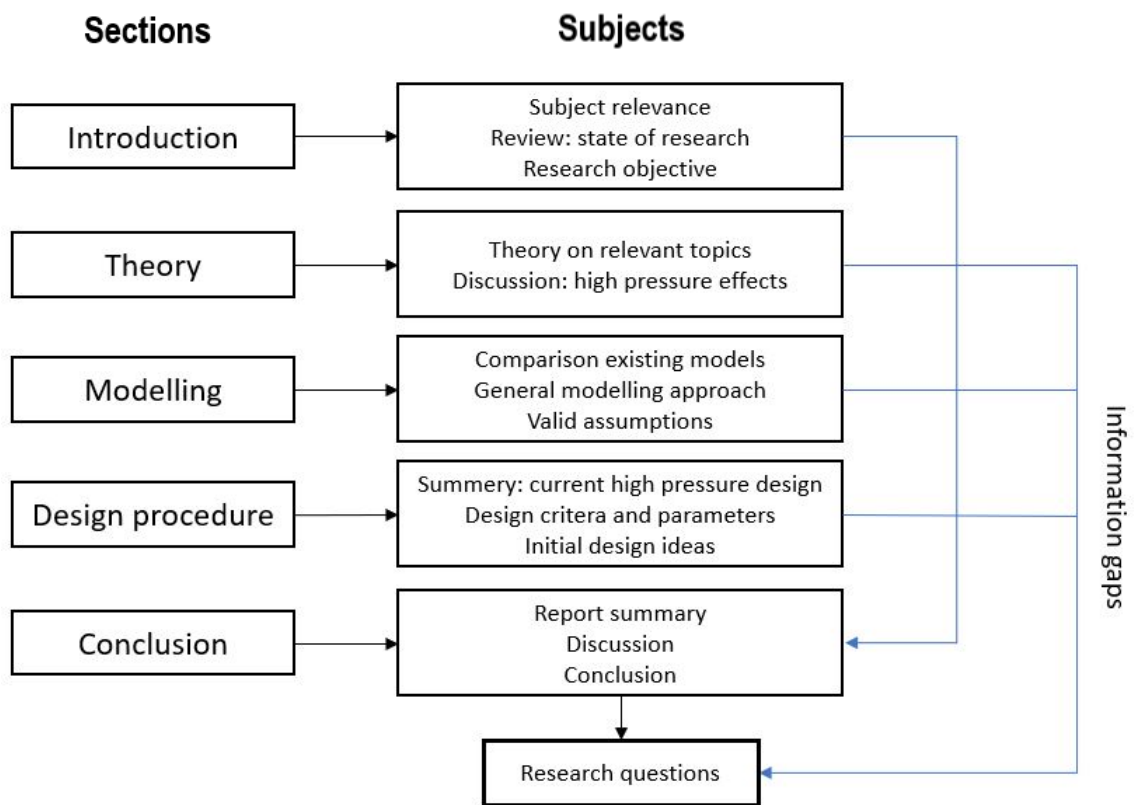


Figure 1.1: Representation of the outline of the literature study. Arrows indicate connections between the chapters.

2

Literature study

2.1. Theory

The next chapter will include a description of the relevant theory, focusing at the subjects: electrochemical reactors, principles of electrochemistry, mass transport phenomena and the effects of high pressure. This information will serve as a basis for the following sections and chapters.

2.1.1. The electrochemical cell

Within chemistry, the field of electrochemistry involves the interaction between chemistry and electricity. It can be divided into two sections: 1) chemical reactions taking place, producing electricity, or 2) utilising electricity, to drive the chemical reactions. The first, perhaps more known section, entails, for example, batteries. This study will focus on the second section, since the goal is to effectively 'store' electricity, by converting it into chemical bonds.

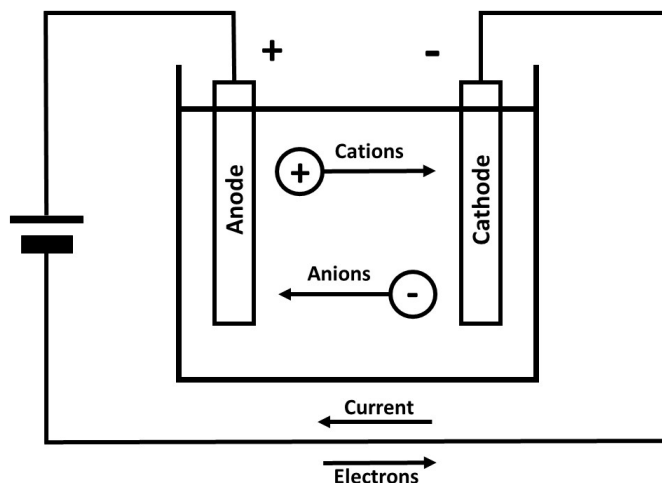
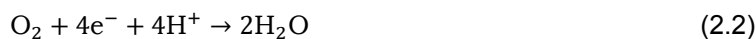


Figure 2.1: A simple schematic representation of a standard electrochemical cell.

An electrochemical cell, as shown in figure 2.1, typically consists of two types of electrodes, an anode and a cathode. The electrodes have two functions, they need to be electrically conductive to conduct electrons and at the same time they need to function as a catalyst for the reactions taking place at their surface. The reactions taking place in an electrochemical cell are called redox reactions. In these

reactions, negatively charged (e^-) electrons are transferred. There are two types of redox reactions taking place within the cell, the oxidation and reduction reaction. Electrons originate from the oxidation reaction at the anode, as shown in equation 2.1. The electrons move towards the cathode, where the reduction takes place, as shown in equation 2.2.



The current, moving from positive to negative, enters the anode and leaves at the cathode. Surrounding the cathode and anode is an electrolyte solution. The function of this electrolyte is to transfer the electric charge to close the electric circuit. In most cases it is a liquid solution, but it can also be solid (ceramic structures or polymers). Most liquid electrolytes are aqueous solutions, consisting of water and added salts. The salts are dissolved in the water and dissociate into ions, the ions are responsible for transferring the electric charge between the electrodes [80]. Ions are also formed in the surface reactions taking place at the electrodes, as can be seen in the half reactions stated above. Ions can be positive of charge (cations) or negative (anions). Since the electrons are regarded as negative, a large negative charge would build up at the cathode, would it not be restored by the ionic current moving from positive to negative through the ions in the electrolyte.

As demonstrated, an electrochemical cell consists of at least two electrodes, the anode and the cathode. General convention is to refer to the electrode of interest (in this work the cathode) as the working electrode, and the other as the counter electrode. Both are connected to a power source; this can be a regular power source or a potentiostat. When operating with a potentiostat, an additional electrode is required, called a reference electrode. This electrode does not participate in the reaction and therefore has a fixed potential. Engaging this third electrode is essential for a correct measurement of the working electrode potential, as measuring against the counter electrode is not an option, since its potential may change during the reaction [80].

The high pressure cascade cell

The cell in figure 2.1 is a simplified version of the reactor structures used today. The reactors commonly used for electrochemical reduction have multiple compartments and consist of a series of stacked components, such as plates, gaskets and housings. The 2020 article by Perry et al., provides a good overview for different reactor designs [79]. The difference between the standard designs and the design required for the experiments of this research, is that this new cell is required to house multiple electrodes in series while, at the same time, handling very high pressures. An example of a cascade system, with two electrodes in series, is represented in figure 2.2.

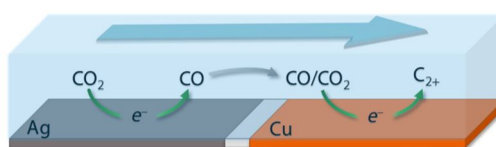


Figure 2.2: Representation of sequential catalysis for the reduction of CO_2 to C_{2+} products. Derived from: [38].

In the cascade system the complicated reaction pathway of electrochemical reduction for the production of C_{2+} products is divided into two steps. The advantage of this is that CO is produced locally in the first conversion step, resulting in a CO concentration for the second step above the solubility limit [63]. This effectively means the mass transport is increased and therefore the reaction rate. In addition, the cascade system utilises COR rather than CO_2R for the second conversion step. This is an improvement, since COR has shown to work at higher activities and lower overpotentials. COR compared to CO_2R requires two less electrons per produced carbon, and therefore requires less driving force (i.e. overpotential) [38]. By breaking up the complicated reaction mechanism into two steps, the level of control can be increased. By changing cell design, the flow, electrode spacing and electrode sizes can be varied. This creates room for experimenting with different electrodes sizes, as Lum and Ager did in

their 2018 study, to systematically tune the product distribution and ratio of oxygenates to ethylene [63].

This increased level of control over the reaction can be very beneficial for the results, however, it also means the cell design becomes more complicated. Both electrodes work at different potentials and need to be actuated separately. Controlling the electrode sizing and gap distance, also means the cell design must be adaptable enough to facilitate these changes.

Apart from housing multiple electrodes, the cell must also be able to work with high pressures. The cell that will be designed in this study, will be based on an existing cell set-up, aimed at producing formate from CO₂ under high pressure conditions. The design process for the designing of this set-up can be found in the 2019 thesis report by Wols [123]. The goal of this study was to design an adaptable reactor (i.e. electrochemical cell), capable of handling high pressures, to perform multiple different experiment configurations with. Most high pressure reactors have complicated designs that consist of many components. Therefore, Wols detected a need for simpler, more adaptable, high pressure designs to perform experiments in. The reactor designed in this study has proven to fulfill its design parameters, however, it still needs to be adapted to fit intended experiments for this research.

The design parameters for the high pressure cascade set-up will be discussed more extensively in section 2.3, 'Design procedure'.

Efficient cell design

To develop an efficient electrochemical cell, it is important to first determine which components influence the efficiency of the system. Therefore, one must determine what factors contribute to possible losses in the system. This section will review these factors, to provide insight into creating an efficient cell, to aid in the designing part of this research as further described in chapter 2.3, 'Design procedure'.

The cell voltage of an electrochemical cell can be found by taking the difference between the anode and cathode potential:

$$E_{\text{cell}} = E_{\text{c}} - E_{\text{a}} \quad (2.3)$$

However, the system is usually far from ideal, and deals with many losses. As in any electrical system, there is resistance. The electrodes, wires and electrolyte all account for ohmic resistance, resulting in a potential drop. To indicate the electronic potential drop originating from the resistance in the wires and other material, ΔV is used. The ionic potential drop, related to the conductivity of the electrolyte, is indicated with $\Delta\phi$. In addition to the electrical resistance in the system, extra potential is required to drive the reaction; this is called the activation overpotential, or charge transfer overpotential. The activation overpotential is related to the voltage loss used to drive the required rate of reaction at the electrodes [80]. It is indicated with η and there will often be a distinction between the anodic and cathodic overpotential, indicated by: η_{a} and η_{c} . Note that the term 'overpotential' refers to these combined losses in the system. It is often defined as the difference between the theoretically required potential (i.e. thermodynamic potential) and the actual required potential. The overpotential is not the same as activation overpotential, since this is only for a small part contributing to the overall overpotential [80]. Overpotential is often indicated with η as well, causing confusion between the two terms. To indicate the overpotential, equation 2.4 – for now – uses η_{tot} . The equation to denote the actual cell potential is expressed in equation 2.5 [41].

$$\eta_{\text{tot}} = E - E_{\text{cell}} \quad (2.4)$$

$$V_{\text{cell}} = E_{\text{cell}} + \eta_{\text{c}} - \eta_{\text{a}} - \Delta\phi - \Delta V \quad (2.5)$$

Hence, decreasing the (ohmic) losses in the system will increase the overall efficiency. To design an efficient cell, it is therefore important to determine which values contribute to these losses, so they can be reduced as much as possible. This will, therefore, be investigated below.

The electronic potential drop is dependent on the ohmic resistance in the system as shown in equation 2.6. It can, for example, be reduced by decreasing the surface, A , of the wires.

$$\Delta V = jAR \quad (2.6)$$

Here i denotes the current density, A the surface area and R the resistance of the component.

The ionic resistance can also be decreased by changing the cell geometry. The current density, i , represents the normalised current against the electrode area, as shown in equation 2.7. The potential drop over the gap between the electrodes (filled with electrolyte) can be calculated using Ohm's law, according to equation 2.8. These equations can, thereafter, be linked to Pouillet's law, as shown in equation 2.9. With this law, the distance between the electrodes and the conductivity of the electrolyte can be linked to the overall ionic resistance. The resulting relation, to describe the ionic potential drop, then becomes equation 2.10, illustrating the dependence on the electrolyte conductivity and the electrode gap length. Reducing the gap and increasing conductivity is, therefore, beneficial for decreasing the ohmic losses.

$$i = I/A \quad (2.7)$$

$$\Delta\phi = IR \quad (2.8)$$

$$R = \frac{L}{A\kappa} \quad (2.9)$$

$$\Delta\phi = iL/\kappa \quad (2.10)$$

Here, I denotes the current, A the surface area, R the resistance in the gap between the electrodes, L the length of the gap between the electrodes, κ the conductivity of the solution and $\Delta\phi$ the resulting potential drop over the electrolyte filled gap.

Lastly, the (activation) overpotentials can be found by finding a relation between the overpotential and the current density. The equation that provides this relation is the current-overpotential equation, which is shown in equation 2.11 [11]. This equation is often simplified by assuming Tafel kinetics are valid. This is the case at high overpotentials, where one half of the reaction dominates over the other (for example: reduction » oxidation). The current-overpotential equation consists of an oxidation and a reduction term. In the regime where reduction dominates, the oxidation term can be neglected. When the resulting equation is linearised, this will form the Tafel equation; relating the overpotential (η) to the current density (j), the concentration (C) and the exchange current density (j_*). The Tafel equation is shown in equation 2.12.

$$i = i_o \left(\frac{C_R}{C_{R,eq}} e^{\frac{\alpha F \eta}{RT}} - \frac{C_O}{C_{O,eq}} e^{-\frac{(1-\alpha)F \eta}{RT}} \right) \quad (2.11)$$

$$i = i_o \frac{C_R}{C_{R,eq}} e^{\eta/b} \quad (2.12)$$

Where b , Tafel equation constant, can be found using:

$$b = \frac{\alpha F}{2.3RT} \quad (2.13)$$

Here, $C_{R/O}$ denotes the concentration at the cathode and anode surface, C_{eq} the equilibrium concentration (away from electrode surface), F indicates the Faraday constant, R the molar gas constant, T the temperature and α the charge transfer coefficient. This coefficient is a dimensionless number, which indicates the symmetry of the reaction barrier. If $\alpha=0.5$, the reaction is symmetrical [11].

In the Tafel regime the activation overpotential can be found with equation 2.14 [80]. This shows the clear dependence of the overpotential on the exchange current density. To decrease the overpotential losses the exchange current density must, therefore, be as high as possible. The exchange current density can be defined as the rate of charge transfer at an electrode in equilibrium. It is a measure of the amount of charge entering from the ions at the electrode surface. The kinetics of i_o are influenced by the reaction process and the catalyst used. Complex reaction processes, where multiple bonds

need to be broken or many adsorption steps are required, result in low exchange current densities.

$$\eta = b \ln \left(\frac{i}{i_0} \right) \quad (2.14)$$

From this it can be concluded that there are a lot of different factors influencing the losses of the system. Key in the development of an electrochemical cell is, therefore, to reduce the (ohmic) losses, by:

- reducing electrical losses, by decreasing wire areas, etc.
- reducing ionic losses, by minimising the gap distance between the electrodes and maximising the electrolyte conductivity
- deploying catalysts which positively affect the kinetics of the reaction, resulting in high current exchange densities

Taking this into account, will aid in the development of a suitable high pressure cascade electrochemical cell. This information will, therefore, be applied in the chapter on the parameters for the cell design, 'Design procedure'.

2.1.2. CO₂/CO reduction

To produce products from CO₂ or CO, both thermodynamic and kinetic barriers need to be overcome. This section will describe the theory behind how reactions take place, what type of reactions there are, and what factors can influence the reactions. This involves the reactions taking place in CO₂ and CO reduction, the chemical reactions in the bulk, the thermodynamics and kinetics of the system and the mass transport within the system. This theory will aid in setting up the equations describing the electrochemical cell behaviour for the modelling chapter.

First of all, the electrochemical reduction of CO₂ to form CO is a relatively simple process, in which only two electrons are transferred. At Ag surfaces CO production is dominant. However, the reduction of CO towards C₂₊ products is much more complex and has a lot of possible reaction pathways and different products. Some possible reaction pathways for CO, formic acid (HCOOH), methanol (CH₃OH), methane (CH₄), ethylene (C₂H₄) and ethanol (C₂H₅OH) are displayed in table 2.1.

Reaction	Formal redox potential vs SHE	Value
CO ₂ + 2H ⁺ + 2e ⁻ → HCOOH	E ⁰ _{redox}	-0.610 V
CO ₂ + 2H ₂ O + 2e ⁻ → HCOOH ⁻ + OH ⁻	E ⁰ _{redox}	-1.491 V
CO ₂ + 2H ⁺ + 2e ⁻ → CO + H ₂ O	E ⁰ _{redox}	-0.530 V
CO ₂ + 2H ₂ O + 2e ⁻ → CO + 2OH ⁻	E ⁰ _{redox}	-1.347 V
CO ₂ + 6H ⁺ + 6e ⁻ → CH ₃ OH + H ₂ O	E ⁰ _{redox}	-0.380 V
CO ₂ + 5H ₂ O + 6e ⁻ → CH ₃ OH + 6OH ⁻	E ⁰ _{redox}	-1.225 V
CO ₂ + 8H ⁺ + 8e ⁻ → CH ₄ + 2H ₂ O	E ⁰ _{redox}	-0.240 V
CO ₂ + 6H ₂ O + 8e ⁻ → CH ₄ + 8OH ⁻	E ⁰ _{redox}	-1.072 V
2CO ₂ + 12H ⁺ + 12e ⁻ → C ₂ H ₄ + 4H ₂ O	E ⁰ _{redox}	-0.349 V
2CO ₂ + 8H ₂ O + 12e ⁻ → C ₂ H ₄ + 12OH ⁻	E ⁰ _{redox}	-1.177 V
2CO ₂ + 12H ⁺ + 12e ⁻ → C ₂ H ₅ OH + 3H ₂ O	E ⁰ _{redox}	-0.329 V
2CO ₂ + 9H ₂ O + 12e ⁻ → C ₂ H ₅ OH + 12OH ⁻	E ⁰ _{redox}	-1.157 V
2H ⁺ + 2e ⁻ → H ₂	E ⁰ _{redox}	-0.42 V

Table 2.1: Examples for reaction equations for CO₂ reduction and the accompanying redox potential vs SHE. Values derived from [107].

The E⁰ of the reaction indicates how thermodynamically favourable the reaction is. The E⁰ values in the table are measured against SHE (Standard Hydrogen Electrode). SHE is a reference scale, determined by putting a platinum wire in a H⁺ solution through which H₂ gas is bubbled. The activity values equal '1', and the system has a potential of '0' volts [80]. In the next section the theory behind

the different reference scales and how to convert between them, will be explained. The value of E^0 indicates how likely a reduction process will occur, reduction reactions with more positive E^0 are more favourable than reactions with more negative values. But, in addition to the thermodynamic barrier, reactions also have a kinematic dependence, so the E^0 is not the only value determining which reaction will take place [107]. This will be explained further in the next sections.

Reference scales

As explained before, the overpotential is defined as the difference between the theoretical potential the system should have and the actual potential of the system. The value of the overpotential is essential for determining the current density, as illustrated in equation 2.11. To determine the overpotential, first the theoretical potential will need to be determined. Its value originates from three important variables: the reaction equation, the temperature and the pH of the system. Additionally, the standard potential (i.e. theoretical potential), E^0 , is referenced against a certain scale. E^0 values in literature are often either referenced against SHE (Standard Hydrogen Electrode) or against RHE (Reversible Hydrogen Electrode) scale. The SHE scale assumes the E^0 for hydrogen to be zero volts at all temperatures and pH. This is then used as a reference for standard potentials of other reactions. E^0 values on the RHE scale, on the other hand, do change with changing pH and temperature. Therefore, it is important to incorporate the potential temperature and pH deviations when referencing to RHE scale.

To model the high pressure cascade system, input variables are required. These will be extracted from other models or experimental data found in literature. As the standard electrode potentials can be expressed against different scales, to align them, conversion between these scales is required.

The SHE scale is determined by placing a Pt electrode in an aqueous solution, where H_2 gas and H^+ protons are supplied at a fugacity of 1.00 bar with an activity of 1.00 [49]. In this case the hydrogen reference electrode used represents the SHE. However, when these values deviate from standard, in other words, if the fugacity and activity are not equal to one, the hydrogen reference electrode represents the RHE [49]. For the RHE, the concentration of hydrogen ions resembles that of the electrolyte concentration employed. Where the SHE has a constant value for all temperatures and pH, the potential against RHE varies with changing the pH or temperature of the system. This principle is shown in figure C.1.

At a temperature of $25^\circ C$ the factor RT/F in the Nernst equation shown in equation 2.27, will be approximately 0.0592. This corresponds to the slope of the graph in figure C.1, identifying the decrease in potential E per unit pH.

$$E = E_0 - \frac{RT}{nF} \ln Q \quad (2.15)$$

Where:

- $Q = K$, (i.e. equilibrium constant) in equilibrium conditions
- $Q = a_{red}/a_{ox}$, when not in equilibrium, where a denotes the activity
- $Q = C_{red}/C_{ox}$, for low concentrations, since the activity often approaches unity in this case

Hence, to convert from SHE to RHE scale the following formula can be used [16]:

$$E_{RHE} = E_{SHE} + 0.0592 * pH \quad (2.16)$$

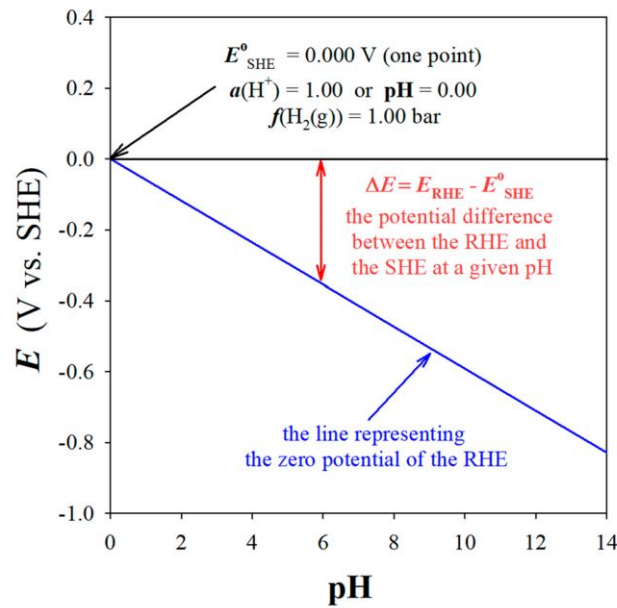


Figure 2.3: Showing the difference between the SHE and RHE scales over different system pH for a temperature of 298 K. Derived from [49].

Chemical reactions

In addition to the reactions taking place at the electrode surfaces, there are also chemical equilibrium reactions taking place in the electrolyte solution. Which reactions take place, depends on the pH of the solution and the added electrolyte. The bulk pH of an electrolyte solution containing 0.1 M KHCO_3 is 8.9, but will decrease to around 6.8 after saturating with CO_2 [85]. When the pressure is increased, the pH will drop even more due to the increased CO_2 solubility. According to the modelled results in the 2019 study of Morrison and co-workers, the pH at high pressures does not drop below 5.4 [72]. In a KHCO_3 electrolyte solution at this pH level, the reactions involving the dissolved CO_2 are [102]:



The equilibrium reaction between OH^- and H^+ is the following:



Note that CO does not react with the electrolyte solution, therefore no chemical reactions for CO are stated. It will only dissolve to a $\text{CO}(\text{aq})$ form.

Here the hydration reaction to form H_2CO_3 and the reaction producing HCO_3^- have been combined to form equation 2.17, since the hydration reaction is very slow compared to the subsequent dissociation reaction [34]. The related equilibrium constants (K_{1-4} and K_w) are also indicated in the reaction equa-

tions. How the values for these constants can be calculated, will be explained in section 2.1.2, 'Kinetics'.

To maintain charge neutrality in the electrolyte and conservation of mass, the following equations must hold as well [72]:

$$[\text{K}^+] + [\text{H}^+] - [\text{HCO}_3^-] - 2[\text{CO}_3^{2-}] - [\text{OH}^-] = 0 \quad (2.22)$$

$$[\text{CO}_2] + [\text{HCO}_3^{2-}] + [\text{CO}_3^{2-}] = [C_{\text{carbon}}] \quad (2.23)$$

Thermodynamics

The thermodynamics of a system describe the type of reactions taking place. With this knowledge it is possible to predict if a chemical reaction will take place spontaneously or if it needs a driving force [80].

Free energy of a system is an example of a thermodynamic function enabling the prediction of reaction behaviour. The free energy, or Gibbs free energy, can indicate the direction of the reaction. It can be defined as the maximum (reversible) work of a system at a given temperature and pressure. In equilibrium state, the amount of work can, therefore, be taken as equal to (minus) the change in Gibbs free energy of the reaction. The change in Gibbs free energy can be calculated as shown in equation 2.24; depending on: the number electrons transferred (n), Faraday's constant (F) and the open cell voltage (E^0).

$$\Delta G = -nFE^0 \quad (2.24)$$

If the change in Gibbs free energy is positive, the free energy of the reactants is smaller than that of the products and the reaction is regarded exergonic. Exergonic reactions have a spontaneous forward reaction. When the change in Gibbs free energy is negative, the free energy of the reactants is larger than that of the products and the reaction is regarded endergonic. Endergonic reactions have a spontaneous backward reaction. In the case of CO_2 or CO reduction the reaction is endergonic, because it requires electricity as driving force.

Another name for the E^0 , as calculated with the change in Gibbs free energy, is the thermodynamic voltage. It indicates the minimal electrical energy required to drive the reaction. Some reactions, however, also require additional heat, these reactions are called endothermic reactions. To indicate whether a reaction is exothermal (requires no external heat) or endothermal, we look at the enthalpy of reaction:

$$\Delta H = \Delta G + T\Delta S \quad (2.25)$$

Here, ΔG indicates the minimal electric energy required and $T\Delta S$ the minimal heat required for the reaction (temperature T times the entropy change ΔS).

With this knowledge it is possible to define the equation for the enthalpic voltage (thermoneutral voltage), which represents the global energy required for the reaction.

$$E_{\text{tn}} = -\frac{\Delta H}{nF} \quad (2.26)$$

Voltages higher than the thermoneutral voltage indicate that the reaction in question is exothermal, meaning that it produces more heat than required to drive the reaction. The thermodynamic voltage and the thermoneutral voltage per reaction equation at standard conditions can be found in tables of standard electrode potentials.

To relate the Gibbs free energy to the actual reaction potential and to link the potential to the concentrations in the bulk of the system, the Nernst equation can be used [11]. The bulk of the system is a term used to describe the (equilibrium) section of the system far enough away from the electrode surfaces to be regarded as unaffected by their reactions.

$$E = E^0 - \frac{RT}{nF} \ln Q \quad (2.27)$$

Here, E represents the actual reaction potential, R the molar gas constant and Q the reaction quotient. The reaction quotient can indicate if the reaction will proceed forward, backward or will be in equilibrium. When the system is in equilibrium Q will equal the equilibrium constant K .

This shows there is a difference between the thermodynamic voltage and the actual voltage of the system (including losses, etc.); this difference is indicated with the previously mentioned term: overpotential [80]. This overpotential, not to be confused with the activation overpotential, consists of three different contributors: charge transfer (activation) overpotential, resistive overpotential and mass transport overpotential.

Kinetics

As explained above, the thermodynamics of a system provide a lot of information on the reactions taking place; they, however, cannot predict the speed of reactions [80]. Therefore, in addition to the thermodynamics, the kinetics of a system must be studied as well. The kinetics describe how fast reactions can occur.

In the case of electrochemistry, the rate of reaction is related to the chemical reaction rate and to the electrical driving force. A simplified chemical reaction is presented in equation 2.28. The rate constants for the forward and reverse reaction are indicated with k_f and k_r .



With these rate constants (s^{-1}) and the concentrations (C), the reaction rates v_f , v_r and the net reaction rate, v_{net} (M/s), can be determined:

$$v_f = k_f C_A \quad (2.29)$$

$$v_b = k_r C_B \quad (2.30)$$

$$v_{net} = k_f C_A - k_r C_B \quad (2.31)$$

With the rate constants, the equilibrium constant (K) for the reaction can be determined. At equilibrium there is no forward or backward conversion, therefore:

$$K = \frac{C_B}{C_A} = \frac{k_f}{k_r} \quad (2.32)$$

The rate of a reaction can, therefore, be determined with the corresponding rate constants. These, however, must first be determined experimentally [80]. To provide an approximation, Arrhenius showed the dependence of the rate constant on the temperature. This eventually led to the Arrhenius equation, relating the rate constant to the activation energy, E_A , the molar gas constant, R , the temperature, T , and the frequency factor, A [11].

$$k = A e^{-E_A/RT} \quad (2.33)$$

The variables E_A and A can be predicted by applying the transition state theory. By applying this method as described in 'Electrochemical Methods Fundamentals and Applications' by Bard and Faulkner (2001), the rate constants can be expressed in the following equation [11]:

$$k = \kappa_t \frac{k_B T}{h} e^{-\Delta G^\ddagger/RT} \quad (2.34)$$

With the transmission coefficient, κ_t , the Boltzmann constant, k_B , the Planck constant, h , and the change in free energy of the reaction, ΔG .

The equilibrium and rate constants for the reaction equations taking place in the bulk of the CO_2R cell, are indicated in equations 2.17 to 2.21. The values for the constants can, for example, be derived from

literature [37] [72] or can be calculated as shown in the 2019 research by Soeteman [102]. Rather than using experimental values, this research uses equations taking into account the temperature dependent behaviour of the reactions. It eventually concludes that especially the K_w and K_3/K_4 values strongly depend on temperature. For this reason, the same approach was adopted in this research as well. Table 2.2 expresses how the values of these (temperature dependent) equilibrium and rate constants can be calculated, while indicating the consulted source for each equation. The parameters for the equations are presented in table A.2 to A.5 in Appendix A.1.

Constant	Equation (T,p) or constant value	Source
PK_1, K_1	$\ln(K) = a_1 + a_2 * T + a_3/T + a_4/T^2 + a_5 * \log(T) + (a_6/T + a_7/T^2 + a_8/T * \log(T)) * (p - p_s) + (a_9/T + a_{10}/T^2 + a_{11}/T * \log(T) * (p - p_s)^2)$ $K_1 = e^{PK_1}$	[58]
PK_2, K_2	$\ln(K) = a_1 + a_2 * T + a_3/T + a_4/T^2 + a_5 * \log(T) + (a_6/T + a_7/T^2 + a_8/T * \log(T)) * (p - p_s) + (a_9/T + a_{10}/T^2 + a_{11}/T * \log(T) * (p - p_s)^2)$ $K_2 = e^{PK_2}$	[58]
PK_w, K_w	$PK_w = \log K_w = A + B/T + C/T^2 + D/T^3 + (E + F/T + G/T^2) \log \rho_w$ $K_w = e^{PK_w}$	[67]
K_3	K_1/K_w	-
K_4	K_2/K_w	-
k_{1f}	$\ln k = A + BS^{0.5} + D/T + E \ln T$	[50]
k_{1r}	K_{1f}/K_1	-
k_{2f}	value: $5.0 * 10^{10} \text{ Kg mol}^{-1} \text{ s}^{-1}$	[97]
k_{2r}	k_{1f}/K_1	-
k_{3f}	$k_{3f} = Ae^{-E_A/RT}$	[91]
k_{3r}	k_{f3}/K_3	-
k_{4f}	value: $6.0 * 10^9 \text{ Kg mol}^{-1} \text{ s}^{-1}$	[30],[97]
k_{4r}	k_{4f}/K_4	-

Table 2.2: Equations used in the 2019 study by Soeteman for the calculation of the required equilibrium and rate constants [102].

With the obtained rate constants and equation 2.31, the reaction rate can be derived. As mentioned before, the current density is proportional to the rate of reaction at an electrode. The equation relating the electrical driving force to the net reaction rate is the following [11]:

$$v_{\text{net}} = v_f - v_r = k_f C_O - k_r C_R = \frac{I}{nFA} = \frac{i}{nF} \quad (2.35)$$

With the concentrations (C_O and C_R) taken at the electrode surfaces, n as the number of consumed electrons at the electrode surface and F as the Faraday constant (i.e. the charge on one mole of electrons).

This clearly shows the dependence of the reaction rate on the current density, which, in turn, is related to the overpotential as shown in equation 2.14 and 2.11. It also shows the relation of the reaction rate to the surface concentrations at the electrode surfaces. This, therefore, expresses the importance of a high mass transfer for high reaction rates and efficient systems.

2.1.3. Mass transport

To ensure a high mass transport in an electrochemical cell, it is important to understand the different ways mass can be transported and the factors influencing this process. In an electrochemical cell, the transport of reactants from the bulk of the solution to the electrode surface is expressed as the flux, or ionic flux (N_i). The flux describes a quantity per unit time per unit area, as is described by the Nernst-Planck equation:

$$\mathbf{N}_i = \underbrace{-D_i \nabla c_i}_{\text{Diffusion}} - \underbrace{z_i u_{m,i} c_i \nabla \phi_1}_{\text{Migration}} + \underbrace{c_i \mathbf{u}}_{\text{Convection}} \quad (2.36)$$

Here, D_i denotes the diffusion coefficient of the species, c_i its concentration, $u_{m,i}$ the mobility of an ion, z_i the charge of the ion, $\nabla \phi$ the electric field strength and \mathbf{u} the velocity vector.

The total flux has contributions from three different forms of mass transport: diffusion, migration and convection. Diffusion is the mass transport that results from a concentration gradient. In the electrochemical cell reactants are consumed at the electrode surface, resulting in a concentration difference with the reactions in the bulk of the solution. This drives the diffusive mass transport of reactants to the electrode surface. Migration is the transport of charged species as a consequence of a potential gradient. In the electrochemical cell this is represented by the ionic charge through the electrolyte solution. The migration contribution to the total transport is small and often regarded as insignificant [80]. The 2019 report by Soeteman, however, states that these migration effects are larger under higher pressures, due to the higher surface concentrations, which implies the migration effects could be significant for this high pressure cascade study [102]. Whether the migration contribution will be incorporated in the model, will be investigated further in the modelling section (section 2.2). The last form of mass transport, convection, is a result of mechanical forces producing a velocity gradient. Some electrochemical cells employ convection transport driven by a mechanical pump, other choose to work without convective transport. The cell utilised in this study will rely on diffusive, migration and convective transport.

In section 2.2, 'Modelling', the functions for the different types of transport will be used to derive the PDEs (Partial Differential Equations) required to set up the eventual model. Below, the theory behind these equations will be discussed and the equations will be introduced.

A common way to describe the flux when dealing with steady state diffusion, is with Fick's laws of diffusion [91]. Fick's first law states that the flux is proportional to the change of concentration over position [80]. Here the flux depends on the diffusion coefficient, D , and the difference in concentration, which changes over distance x .

$$N = -D \frac{\partial C}{\partial x} \quad (2.37)$$

At the surface of the electrode, the reactants are reduced, resulting in a lower local concentration. Because of mass conservation, this loss of reactant at the electrode surface must be equal to the products formed. This results in the following equation [80]:

$$-D_{Ox} \frac{\partial C_{Ox}}{\partial x} = \frac{i}{nF} = D_R \frac{\partial C_R}{\partial x} \quad (2.38)$$

The law of Faraday states that the change in number of moles of substance over time is equal to the current divided by the number of electrons transferred, times the charge of an electron [80]. This effectively means that Fick's first law can be combined with Faraday's law, as shown in equation 2.38.

However, in most cases the concentration will vary with both time and distance. In this case, Fick's second law of diffusion can be used [91] [12]:

$$\frac{\partial C_i}{\partial t} = D_i \frac{\partial^2 C_i}{\partial x^2} + V_i(x, t) \quad (2.39)$$

With t indicating the time, x indicating the changing distance and V_i indicating the net rate of formation

of species i (due to chemical reactions) [12].

For the contribution caused by migration we look at the current transported by the ions in the solution. The transport number / transference number (t_+ or t_-) indicates how much current an ion can carry. It can be considered as the ratio of charge carried by an ion, i_i , relative to the total charge carried, i . The equation for the transport number is shown in equation 2.40 [11]. The transport number is dependent on the conductivity of the electrolyte solution, which, in turn, depends on: the ion charge (z_i), the mobility of an ion (u_i) and the ion concentration (C_i). The conductivity of a solution can be expressed as in equation 2.41 [11]. The more conductive the electrolyte solution, the higher the transport numbers [102]. By looking at the magnitude of the transport numbers for the ions involved, an indication can be made of the significance of the migration contribution to the total transport. In the 'Modelling' section, will elaborate on the reasoning behind the choice to incorporate the migration transport.

$$t_i = \frac{i_j}{i} = \frac{|z_j| u_i C_i}{\sum_k |z_k| u_k C_k} \quad (2.40)$$

$$\kappa = F \sum_i |z_i| u_i C_i \quad (2.41)$$

If the migration contribution is found to be significant, the next step is to determine its effect on the flux. The migration contribution on the total flux is already shown in equation 2.36 and can be determined in the following way. The migrating ions will attain a velocity in the direction of the electrical force (F), which is described in equation 2.42. The electric force is equal to the charge, q , times the electric field, $\nabla\phi$, as denoted in equation 2.43. The charge, q , is represented by the charge number of an ion, times the elementary charge on an electron, as shown in equation 2.44.

$$\mathbf{F} = -z_i e_0 \nabla\phi \quad (2.42)$$

$$\mathbf{F} = -q \nabla\phi \quad (2.43)$$

$$q = z e_0 \quad (2.44)$$

The velocity the ions will attain, will depend on the collisions with other molecules, expressed in the mobility (u_i) of the ion, and the force acting on it. This velocity is indicated with the drift velocity, v_d , and is expressed in equation 2.45 [1].

$$v_d = \frac{u_i}{e_0} \mathbf{F} \quad (2.45)$$

The migration flux of an ion, as a result of its drift velocity, is a product of the drift velocity and the concentration [1]. The mobility of an ion can be found using the Nernst-Einstein relation [12], as shown in equation 2.46. In combination with the derived relation for the drift velocity, this leads to equation 2.47, which expresses the migration contribution to the overall flux as was indicated in equation 2.36.

$$u_i = D_i \frac{F}{RT} \quad (2.46)$$

$$\mathbf{N}_{migration} = v_d C_i = \frac{u_i}{e_0} C_i \mathbf{F} = -z_i u_i C_i \nabla\phi \quad (2.47)$$

The contribution because of the convection is usually much larger than the migration contribution. It can be expressed mathematically for laminar flows in the following relation [12]:

$$\frac{\partial C_i}{\partial t} = -v_x \frac{\partial C_i}{\partial x} \quad (2.48)$$

Here, v represents the flow-rate and C the concentration of species i .

Based on this theory on mass transport inside electrochemical cells, the governing equations for the eventual model will be set up. The details regarding the defining the transport equations for the species involved and how these will be solved, will be further detailed in the 'Modelling' section (section 2.2). From how these mass transport equations are set up, the large dependence on the reactant concentration in each of the different forms of mass transfer becomes apparent. This relation will be utilised in the next section, which will investigate the effects of high pressure on the system.

2.1.4. High pressure effects

As mentioned in the introduction, the hypothesis of this study is that pressure will have a positive effect on both sequential steps in the cascade electrochemical cell. Previous studies have shown the solubility of CO_2 can be increased dramatically with pressure, effectively increasing mass transport [29] [39] [115]. For CO there have also been studies which indicated it could present similar behaviour as CO_2 , although it was only tested at lower pressures (<2.4 atm) [119] [57]. However, apart from solubility – and therefore mass transfer– putting pressure on the system might have an effect on the reaction kinetics as well. There are studies proposing the rate determining step of the reactions might change at increased pressure [102] [98]. This could explain the experimental results found by Todoroki et al. (1995), showing a change in the Tafel slope at 40 atm compared to 5 atm, as shown in figure 2.4 [115]. This section will provide an overview of the documented effects of pressure on the solubility and the kinetics as this is described in literature.

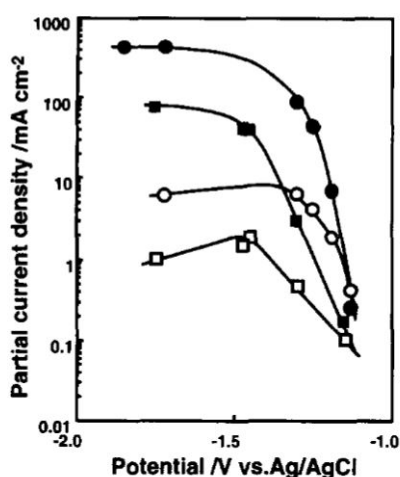


Figure 2.4: Tafel plot from experimental results by [115]. HCOOH at 5 atm (■), 40 atm (●) CO at 5 atm (□), at 40 atm (○).

Solubility of CO_2/CO

As mentioned before, the low solubility for CO_2 and CO are important limiting factors in the electrochemical production rates of C_{2+} products. However, by increasing the pressure in the system, this low solubility can be increased dramatically. To determine how these solubilities will behave, in order to accurately model them later, a number of things need to be considered. In a normal CO_2 reduction, finding the CO_2 solubility is the most challenging aspect, as this is influenced by the temperature, pressure and other particles present in the solution. However, because of the cascade, a more complicated system arises. The question is therefore, how will the solubility behaviour change if an additional gas will be dissolved as well? The next sections will be dedicated to describing the possible solubility behaviour of this system from a theoretical point of view. To what extent these phenomena will be incorporated in the eventual model, will be discussed in the section 2.2.

CO solubility

There are different ways to determine the solubility as a function of the pressure. The simplest way to consider this relation, is by using Henry's law, where H_{cp} represents Henry's constant [$\text{mol}/(\text{Lbar})^{-1}$]. This relation shows the concentration (C_i) increases with increasing pressure (p_i), as expected.

$$H^{cp} = \frac{C_i}{p_i} \quad (2.49)$$

This equation is a good representation of the general relation between pressure and concentration. It is, however, limited to dilute solutions under low pressures (< 5 bar) [12]. For the solubilities in

this study additional expressions must therefore be used. Since CO has relatively simple solubility behaviour compared to CO₂, the values can be found from experimental data describing the solubility as a function of pressure. Table 2.3 displays the CO solubility data in terms of Henry's constant as a function of pressure. Applying these values to equation 2.49 will result in a CO solubility expressed in moles of solute (CO) per mole of solution [78].

CO pressure		H *10 ⁻⁴	
mm Hg	bar	T= 17 °	T= 19 °
900	1.19	4.77	4.88
2000	2.67	4.77	4.91
3000	4.00	4.77	4.93
4000	5.33	4.78	4.95
5000	6.67	4.80	4.97
6000	8.00	4.82	4.98
7000	9.33	4.86	5.02
8000	10.67	4.88	5.08

Table 2.3: CO solubility data under different pressures. Derived from: [78].

CO₂ solubility

Determining the CO₂ solubility will be a little more complex because CO₂ reacts to bicarbonate, as shown in equation 2.17. In addition to high pressure effects, the expression for the CO₂ solubility should, therefore, also account for salting out effects. The salting out effect is the effect referring to the decrease in reactant solubility in the solution, due to the presence of added electrolyte. According to the 2019 study by Morrison et al., the salting out effects of bicarbonate (and other salts) can decrease the CO₂ solubility up to 20% [72]. This is a significant amount, therefore these effects cannot be neglected in the solubility calculation. The salting out effect can be described using an extension on Henry's law, the Sechenov equation [102] [61]:

$$\log \frac{\gamma_i}{\gamma_i^0} = \log \frac{S_i^0}{S_i} = k_s C_s \quad (2.50)$$

Here γ_i and γ_i^0 indicate the molar activity coefficients of the reactant in water and in electrolyte solution. S_0 indicates the CO₂ solubility in water; S the CO₂ solubility in the electrolyte solution at concentration C_s . K_s is the salting out parameter. The salting out parameters per electrolyte solutions can be found in literature from experimental data. This relation clearly shows the relation between the concentration and the salting out effects; the larger the salting out parameter, the smaller the concentration CO₂.

However, since this work aims to investigate the effects of high pressure, it is important to adopt a model for the calculation of the solubilities which incorporates the pressure effects in addition to the salting out effects. At present, multiple models exist, capable of accurately calculating the CO₂ solubility in several electrolytes, which incorporate: high pressures, large temperature ranges, high electrolyte concentrations and salting out effects. A complete overview comparing a number of these models can be found in the 2017 study by Shi and Mao [100]. These models are often based on the fact that the CO₂ solubility in electrolyte solutions can be found by expressing the balance between the chemical potential of the liquid $\mu_{CO_2}^L$ and the chemical potential of the gas $\mu_{CO_2}^V$. The chemical potential in liquid phase can then be expressed in terms of fugacity (f_{CO_2}) and in the vapor phase in terms of activity (α_{CO_2}), as shown in the equations 2.51 to 2.53 below [109].

$$\mu_{CO_2}^V = \mu_{CO_2}^L \quad (2.51)$$

$$\mu_{CO_2}^V = \mu_{CO_2}^{V(0)}(T) + RT \ln(y_{CO_2}P) + RT \ln \phi_{CO_2}(T, P, y_{CO_2}) \quad (2.52)$$

$$\mu_{CO_2}^L = \mu_{CO_2}^{L(0)}(T, P) + RT \ln m_{CO_2} + RT \ln \gamma_{CO_2}(T, P, m_{CO_2}) \quad (2.53)$$

Here the molarity in the liquid phase is indicated with m_{CO_2} , the mole fraction of CO_2 in the vapor phase with y_{CO_2} , the activity coefficient with $\gamma_{CO_2}(T, P, m_{CO_2})$ and the fugacity coefficient with $\phi_{CO_2}(T, P, y_{CO_2})$.

To solve the resulting equation, and find the solubility, the following parameters, therefore, need to be determined: $\mu_{CO_2}^{L(0)}(T, P)$, $\mu_{CO_2}^{V(0)}$, y_{CO_2} , m_{CO_2} , $\phi_{CO_2}(T, P, y_{CO_2})$ and $\gamma_{CO_2}(T, P, m_{CO_2})$.

An example of how these can be determined according to literature [109] [100] [66], is provided below:

- The standard chemical potential in the vapor phase, $\mu_{CO_2}^{V(0)}$, is often assumed to be zero
- The standard chemical potential in the liquid phase, $\mu_{CO_2}^{L(0)}(T, P)$, can be found, for example, with Pitzer's method [82]
- The mole fraction CO_2 in the vapor phase, y_{CO_2} , is dependent on the pressure (of H_2O and CO_2) and is often found with empirical relations or from models [8]
- The m_{CO_2} is the molarity of CO_2 in the liquid phase
- The activity coefficient $\gamma_{CO_2}(T, P, m_{CO_2})$, is complicated to determine. It can be determined with viral expressions regarding the excess Gibbs energy [66] [109], which can, in turn, be solved with the Pitzer method [83]
- The fugacity coefficient, $\phi_{CO_2}(T, P, y_{CO_2})$, can be found by applying equations of state [26] [104]

How the different parameters in the resulting equation will be found depends on the model, it is usually a combination of equations of state (Peng Robinson, Redlich-Kwong, etc.), fitting to experimental data and using pre-existing models.

Most models, however, focus on the ions: Na^+ , K^+ , Mg^{2+} , Ca^{2+} , Cl^- and SO_4^{2-} . For this study, because of the added $KHCO_3$ electrolyte, the ions of interest are K^+ and HCO_3^- . Since HCO_3^- is not one of the incorporated ions in the conventional models, this merits further research. In this respect, the 2015 study by Tang et al. investigated whether existing models for different ions could also work for HCO_3^- [109]. They found that, although HCO_3^- is larger, has a larger molecular weight and a smaller salting out effect (less hydration action), it presents similarly to Cl^- . Their premise was that this results from the equilibrium between CO_2 and HCO_3^- , where the HCO_3^- suppresses the CO_2 dissolution, eventually resulting in a similar salting out effect as Cl^- [109]. They came to this conclusion, by matching experimental results to three different models, including: the model of Duan et al. [27] and the PR-HV model [43] [77]. In doing so, they aimed to find whether these models could also predict sufficiently for a bicarbonate solution. The results indicated that the Duan model is a better fit for the experimental data at low salt concentrations (<0.7 mol/kg), while the PR-HV model fits better at high salt concentrations.

This research will utilise 0.1 M $KHCO_3$ electrolyte for the solution. Therefore, the Duan model will provide the most accurate results regarding the CO_2 solubility. Hence, the choice has been made to deploy the Duan model. Furthermore, this is the same solubility model as used in the studies on which the model in this research will be based [102] [72]. The implementation of this model into the high pressure cascade model will be described in more detail in section 4.4.

Partial pressure progression

The solubility of the CO_2 will not be constant throughout the system. There will be some dissolution because of a reduced partial pressure as a result of the production of products (gasses) [28]. In the first step, CO and H_2 are formed in the reduction of the aqueous CO_2 .

To illustrate this changing partial pressure effect, we will momentarily assume:

- Ideal gas behaviour
- Dalton's law holds (no reaction gasses)

- No other gasses are produced (negligible amounts) except for H₂ and CO
- Henry's law holds (low pressures and dilute solutions)
- Equilibrium and constant pressure/volume (*V*) in the head space

According to equation 2.54, the total pressure in the head space is based on the total number of moles (n_{tot}) present, independent of the type of gas. According to Dalton's law, the total pressure (P_{tot}) is the sum of each individual partial pressure (p_i), as shown in equation 2.55. By consulting Henry's law (equation 2.49) once again, the partial pressure can be related to the concentration with a constant, Henry's constant. Therefore, if a high concentration CO₂ as a result of a high partial pressure would start to react, the dissolved CO₂ concentration would decrease because its partial pressure is reduced in the creation of products. Initially, the total pressure in the system only contains p_{CO_2} (partial pressure of CO₂), as this is the only gas present. After it is partly reacted, H₂ and CO are created. Hence, the partial pressure p_{CO_2} will decrease, according to Dalton's law, as the total pressure is now divided over all three partial pressures. The partial pressure for a component i , can therefore be found with equation 2.56.

$$P_{tot} = \frac{n_{tot} * RT}{V} \quad (2.54)$$

$$p_{tot} = \sum_{i=1}^n p_i \quad (2.55)$$

$$P_i = \frac{n_i}{n_{tot}} * P_{tot} = x_i * P_{tot} \quad (2.56)$$

This means that the solubility behaviour of CO₂ will decrease during the reaction. This could be an important effect to incorporate in the model of this research, because literature has shown that not all CO₂ is reduced in the first step [63] [112]. This phenomena was investigated in the 2014 study by Dufek et al. Here they studied these changing partial pressures, and with the experimental data obtained, they set up an equation to relate the number of moles of CO₂ present (n_{CO_2}) to the number of moles of products produced [28]. With this knowledge, the ideal gas law, a known system volume (V) and P_{tot} , they can calculate the corresponding partial pressures: p_{CO_2} , p_{CO} and p_{H_2} . Note that their equations are derived for electrochemical generation of CO and H₂ in neutral and slightly basic operating conditions; in other situations the equations need to be modified.

$$n_{CO_2} = n_{CO_2, ini} - n_{CO} + n_{CO_2, entering} - n_{CO_2, leaving} - 2(n_{CO} + n_{H_2}), \quad (2.57)$$

With this formula (or an adapted form) an indication of the pressure changes due to product formation in the system can be obtained. This can be used to further specify the solubility behaviour of the gasses throughout the reaction, in order to model it accurately.

Cascade system

Having the reduction steps in a cascade further complicates the solubility behaviour. As explained before, CO is not the only molecule present in the solution; there is still CO₂ available as well. It was shown that their competing partial pressures reduce their solubility. However, their presence might affect their solubilities in another way as well. CO and CO₂ dissolve in water because the water molecules are attracted to the polar areas in the molecule and will locate around it. Therefore, one could hypothesise that there will be competition between CO and CO₂ for dissolving, on account that their presence reduces the 'free volume' in the solution. Therefore, the presence of the CO₂ molecules could have a negative effect on the level of solubility for the produced CO. In his thesis report, Soeteman mentions the possibility of this competing effect between CO and CO₂, although in his study CO is only produced as a side product (in low amounts) [102]. To determine the magnitude of this effect, Soeteman made an approximation using Henry's law (equation 2.49), estimating the impact of CO on the CO₂ solubility.

In this approximation he assumes:

- 10% of the vapor is CO
- 100% competition: each dissolved CO molecule would mean one less CO₂ molecule can be dissolved
- Standard conditions, $H^{CO_2} = 0.034$ mol/kg bar and $H^{CO} = 0.00099$ mol/kg bar

With this analysis, Soeteman found the effects to be insignificant. However, for this study the assumption that only 10% of the gas will be CO might not hold. When reviewing figure 2.5, showing the CO₂ and CO concentrations as found in the study of Gurudayal et al. [38] (supplementary data), it is clear that in this kind of set-up a lot more CO is produced. The article states that when deploying just the Ag electrode at a potential of -1.0 V vs RHE, about 90% of the products consists of CO, and 10% of H₂ (neglecting the small amounts of produced formate, methane, ethylene, etc.). So if we now assume the percentage of CO present is not 10% but rather 90%, and we follow the same approach as Soeteman, we see that under atmospheric conditions ($p = 1$ bar and $H^{CO} = 0.00099$ mol/kg bar) the concentration dissolved CO becomes 0.000891 mol/L, while the CO₂ concentration becomes 0.0034 mol/L. Under these conditions the competition suddenly does seem significant. Of course this is an approximation made with hypothetical exaggerated values, so it cannot be used for proving this concept.

After consulting literature, no research seems to be available on CO₂/CO competition in electrolyte solutions. However, some molecular simulation studies have been done in ionic liquids (i.e. liquid salts). The 2008 study by Shi and Maginn, investigating the mixed gas absorption effects of CO₂ and O₂ in ionic liquids, shows that at high pressures they compete with each other [99]. Also, this principle of competition is used to protect rape seed oil from oxidation, by dissolving CO₂ in the oil, so less oxygen can be dissolved [108]. The lack of research on this topic can, however, not be taken as an indication of the effect being insignificant, since the studies where this effect would be significant (cascade reduction) are not that common. To accurately describe this effect in a model, we depend on new molecular simulation studies for predicting these effects in electrolyte solutions.

Recommendations for the model

The sections above have shown that accurately modelling the solubility behaviour of CO and CO₂ as a result of high pressure, can be done with the Duan model and experimental results. However, the modelling of the combining of the two steps in the system will prove to be a challenge. There are clear indications that the dissolving of both gasses will affect the solubility behaviours, because of changing partial pressures and competition effects. However, this dissolving competition between molecules had not yet been investigated in electrolyte solution systems, and will therefore be too complicated to model at this point. In addition, there have been reports of the local CO concentration to rise above the CO solubility limit in simulations of cascade systems [63] [38]. This indicates that these pressure effects and competition effects might play a significant role in the solubility behaviour. The changing partial pressures can be calculated with the formula by Dufek et al. (2014) [28] and checked with the experimental data from Wang et al. [121]. But since the competition effects are not precisely known / not extensively expressed, they will be complicated to model. Hopefully in time, possibly after running the experiments, more will become clear on this subject.

To still account for these effects, a possible route could be to check with results of current models and systems. Therefore, the experimental results of local concentrations found in literature (as shown in figure 2.5) could be consulted to indicate local CO and CO₂ concentrations for the second reduction step. After obtaining experimental results, these values can then be updated.

If these effects will be simulated in the high pressure cascade model will be discussed in section 2.2 and section 4.3. Even if these described effects are deemed outside of the scope of this research in the modelling stage, they could still be useful in describing possible relations and results and their match with experimental research in the discussion of this report.

Kinetics

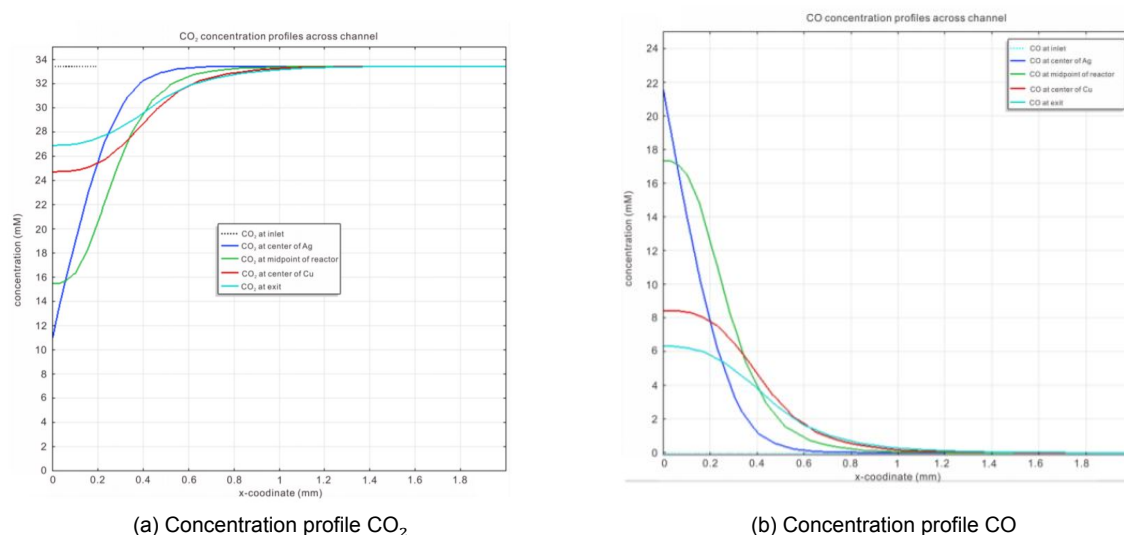


Figure 2.5: Comparison of the concentration profiles of CO₂ and CO throughout the channel ($Q=2 \text{ cm}^3/\text{min}$) and with $J_{Ag}=3 \text{ mA}/\text{cm}^2$, in the set-up from [38].

So far, there has been some research on high pressure CO₂ reduction, but not much on high pressure CO reduction. It would be interesting to know if the response to pressure of CO reduction is similar to that of CO₂. This work hypothesizes that high pressure will also have a positive effect on the CO reduction step. The effects of pressure can of course be seen in the solubility behaviour, but there have been signs that pressure could also influence the reaction mechanism / kinetics. To find out how both sequential reduction steps might react under high pressures, the effect of pressure on the reaction kinetics needs to be investigated further. This section will describe literature findings on this subject, to predict this behaviour from a theoretical point of view.

The 2019 report by Soeteman investigates the effect of the pressure on the reaction kinetics on the surface of the CO₂ reducing cathode [102]. They propose the change in Tafel slopes found in figure 2.4, can be induced by a change in the rate limiting step, or by an increased CO₂ adsorption at higher pressures. The rate limiting step, or rate determining step, refers to slowest step in the reaction kinetics. This step is often much slower than the others, therefore it largely dominates the electrode kinetics. In the case of complicated reaction mechanisms (i.e. mechanisms with multiple electron transfer steps), such as in CO₂R to CO, the Tafel slope is determined by the rate determining step in the mechanism. Hence, the observed change in the Tafel slope in the experimental results of Todoroki et al. (1995) [115], could indeed indicate a change in the rate determining step as proposed by Soeteman. In his research he investigated this claim and concludes that, however possible, there is too little experimental data available to prove the mechanism of reduction changes at higher pressures. The data they used originated from an investigation in 1995 by Todoroki et al., showing the Tafel plots for CO and HCOOH production at 5 and 30 bars, which is shown in figure 2.4 [115]. There is a non-linearity in the plot for 40 bars, which is hard to explain theoretically. It would therefore be interesting to provide additional experimental data (Tafel plots at different pressures) to further prove the hypothesis of Soeteman in this research.

However, in 2020 another study came out, executed by Shaughnessy et al., investigating the effects of pressure on CO₂ reduction reaction rates [98]. In this study they used a COMSOL-based mechanistic model to simulate CO₂R at Au electrodes at elevated pressures. The model determines the rate determining step under different conditions by setting up the rate equations and by varying the rate constants (k_i) or electron-transfer kinetic rate constants (k_i^0), to determine if this affects the CO formation. The reaction mechanism they assume is shown in figure 2.6.

The results they found, indicate that the rate determining step under ambient conditions is indeed the

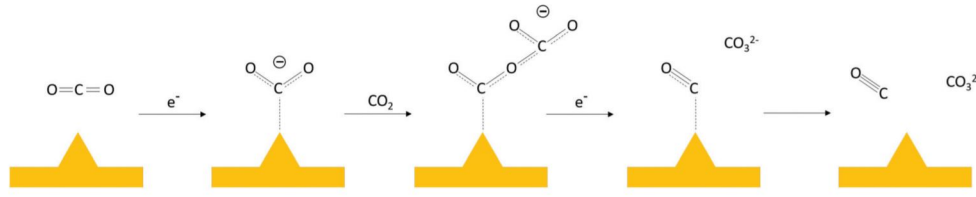


Figure 2.6: Reaction mechanism for CO_2 reduction on Au, producing CO. Derived from: [98].

first step for all potentials. Varying the catalytic site density had no effect on the results, which indicates that the CO_2 concentration is the limiting factor. Interestingly, when increasing pressures, there is a point (3.1 MPa) where the limiting factors become: k_1^0 , k_3^0 and the catalyst site density S^* . The fact that increasing the available catalyst sites does have an effect on the CO formation, indicates that under high pressure conditions this is the limiting factor. At these high pressure conditions (3 MPa) the results indicate that it does not have a sufficient effect to increase the k_1^0 . However, when simultaneously increasing k_1^0 and k_3^0 , an effect is visible. This indicates that when dealing with high pressure situations, the rate determining step does in fact partly change. In addition, the CO_2 adsorption may indeed be limited due to too few available sites, as was expected by Soeteman. Shaughnessy et al., conclude that at high pressures, to increase the reduction rate (CO_2 to CO), catalysts which increase the number of sites and increase fast electron-transfer kinetics for the first and third steps, need to be developed.

The rate for the first and third steps is expressed as:

$$r_1 = k_1 [\text{CO}_2] [S^*] \quad (2.58)$$

$$r_3 = k_3 [\text{OCOCO}_2^{\ominus} (\text{ads})] \quad (2.59)$$

Where:

$$k_1 = k_1^0 e^{-\alpha f(E-E^{\circ})} \quad (2.60)$$

$$k_3 = k_3^0 e^{-\alpha f(E-E^{\circ})} \quad (2.61)$$

This shows that pressure influences the kinetics of CO_2 R for forming CO, but the main question is: 'does it have an effect on CO reduction reaction kinetics as well?' The second reduction step in the cascade process involves many electron and proton transfers, making it significantly more complex than the first. Many different products can be produced in this reaction step, each with different proposed reaction pathways. Research is still being performed to map all these different pathways, but some consensus has been reached on the general process (from CO_2 to C-C coupling, with CO as key intermediate): 1) CO_2 is adsorbed on the catalyst surface, 2) electron transfer and/or proton transfer takes place to break the C-O bonds and form C-H bonds, 3) product species get rearranged and desorb from the catalyst surface [107]. But how exactly these surface bonds are formed, is hard to determine.

According to the 2018 study by Schreier et al., there are two possible surface-reaction mechanisms which could be in play: the Langmuir-Hinshelwood (LH) or the Eley-Rideal (ER) [96]. In the LH, the species bound to the surface react with each other, as shown in figure 2.7 a. In the ER, the species bound to the surface react with species in the solution, as shown in figure 2.7 b. Which of these surface reactions takes place in a reaction mechanism, is important for its response under increased pressure. In the case of an ER mechanism, increasing the CO concentration at the surface will increase the reaction, but for the LH mechanism this will not work as well, because increasing the CO surface concentration, leaves less spaces for the – also required – H species to bond with the surface.

With this basic knowledge on the reaction processes, we can hypothesise if similar pressure effects on the kinetics could take place in the second step as well. The exact pathways depend on the specific C_{2+} product, but all of them require multiple proton (H^+) and electron (e^-) transfer steps. Some possible reaction routes for CO_2 reduction (with CO as intermediate), based on DFT (Density-Functional Theory) results and experimental results, are displayed in figure 2.8.

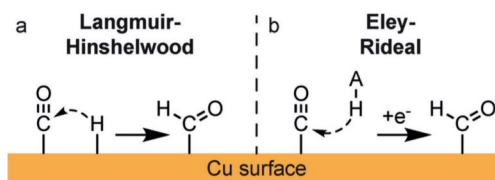


Figure 2.7: Two types of surface reactions: a) Langmuir-Hinshelwood LH. b) Eley-Rideal. Derived from: [96].

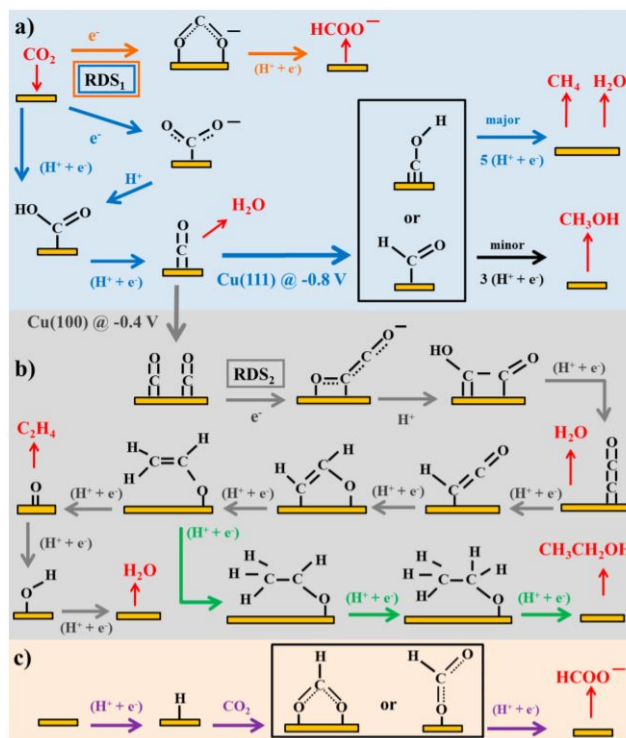


Figure 2.8: Possible reaction pathways for CO_2 reduction (with CO as intermediate) to form: a) formate, methane and methanol, b) ethylene and ethanol, c) formate. Derived from: [54].

The 2018 study by Schreier et al., investigates the effects of partial CO pressure on the reaction kinetics for the production of methane and ethylene on Cu [96]. They study the likelihood of the reaction mechanism to depend on a LH or ER surface mechanism, and provide insight in the species involved in the steps leading up to the rate limiting step. The precise identity of the products in the rate determining step are, therefore, not specified. They started with the theory that, when increasing the CO pressure p_{CO} , there is more CO and surface bound *CO present at the electrode (as there was in the first step of the CO_2 reduction on Au). However, the results of the investigation showed that when increasing the p_{CO} , the methane production was largely suppressed. This indicates this reaction most likely follows a LH surface mechanism, since, even though CO is an important reactant for methane production, the reaction would depend on surface bound *H as well. The increased presence of *CO would constrain the available surface sites for *H , and therefore constrain the reaction. For the formation of ethylene, on the other hand, the rate limiting step is often indicated as the coupling of two CO species, either via LH or ER [103] [96] (see figure 2.8). Results from the study indicate the LH pathway, again, is more likely in this case. The reaction is found to be not too sensitive to the CO pressure, as *H was never involved in the rate determining step, which is therefore not influenced as much by the restricted available surface space for *H species.

Later, in 2020, Song et al., also investigated the effects of partial pressure on the reaction mechanism

for ethylene production [103]. In this research, the dependence of ethylene production by CO_2RR on partial CO_2 pressure was investigated. Their results indicate that low CO_2 partial pressures aid in the C-C coupling, because of the competition between the $^*\text{CO}_2$ and $^*\text{CO}$ species on the surface under high pressures, leaving little room for the required $^*\text{CO}$ $^*\text{CO}$ coupling. They show that, under large CO_2 partial pressures, CO is the most dominant reaction product, while only a limited amount of C_2H_4 is produced. This is partly caused by the limited space on the surface for the $^*\text{CO}$, but also by the increased adsorbate-adsorbate interactions between $^*\text{CO}$ - $^*\text{CO}$ or $^*\text{CO}$ - $^*\text{CO}_2$. These interactions have been known to lead to CO desorption from the surface, before the C-C coupling can take place.

Knowing this, this only adds to the list of advantages of separating the two reduction steps in a cascade cell. This way the Cu surface will not be as occupied with $^*\text{CO}_2$, restricting $^*\text{CO}$ surface binding, as it would otherwise be. The high partial CO_2 pressures could, therefore, increase the CO production in the first step, while containing the negative effect on the second step reactions, since the CO_2 concentration and partial pressure will be lowered. Also, when comparing the effects of pressure on both of the sequential reduction steps, we see that in the first step there is likely little to no dependence on proton transfer steps (depending on the assumed reaction pathway). Therefore, pressure can increase the kinetics, by increasing the surface concentration of $^*\text{CO}_2$, without being limited by the limitation in available surface sites for $^*\text{H}$ species. For the second step this is not the case, the reactions, overall, do depend on multiple protonations, which could mean the lack of available surface sites can become limiting for the reaction kinetics. This, however, will depend on the product and the surface-reaction mechanism.

This behaviour is too complicated to be added to the model in this research. However, this information could later aid in explaining experimental results. It would therefore be interesting to set up some experimental checks, to see if this described course of reaction is an accurate description of the kinetics of the system. To check if the restricted concentration of $^*\text{H}$ influences the kinetics of the second step, a higher concentration of electrolyte can be added to the system, so the available level of protons will be increased. If this would result in faster kinetics, it could be an indication of the level of protons at the electrode surface being restricting the kinetics. Another indication for this phenomenon would be to monitor the selectivity for methane production, since increasing the CO pressure will lead to a larger $^*\text{CO}$ concentration, suppressing the $^*\text{H}$ formation and therefore CH_4 and H_2 production. Hence, the selectivity for ethylene increases (but not the production rate), while the selectivity for methane will be very low [96].

2.2. Modelling

A good way to provide insight into the response of the high pressure cascade system to certain parameters and conditions, is by developing a model. The model will be based on theoretical knowledge, as explained in the previous sections. Although these relations and equations are already known, there are so many variables impacting the system, a numerical approach will be required to provide an accurate overview of the response. Subsequently, the modeled results will be compared to experimental studies. This way the discovered results and relations can be analysed, providing newfound insights into this new high pressure cascade system. Therefore, this chapter will be dedicated to finding the design parameters for the construction of a model that simulates the behaviour inside the new reactor set-up as closely as possible.

2.2.1. Existing models and limitations

In this section the modelling approach of several studies in literature will be compared and assessed on their assumptions and agreement with reality. The general set-up for a model describing an electrochemical reduction step will be followed, and the assumptions made in each step per model will be investigated on validity. This will eventually lead to the design parameters the model in this study will be based on.

The models that will be compared throughout these sections are:

- Gupta et al. 2005 [37]
- Burdyny et al. 2017 [18]
- Kotb et al. 2017 [55]
- Raciti et al. 2017 [85]
- Soeteman 2019 [102]
- Morrison et al. 2019 [72]
- Chen et al. 2020 [21]

Although there are more models available in literature, the decision has been made to include the most recent and representative models in this study. Most of the models are based on the approach (or values) taken by the 2005 model of Gupta et al., therefore, this model is included as well [37].

The first difficulty in modelling the two-step CO_2 conversion reaction towards C_{2+} products, is the fact that CO_2 participates in the equilibrium (buffer) reactions, while also being the reactant. Therefore, the CO_2 concentration profile near the electrode becomes nonlinear, requiring numerical calculation methods [37].

In literature, the usual approach for the modelling of the reactions in an electrochemical cell, is to set up a set of partial differential equations (PDEs) for describing the transport of the species in the bulk (diffusion, migration and convection), to the electrode surface. These equations will then be solved using numerical analysis, by defining initial conditions and boundary conditions. These can be defined from the bulk equilibrium reactions and the electrochemical reactions at the electrode surface. To model the transport, the cell is often divided into three sections: the bulk, the diffusion layer and the electrode surface, as shown in figure 2.9. Within these separate sections, different assumptions hold and different transport phenomena dominate. Therefore, all three areas and the accompanying assumptions and equations will be described separately.

The general assumptions made while setting up these kinds of models are [102]:

- The focus is only on the cathodic part of the cell, assumed is therefore that the anodic reactions are not limiting the system
- Constant temperature of 298.15 K is assumed
- The pH of the bulk is in range for reactions 2.19 and 2.20 to dominate (acidic)
- The pH near the electrode surface is considered alkaline as a result of the produced OH^- , therefore, the electrochemical reactions are regarded to be basic

The bulk

The general assumptions made to model the bulk section:

- The bulk concentrations are constant over time:
 - The bulk volume is large compared to the electrode areas
 - Mass transfer phenomena in the bulk phase are negligible
 - The bulk solution is always in equilibrium with $\text{CO}_2(\text{g})$
 - The bulk solution is ideally mixed (depending on cell design)
- The bulk concentration only depends on temperature, (CO_2) pressure and the salting out effects
- The concentration of products in the bulk is assumed to be zero

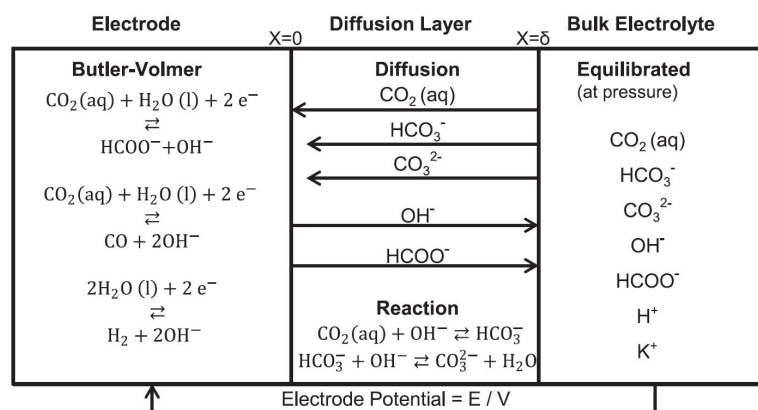


Figure 2.9: Schematic representation of the three sections considered in the model: the bulk solution, the diffusion layer and the electrode surface. The travelling species are also indicated per layer. Only diffusion is taken into account in this model. Derived from: [72].

- The products will immediately enter the gas phase and will not interact with the partial pressure of the reactant

In the bulk the concentrations are assumed to be constant over time. This assumption is based on the assumptions that: the bulk volume is very large compared to the electrode areas, the concentrations of the species are not dynamically influenced by mass transport phenomena, in the bulk the electrolyte solution is always in equilibrium with the CO_2 gas and the solution is ideally mixed. Therefore, the changing concentrations at the electrodes are assumed not to change the bulk concentrations significantly. Note that, to achieve an equilibrium between $\text{CO}_2(\text{g})$ and the electrolyte solution, $\text{CO}_2(\text{g})$ needs to be supplied continuously to the solution.

The first step in setting up the model is to determine the equilibrium concentrations of the dissolved species in the system. For this, the equilibrium reactions for the dissolved CO_2 are required. These are defined in section 2.1.2 'Chemical reactions', in equation 2.17 to 2.21. It will depend on the pH in the system which of these reactions will dominate, in alkaline solutions this will be equation 2.19 to 2.20, while in acid solution equations 2.17 to 2.18 will dominate. As described in the theory section, the pH of a 0.1 M KHCO_3 solution is 8.9, but will decrease to 6.8 after saturating with CO_2 . Most models assume pH conditions to be slightly acidic (<7), and therefore assume equations 2.19 to 2.20 to describe the system [21] [37] [55] [102] [85].

The concentrations of the species will be determined with these equilibrium equations (including equilibrium constants, K) and the $\text{CO}_2(\text{aq})$ concentration. This process and the accompanying formulas are accurately described in the 2017 research by Kotb et al. (equations 25 to 29) [55]. The equilibrium equations are often taken from literature or calculated with, for example, the Van't Hoff equation (assuming constant pressure and C_p) or the temperature dependent heat capacity and pressure dependent model by Li and Duan (2007) [58]. This last model is particularly of interest for the models incorporating high pressure effects [102] [72]. The next thing to determine, is the concentration of $\text{CO}_2(\text{aq})$ in the solution. The CO_2 solubility can be calculated with different types of models, as explained in section 2.1.4. Most models in literature assume the $\text{CO}_2(\text{aq})$ concentration is a constant at given pressure and temperature. They, therefore, model the CO_2 solubility according to Henry's law (equation 2.49) [21] [85], with an optional addition of the Sechenov equation (equation 2.50), to account for the salting out effects of the ions in the solution [55] [37] [18]. The only models taking into account high pressures in their solubility calculations [102] [72], are the models considering the Duan approach [27]. This method was explained in section 2.1.4.

Following this approach, the bulk concentrations, which are assumed constant over time, can be calculated and used in the next sections.

The diffusion layer

The general assumptions made to model the diffusion layer are:

- Products will bubble (away) directly after formation
- Products will transfer to the bulk, without interacting with other species (no reactions with products take place)

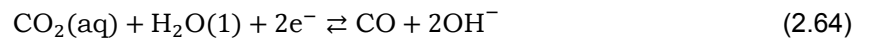
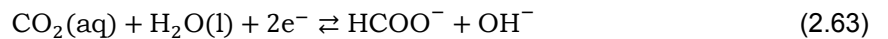
In this layer the species are transported from the bulk and the electrode surface, meaning that the concentrations are no longer constant over time and space. The different ways of transport of species are explained in detail in section 2.1.3, 'Mass transport'. Here it was explained, that there are three different types of transport: diffusion, migration and convection. Most models only take into account the diffusion transport in the diffusion layer [37] [85] [18] [72], since they neglect the convection contribution due to the fact that the bulk solution is well mixed and always in contact with the diffusion layer. Some models also neglect convection as they assume a large stagnant layer (i.e. hydrodynamic boundary layer), as a result of friction at the channel wall [21]. When this stagnant layer has approximately the same size as the diffusion layer ($\approx 100 \mu\text{m}$) the convection is assumed negligible in this section. Apart from this, the migration term is often neglected, based on the fact that the most important species, $\text{CO}_2(\text{aq})$, is not charged, so it will not be affected by migration. Another reason to neglect the migration transport, is that even with the (bi)carbonate ions, which are charged, the diffusion layer is regarded as more conductive than the bulk, due to the created OH^- at the electrode surface or a sufficiently high electrolyte concentration [72]. Other models do include the migration term [55] [102] [21]. They include this term, since they take into account that the electrolyte is not just supporting in this case, but it actually takes place in the reactions. Therefore, the transportation of HCO_3^- influences the local CO_2 concentration, according to reaction 2.19. As explained before, the CO_2 concentration in the diffusion layer depends on the transport from the bulk solution and the reactions taking place at the electrode surface. The CO_2 concentration near the surface will therefore decrease, because of the migration of HCO_3^- . According to Soeteman (2019), a large part of the current will be carried by K^+ and HCO_3^- (calculated with the transport numbers, as described in section 2.1.3 ('Mass transport'), and this effect will only increase with pressure, due to the higher product concentrations produced [102]. Not accounting for migration will, therefore, result in an overestimation of the limiting current.

We, therefore, observe a division in the modelling of the mass balances (PDEs). The models only taking into account diffusion, model the transportation assuming film theory, with Fick's diffusion equation, as shown previously in equation 2.39. The models that do take into account the migration, will add an extra term, as shown in equation 2.62 [102]:

$$\frac{\partial C_i}{\partial t} = D_i \cdot \frac{\partial^2 C_i}{\partial x^2} + \frac{z_i F}{RT} D_i C_i \cdot \frac{\partial^2 \phi}{\partial x^2} + V(C_1, C_2, \dots, C_n) \quad (2.62)$$

Here, ϕ denotes the potential, z_i the ion charge, D_i the diffusion coefficient, R the molar gas constant and C_i the concentration of species i .

To provide an example of the resulting mass balance equations (PDEs), the reactions taking place in the studies by Gupta et al. (2005), Burdyny et al. (2017), Soeteman (2019) and Morrison et al. (2019), producing HCOO^- , OH^- and CO , are taken into account [37] [18] [102] [72].



These equations give the following partial differential equations. Note that, in the case of Gupta et al., Burdyny et al., and Morrison et al., the migration terms shown below are not included.

$$\frac{\partial C_{\text{CO}_2}}{\partial t} = D_{\text{CO}_2} \cdot \frac{\partial^2 C_{\text{CO}_2}}{\partial x^2} - r_3^f + r_3^r \quad (2.66)$$

$$\frac{\partial C_{\text{HCO}_3^-}}{\partial t} = D_{\text{HCO}_3^-} \cdot \frac{\partial^2 C_{\text{HCO}_3^-}}{\partial x^2} - \frac{F}{RT} D_{\text{HCO}_3^-} C_{\text{HCO}_3^-} \cdot \frac{\partial^2 \phi}{\partial x^2} + r_3^f - r_3^r - r_4^f + r_4^r \quad (2.67)$$

$$\frac{\partial C_{\text{CO}_3^{2-}}}{\partial t} = D_{\text{CO}_3^{2-}} \cdot \frac{\partial^2 C_{\text{CO}_3^{2-}}}{\partial x^2} - 2 \cdot \frac{F}{RT} D_{\text{CO}_3^{2-}} C_{\text{CO}_3^{2-}} \cdot \frac{\partial^2 \phi}{\partial x^2} + r_4^f - r_4^r \quad (2.68)$$

$$\frac{\partial C_{\text{OH}^-}}{\partial t} = D_{\text{OH}^-} \cdot \frac{\partial^2 C_{\text{OH}^-}}{\partial x^2} - \frac{F}{RT} D_{\text{OH}^-} C_{\text{OH}^-} \cdot \frac{\partial^2 \phi}{\partial x^2} - r_3^f + r_3^r - r_4^f + r_4^r \quad (2.69)$$

$$\frac{\partial C_{\text{HCOO}^-}}{\partial t} = D_{\text{HCOO}^-} \cdot \frac{\partial^2 C_{\text{HCOO}^-}}{\partial x^2} - \frac{F}{RT} D_{\text{HCOO}^-} C_{\text{HCOO}^-} \cdot \frac{\partial^2 \phi}{\partial x^2} \quad (2.70)$$

Since we established that K^+ also plays a role in determining the concentrations, the following equation should also be considered:

$$\frac{\partial C_{\text{K}^+}}{\partial t} = D_{\text{K}^+} \cdot \frac{\partial^2 C_{\text{K}^+}}{\partial x^2} + \frac{F}{RT} D_{\text{K}^+} C_{\text{K}^+} \cdot \frac{\partial^2 \phi}{\partial x^2} \quad (2.71)$$

With:

$$\begin{aligned} r_3^f &= k_3^f [\text{CO}_2] [\text{OH}^-] \\ r_3^r &= k_3^r [\text{HCO}_3^-] \\ r_4^f &= k_4^f [\text{HCO}_3^-] [\text{OH}^-] \\ r_4^r &= k_4^r [\text{CO}_3^{2-}] \end{aligned} \quad (2.72)$$

The diffusion coefficients, D_i (m^2/s), used in these equations, are generally derived from literature. Often they are regarded as constant, but some studies do include a correction for the changing viscosity, originating from changing electrolyte concentrations [37]. The molecular simulation study by Zeebe (2011), provides equations describing the diffusion coefficients of dissolved CO_2 , HCO_3^- and CO_3^{2-} in a temperature range of 0-100°C dependent on isotopic mass and is, therefore, an appropriate way to determine the diffusion coefficients [125]. This last approach was adopted by Soeteman for the modelling of the corresponding diffusion coefficients in his study [102].

With these second order time dependent partial differential equations, the transport behaviour in the diffusion layer can be described. To solve them, a number of initial and boundary conditions are required. The diffusion layer ranges from $x=0$, the bulk, to $x=\delta$, the electrode surface, as can be seen in figure 2.9. Distance is indicated with x and time with t .

Initial conditions

For the initial conditions, the diffusion layer is assumed to be in equilibrium with the bulk solution, therefore the initial concentrations equal the bulk concentrations at $t=0$. Note that most models, except Soeteman's, do not incorporate the balance for K^+ (equation 4.5), therefore leave out the last initial condition [37] [18] [85] [72].

$$\left\{ \begin{array}{ll} [\text{CO}_2]_x^{t=0} = [\text{CO}_2]_{\text{bulk}} & \text{for } 0 \leq x \leq \delta \\ [\text{HCO}_3^-]_x^{t=0} = [\text{HCO}_3^-]_{\text{bulk}} & \text{for } 0 \leq x \leq \delta \\ [\text{CO}_3^{2-}]_x^{t=0} = [\text{CO}_3^{2-}]_{\text{bulk}} & \text{for } 0 \leq x \leq \delta \\ [\text{OH}^-]_x^{t=0} = [\text{OH}^-]_{\text{bulk}} & \text{for } 0 \leq x \leq \delta \\ [\text{HCOO}^-]_x^{t=0} = 0 & \text{for } 0 \leq x \leq \delta \\ [\text{K}^+]_x^{t=0} = [\text{K}^+]_{\text{bulk}} & \text{for } 0 \leq x \leq \delta \end{array} \right. \quad (2.73)$$

Boundary conditions

Two sets of boundary conditions are considered; one at the diffusion layer bulk interface ($x=\delta$, $t>0$) and the other at the diffusion layer electrode interface ($x=0$, $t>0$). Note that in some models, the location of the bulk is indicated with $x=0$, so the electrode layer will be at $x=\delta$ [37] [85].

At $t>0$ and $x=\delta$ the boundary conditions are [102]:

$$\left\{ \begin{array}{ll} [\text{CO}_2]_{x=\delta}^t = [\text{CO}_2]_{\text{bulk}} & \text{for } t > 0 \\ [\text{HCO}_3^-]_{x=\delta}^t = [\text{HCO}_3^-]_{\text{bulk}} & \text{for } t > 0 \\ [\text{CO}_3^{2-}]_{x=\delta}^t = [\text{CO}_3^{2-}]_{\text{bulk}} & \text{for } t > 0 \\ [\text{OH}^-]_{x=\delta}^t = [\text{OH}^-]_{\text{bulk}} & \text{for } t > 0 \\ [\text{HCOO}^-]_{x=\delta}^t = 0 & \text{for } t > 0 \\ [\text{K}^+]_{x=\delta}^t = [\text{K}^+]_{\text{bulk}} & \text{for } t > 0 \\ \frac{d\phi}{dx}(x = \delta) + \phi(x = \delta) = 0 & \text{for } t > 0 \end{array} \right. \quad (2.74)$$

As mentioned at the start of this section, assumed is that the products (here: formate) are removed from the solution after formation, so there will be none present in the bulk solution.

At $t > 0$ and $x = 0$ the boundary conditions are [102]:

$$\left\{ \begin{array}{l} D_{\text{CO}_2} \frac{d[\text{CO}_2]}{dx} \Big|_{x=0} = \text{CO}_2 \text{ consumption} = -10^{-2} \left(\frac{j_{\text{HCOO}^-}}{n_{\text{HCOO}^-} F} + \frac{j_{\text{CO}}}{n_{\text{CO}} F} \right) \\ D_{\text{HCO}_3^-} \frac{d[\text{HCO}_3^-]}{dx} \Big|_{x=0} - \frac{F}{RT} D_{\text{HCO}_3^-} C_{\text{HCO}_3^-} \cdot \frac{d\phi}{dx} \Big|_{x=0} = 0 \\ D_{\text{CO}_3^{2-}} \frac{d[\text{CO}_3^{2-}]}{dx} \Big|_{x=0} - 2 \cdot \frac{F}{RT} D_{\text{CO}_3^{2-}} C_{\text{CO}_3^{2-}} \cdot \frac{d\phi}{dx} \Big|_{x=0} = 0 \\ D_{\text{OH}^-} \frac{d[\text{OH}^-]}{dx} \Big|_{x=0} = \text{OH}^-_{\text{formation}} = 10^{-2} \left(\frac{j_{\text{HCOO}^-}}{n_{\text{HCOO}^-} F} + 2 \frac{j_{\text{CO}}}{n_{\text{CO}} F} + 2 \frac{j_{\text{H}_2}}{n_{\text{H}_2} F} \right) \\ D_{\text{HCOO}^-} \frac{d[\text{HCOO}^-]}{dx} \Big|_{x=0} = \text{HCOO}^-_{\text{formation}} = 10^{-2} \frac{j_{\text{HCOO}^-}}{n_{\text{HCOO}^-} F} \\ D_{\text{K}^+} \frac{dC_{\text{K}^+}}{dx} \Big|_{x=0} + \frac{F}{RT} D_{\text{K}^+} C_{\text{K}^+} \cdot \frac{d\phi}{dx} \Big|_{x=0} = 0 \\ \frac{d\phi}{dx} \Big|_{x=0} = 0 \end{array} \right. \quad (2.75)$$

Illustrated in this set of equations is that the production/consumption of HCO_3^- , CO_3^{2-} and K^+ is zero, since these species do not participate in the electrochemical surface reactions. At the same time, the boundary condition shows that the consumption of reactants and formation of products that do participate, is dependent on: the current density at the electrode surface (j), the Faraday constant (F) the stoichiometric coefficient (ν_i) and the amount of participating electrons, (n_i). This relation can be derived from the mass continuity equation and a source/sink relation. The mass continuity equation, equation 2.76, illustrates that the mass flux must be equal to the present source/sink (R_i) [55]. Here the source/sink is the formation or consumption of species, which can be found with the following formula [55]:

$$\nabla \cdot \mathbf{N}_i = R_i \quad (2.76)$$

$$R_i = \frac{\nu_i j_{loc}}{n_i F} \quad (2.77)$$

The stoichiometric coefficients and the number of electrons participating can be found in literature [37] [85]. The sign of the relation depends on whether the species involved is a product (source) or a reactant (sink) [72]. How the partial current densities of the species (j_i) can be found, is described in the next section 'The electrode surface'.

2.2.2. The electrode surface

The general assumptions made to model the electrode surface are as follows.

- The overpotentials are high enough to assume Butler-Volmer kinetics for the electrochemical reactions ($\gg 52$ mV)
- The water concentration is constant
- There are no mass transfer limitations constricting the H_2 production

- The H₂ production is seen as independent from the CO₂ (not influenced by it)

At the electrodes the electrochemical reactions take place (equations 2.63 - 2.65), therefore, species are reduced and produced, changing the local concentrations. To determine how much is produced/consumed, the partial current densities of the species (j_i) need to be found. The relation that can provide the current density in this regime, is the Butler-Volmer equation. This equation originates from the current overpotential equation which was shown before, in equation 2.11. As explained before (section 2.1.1 'Efficient cell design'), at high overpotentials, the kinetics can be modelled with Butler-Volmer kinetics (Tafel equation). If the solution is well stirred, surface concentrations do not differ too much from the bulk and the currents are low, equation 2.11 will reduce to the Butler-Volmer equation [11]. The Butler-Volmer equation for the cathode side is shown below, in equation 2.78.

$$i_j = i_{o,j} \exp\left[\frac{-\alpha_{c,j}F}{RT}\eta_i\right] \quad (2.78)$$

Here, the overpotential denotes the difference between the thermodynamic potential and the actual potential, as shown in equation 2.79 [21]. The exchange current density can be found with equation 2.80 [72].

$$\eta_i = E - E_{th,j} \quad (2.79)$$

$$i_{o,j} = C_j n_j k_{s,j} F \quad (2.80)$$

Here C_j denotes the reactant concentration at the electrode surface and $k_{s,j}$ the reaction rate constant.

Afterwards, the last two parameters, the charge transfer parameter (α) and the reaction constant (k_s) must be established. The 2019 study by Morrison et al. explains this can either be done by modelling surface coverages, or by fitting experimental data in the Tafel regime [72]. The latter is the simpler choice and is therefore used more often in literature [102] [72]. The experimental data used to fit these parameters on, often originates from the work of Todoroki et al. (1995) [115].

With these PDEs and the initial/boundary conditions, the system can be solved numerically, by using Matlab, COMSOL or another solver program. An overview of the differences between the investigated models is provided in table 2.4.

Model:	High pressure effects	Transport types	Electrode type	Solubility model includes	CO ₂ R/ COR	Main product	1D/ 2D	Solver program
Gupta et al. 2005 [37]	No	Diffusion	Planar	Low pressure Salting out	CO ₂ R	CH ₄	1D	Matlab
Burdyny et al. 2017 [18]	No	Diffusion	Nano-structure	Low pressure Salting out	CO ₂ R	CO	1D	Matlab
Kotb et al. 2017 [55]	No	Diffusion Migration Convection	GDE (porous)	Low pressure Salting out	CO ₂ R	CH ₃ OH	2D	COMSOL
Racity et al. 2017 [85]	No	Diffusion	Nanowires	Low pressure	CO ₂ R	OH ⁻	1D	Matlab
Soeteman 2019 [102]	Yes	Diffusion Migration	Planar	High pressure Temperature Salting out	CO ₂ R	CHOO ⁻	1D	Matlab
Morrison et al. 2019 [72]	Yes	Diffusion	Planar	High pressure Temperature Salting out	CO ₂ R	HCOO ⁻	1D	Matlab
Chen et al. 2020 [21]	No	Diffusion Migration	GDE	Low pressure	CO ₂ R COR	CH ₄ C ₂ H ₄	1D	COMSOL

Table 2.4: An overview of the characteristics of the different models discussed in this section.

Diffusion layer thickness

The thickness of the diffusion layer (δ) can be approximated in a number of ways. First, there is a distinction between the models modelling (porous) gas diffusion electrodes (GDEs) and the models modelling planar electrodes. One of the upsides of GDEs is that they reduce the boundary layer thickness substantially, to increase the operating current density (see equation 2.82) [21]. Therefore, the approximation of this smaller diffusion layer thickness will not be representative for the situation in this study. Hence, the focus of this part will be on the models describing planar electrode boundary layer thicknesses [37] [102] [72].

The diffusion layer thickness is related to the limiting current density. The limiting current density can be defined as the current at which the reactant concentration at the electrode surface falls to zero, indicating that the situation is mass transport limited [80]. When applying this case to Faraday's law for current density, the concentration difference over the distance becomes equal to the bulk concentration, divided by the diffusion layer length. This eventually leads to a relation between the diffusion layer thickness and the limiting current density, as is shown below.

$$i = nFN = nFD \frac{\partial C}{\partial x} = nFD \frac{C_0 - (C_0)_{x=\delta}}{\Delta x} = \frac{nFDC_0}{\delta_N} \quad (2.81)$$

$$i_{lim} = \frac{nFDC_0}{\delta_N} \quad (2.82)$$

$$\delta_N = nFD \frac{C_0}{i_{lim}} \quad (2.83)$$

Where δ indicates the diffusion layer thickness, C_0 the reactant concentration in the bulk, D the diffusion coefficient, n the amount of transferred electrons and F the Faraday constant.

Both the limiting current density and the diffusion layer thickness are often unknown without consulting models or experimental data. However, since it is often not possible to measure the diffusion layer thickness [80], usually the limiting current density will be measured or modelled (i.e. found with maximum current density). Therefore, equation 2.83 can be used to find this value. This is what Morrison et al., for example, chose to do. They modelled the limiting current density, fitted it to experimental data and found their diffusion layer thickness from there. One must note, that this method assumes the reactor operating conditions from the experimental data source to be exactly the same as for the modelled case.

Another way to describe the diffusion layer thickness, is by relating it to the mass transport rate constant. The equation relating the mass transfer coefficient to the thickness (δ), is stated below.

$$\delta_i = \frac{D_i}{k_m} \quad (2.84)$$

Most models assume the diffusion layer thickness to be constant; however, in reality it will change with the flow conditions [102]. The k_m is related to the flow conditions of the cell, so it will be cell specific. It can be measured by experimentation or approximated with a series of empirical relations accounting for the mass transport contributions present in the cell. This way one can even incorporate the bubble-induced momentum of the gas-evolution at the electrode. This process is accurately described in the modelling steps of Burdyny et al. (2017) [18].

2.2.3. Cascade modelling

In this research, the three section approach as displayed in figure 2.9, will have to be updated, since there are two electrodes in tandem on the cathode side. This effectively creates a fourth and fifth section; a second diffusion layer section and a second electrode surface section. Therefore, also additional initial and boundary conditions are required. To develop a strategy for the coupling of this second sequential electrode to the usual model approach, we will look at cascade models in literature. For this, we will focus on the research of Lum and Ager (2018) [63] and the subsequent research of Gurudayal

et al. (2019) [38].

The Lum and Ager model for calculating CO₂ surface concentration and surface pH, has been based on the model by Gupta et al. [37]. This results in a similar approach as described in the previous section. To add the extra step, the modelling of the CO transport, they make a 2D diffusion transport model, which is solved in COMSOL Multiphysics 5.1. They model the transport of the species according to equation 2.85, which relates Fick's second law of diffusion to the source/sink term (stated in equation 2.77) representing the consumed or produced species.

$$\frac{\partial C}{\partial t} + \nabla \cdot (-D\nabla C) = R \quad (2.85)$$

Here C denotes the concentration of CO, D the diffusion coefficient of CO and R the rate of production of CO.

They assume no initial CO concentration in the bulk, they calculate the CO production on the Au electrode and investigate the response when assuming the Cu electrode acts as an ideal sink, meaning that there is zero CO present on the Cu electrode surface. Earlier in this chapter (section 2.1.4 'High pressure effects' – and section 2.1.4 'Solubility of CO₂/CO'), it was mentioned that it would be hard to include the changing solubility conditions of CO and CO₂ between the sequential steps. Here this phenomena is simplified initially, by assuming all produced CO will dissolve and all dissolved CO will react on the Cu surface.

The 2019 research by Gurudayal et al., is an extension on the Lum and Ager research, the research group therefore includes both Lum and Ager [38]. In this research they aim to investigate the effect of adding convection to the transport balance. This way the flow rate and the cell geometry can be used to control the conversion rate. To model this, they set up a 2D model, simulating the flow of electrolyte solution, the transport of the reactants and the buffering effects related to bicarbonate. This model was solved using finite element modelling (FEM) in COMSOL 5.4. The model was largely based on their previous research, but with the addition of the convective flow. The convective contribution was modelled similar to their other previous work, by Monroe et al. (2017), for modelling the separation of products in a laminar flow cell [70]. Firstly, they assume laminar flow in the channel, which they verify with the cell geometry and a Reynolds number calculation. They also found entrance effects to be minimal, so they were neglected. The CO₂ surface concentrations and buffer chemistry were calculated similarly to the models described in the previous section. Assumed was, that they also assumed steady state flow conditions, no slip boundary condition at the channel walls and an open boundary condition at the outlet, similarly to the model of Monroe et al. [70]. However, how the flow was modelled was not explained extensively in both studies (and supplementary data), therefore we will assume the convective flow is modelled as it was done in the Kotb et al. model [55]. In this model they also assume incompressible laminar flow and use the Navier-Stokes equation, in combination with the continuity equation. The incompressibility is shown in equation 2.87, and the equation describing the laminar flow is shown equation 2.86.

$$\mathbf{u} \cdot \nabla \mathbf{u} - \nu \nabla^2 \mathbf{u} + \frac{1}{\rho} \nabla p = 0 \quad (2.86)$$

$$\nabla \cdot \mathbf{u} = 0 \quad (2.87)$$

Here the \mathbf{u} denotes the velocity vector, P the pressure, ρ the liquid density and ν the kinematic viscosity.

The stoichiometry of equation 2.88 was used to determine the flux boundary conditions for the Ag electrode in the Gurudayal model. This shows that the CO flux is equal (and opposite) to the CO₂ flux, while the OH⁻ flux is equal to twice the CO flux.



As in the previous model of Lum and Ager, they again make use of the boundary condition of assuming zero CO concentration at the Cu cathode. This way they predicted the maximum conversion efficiency to CO of the system. They also make the simplification of assuming all the produced CO in the first

step will remain dissolved throughout the reduction steps. Both models, Lum and Ager and Gurudayal et al., make this assumption, while also reporting to find local CO solubility values above the solubility limit of CO in water. From the available information it seems as if this phenomenon can be at least partially explained with their assumptions made regarding the dissolving behaviour of CO and CO₂. However, not enough information is disclosed on the model determine this with certainty. In addition, they provide experimental results indicating this increased CO solubility as well. Therefore, this effect will be interesting to investigate in this research.

Both models make significant assumptions and are therefore very simplified simulations of the actual system. They incorporate an relatively extensive study on the flow conditions inside the reactor, which is an interesting attribution to most models investigated prior. Since the flow conditions are significant when researching sequential electrode operation, taking into account these models in addition to the models investigated in the section above, will provide for a good basis for the model in this research.

2.2.4. Valid assumptions

The following section will list the most important assumptions made in the described design approach followed by the different models. The bold assumptions are deemed valid for this model in this study as well. Why the other assumptions are regarded not valid for the high pressure cascade model will be explained below.

General assumptions:

- **The focus is only on the cathodic part of the cell, assumed is therefore that the anodic reactions are not limiting the system**
- **Constant temperature is assumed (i.e. the reactions are assumed not to influence the temperature)**
- **The pH bulk of the system is in range (acidic) for reactions 2.19 and 2.20 to dominate**
- The cell can be modelled accurately by dividing the cell in three schematic sections, as shown in figure 2.9
- **The fluid has a laminar flow velocity profile [kotb_Modeling_microfluidic_cell_2017] [38]**
- **The volume in which the reactions take place, will remain the same**

For this research there will be more sections required, since there is another electrode present. Therefore, the three sections approach as explained above will have to be updated.

Assumptions bulk section:

- **The bulk concentrations are constant over time:**
 - **The bulk volume is large compared to the electrode areas**
 - **Mass transfer phenomena in the bulk phase are negligible**
 - **The bulk solution is always in equilibrium with CO₂(g)**
 - **The bulk solution is ideally mixed (depending on cell design)**
 - **The bulk electrolyte remains saturated with CO₂**
- **The bulk concentration only depends on temperature, (CO₂) pressure and the salting out effects**
- **The concentration of products in the bulk is assumed to be zero (no CO present in the bulk solution [63] [38])**

All of the assumptions for the bulk section are assessed as valid for this study. The bulk concentrations are assumed to only depend on temperature, pressure and the salting out effects. Therefore, the Duan

et al. model can be used for the CO₂ solubility [27].

Assumptions diffusion layer:

- Mass transfer can be modelled accurately in 1D [37] [18] [85] [102] [72] [21]
- Migration effects on the transport are negligible [37] [18] [85] [72] [63] [38]
- There is no convective transport present in this layer [37] [18] [85] [102] [72] [21] [63]
- The products produced will immediately enter the gas phase and will not interact with the partial pressure of the reactant
- The produced CO will dissolve completely after production [63] [38]
- **Products (H₂, C₂₊) are produced in the gas phase, and because of low solubility, will bubble (away) directly after formation**
- **Products (except for CO) will transfer to the bulk, without interacting with other species (no reactions with products take place)**

As discussed above, migration effects will be included in this model, since Soeteman (2019) calculated their effects to be significant and the effect will increase with pressure [102]. Convection will be included in this model as well, as the experimental set-up operates with a pump, and one of the research goals is to investigate the effect of controlling the selectivity instated by convective flow as proposed by Gurudayal et al. [38]. This is interesting to investigate, especially since the model will aid in the development of an experimental set-up (section 2.3). Therefore, knowledge on the optimal flow conditions and configuration could reduce the otherwise required experimental investigations.

Apart from that, The assumption that the partial pressures of the produced products will not affect the reactant partial pressure will not be valid in this case, as shown by Dufek et al. [28]. However, the possibility of fast transport of CO to the second step, before it can dissolve or bubble to the bulk, as described by Lum and Ager and Gurudayal et al. is a plausible phenomena as well. Since the concentration of CO and CO₂ at the second step will have an important effect on the results, this will be interesting to investigate. Section 4.3 will provide a detailed description and calculation driven decision on how to model this section and the resulting ramifications.

Assumptions electrode surface:

- **The overpotentials are high enough to assume Butler-Volmer kinetics for the electrochemical reactions (»52 mV)**
- **The only species that are reduced are CO₂, CO and H₂O, other species acting as reactant are neglected**
- **The water concentration is constant and abundant**
- **There are no mass transfer limitations constricting the H₂ production**
- **The H₂ production is seen as independent from the CO₂ (not influenced by it)**
- **The kinetics of the cathode are rate-determining**
- **The CO flux is equal and opposite to the CO₂ consumption flux in the CO production step [38]**
- Bubble coverage is present and constant at a value of 25% [18]
- Kinetics for CO₂R are assumed pH dependent, while COR kinetics are not [21]

It is possible other species will reduce on the Ag or Cu surface as well, however, these will likely be low amounts and are therefore neglected in this model (as in the other models). The model of Burdyny

et al. (2017), include the effects of bubble formation in their calculations [18]. This effect results from bubbles of produced reactants blocking the electrode surfaces and, therefore, reducing the production rate as they reduce the active electrode area. The modelling of these bubbles is seen as an additional correction step, which is a little outside of the scope of this research and will, therefore, not be taken into account in the initial model. After evaluation, it can still be added in a later stage. If this effect were to be modelled, the approach of the study of Burdyny et al. could be followed.

2.2.5. Cascade high pressure model

Apparent from the comparison made in the last sections, is that the model of Soeteman seems to be the most complete. In addition, because of the incorporation of the high pressure effects, it fits well with the intentions of this research. The high pressure cascade model will, therefore, be largely based on the Soeteman model. To incorporate the phenomena specific for this research (convection, cascade, other formation products, etc.), features of the other models will be incorporated as well.

The section on the cascade modelling made it clear that the main challenge will be to accurately model the connection between the two reaction steps. The available models and literature study have proposed different solutions to effectively model this section. In the section, 'Assumptions and limitations', a more detailed description will be provided regarding the considerations for determining the approach for this section.

A difficulty with choosing the Soeteman model as a foundation for the high pressure cascade model, is that the model is one dimensional. Therefore, it will be hard to incorporate the flow conditions as was done in the cascade models [63] [38]. A challenge will be to find a way to partially incorporate this effect in the chosen model structure and solver program. However, by adopting a different approach for the cascade modelling, it would be even more interesting to compare eventual results to the 2D cascade models. A possibility to incorporate these important effects, would be to include the flow condition results from the cascade models into the new model.

To evaluate the performance of the model, its results will be compared to experimental studies researching similar effects [40] [56] [120] [63] [38]. In addition, the designed high pressure cascade set-up will also aid in the validation of the model, as the model is set up to simulate this exact reactor design.

2.3. Design procedure

As explained in the theory chapter, there are three main factors influencing the efficiency of the reactor: 1) the electrical losses, 2) the ionic losses and 3) the activation overpotential losses. Although there is value in knowing these factors, since the goal of this research is not to create the most optimal design, they will not be governing the design decisions. Instead, the setting up of the design will be done according to priorly determined design parameters, which will fit the goals of the experimental research. These design parameters will be determined based on the performance of the current design by Wols (2020) [123] and the required improvements to perform the necessary experiments for this research.

This chapter will, therefore, focus on the theory behind the design and construction of an electrochemical reactor. As explained before, the design in this research will be based on an existing high pressure reactor, designed for high pressure CO₂ reduction for formate production. This design will be denoted by 'the 2020 high pressure reactor', throughout this chapter. The design approach for this set-up is detailed in the thesis report by Wols (2020) [123]. The various steps in the design procedure for designing this reactor, will be discussed and used to define the design demands and parameters for the high pressure cascade reactor for this research.

2.3.1. The 2020 high pressure reactor

In the study by Wols (2020), a continuous-flow reactor with only one chamber was designed, capable of handling pressures up to 100 bar. In general, high pressure (CO₂ reduction) reactors consist

of many components, making them complex and specifically designed for only one experiment type [123]. Therefore, the aim of the research by Wols was to create a simpler reactor, allowing for various kinds of experimental research. After extensive research on the available reactor designs in literature, he decided on a single chamber continuous-flow reactor. With this simplified design, the design will be able to operate in varying conditions, it will be easy to scale up and it will be convenient for small scale experiments. Other possible reactor design types, including their advantages and disadvantages, are explained extensively in the 2020 study by Perry et al. [79]. The next sections will discuss which design parameters were defined for the reactor, how the resulting reactor operates, the evaluation of its performance and the recommendations for further improvement. These will, thereafter, be used to define the design parameters and demands for the high pressure cascade reactor of this research.

Design parameters

The design approach utilised in the research was to, firstly, identify the demands required for a successful reactor design, which could, thereafter, be used to define the design parameters to adhere to in the designing phase. To aid in setting up the design parameters, a literature research into existing cell types and set-ups was carried out. The design parameters that originated from this research served as a basis for the final set of parameters.

The design parameters specified for 2020 high pressure reactor were the following:

- **High pressure containment** – to account for high pressure experiments, by ensuring enough pressure can be built up, without any leaking
- **Chemical resistance** – to include the option to work with corrosive electrolytes and products
- **Adaptability** – to enable many different types of experiments by, for example, varying the configuration, adding additional components and changing operating conditions
- **Fast assembly/disassembly** – to increase the ease of use for carrying out experiments, so a lot of experiments can be carried out in as little time possible; this can be done by, for example, reducing the number of involved components and set up steps
- **Location adaptability** – so experiments can be performed in multiple locations; even outside of the lab
- **Safety** – to ensure the safety of the operator

With these demands in mind the reactor design was developed. The performance of the manufactured reactor was also evaluated based on these parameters, to illustrate if the reactor performed as was intended. Note that it was not a goal of the research to design the most efficient reactor system, therefore, things such as: minimising the electrical resistance of the system, were not included in the design parameters.

Set-up

A schematic representation of the set-up of the reactor is outlined in figure 2.10. As shown, the system includes a reservoir for holding the electrolyte solution, while dissolving the CO₂ originating from a pressurised gas bottle. The reservoir is connected to a pump and to the reactor stack, so the CO₂ containing electrolyte solution can be pumped to the reactor stack. In the reactor stack the electrodes are positioned. The reactions take place inside of the reaction chamber and the electrodes are connected to the power supply; the power supply – a potentiostat – is connected to the anode, cathode and reference electrode. After leaving the reactor, the electrolyte solution containing the products will be recirculated through the system. A manual valve can be used to collect a small portion of the solution, for sample analysis.

The demands this set-up has to adhere to are listed below. The set-up must be able to:

- supply electrolyte solution throughout the reactor

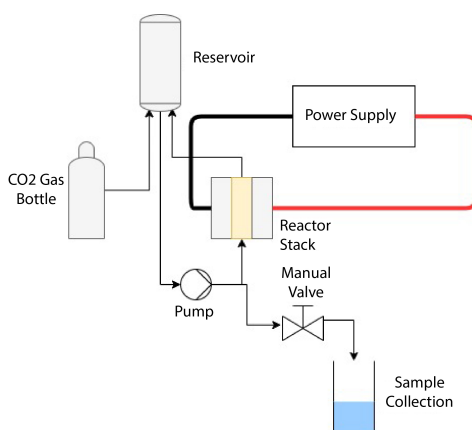


Figure 2.10: Schematic representation of the set-up of the 2020 high pressure reactor. Derived from: [123].

- supply potential to the reactor
- contain pressures up to 100 bar
- saturate the electrolyte with CO₂ gas
- Allow for sample analysis of the electrolyte solution
- handle corrosive materials

The described system in figure 2.10 was designed to meet these demands. To describe the resulting design, an overview of the components, the design choices and the corresponding reasoning can be found in table 2.5. The most important section of the design – relating to the high pressure cascade reactor design in this study – is the reactor stack. The reactor stack will, therefore, be discussed in more detail.

The reactor stack

The reactor stack consists of four small cylinders, two electrode casing parts and two reaction chambers. The pieces are pressed together at high pressure to prevent leaking. The choice has been made to keep the reactor stack small (40 mm in diameter), as the required pressure would otherwise result in high forces. The two electrode casing parts hold the electrodes and press them against the reaction chamber. The flow of electrolyte solution will enter the reaction chamber from above, it will flow past the electrode and leave from the bottom of the reaction chamber. The material of the reaction chamber, is polyetheretherketone (PEEK). This decision was made on the grounds of a CES EduPack (2019) plot of materials resistant against acids, alkali and solvents (a design parameter), plotted with their price against their mechanical strength. These material parameters were chosen, since the reaction chamber needs to be corrosion resistant, as it will be in contact with a possibly corrosive solution. It must also be strong enough to contain the large pressures and it cannot be conductive, as this would result in a short circuit in the reactor, since the chamber is in contact with both electrodes.

The electrode casings, on the other hand, do need to be electrically conductive, so they can connect the electrodes to the potentiostat. This way a simple electrical connection is created to the anode and cathode. In this situation, this set up was favored over foils and wire connections, as these are more complicated solutions – which are also harder to assemble – since a connection to the small electrodes would have to be created. Again CES EduPack 2019 was used to determine a suitable material, which is conductive and chemically resistant (to acids, alkali and organic solvents). These were plotted with their price against their yield strength. Based on this evaluation, stainless steel 316 was chosen as the electrode casing material. To prevent leaks, an o-ring was fitted in the plates, around the electrodes. The pressure on the stack will be instated by a mechanical clamp, the heavy pressure rod pusher 6842. With this clamp a force of 4 kN can be produced, which definitely meets the pressure requirements.

Component	Design choice	Reasoning
Reactor	Stack configuration	Simple to design, easy to scale up, eligible for different configurations and convenient for small scale experiments
	PEEK reaction chamber	Simple design due to non-conductivity
	Stainless steel electrode casing	Simple design due to conductivity
	Female fittings	Reliable and simple manufacturing
	Kalrez or EPDM O-ring seals	Good corrosion resistance
	Ring terminal electrical contacts	Stable electrical connection
	Clamp holding the stack together	Simple, compact, no tools required and cheap
	Bolt with star know for adjusting clamp force	Simple, compact, no tools required and cheap
	Aluminium plate frame on beams	Different configurations possible
	bolts through the reactor	Option to run and test the reactor outside of the lab set up
Reservoir	Cylinder with piston configuration	Variable volume of the reservoir
	Stainless steel thick walled cylinder	Good dimension, good corrosion resistance, capable to house different configurations
	PEEK piston	Good corrosion resistance, available material, it will not scratch the inside of the cylinder
	Kalrez or EPDM O-ring seals	Good corrosion resistance
	Female fittings in the moving piston	Reliable and simple manufacturing
	Additional piston with alternative fitting	Reliable and simple manufacturing and ability to test additional design choice
	Aluminium plate frame	Different configurations possible and supports the use of the moving piston
	Aluminium placement blocks	Different configurations possible and supports the use of the moving piston
Pump	The GAH series pump of microfluid	Good quality pump which satisfies the demands
Tubing	IDEX 1/8 inch PEEK tubing	Corrosion resistance, low pressure drops, wide variety of products
Power supply	Potentiostat	Option to control the absolute potential of the working electrode
Main frame	ITEM aluminium profile frame	Good availability, light weight and easy to adjust and add components

Table 2.5: A list of the design choices and reasoning behind them per component. Derived from: [123].

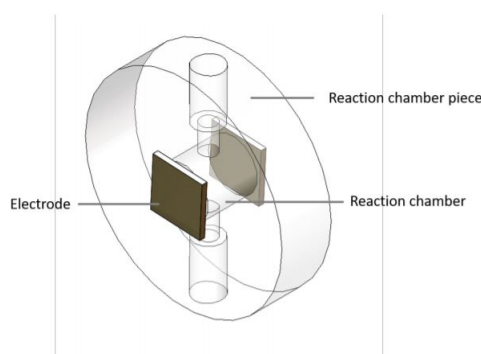


Figure 2.11: An illustration of the designed reaction chamber piece (including the electrode fit), as designed in SolidWorks. Derived from: [123].

To control the pressure on the stack, an additional correction bolt is added. With this bolt the pressure can be adjusted as required. Illustrations of the clamp and bolt can be found in appendix B.1.

Performance

After construction, the design was tested on each of the determined design parameters. The results showed no problems with the pressure containment. In addition, the chemical resistance was adequate, as no corrosion was detected in the components. The system was also found to be sufficiently adaptable, the report even includes possible additions in the appendix [123]. Furthermore, the assembling and dissembling was experienced as easy and fast, except for the positioning of the pistons in the reservoir. The reactor was capable of operating in multiple locations (also outside of the lab). Lastly, no safety breaches or dangerous leaks occurred during the testing, therefore, the design was deemed sufficiently safe as well. The testing illustrates that the design performs sufficiently according to the set design parameters.

As explained before, an efficient performance of the system was not a design demand for the 2020 high pressure design. Therefore, the low efficiency of the electrochemical reactions will not influence the success of the results. However, if this reactor will be used for extensive experimental research, the reaction efficiency needs to be improved. To explain the small amount of CO₂ conversion in the testing results, the global flow pattern throughout the reaction chamber was described with a 3D flow model in COMSOL. Here, the assumption was made, that the electrolyte can be modelled accurately with water properties. The modelling results, as illustrated in figure 2.12, show that most of the flow bypasses the electrodes.

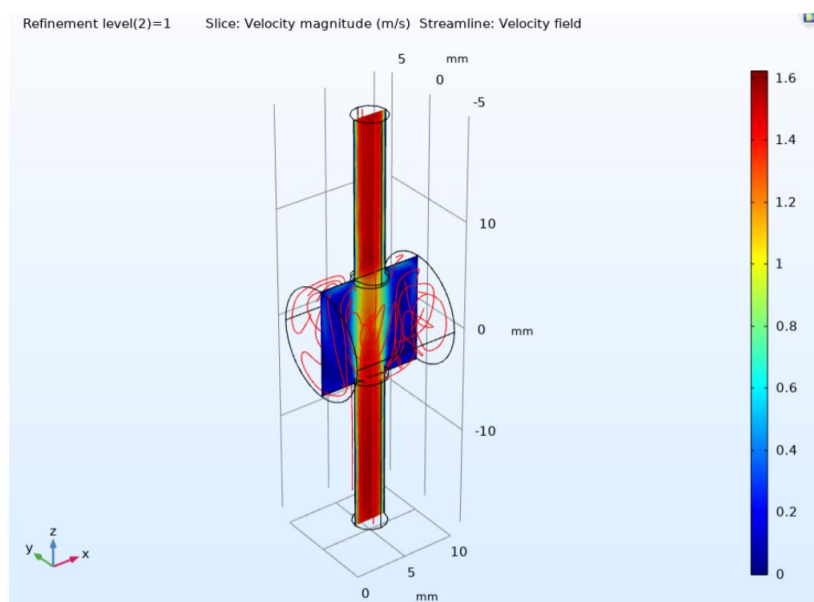


Figure 2.12: A 3D simulation of the global flow throughout the reaction chamber, modelled in COMSOL. The location of the electrodes is indicated with the circles on the sides. Derived from: [123].

The most important objective of the designed set-up was to facilitate a high pressure CO₂ reduction reaction. The tests showed that the reactor can contain the required pressures, but the amount of converted CO₂ is rather low. For the 2020 study of Wols, this was an acceptable result, however, for this research this feature needs to be improved in order for the experiments to be conducted properly.

Recommendations for improvement

Although the designed reactor proved to work sufficiently within its set goals and parameters, there is

still room for improvement. Most of the recommended improvements stated in the report are related to small progress in the handling of the reactor [123]. For this research, these are not the most important improvements, therefore, only the relevant recommendations from the 2020 report will be mentioned here [123]. These proposed improvements contain:

- Adding grooves and holes, to increase the fit with the o-rings, to decrease the possibility of leaks
- Using smaller, possibly non-metallic bolts, to create more space in the reaction stack and eliminate the need for electrical insulation
- Increase the assembling ease of the reservoir by:

Some of the proposed improvements have already been worked out in more detail and can be found in the appendix of the thesis report by Wols [123].

In addition to these general design improvement recommendations, there are also improvements required specifically related to the reactor design for present research. These entail:

- Improving the flow conditions in the reaction chamber, so more flow will come in contact with the electrodes
- Redesigning the electrical connections, so they will fit multiple electrodes, which can be operated separately from each other
- Redesigning the reaction chamber stack to fit multiple electrodes and configurations (for example gap distance) can be changed easily

These improvements will be regarded in the setting up of the design parameters and conditions for the high pressure cascade reactor design.

2.3.2. The new design

As discussed in the theory chapter, a number of aspects need to be redesigned to fit the intentions of this research. The section 'The high pressure cascade cell' (Theory chapter) pointed out that it will be important to instate controlling in the electrode sizes, distance and configuration (i.e. two sequential electrodes). The articles by Lum and Ager (2018) [63] and Gurudayal et al. (2019) [38] both investigate the effects of changing the electrode configurations and sizes. The results of Lum and Ager illustrate that varying the distance between the electrodes can influence the conversion efficiency. They also show that it is possible to tune the oxygenates to ethylene ratios by varying the Cu coverage substrated on Ag lines. This reveals it is possible to control the reaction by tuning the configuration. Therefore, it is important to add this as a feature to the reactor design. For this to be realised, the design needs to become even more adaptable, especially in the holding/housing of the electrodes. A possible solution for this needs to be leak-tight at high pressures.

From the results of the 2020 high pressure reactor design, it becomes apparent that a number of things need to be redesigned as well, to make the set-up more suited for the experiments in this study. The 3D COMSOL flow model, from the report of Wols (2020), illustrates that the flow through the 2020 high pressure reactor is far from optimal for significant product formation. The profile shows that most of the flow will bypass the electrodes when passing through. For the 2020 high pressure design, it was not essential to convert a lot of CO₂, since the goal was to make a functioning reactor. However, for present research it is relevant to conduct experimental work to generate results required to determine the potential of this research pathway. Therefore, it becomes important to increase the flow characteristics in the design for this study.

Another complicating factor is the electrical connections. In the Theory chapter (section 'The electrochemical cell'), it was explained that an electrochemical cell consists of at least two electrodes on each side (reduction/oxidation). Each has to be connected to a power source, for the electricity required to drive the reactions. Since CO₂ reduction and CO reduction both operate at different potentials, the

sequential electrodes need to be connected to the power source separately. This way both electrodes can operate in the most optimal overpotential domain, while at the same time control is instated to separately operate the electrodes. This means that the reaction chamber set-up needs to be reinvented, as the conducting back plate will connect both electrodes to the same connection. Therefore, the construction and material selection of the reaction chamber section need to be redesigned for this new reactor.

Design criteria

Based on these new demands and the recommendations from the last section, the additional design criteria for the new design were set up. These design criteria are listed below.

The high pressure cascade cell must be able to:

1. contain the pressure (up to 35 bar) without leaking
2. be adaptable in electrode configuration and size
3. ensure easy operation and fast replacement
4. sustain separate electrical connections for both sequential cathodes
5. be resistant against corrosion
6. provide for better internal flow characteristics, to ensure sufficient conversion

These design criteria will be leading in the conceptualisation of new design ideas. These design ideas will, thereafter, be assessed based on the determined design parameters below.

Design parameters

The main goal of the new design is to operate at high pressures with a cascade electrode set-up. Therefore, a lot of the 2020 high pressure reactor design parameters can be adopted by the new design as well. However, the possibility to also conduct experiments outside of the lab (and fume hood), will not be included. The main reason for this is because of the production of dangerous products like CO. For safety reasons, therefore, the experiments need to be conducted inside of the lab and fume hood.

Additions originating from the new demands, are the requirement for increased adaptability (denoted here with versatility) and increased flow conditions. This results in the following design parameters.

- High pressure containment
- Chemical resistance
- Fast assembly/disassembly
- Safety
- Sufficient conversion
- Experimental versatility
- Separate electrical connections

These are the design parameters along which the new reactor design will be set up. They will also be used to evaluate the actual performance of the new reactor, in a later stage.

Design ideas

Some initial design ideas adhering to these constructed parameters will be discussed in this section. They will be focused mainly on redesigning the reactor stack, as this was identified as the region requiring the most improvement.

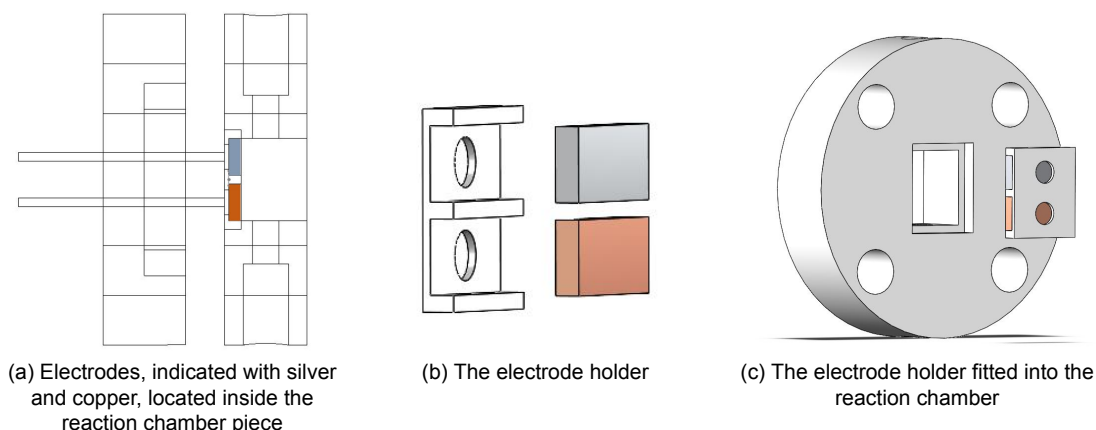


Figure 2.13: Designs of the new reaction stack made in SolidWorks 2019.

To increase the flow conditions, to be able to produce more product, the reaction chamber was re-designed. In this new reaction stack configuration, the electrodes will fit into the reaction chamber instead being pressed against it. This will allow them to be located closer to the incoming electrolyte solution flow, as can be seen in figure 2.13.a. To enable fast assembly/disassembly of different electrode configurations (gap sizes, etc.), the electrodes will be housed in an electrode holder part, illustrated in figure 2.13.b. When the gap distance or electrode sizing needs to be changed, the only part that needs to be altered will be this holder. The holders will always have the same outer dimensions, so they will fit into the reaction chamber and end plate, as shown in figure 2.13.c. Therefore, no major changes need to be made in the reactor stack itself, when new configurations need to be tested.

The reaction chamber in this case will – as in the 2020 high pressure design – be made of PEEK, for the same reasons as explained in previous sections.

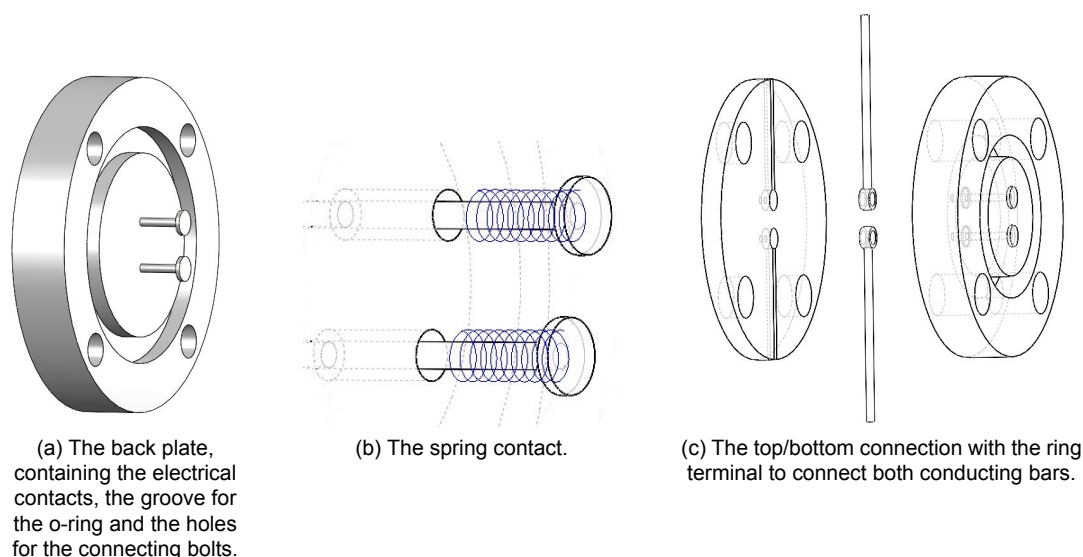


Figure 2.14: Designs for the back plate, the spring contact for the electrical connection to the electrodes and the ring terminal connection to lead the wires to the top/bottom of the stack. Designs are made in SolidWorks.

Another challenge in the new design will be to make good separate electrical connections to the electrodes. This can no longer be done with a steel back plate – since this would connect both electrodes to the same source – therefore, slots are cut out of the electrode holder, at the back of the electrodes, for an electrical connector to fit in. The location of these slots is illustrated in figure 2.13.b. The back plate

will in this case also be made of PEEK, instead of metal. It will contain a groove for the o-ring around the electrode holder, to prevent leaks. The design for the back plate can be found in figure 2.14.a. To ensure a good connection to the electrode surface, a spring contact can be used. How this can be achieved is illustrated in figure 2.14.b. The spring will press the contact against the electrode, when the back plate is pressed against the reaction chamber piece. Since the reaction stack is pressed together by means of a clamp from the back of the back plate, the electrical connection should surface from the top and bottom of the stack, instead of the back. To realise this, a set-up was designed containing a ring terminal to connect the conducting cylinder to a bar leaving from the top/bottom. To make this easy to assemble, the back plate was divided into two separate plates, in which grooves are cut out to fit the conductive bars and the ring terminal components. A preview of this construction is shown in figure 2.14.c.

These designs represent the first design ideas for the new high pressure cascade reactor. They were based on the defined design parameters and demands, to solve the issues of the 2020 high pressure reactor, for it to be used in this research. More design iteration steps will follow these initial ideas in a later stage. The eventual design, the production and the testing will be detailed in the chapter 'The reactor design'.

According to the 2020 study by Perry et al., the increasing availability of 3D printing opportunities, produces an interesting option for rapid prototyping of reactor components [79]. Therefore, to test the performance and fitting of newly designed components, they will first be 3D printed before more time consuming / intensive production methods are considered.

In the next phase of this research, the design will be worked out in more detail, after which it will be tested with prototypes and eventually manufactured to fit the existing set-up.

2.4. Conclusion: Research questions

This literature study was conducted to explore which segments within high pressure cascade electrochemical reduction are most valuable to investigate further. By outlining the available literature on these topics, a clear overview can be compiled on the 'information gaps' left to investigate. These gaps will then lead to the research questions for the research to come.

The available literature reviewed in this report has proven that the topic of high pressure cascade electrochemical reduction is promising, although a lot of research is yet to be conducted. This topic combines two rather new technology advances – high pressure and cascade operation – therefore, extensive further research is required to show its potential.

2.4.1. Literature study summary

In the introduction of this report three factors were mentioned that will influence the efficiency of an electrochemical system: the current density (the reaction rate), the selectivity (the FE) and the overpotential (the losses). Research has shown that innovative technologies as a cascade reaction operation and high pressure reactors, can aid in increasing the system efficiency. Cascade operation increases efficiency by splitting the conversion up into two separate conversion steps; the operating conditions for both steps can thus be optimised separately. The conversion to C_{2+} in a cascade operation results from COR instead of CO_2R . This is beneficial, since COR has a higher C_{2+} selectivity and higher activity. However, techno-economical studies have shown that this technology has a too low feasibility for it to be commercially competitive at this point, since the second conversion step is not efficient enough. A limiting factor in the second conversion step, is the low solubility of CO in electrolyte solution. Another limiting factor is the low selectivity for a single product on Cu catalysts. Therefore, this research proposes to combine high pressure reactors with a cascade operation. By means of increasing the pressure, the solubility of the reactants can be increased, which has shown to increase the reactant transport (current density) of the system. In addition, by working with a cascade system operating a conductive flow, the selectivity of the system towards C_{2+} products can also be increased and possibly

even partially controlled. Combining these two technologies could, therefore, increase the system efficiency in terms of: reaction rate, selectivity and overpotential losses. Since this combination has not been investigated before, and both technologies are still rather new, there will still be a lot to investigate to show the promise of this new technology.

By investigating the underlying theory, the dependence of the reaction rate on the local concentration of reactants was evident. Since the current density is proportional to the rate of reaction at the electrode, this also proves the relation between the increased mass transfer and the increase in current density, explaining the positive effects of the high pressure reactors. The theory on the mass transfer provides the required formulas to describe the mass balances, to be used in the modelling chapter. The possible high pressure effects on the solubility and the kinetics are, subsequently, further detailed in the theory chapter. The high pressure section indicates that the most challenging aspect to model would be the connection between the first and second cascade step, since the solubilities of CO_2 and CO change in between. The available literature suggests possibilities for competition for solubility between the molecules and changing partial pressures. These effects have not been taken into account in existing models yet, but could possibly affect the accuracy of the model.

To investigate whether the pressure behaviour of the second and first step would be similar, the kinetics were investigated as well, from a theoretical point of view. Different articles investigating the effects of partial CO_2 and CO pressures indicate that the kinetics of the first step will likely be influenced positively, whereas the second step could experience some limitations in the kinetics when high pressure is instated. The combination of both steps, however, would aid in the creation of C_{2+} products, since the CO_2 reduction step is disengaged from the C_{2+} production step. The study by Song et al. (2020) indicates that a high CO_2 partial pressure, could result in the limiting of the required CO^*-CO^* coupling, as the available surface sites would be filled with CO_2^* . Therefore, splitting the two steps could increase the efficiency, possibly explaining why operating in cascade can increase the C_{2+} production.

With this theoretical knowledge and the defined mass transfer equations, the approach for the model was set up. By comparing available models in literature, a general modelling approach was showcased, in which the differences between the models were explained. This led to a comparison between the models, from which decisions were made for a modeling approach per section. Overall, the model of Soeteman (and Morrison et al.) seemed most complete and most suited to function as a basis for the model in this research. However, since these models do differ in vital areas from the intentions of this research, the eventual model will be based on these, in combination with additions from other modelling studies. Therefore, for the high pressure modelling the models of Soeteman [102] and Morrison et al. [72] can be consulted, while for the convective mass transport the model of Kotb et al. [55] will be utilised. The migration modelling will be carried out like in the models of Chen et al. [21], Soeteman [102] and Kotb et al. [55]. Possible bubble effects can be incorporated by reviewing the model of Burdyny et al. [18], and the modelling of COR can be approached as in the model of Chen et al. [21]. The major challenge for setting up the model in this study will be the modelling of the second reduction step, and more specifically the connection of the first to the second reaction reduction step. The cascade models of Lum and Ager [63] and Gurudayal et al. [38] were consulted for a possible approach. However, from the available information on their modelling approach it seems as if they have made many simplifications in their modelling. It would, therefore, be interesting to see if these hold by conducting further research into this topic.

To verify the modelling results and to provide experimental data on this new set-up, a reactor needs to be designed to accommodate all desired experimental research. The new reactor design will be based on an existing set-up for high pressure CO_2 reduction, as built and described by Wols (2020) [123]. To adapt the current design to accommodate the desired experiments for this research, a number of things need to be modified. The formulated design criteria, containing the demands for the new design and the recommendations from the old design by Wols, will be leading in the development of the new design. To validate its performance after construction, the design will be analysed based on the compiled design parameters. These include: high pressure containment, sufficient reactant conversion, chemical resistance, experimental versatility, ease of assembly/disassembly and safety. The first design ideas for the reactor stack include: changing the materials, addition of an electrode holder –

for fast changes in configuration – redesigning the electrical connection and increasing the flow inside the reaction chamber. These ideas will be further elaborated on and tested in the chapter 3, about the design of the high pressure cascade reactor.

The next section will provide more detail on the information gaps and unverified information found in the literature study.

2.4.2. Discussion

The evaluated literature has shown promising results, however, there were also a lot of discrepancies found while combining theory with modelling and experimental results. Since there are not many experimental results available, at this moment it is hard to explain these results with much certainty. This section will list the discrepancies and unclarities and discuss possible outcomes and solutions to be tested in this research.

First of all, there has been some research on the effects of high pressures on CO₂ conversion. However, not much research on the high pressure effects on CO has been done so far. There are some promising results indicating increased performance at slightly elevated CO pressures, but no conclusive proof yet. To predict the effect of pressure on the CO conversion, we therefore need to rely on theory. The theory in this research explained that pressure can affect the solubility of reactants and therefore the reaction rate and, moreover, it might also have an effect on the kinetics of the system.

The theory on high pressure effects on the solubilities of the reactants present in the cascade, shows that there are a lot of different factors affecting solubility, making it hard to accurately model this behaviour. A lot of these effects have not been studied at all, or at least not in this context, therefore this research needs to provide authentic ways to incorporate these results (if possible) in the modelling. So far the modelling of CO solubility and CO₂ solubility under high pressures has been performed with sufficient accuracy. The problem lies in their behaviour when both gasses need to dissolve in the same solution and when their solubility changes with their changing partial pressures due to the product formation.

There have been molecular simulation studies describing the competing effect between two gasses when dissolved in the same solution. However, these studies were conducted in ionic liquids instead of electrolyte solutions. These molten salts have a very different charge compared to electrolyte solutions, hence the solubility behaviour of molecules will differ between these solutions as well. These investigations can therefore not be used as proof for the existence of this behaviour in electrolyte solutions, nor can the absence of information on this topic can be taken as proof against this principle, as the studies in which this effect would be significant are not that common. Therefore, this effect cannot be included in the model, since there is not enough theory on it available. Nevertheless, this information can be used analysis of the results in this research, possibly leading to more insight into this principle.

The changing partial pressures after the creation of the products (gasses) in the first step, can be incorporated in the model, by deploying the formula as stated in the study of Dufek et al. [28]. Arguably, incorporating this effect, can improve the modelling approach of the linking between the first and second step of the system. To determine an approach for this connection, the models of Lum and Ager [63] and Gurudayal et al.[38] were investigated. As not a lot of information on the modelling structure was released, it is difficult to establish the validity of their approach with certainty. However, both articles state that they initially assumed that the produced CO was equal to the consumed CO₂ in the first step, assuming 100% conversion and (seemingly) assuming 100% solubility. In most cases, they also assume the second electrode to be a perfect sink, meaning that all produced CO will be converted here. From the theory on solubility mentioned above, these assumptions seem to be an oversimplification of reality. This assumption could explain why both articles have found results indicating CO solubilities above their solubility levels, however, not sufficient information on the modelling is disclosed to be certain of this. In their second article, the study by Gurudayal et al. [38], they do conduct an experimental test, to support this claim. In this test, they operated the reactor with the Cu as the only activated electrode and inserted a flow saturated with CO. In doing this, they showed that the oxygenate production

was lower in this case compared to the cascade operation, at the same potentials. Since high CO concentrations favour oxygenate production, they adopted this as evidence of the supersaturated CO condition in cascade operation. To evaluate this claim, the 2019 study by Wang et al. was consulted [121]. This study shows that the presence of CO₂ in the feed will increase the ethylene formation. Therefore, the oxygenate to ethylene ratio should have been higher in the COR operation compared to the cascade case in the experiment by Gurudayal et al. [38]. Hence, this could indicate that there would actually be an increased CO concentration. A possible explanation for this effect could be, that the transport to the second electrode is so fast, most of the dissolved CO will not have been transported outside of the diffusion layer section yet. As the presence of supersaturated CO represents a major benefit to the cascade approach, this is definitely something worth investigating further in this research.

As mentioned above, there have been indications of pressure influencing the kinetics of electrochemical reactions. Possible reasons for these indications were explained in the theory chapter. Here, the effects of pressure on the reaction mechanisms for both steps were investigated. The results indicate that the pressure could indeed affect the kinetics, and even (partially) change the rate determining step of the system. To predict what can be expected in the high pressure cascade system, studies relating to the effects of partial CO and CO₂ pressures were consulted. The results show that in the first reduction step the increased availability of CO₂ can increase its surface coverage, which will result in few instances of CO*–CO* coupling (little C–C coupling) and therefore a lot of CO production, as the adsorbate–adsorbate interactions will increase the desorption of CO* from the electrode surface. The second conversion step, however, does require a lot of CO*–CO* coupling and protonation to produce the required C₂₊ products. Because of the created CO (and H₂) in the first reduction step, the CO₂ concentration and partial pressure will have decreased, leaving less competition from CO₂ for the CO* on the surface of the Cu. This, in combination with the high CO pressure, will result in a high CO* coverage on the Cu surface. This leaves little room for H* to bond to the surface. Therefore, kinetics of the products requiring proton transfers will be limited by the available H*. These are indications that from a theoretical point of view, the increase in pressure might speed up reaction for the first step, but simultaneously could limit the second step, depending on the product.

This theory could also aid in explaining the advantages of a cascade operation. The research of Song et al. (2020) has shown that the availability of CO₂ abundance on the electrode can reduce the possibilities for CO*–CO* coupling, since a lot of the available sites will be filled with CO₂* [103]. Since CO is the key intermediate for C₂₊ production, this would limit the system kinetics. Therefore, splitting these two steps, could be very beneficial. That way, when first producing a lot of CO (because of the high CO₂ pressure and availability), the Cu surface sites will not be occupied by CO₂, since its concentration and partial pressure would have decreased. This will lead to more available spaces for the CO* on the surface and could therefore lead to more C–C coupling. However, as explained above, this reaction step could still be limited by the restriction in available H* on the surface, due to the abundance of CO*. This, however, will largely depend on the precise reaction pathways for the products. Experiments need to be performed, to see if this theory could possibly explain the experimental results.

Apart from the connection to the second sequential step, the model for this research can be largely based on approaches used in existing models in literature. The choice has been made to also include migration in the modelling, as the report by Soeteman (2019) showed this effect may be larger than most of the other models assume [102]. In addition, the effect will only increase with pressure, as the product concentrations increase. Not accounting for these effects will, therefore, result in an overestimation of the limiting current density, as illustrated in equation 2.82.

To be able to provide answers for all these remaining questions at the end of this research, the model will have to be verified with experimental results. Since these are not, or barely, available in literature, this research also entails the development of a new reactor set-up. This set-up can, subsequently, be used to verify the modelling results and investigate its findings in more detail. With the experimental results, the underlying theory and the model to connect them, the occurring phenomena in this new technology can be explained.

2.4.3. Conclusion: research questions

As stated in the introduction section, 'Scope and goals', the goal of this research is to investigate the potential for a high pressure cascade system. To do this the effects of pressure on the efficiency of the sequential reduction steps needs to be investigated. To do this, the proposed approach is to: 1) to develop a mathematical model, to indicate the important system parameters and their relation to the results, 2) to design a new high pressure cascade reactor, and 3) to conduct experiments in this reactor, for further research and validation of the model. The literature study has provided a clear approach to set up each of these three processes. This way it has aided in determining the further direction of this research.

Based on the information derived from literature and the subsequent evaluation, a clear approach can be set up for the remaining research on this new topic. Literature has provided some possible clarifications of phenomena observed from the scarcely available experimental or simulation research. On the whole, most of these theories need to be substantiated by producing more available experimental results. Other unexplained results, on the other hand, require more detailed theories to explain them. Therefore, the combination of the model and the conducting of experiments as proposed, will be very valuable in linking the theory to results. This research will, to that end, focus on clarifying the effects of high pressure on the efficiency of a cascade system, specifically focusing on the factors contributing to system efficiency: the reaction rate, selectivity (FE) and the onset potential. Therefore, the main research question for this thesis will be the following.

How can high pressure influence the efficiency (reaction rate, selectivity and onset potential) towards C_{2+} products in a cascade system?

From the theory chapter it becomes clear that there is still much that is unknown with regard to the effects of pressure on the kinetics and solubilities in a cascade system. Literature research indicates that a cascade operation will increase the reaction rate and has the ability to influence the selectivity of the system. It has shown that, by regulating the ratio of CO_2/CO reaching the second electrode, control can be exerted on the product distribution (oxygenate/ethylene ratio) [63]. The literature on high pressure operation has illustrated its positive effects on the reactant solubility and therefore the reaction rate. Furthermore, since the reaction rate of the conversion of desired reactants (CO_2 , CO) increases with pressure, but the hydrogen evolution reaction (HER) remains unaffected, the selectivity in high pressure systems is increased as well [72]. This means that both a cascade and high pressure operation will increase the efficiency by impacting the selectivity and reaction rate in this system. Therefore, it is difficult to determine from the available information how exactly the overall system efficiency will react to a system combining both technologies. In this respect, it will contribute significantly to the general theory and modeling studies in the future, if these effects are made clear. Therefore, the following sub-questions were defined for this research.

What is the effect of pressure on each individual electrochemical step (CO_2 to CO and CO to C_{2+} products)?

How can the selectivity towards specific C_{2+} products be controlled by regulating the CO_2/CO ratio in the feed of the high pressure cascade reactor?

The modelling chapter reviewed the modelling approaches and assumptions of multiple available models in literature. This model will use theoretical knowledge to generate simulated results. By comparing these with the experimental results, clarifications can be made on the theoretical principles to explain the experimental results. The decision has been made to use the model of Soeteman (2019) as a basis for the model in this research [102]. Additional factors to incorporate into the model, will be adopted from the other investigated models, to create a more optimal simulation of the high pressure cascade reactor. The connection of the first to the second sequential step will be novel to this research, as the available literature did not provide a sufficiently accurate approach for this. After generating experimental results, the choice can be made to iterate and use these to improve this modelled connection and other input-parameters. To assess this specific step and the overall model, in order to provide the link

between theory and experimental results, the simulated results of the model should be carefully compared to experimental results. The match between the two is essential in explaining the discrepancies discussed in the last section. Therefore, it will be essential to extensively investigate the fit between them. This leads to the following sub-question.

How do the modelled results regarding the high pressure cascade electrochemical reduction relate to the literature and the experimental results?

The model can also aid in the design process of the reactor. By simulating the process, recommendations on electrode sizes and configurations can be made, as was done in the 2018 research by Lum and Ager [63]. By varying the gap distance between the electrodes, they showed they could influence the conversion efficiency. By the additional controlling of the Cu coverages substrated on the Ag electrode lines, they also demonstrated control on the oxygenates to ethylene ratios. It would therefore be interesting to investigate the effects of changing configurations on the production results, to create more insight in the possibilities of operating in a cascade.

To design a suitable reactor, capable of handling all experiments and requirements for the investigation, a set of design parameters was set up. The design will be evaluated on: high pressure containment, sufficient reactant conversion, chemical resistance, experimental versatility, fast assembly/disassembly and safety. An evaluation of the prior design, the 2020 high pressure reactor [123], in addition to the design criteria for this new design, have led to the conclusion that the main implementation will be the redesigning of the reactor stack. The current stack does not provide sufficient flow conditions for proper reactant conversion. It also cannot operate in cascade mode, since the electrical connection would connect both sequential electrodes to the same source. Lastly, it does not provide for easy adaptability in electrode configurations, to test their effect on the production. Therefore, the stack needs to be redesigned, according to the design parameters mentioned above, to satisfy these conditions. To continue this investigation aimed at producing a design capable of handling all desired experiments for this research, whilst also incorporating the possibility to investigate the effects of changing electrode configurations, the following research question is defined.

How to design an adaptable electrochemical cell capable of safely executing multiple experiments with the option for high pressures and cascade electrocatalysis?

Investigating the changing arrangements and operating conditions, will create insight in the effects of losses (overpotential) on the system efficiency. Investigating this, in combination with the first two sub questions, relating to the effects on selectivity and reaction rate, will provide understanding on the contribution of this new system combination on the overall efficiency, in terms of: overpotential, selectivity and reaction rate.

This literature study has created a clear overview on the availability of information in the existing literature. This research shows that there is still much that is unknown or unverified. Therefore, a lot of further research needs to be performed in this study. With the combination of generating new experimental data and linking it to the theory with the model, a clear first indication can be made to explain the phenomena and prove the potential of this new combination of technologies.

3

The reactor design

In the chapter about the design procedure, a range of design ideas has already been discussed. As stated, this research will focus on the redesigning of the reactor stack, as this is the area that needs to be redesigned, to allow for cascade high pressure experiments. The procedure to move from these initial design ideas to an ultimately working reactor, is as follows: First, a proposal for the first design iteration – based on the design ideas – will be constructed in SolidWorks. Thereafter, the design will be rendered into construction drawings, after which it will be machined by means of lathing, milling and drilling. After the production, this initial design will be tested in the lab, first with harmless water, and after proving to be leak-tight, the connection and production will be analysed. If problems are encountered, the design will be adapted and a new design iteration will be made. This procedure will continue, until the design operates as adequately as intended.

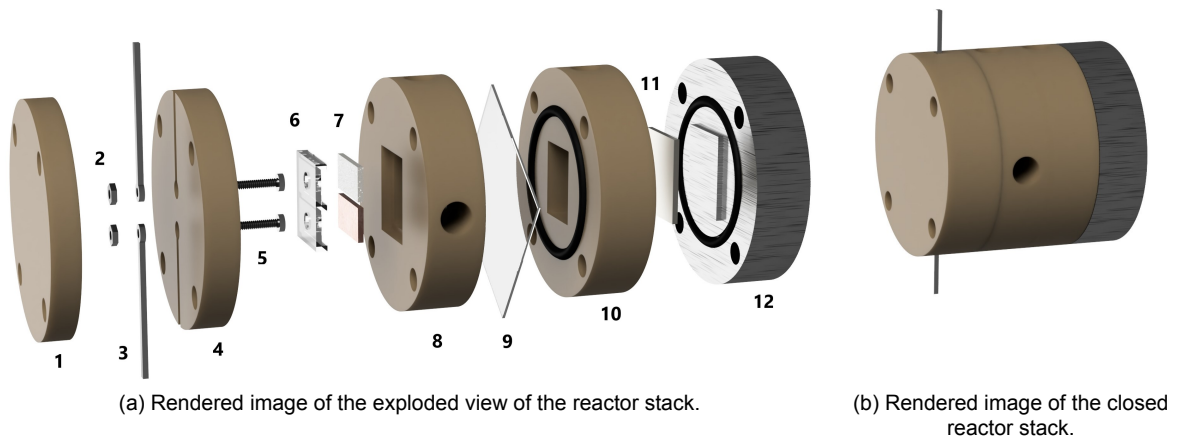
The following sections will elaborate on the implementation of this design procedure and the resulting final design.

3.1. The SolidWorks model

As discussed in the section 'Design procedure', the main demands (criteria) for the new reactor stack are as follows.

1. contain the pressure (up to 35 bar) without leaking
2. be adaptable in electrode configuration and size
3. ensure easy operation and fast replacement
4. sustain separate electrical connections for both sequential cathodes
5. be resistant against corrosion
6. provide for better internal flow characteristics, to ensure sufficient conversion

Apart from meeting these demands, it is very crucial that the design will not become too complex. The more complex the design, the more prone it will be to malfunction at some point, and in addition, the higher the chance at failures while constructing. This regards in particular the electrical connection. To meet the demands and to keep the structure as simple as possible, the following design, as shown in figure 3.1, was proposed. All materials regarding the stack, with the exception of the steel endplate, are made from PEEK (Polyetheretherketon). The stack has the same diameter and roughly the same thickness as the prior design, to ensure it will fit the lab set-up.



(1) Endplate cathode back (2) Connection nuts (3) Connection rods (4) Endplate cathode front (5) Connection bolts (6) Electrode holder (7) Cathodes (8) Reaction chamber cathode (9) Membrane (10) Reaction chamber anode (11) Anode (12) Conductive endplate.

Figure 3.1: The SolidWorks 3D model, rendered in Fusion 360.

The final design resembles some of the initial design ideas as stated before, however, some changes have been made and some new ideas were implemented as well. These adaptations will be highlighted below.

Separation of the compartments

As shown in the figure, the anode and cathode reaction chambers are separated by a cation exchange membrane, indicated by the number 9 in figure 3.1. As discussed before, the cathode section and anode section are separated and both operate with different in/out-flows and pumps. They are connected at the membrane, which only allows cations to pass through. This way, the produced protons at the anode can pass through to the cathode section.

Anode section

The anode section of the stack is relatively similar to the old stack, the electrical connection is still realised by a steel endplate, connected to the electrode (nr. 12). However, since the electrodes are now located inside the reaction chambers, a protrusion of the steel endplate will push the electrode in the chamber, and will ensure there will always be an electrical connection to the nickel electrode. To make this section leak-tight, an o-ring was added to the endplate.

Cathode section

The cathode side is very different from the old design, as at the anode side, the silver and copper electrodes (nr. 7) will be pressed into the reaction chamber (nr. 8). However, since they both require a separate electrical connection, they are fitted into a frame. This frame was introduced before, under the name 'electrode holder'. The holder has the same length as the outer section of the cutout in the reaction chamber and, therefore, will fit perfectly into this part and can never fall into the reaction chamber (nr. 6). The electrodes have the same width as the outer section of the cutout, which prevents these as well from falling into the reaction chamber, while retaining a maximum exposed surface area. At the same time, the electrode holder also ensures both cathodes will never make connection with each other, by means of a small 1mm protrusion barrier in between them. This is illustrated more clearly in figure 3.2a.

At the back of the electrode holder, two holes are cut out, to electrically connect the electrodes to the

back. The priorly described ring terminal configuration was replaced with small (1.6 mm diameter) bolts (nr. 5) and nuts (nr. 2), which connect to two, steel, laser-cutted, rods (nr. 3). This decision was made in order to retain a simple design, as the production of small connector pieces in the range as small as millimeters would be unnecessarily complicated. Instead, these parts are replaced with readily available bolts. The ring terminal parts were swapped for customised steel rods, as it would be too difficult to make a groove in the cylindrical part to perfectly conceal the complicated shape of the ring terminal. Instead, these customised parts can be easily produced in-house, in the desired sizes, so they will always fit perfectly in the assembly. To ensure there will be a connection between the bolt and the rod, a nut was added. This nut will be used to secure the rod into the groove in the back of the plate, using the thread of the bolt. This guarantees that there will be contact between the rods and the bolts. The nuts will be concealed by grooves in the endplate (nr. 1). This way the electrical connection can surface from top and bottom, with a simple construction, while the plates in the stack will still fit seamlessly together, when pressed by the clamp. To illustrate this, the electrical connection configuration is visualised in figure 3.2b and figure 3.2c. The spring contact design idea, shown in figure 2.14b was dropped as well, as it proved unnecessarily complicated. Instead, the heads of the connection bolts are chosen to be slightly thicker than the electrode holder thickness, to make sure they will always make contact with the electrodes in the holder.

Connections

To position the stack in exactly the same way every time while assembling, four long (4 mm diameter) bolts were utilised. These will penetrate the stack in longitudinal direction, as indicated in appendix figure B.4. These bolts can be used to tighten the stack to keep all components (with emphasis on the membrane) in place before transferring the stack to the clamp in the reactor set-up. In the new design, the diameter of these bolts was reduced, as a consequence of the recommendation to create more space in the stack. In addition, this recommendation implied to make the bolts non-conducting to remove the need for insulation. However, as the stack in the new set-up will be produced from PEEK, there is no need for extra insulation.

To connect the required tubing and the reference electrode to the reaction chambers, holes are created in the sides and the top, as indicated in figure B.15c. Threading will be added to these holes, so 1/4 inch connector pieces can connect the tubing to the stack. To ensure there will be no leaking through these connections, small o-rings will be fitted in around the tubes and in the holes. An illustration of these fittings including their measurements, can be found in appendix B.1. Another aspect aiding the fittings in making them leak-tight, are the added ferrule fittings. These consist of tapered cylinders, to be compressed on a seal, which are positioned around the tubing. When the fitting is tightened, the ferrule will create radial compression, keeping the fitting and tubing compressed together [2].

All the materials and parts that are used in this new design and their origin, are summarised in table 3.2.

3.1.1. Design criteria

The following section will detail how the new design meets the design criteria that were set up in the last chapter.

1) Pressure containment up to 35 bar without leaking

To ensure the sealing between the parts, a number of o-rings were added. The required sizes of the o-rings can be calculated with the o-ring calculator, on the website of the company where they were ordered (Eriks). They are located: 1) between the membrane and both of the reaction chambers (anode and cathode), 2) between the steel endplate and the reaction chamber, and 3) between the part pressing the electrode holder in the reaction chamber. To establish sealing around the bolts and connections, Teflon tape can be inserted.

In addition, as opposed to having a PEEK electrode holder, the decision was made to make the holder

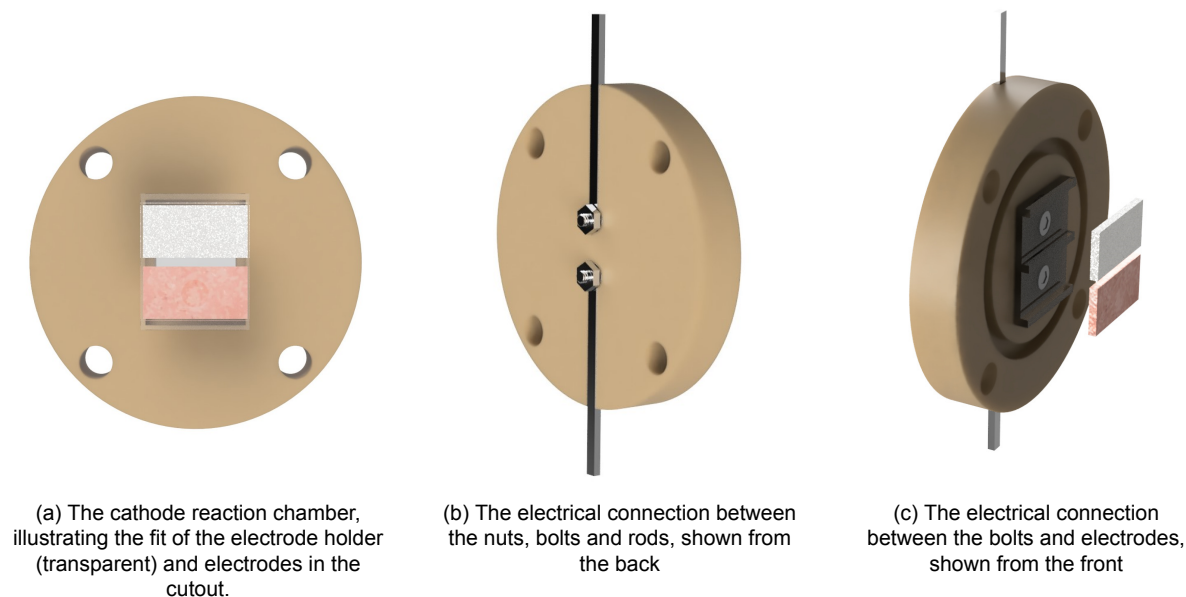


Figure 3.2: Designs are made in SolidWorks and subsequently rendered in Fusion 360.

from a moldable silicon or rubber material. This way it can function as a holder while simultaneously functioning as a seal, to aid in the sealing of the stack at the cathode side.

This way, the stack will be sealed to facilitate the pressures required for the experimental research.

2) Adaptability in the electrode configuration and size

To ensure the required adaptability in the electrode configuration and amount of electrodes, the electrodes will not fit directly into the cutout, but are held together by a frame, the electrode holder. The upside of using a holder instead of just the electrodes, is that when changing operating configurations and conditions, only this part will need to be changed, rather than the entire reaction chamber. This way it becomes possible to vary the distance between the electrodes, the electrode sizes or their configuration (i.e. parallel / in series).

In addition, as both electrodes at the cathode section are connected to the power source separately, it is also possible to conduct single electrode experiments. Apart from that, as they have separate connections, the set-up allows for testing various different potential ranges between the electrodes. Furthermore, the electrodes can be switched for electrodes of different materials as well, in order to experiment with different catalysts. This assembly, therefore, allows for a multitude of different experiments.

3) Easy operation and fast replacement

To ensure easy operation and fast replacement, first of all, the set-up is kept as simple as possible. Secondly, it was constructed with a view to include as many readily available parts as possible. For example, as described above, the electrical connection consists mostly of nuts and bolts to make sure the assembly remains easy and the parts can be easily replaced.

Apart from that, the long (4 mm diameter) longitudinal bolts ensure that placement and construction of the stack will be simple and precise. An image illustrating the construction of the stack by means of the placement bolts, can be found in appendix figure B.4. These bolts are also readily available and can be tightened with 4 mm diameter nuts and basic tools, such as an open-end wrench.

Most parts of the stack are available to be purchased, only a few had to be produced/constructed. These parts were designed in such a way that they could be produced in-house at the university, to limit construction delays.

The stack itself is produced from mechanically machining steel and PEEK rods. This was done in-house in the university workshop, but it can also be outsourced to companies such as Beamlar. The steel connection rods are also produced in-house, by means of laser cutting a stainless steel plate (1 mm thickness). The electrode holder part was, again, produced in-house, with the aid of a Formlabs 3D printer. This printer has the ability to print not only hard plastics, but also elastic resins into the desired shapes. The resin used for the electrode holder is the elastic 50A Resin, which has the looks and characteristics of silicone, with a high durability [31].

4) Separate electrical connections

As explained before, at the cathode section, separate electrical connections are instated to separately connect both working electrodes. The electrodes are connected at the back to a steel bolt. The bolts are connected to RVS rods, by means of two nuts. The connections are concealed in separate grooves and are insulated from leaking, so they are ensured to never make contact and thus preventing short circuits. The rods surface from the top and bottom of the stack, and can be easily connected – with an alligator clip – to the potentiostat (i.e. the power source).

5) Resistance against corrosion

The PEEK stack components have a good resistance to corrosion. The CES Edupack library states that this material has an excellent resistance against most acids and all alkalis. Besides, it also has an excellent resistance against alcohols, aldehydes and ketones, such as, ethanol [25].

The stainless steel parts – the steel endplate, the nuts, the bolts and the connection rods – also have a good resistance against corrosion. The CES Edupack library shows that this material has an excellent resistance against water and aqueous solutions. In addition, it has a good to excellent resistance against acids and alkalis. The same goes for alcohols, aldehydes and ketones [25].

The o-rings are made from EPDM, a rubbery material, which is known to have a good corrosion resistance. The Chemical Resistance Guide expresses this as well, it shows that this material only becomes susceptible to corrosion at higher temperatures (for example, at 100°C for acetic acid) [48].

The electrode holder is produced from a special type of resin, which behaves like silicon. According to CES Edupack, silicon resins have an excellent durability in water and aqueous solutions. They also have an excellent resistance against acetic acids (10%), alkalis and alcohols [25].

6) Better internal flow characteristics

To create better flow conditions, in order to ensure sufficient conversion, the electrodes are placed 'inside' the reaction chambers, instead of 'against'. This is achieved by the tailored frame slots, which allow the electrodes to fit into the chamber, while ensuring that they cannot fall in completely.

Apart from that, another possibility to increase the flow over the electrodes, is to turn the stack, so that the flow will move from right to left and the reference electrode will be located on top or at the bottom. This ensures that, even when the reaction chamber would not be filled completely, CO₂ saturated electrolyte will flow over both electrodes in series.

After validating that the proposed design meets the design criteria, construction drawings can be produced in order to move to the next phase, the production. However, before the design can be produced and tested, an evaluation needs to be carried out regarding the material strength, to determine whether

the design will hold under the required system pressures.

3.2. Strength calculations: the reactor stack

To determine whether the design will be able to withstand the applied stresses, strength calculations were carried out. There are two main stresses acting on the reactor stack, 1) the stress from the clamp holding the stack together and 2) the stress from the high pressure within the reactor. The program CES Edupack was consulted for the yield stresses of the materials in question. The following stress analyses are an expansion of the analysis carried out in the 2020 report by Wols, adapted and specified for the new reactor stack design [123].

3.2.1. Stress originating from the clamp

The clamp exerts a force of 4000 N on the reactor stack. The force is concentrated on the center of the circular back plate, on a circle with a radius of 10 mm. As the plates are stacked together, the bending of the plates – as a result of this stress – is minimised. Therefore, when not taking into account the small holes, the stress in the material can be approximated with equation 3.1 [123].

$$\sigma_{\text{compression}} = \frac{F}{A} \quad (3.1)$$

This results in a material stress of 12.73 MPa. The cylinders in the reaction stack on the cathode side, are produced from PEEK, which, according to CES Edupack, has a yield strength ranging from 65 MPa to 95 MPa [25]. On the anode side, the reaction chamber material will also be PEEK, but the back plate will be made from steel. According to CES Edupack the yield strength of stainless steel 316 alloys ranges from 205 - 310 MPa [25]. Hence, according to this initial analysis, both materials will not yield under the stress originating from the clamp.

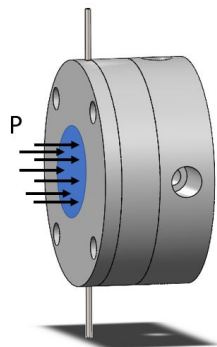


Figure 3.3: Representation of the stress on the reactor stack originating from the clamp.

The only area where a bending moment will have an effect, is where the plate is not supported by other plates, the holes. For both back plates the holes are so small (1.6 mm in diameter) compared to the thickness and area of the plate, that this effect can be neglected. The place where this effect will be the largest, is in the reaction chamber plate, since this plate does contain a substantial hole. To calculate whether this bending moment will cause significant stresses, the following analysis was carried out.

The reaction chamber plate will be simulated with a circular plate with clamped edges, due to the bolts at its ends, carrying a uniform load of 4000 N. The situation is represented in figure 3.4.a. By following the approach as described in Theory of plates and shells (1889) by Timoshenko, the following formulas can be derived to calculate the maximum bending stress (σ_{max}) and deflection (w_{max}) as a result of a uniform load on a circular plate with a circular hole [114]:

$$\sigma_{\text{max}} = k \frac{qa^2}{h^2} \quad (3.2)$$

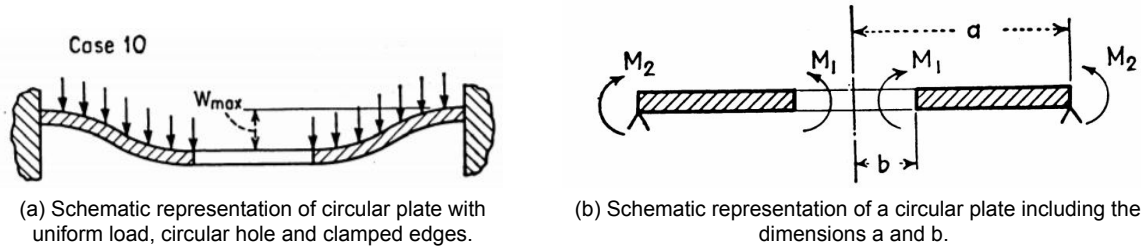


Figure 3.4: Derived from [114]

$$w_{\max} = k_1 \frac{qa^4}{Eh^3} \quad (3.3)$$

With: k a shape factor, q as the load, a the radial distance (shown in figure 3.4b), E the Young's modulus and h the thickness of the plate.

Assumed is, therefore, that the rectangular hole in the reaction chamber piece can be simulated with a circular hole. To account for the worst case scenario, the longest face of the rectangle was selected as the value for the supposed diameter of the simulated circular hole, which is 15 mm. This results in a ratio a/b , the radius of the plate divided by the radius of the hole, of 1.67. The associated k values for the ratio a/b can be found by interpolation and are [114]:

Ratio a/b :	k	k_1
1.67	0.3617	0.0218

Table 3.1: K values for ratio a/b for case 10. Derived from: [114].

This results in a maximum bending stress of 23.3 MPa. Which is still below the yield strength of PEEK, therefore the design is expected to hold under the applied clamping force. The full calculation carried out in MATLAB can be found in appendix B.2.

3.2.2. Stress originating from internal pressure

To calculate the share of stress originating from the pressure inside the reactor, the reactor stack will be analysed as a thick walled cylinder. According to the study by Phalguna (2017), this analysis is valid as long as the wall thickness is larger than 1/10th of the internal radius [81]. For the reaction stack this is certainly the case, therefore this analysis was adopted to calculate the circumferential, axial and radial stresses.

The radial stress (σ_r) and circumferential stress (σ_θ) can be expressed using Lamé's equations [81]:

$$\sigma_r = \frac{p_i r_i^2 - p_o r_o^2}{r_o^2 - r_i^2} - \frac{(p_i - p_o)(r_i^2 r_o^2)}{r^2 (r_o^2 - r_i^2)} \quad (3.4)$$

$$\sigma_\theta = \frac{p_i r_i^2 - p_o r_o^2}{r_o^2 - r_i^2} + \frac{(p_i - p_o)(r_i^2 r_o^2)}{r^2 (r_o^2 - r_i^2)} \quad (3.5)$$

Where the pressure inside the reactor is denoted with p_i , the pressure outside the reactor with p_o , the inner radius of the cylinder with r_i , the outer radius of the cylinder with r_o and the radius at any point in the cylinder (between r_i and r_o) with r .

The axial stress component (σ_z) in the case of a cylinder with closed ends can be calculated with the following formula [122]:

$$\sigma_z = \left(\frac{P_i r_i^2 - P_o r_o^2}{r_o^2 - r_i^2} \right) \quad (3.6)$$

Where p_o was taken to be the clamping force (4000 N) divided by the area of the cylinder ends ($\pi * a^2$).

Figure 3.5 portrays the calculated stress profiles throughout the stack ($r = 0$ to $r = r_o$) for a maximum internal pressure of 100 bar (which is well above the required 35 bar for this reactor stack). As illustrated in this figure, the circumferential stress (σ_θ) is positive and therefore indicates a tensile stress, while the radial stress is compressive, as this stress is always compressive (independent of the sign) [81]. The axial stress component is constant and negative, due to the exerted clamping force on the cylinder end. The profile illustrates that the maximum stresses are located at the inner surface of the cylinder ($r \approx r_i$).

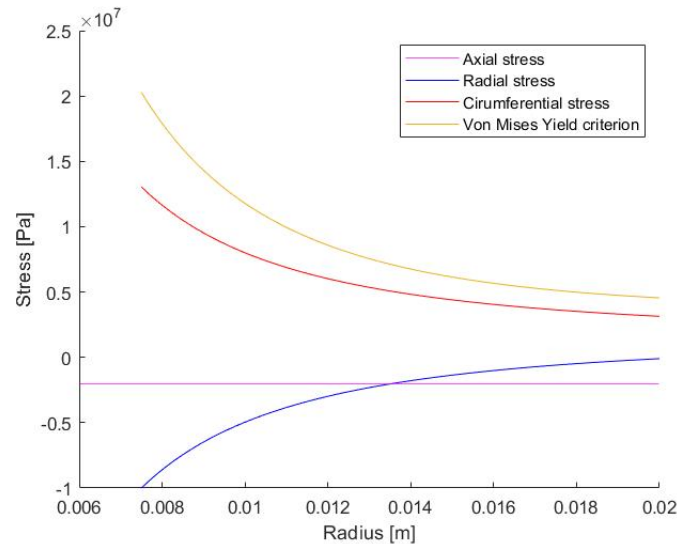


Figure 3.5: Calculated stress [Pa] in the thick walled cylinder as a function of the radius r [m].

In this initial analysis the additional holes in the material are assumed to be insignificant. However, in reality, these holes will locally increase the stress, with a maximum stress at the interface between the main hole and the crosshole [65]. For the most accurate representation of the local stresses, a finite element model can be constructed. However, since the goal of this analysis is to determine whether the design is safe and not to make an exact representation of the stresses in the stack, an analytical representation will suffice, as long as the stresses are found to be well under the yield strength of the materials.

To indicate the local stress around the crosshole, often the factor SCF is used. The SCF is the ratio between the maximum principle stress and the lame's circumferential stress on the inside of the cylinder and can be used to indicate the contribution of the hole to the total stress. With available empirical relations for SCF values for similar hole/cylinder configurations, the maximum local principle stress can be calculated [74]. The SCF for a circular radial hole can be approximated with [65]:

$$SCF = \frac{\sigma_{\theta \max}}{\sigma_\theta} = \frac{4(a/b)^2 + 1}{(a/b)^2 + 1} \quad (3.7)$$

Where a denotes the outer radius of the cylinder and b the inner radius.

This leads to a SCF value of 3.2 and an approximate local stress of 16.4 MPa at the intersection between the crosshole and the cylinder hole ($r = r_i$), which is in accordance with the determined and published SCF values in the 2004 study by Makulsawatudom et al. [65].

To calculate if these stresses will lead to yielding, the Von Mises yield criterion needs to be determined. When the calculated Von Mises stress (σ_v) exceeds the yield stress of the material, this is an indication that the material will yield. Since this is an axis symmetric situation, the principal stresses of the Von

Mises yield criteria are the radial, circumferential and axial stresses, while there are no shear stresses present [86]. The Von Mises stress can be calculated with equation 3.8, which leads to a value of 14.2 MPa for the normal situation and to 17.6 MPa when the local stress around the holes is considered. These values are both lower than the reported yield stress for both materials (PEEK and steel), therefore, the material will not yield under the stresses originating from internal pressure up to 100 bars.

$$\sigma_v = (1/2) \left((\sigma_\theta - \sigma_r)^2 - (\sigma_r - \sigma_z)^2 - (\sigma_z - \sigma_\theta)^2 \right) \leq \sigma_y^2 \quad (3.8)$$

The complete calculations performed in MATLAB can be found in appendix B.2.

3.3. Production

Once the production phase is initiated, the design must be fully validated. Production is a time consuming process, therefore, it is preferable if it does not have to be repeated too often. To make sure the design is safe to use, the strength calculations were carried out. Afterwards, prototypes of the reactor components are 3D printed, to check the physical version of the design with a less time intensive rapid prototyping technique. After validating the design, the production phase starts.

As stated before, only some of the parts need to be produced instead of ordered. Either since they are not available to buy, or in order to save on valuable construction time. Table 3.2 lists the different parts, their size, the amount required for the stack, their material and their origin. The numbers mentioned in the table, refer to the numbered parts from figure 3.1. The construction drawings of the produced parts can be found in appendix B.3.

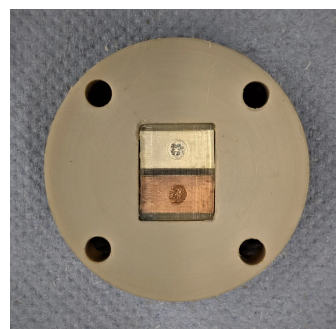
The produced parts indicated in the figure, were all produced at the university workshop, by the author. For the sake of reproducibility, a detailed description of the production process can be found in appendix section B.4. This section describes the 3D printing, laser-cutting, lathing, milling, drilling and tapping processes in a comprehensible manner.



(a) The cathode front endplate including the electrode holder connected at the top connection.



(b) The cathode front endplate fitted with the connection rod at the top side.



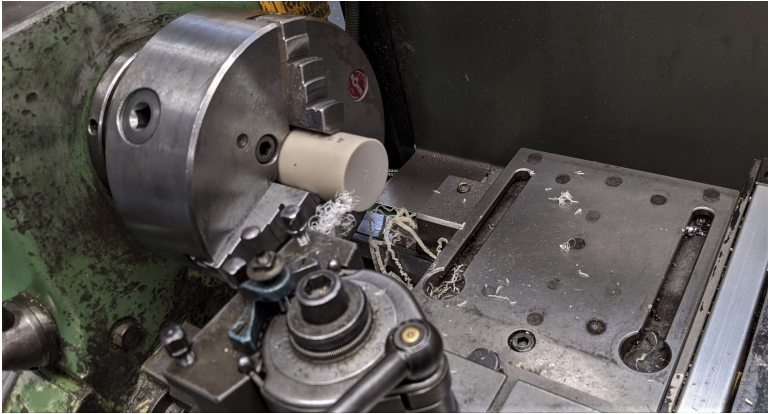
(c) The cathode reaction chamber fitted with the electrodes and electrode holder

Figure 3.6: Images of the produced parts of the reactor stack including the lasercut and 3D printed parts.

nr	Part	Amount	Material	Sizing [mm]	Origin	From
1	Endplate cathode back	1	PEEK	Appendix figure B.6	Produced	Lathing Milling Drilling
2	Connection nuts	2	Stainless steel A2	M1.6 Height = 1.6	Ordered	Accu: * Thin hexagon nuts HFN-M1.6-A2
3	Connection rods	2	Steel	Appendix figure B.7	Produced	Laser cutting
4	Endplate cathode front	1	PEEK	Appendix figure B.8	Produced	Lathing Milling Drilling
5	Connection bolts	2	Stainless steel A2	M1.6 Length = 8 Diameter = 3.2 Head length = 1.42	Ordered	Accu: * Pan head machine screws SIP-M1.6-8-A4
6	Electrode holder	1	Silicon resin (Elastic 50A)	Appendix figure B.9	Produced	Formlabs 3D printer
7	First cathode	1	Silver	width = 10 height = 6 thickness = 1	Ordered	-
7	Second cathode	1	Copper	width = 10 height = 6 thickness = 1	Ordered	-
8	Reaction chamber cathode	1	PEEK	Appendix figure B.10	Produced	Lathing Milling Drilling
9	Cation exchange membrane	1	Nafion 117	Width = 29 Height = 29	Ordered and cut	Sigma Aldrich
[-]	O-rings	4	EPDM	Diameter = 22 Thickness = 2.5	Ordered	Eriks: ** EPDM 70 55985
10	Reaction chamber anode	1	PEEK	Appendix figure B.11	Produced	Lathing Milling Drilling
11	Anode	1	nickel	Width = 12 Height = 15	Ordered	-
12	Conductive endplate	1	Stainless steel	Appendix figure B.12	Produced	Lathing Milling Drilling
[-]	Longitudinal placement bolts	2-4	Stainless steel	M4 Length = 55	Available in-house	x
[-]	Tubing	Dependent	PEEK	1/8 inch	Ordered	IDEX ***
[-]	Female fittings	-	PEEK	1/4 inch Appendix figure B.3	Ordered	IDEX ***
[-]	O-rings fittings	4	EPDM	Diameter = 3.3 Thickness = 1	Ordered	Eriks **
[-]	Reference electrode	1	Ag/AgCl	Appendix figure 5.7c	Ordered	-

Table 3.2: *<https://www.accu.co.uk/en/>. **<https://shop.eriks.nl/nl/>. ***<https://www.idex-hs.com/>
The numbers indicating the various parts originate from figure 3.1.

The operations executed in the production process:



(a) Lathing the PEEK rod to produce a series of cylindrical slabs.



(b) Making the o-ring grooves on the milling machine.



(a) Milling the reaction chamber cutout.



(b) Drilling the holes in the reaction chamber with the milling machine.



(c) Tapping the thread into the holes, with the drilling machine



(a) Making the connection rod slots on the milling machine.



(b) The cylindrical slabs during production phase.

3.4. Design validation

To validate the functioning of the design, it needs to be tested in the lab, and scored on the predetermined design parameters. In order to do this, a testing methodology was set up and carried out.

3.4.1. Methodology

The following section will describe the methodologies employed for the testing of the new design, per design criterion.

High pressure containment

In the preceding section, calculations were made to test whether the reactor would be able to handle stresses up to 100 bar. In reality, for the required experiments, it will only have to operate at pressures up to 35 bar. Therefore, testing the high pressure containment will be up to a maximum of 35 bar. The first step in testing whether the new reactor is able to operate at high pressures (35 bar), is to run water through the stack to check for large leaks. After passing this initial test, the stack will be fitted into the reactor set-up and connected to the pumps. Water will be pumped through the system to check for leaks at ambient pressure operation. After confirming that there are no major leaks in the system, the testing for higher pressures can begin.

To put pressure into the system, the entire set-up, as described in the last chapter (figure 2.10), needs to be connected. Consequently, when increasing the gas-feed pressure, the pressure in the reservoir will build, causing the pressure in the system to rise. The amount of pressure, after a small initialising delay, can be reviewed at the pumps index screens. To test if the reactor is leak-tight up to the desired 35 bars, the pressure in the system will be slowly increased (increments of 5 bar), while the system is monitored for possible leaks. The system will be deemed successful at building pressure, if it is able to operate without leaking at a pressure up to 35 bars.

Chemical resistance

The system will be regarded sufficiently chemically resistant, when no major corrosion will have built up after operation, while testing.

Fast assembly/disassembly

Fast and easy assembly will be tested by assembling the set-up and taking it down. Afterwards, this process will be reviewed on problems or difficulties. Here, the focus will be mainly on the reactor stack, as this is the part of interest for this research. The assembly/disassembly of the stack will be assessed as sufficiently fast and easy, when: 1) it can be successfully constructed and destructed without issues, 2) when all required tools and parts are available along with the set-up.

Separate electrical connections

For testing the electrical connections to the cathodes, the system will be set up (excluding the CO₂ saturation part) and connected to the potentiostat. Appendix figure B.18 depicts the connection to the potentiostat. Both cathode connections will be tested separately, in all tests. The tests will be conducted with a 0.1 M KHCO₃ electrolyte solution, to ensure the conductivity of the eluent solution. To review the connections and for running the experiments, EC-LAB software is used. Apart from running experiments, this software displays the potential difference between the reference and the working electrode and, thus, can provide an initial estimation of a proper electrical connection.

To determine the ohmic resistance inside the reactor and, therefore, to confirm an electrical connection, a potentiostatic electrochemical impedance spectroscopy (PEIS) measurement will be carried out. During this measurement an initial cell potential E , whose value should lay around the equilibrium potential of the cell, is set. Next, the frequency will be varied over a specified range, resulting in a sinusoidal

potential profile for the working electrode, around the set value for E [45]. The system will plot this information into a Nyquist plot, plotting $-Z_{Im}$ vs. Z_{Re} [127]. An example of a Nyquist plot and its interpretation can be found in figure 3.7. By performing a linear fit on the high frequency part and calculating the intersection with the Z_{Re} axis, the reactor resistance can then be found [113]. This value should optimally be low, to indicate there is a good connection and a low cell resistance. To test the response of the new reactor to the required different pressures, these PEIS measurements will be conducted over the following pressure ranges: 5, 10, 20 and 30 bar. Frequencies will be varied from 200 kHz to 100 mHz, with a sinus amplitude of 10 mV and a logging delay of 0.10 periods after each measurement. The graph will be recorded with 20 points per decade.

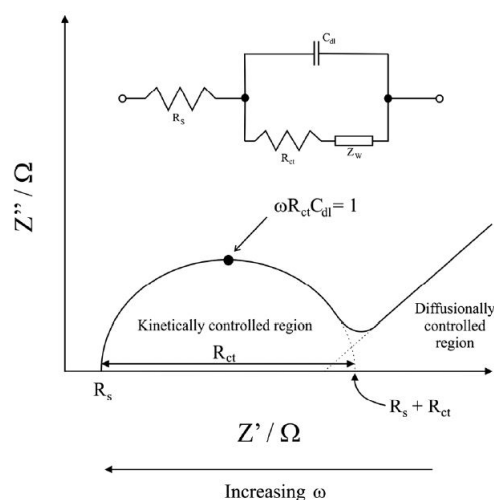


Figure 3.7: A Nyquist plot representing an EIS measurement. Here R_{ct} represents the charge transfer resistance and R_s the solution resistance. C_{dl} indicates the double layer change at the electrode surface and Z_w , the Warburg element (i.e. diffusion of the ions in the solution). Image is derived from [88].

In summary, the separate electrical connections are regarded to be sufficient when their mutual potentials are in the range of mV, instead of Volts or μV , as this would indicate the connection is off or short circuited. In addition, the PEIS measurements should deliver stable measured values within the range of 10-80 Ω . When the pressure on the system is increased, the graph is expected to shift to the left, as the increased mass transfer properties could result in a lower resistance. Lastly, all the obtained measurements and values should be similar for both cathodes.

Safety

Safety is a very important design parameter, especially, since the set-up works with high pressures and potentially dangerous gasses (CO, H₂, etc.). Therefore, the reactor will be regarded as safe when no gas can escape while operating and when it proves to be successfully leak-tight at high pressures. In addition, the stack must be able to be constructed and deconstructed without coming into contact with the electrolyte. When these tests are carried out successfully, the design is regarded as sufficiently safe.

Sufficient conversion

To test if the reactor can ensure sufficient conversion for the experimental work in mind, the entire system will be set up. The gas output will be connected to the Gas Chromatograph (GC), after operating with CO₂ saturated electrolyte (0.1 M KHCO₃) for a minimum of 30 minutes. The reactor pressure for these experiments will be set to be 5 bars, and the CO₂ gas pressure will be set to 4 bars. First the flow-rate to the GC will be kept low (0.3 mL/min) for 20 minutes, to build up the gasses in the system. Afterwards the flow-rate will be increased to 8 mL/min, and the system will run for another 70 minutes, while the GC documents the products produced. Afterwards, the results will be analysed

and the Faradaic efficiencies will be determined for the produced products. This test will be executed two separate times at these conditions. First, only the silver electrode will be actuated, to check the resulting amount of CO and H₂. For the second test, only the Cu electrode will be actuated, and the GC will be consulted for (mainly) C₁ and C₂+ products.

To test the connection and to determine the corresponding current densities, a Chronoamperometry (CA) measurement will be conducted during the CG analysis. During this measurement, the response of the current on a perturbation in the applied potential against the time is monitored. Here, the applied potential must be high enough to induce an electrochemical reaction. Details about the reactions taking place can be attained, by comparing the response of the system to the Cottrell equation (equation 3.4.1). This equation accurately describes the system in the diffusion limited domain, where the applied potential is high enough for the system to be diffusion limited (i.e. the surface concentration of the oxidant goes to zero) [47]. Therefore, if the system behaves as described by this equation, showing a current proportional to $\frac{1}{t^{1/2}}$, it indicates the system is indeed in the diffusion limited domain. Sometimes the graphs deviate from this response, this could indicate a slow reaction step in the reaction kinetics (chemical or electron transfer) [93].

$$i = \frac{nFAD^{1/2}C_0}{(\pi t)^{1/2}} \quad (3.9)$$

Where: n denotes the number of electrons, F Faraday's constant, D the diffusion coefficient, C_0 the bulk concentration, and A the electrode area.

Summarising, the system will be deemed successful at ensuring sufficient conversion when the GC results will indicate a clear distinguishable amount of CO, C₁ and C₂+ products and the CA plot will show a flat/stable current time plot.

Experimental versatility

Of the different design parameters, experimental versatility is one of the harder things to verify. Most likely this parameter will be verified over time, when new experiments will be devised and executed in the set-up. Therefore, this design parameter will be regarded successfully met, if the set-up is deemed sufficiently versatile for all experiments regarding this research. Consequently, this parameter is an accumulation of the preceding parameters.

Hence, the reactor must be able to operate at different pressures ranging up to 35 bars. It must also be possible to separately connect the two cathodes. This parameter also entails the easy substitution of electrodes, as the system is designed to work with multiple different electrodes.

3.4.2. Results & Discussion

To evaluate the design, all the preceding tests were performed. Table 3.3 summarises the results, the encountered problems and the accompanying devised solutions. An analysis of the results requiring further explanation will be made below. This information will ultimately lead to the conclusion as to the overall performance of the design.

Design parameter	Test	Success	Problems	Solutions
High pressure containment	Initial water leak testing	Yes	No	No
	Ambient pressure pumping water	Yes	No	No
	Increasing pressure (5 bar) up to 35 bar	After iteration	Occasional leaking in multiple compartments, because of poor fitting o-rings	New, better fitting o-rings, see table 3.2
Chemical resistance	Monitoring corrosion during testing	No	The combination of the nickel anode, connected with the conductive endplate is causing corrosion. In addition, corrosion is also detected on the cathodes after the experiments.	A gold layer was added to the protrusion on the steel plate, so the nickel is no longer directly in contact with the steel
Fast assembly/disassembly	Availability of the required tools	After iteration	Tools are required for the tightening of the fittings to ensure they remain leak-tight. In addition, a tool for the tightening of the nut on the placement bolts is also required.	Tongue-and-groove pliers and a M4 wrench
	Successful construction/deconstruction every time (exactly the same)	Yes	No	No
Separate electrical connections	EC-LAB potential difference range	Yes	No	No
	PEIS measurements at 5, 10, 20 and 30 bar	Yes	No	No
	Cathode connection symmetry	Yes	No	No
Safety	Safe construction/deconstruction	Yes	No	No
	No escaping gas near the operator	Yes	No	Experiments performed in the fumehood
	No leaks in the set-up	Yes	No	Solved with new o-rings
Sufficient conversion	Testing for: only Ag electrode actuated at ambient pressures			
	Testing for: only Cu electrode actuated at ambient pressures			
Experimental versatility	Proven versatility in all completed tests	Yes		

Table 3.3: A summary of the tests for the different design parameters and the performed results.

High pressure containment test results

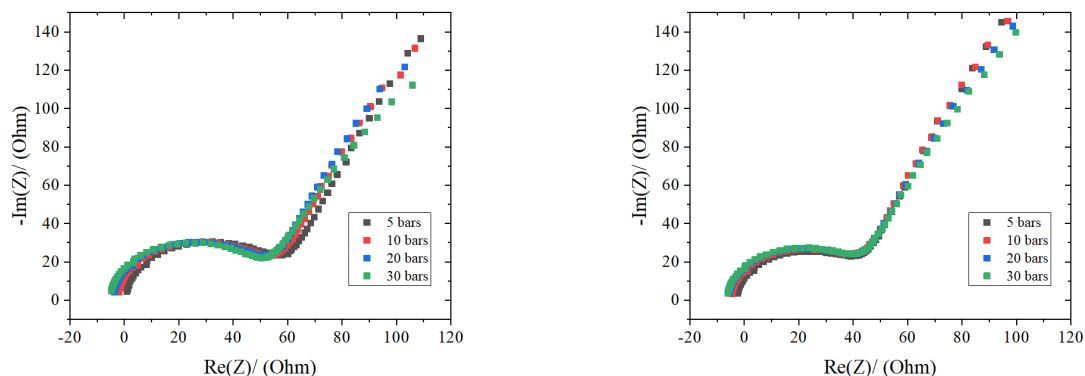
To test whether the reactor can contain the required high pressures, the pressure was increased in steps of 5 bars, starting from ambient conditions and reaching up to 35 bars. During the tests, no leaking occurred at the cathode section of the reactor, and after replacing the o-rings for better fitting ones, no leaks formed at the anode section either. A video recording of the reactor operating at 35 bars during this testing procedure can be found at: <https://youtu.be/m8fC6NrQG0M>, or by scanning the QR code presented in figure 3.8.



Figure 3.8: QR code directing the reader to a short recording showing a successful 35 bar pressure test. Same file can be accessed via: <https://youtu.be/m8fC6NrQG0M>.

Potentiostatic electrochemical impedance spectroscopy (PEIS)

The PEIS measurements were carried out at different pressures (5, 10, 20 and 30 bar) for both cathodes separately. This way, the connection to both cathodes could be investigated, while also creating insight into possible pressure dependent trends in the system resistance. All measurement were conducted a minimum of two times, to monitor the stability in the response of the system.



(a) The PEIS measurement for the Ag electrode connection at different pressures

(b) The PEIS measurement for the Cu electrode connection at different pressures

Figure 3.9: Measurements completed with EC-Lab software.

The figures illustrate stability in the resistance and show the initial symmetry between the Ag and Cu electrode connections. The resistance is demonstrated to decrease with increasing pressure (move leftwards), indicating increased mass transfer properties in the system at higher pressures.

This test is regarded as successful, as the results clearly demonstrate the electrical connections of the reactor to function, while they are connected separately.

Reference electrode

Problems with the reference electrode can greatly influence the response of the system [46]. This is particularly important regarding experiments operating with increased pressures. To determine if there is a problem, and to indicate the nature of a problem, the reference electrode impedance need to be determined. This is necessary, as the reference electrode applied in this design is known to have a

very high junction resistance.

To test the performance of the reference electrode, an Open Circuit Potential (OCP) measurement was carried out. To set up this measurement, the reference electrode in question is placed into a vessel containing 3 M KCl, along with a second reference electrode, which is only used for validation purposes. The latter is often referred to as the 'master' or 'golden' reference electrode [13]. To set up the OCP, the master reference is to be connected to both the counter and reference cables, while the reference electrode is connected to the working drive and the working sense cables [105]. The connection scheme is shown in more detail in appendix figure B.19. The OCP will be measured for two minutes, after which the difference between the maximum and minimum potential values will be evaluated. Preferable this difference will be in the range of 5 mV and remain stable [127].

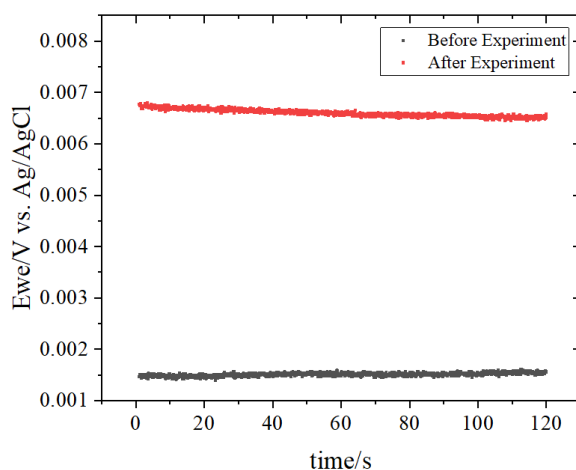


Figure 3.10: Comparison between the results for an OCP measurement, conducted before and after a high pressure experiment.

The OCP data usually presents to be stable and in range, however, the resistance drastically increases after conducting high pressure experiments, as demonstrated in figure 3.10. This effect indicates this type of reference electrode might not be suitable for high pressure experiments. After leaving it in a KCl solution for a certain period, it will restore. This could explain why the reference electrode sometimes gives strange PEIS values, whereas it works fine at other times. The most likely cause for this phenomena, is the loss of solvent (KCl). At high pressures the CO_2 enters the tube, therefore, when depressurising, the bubbles inside the tube force the solvent out. This decreases the activity, resulting in the effects shown in figure 3.10. This would explain why restoring in a KCl solution for long enough, brings the resistance down again.

Electrochemical conversion results

Due to unforeseen problems with the experimental set-up, the CV measurements could not be conducted to validate the conversion characteristics in the system. To provide a preliminary indication regarding the ability of the design to ensure electrochemical conversion an CV analysis was conducted over the course of an hour. As described above, a good CV measurement will display a stable trend. Figure 3.11 illustrates, the CA measurement shows the effect of bubble formation and detachment from the surface, this is indicated by the sudden jumps in the trend. It is still too early to make conclusions regarding the conversion in the system. However, this result indicates the system is seemingly stable over the course of an hour, indicating the preliminary results are promising.

Corrosion issues

During testing, some issues with corrosion on the electrodes occurred. Figure 3.12 shows the electrodes after the experiments. Before conducting experiments, the electrodes were polished according

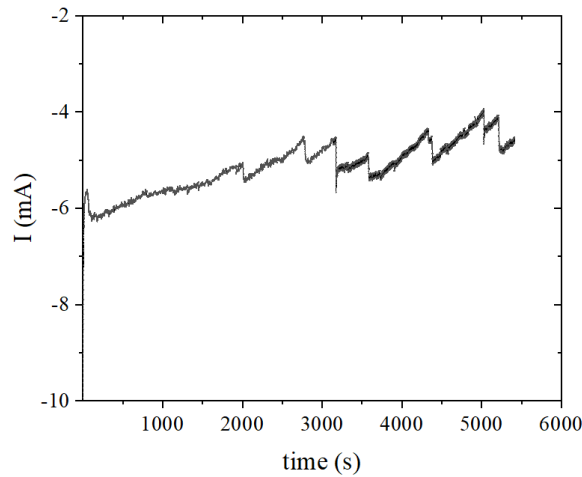
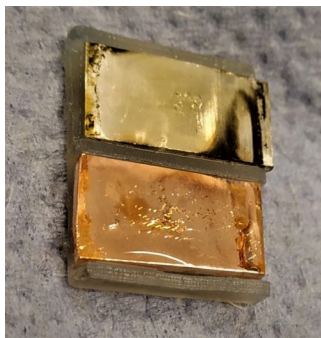


Figure 3.11: Chronoamperometry measurement result.

to basic the polishing techniques and additional electropolishing.



(a) The Cu and Ag electrodes after conversion testing with only the Ag electrode electrically connected.



(b) The Cu and Ag electrodes after the PEIS measurements.



(c) The nickel electrode after conversion testing with the Ag electrode electrically connected as cathode.

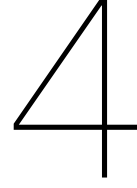
Figure 3.12: Corrosion on the electrodes after different experiments.

Figure 3.12a portrays the cathodes after the conversion experiment and CA analysis, where only the Ag was actuated. The image shows a black deposit on the Ag electrode. Figure 3.12c shows the anode to have black/blue deposit as well after this experiment. Figure 3.12b shows the cathodes after the PEIS measurements. This image shows the cathode to have a grey deposit, while the Ag electrode has no deposit.

One identified cause of corrosion is, a reaction between the steel endplate and the nickel anode. To solve this problem, an inert gold foil was added to the protrusion on the steel endplate. This is illustrated in appendix figure B.20. This way the steel would no longer be in direct contact with the nickel. This design iteration was deemed successful, as no corrosion appeared on the steel endplate.

3.4.3. Conclusion

This section demonstrated the production process for the high pressure cascade electrode. This has resulted in a new innovative design idea, which was designed to be adaptable and consists of as many replaceable (readily available) parts as possible. The parts that did have to be manufactured, were created in house, by the author, to save valuable production time. After production the design was tested and adapted, in order to satisfy the devised design criteria. Overall, the preliminary test results are promising, indicating this design could be suitable for high pressure cascade experiments in the near future.



The high pressure cascade model

To determine the response of the cascade system to high pressures, in order to determine the potential of this proposed combined system, a mathematical model was constructed. The following section will provide a detailed description of the modelling strategy, the model structure, the underlying theory and the underlying assumptions.

4.1. Mathematics

As described in section 2.2, the transport of the species inside the diffusion layer is determined by a set of partial differential equations, the transport equations. Partial differential equations (PDEs) is a term describing any differential equation in which the functions depend on more than one independent variable and its partial derivative. Differential equations where the functions depend on only one variable and its partial derivative, are indicated as ordinary differential equations (ODEs).

The system of PDEs describing the transport of species in the model is specified below.

$$\frac{\partial C_{CO_2}}{\partial t} = D_{CO_2} \cdot \frac{\partial^2 C_{CO_2}}{\partial x^2} - r_3^f + r_3^r \quad (4.1)$$

$$\frac{\partial C_{HCO_3^-}}{\partial t} = D_{HCO_3^-} \cdot \frac{\partial^2 C_{HCO_3^-}}{\partial x^2} - \frac{F}{RT} D_{HCO_3^-} C_{HCO_3^-} \cdot \frac{\partial^2 \phi}{\partial x^2} + r_3^f - r_3^r - r_4^f + r_4^r \quad (4.2)$$

$$\frac{\partial C_{CO_3^{2-}}}{\partial t} = D_{CO_3^{2-}} \cdot \frac{\partial^2 C_{CO_3^{2-}}}{\partial x^2} - 2 \cdot \frac{F}{RT} D_{CO_3^{2-}} C_{CO_3^{2-}} \cdot \frac{\partial^2 \phi}{\partial x^2} + r_4^f - r_4^r \quad (4.3)$$

$$\frac{\partial C_{OH^-}}{\partial t} = D_{OH^-} \cdot \frac{\partial^2 C_{OH^-}}{\partial x^2} - \frac{F}{RT} D_{OH^-} C_{OH^-} \cdot \frac{\partial^2 \phi}{\partial x^2} - r_3^f + r_3^r - r_4^f + r_4^r \quad (4.4)$$

$$\frac{\partial C_{K^+}}{\partial t} = D_{K^+} \cdot \frac{\partial^2 C_{K^+}}{\partial x^2} + \frac{F}{RT} D_{K^+} C_{K^+} \cdot \frac{\partial^2 \phi}{\partial x^2} \quad (4.5)$$

$$\frac{\partial C_{CO}}{\partial t} = D_{CO} \cdot \frac{\partial^2 C_{CO}}{\partial x^2} \quad (4.6)$$

$$\frac{\partial C_{H_2}}{\partial t} = D_{H_2} \cdot \frac{\partial^2 C_{H_2}}{\partial x^2} \quad (4.7)$$

$$\frac{\partial C_{HCOO^-}}{\partial t} = D_{HCOO^-} \cdot \frac{\partial^2 C_{HCOO^-}}{\partial x^2} - \frac{F}{RT} D_{HCOO^-} C_{HCOO^-} \cdot \frac{\partial^2 \phi}{\partial x^2} \quad (4.8)$$

$$\frac{\partial C_{CH_4}}{\partial t} = D_{CH_4} \cdot \frac{\partial^2 C_{CH_4}}{\partial x^2} \quad (4.9)$$

$$\frac{\partial C_{C_2H_4}}{\partial t} = D_{C_2H_4} \cdot \frac{\partial^2 C_{C_2H_4}}{\partial x^2} \quad (4.10)$$

$$\frac{\partial C_{C_2H_5OH}}{\partial t} = D_{C_2H_5OH} \cdot \frac{\partial^2 C_{C_2H_5OH}}{\partial x^2} \quad (4.11)$$

$$\frac{\partial C_{CH_3COO}}{\partial t} = D_{CH_3COO} \cdot \frac{\partial^2 C_{CH_3COO}}{\partial x^2} - \frac{F}{RT} D_{CH_3COO} C_{CH_3COO} \cdot \frac{\partial^2 \phi}{\partial x^2} \quad (4.12)$$

Where:

$$\begin{aligned} r_3^f &= k_3^f [CO_2] [OH^-] \\ r_3^r &= k_3^r [HCO_3^-] \\ r_4^f &= k_4^f [HCO_3^-] [OH^-] \\ r_4^r &= k_4^r [CO_3^{2-}] \end{aligned} \quad (4.13)$$

There are a lot of different types of PDEs, which all require different solution strategies. Therefore, to determine how to solve a set of PDEs, they have to be classified first. More information on this procedure and the different solution strategies can be found in appendix C.1.

Boundary conditions

As described in section 2.2, to solve a set of PDEs, a selection of boundary and initial conditions is required. These conditions describe the known behaviour of the solution at a certain boundary or starting position. If the boundary condition gives information on the $u(x)$, it is specified as a Dirichlet boundary condition. When the boundary condition provides information on the derivative of the problem, $\frac{\partial u}{\partial x}$, it is regarded as a Neumann boundary condition [35]. The Dirichlet and Neumann boundary conditions deployed in this model are specified in section 4.4. They are also indicated in figure 4.1a, showing how they are applied in solving the equations.

Numerical mathematics

The solving of a system of PDEs becomes very complicated and time consuming very quickly, therefore, numerical programs are often employed for this purpose. Numerical mathematics is a collection of many different solution strategies for approximating sets of equations. These methods, however, can only make a discrete approximation of the actual solution. It is, therefore, not guaranteed that the numerical approximation will converge to a physical solution [9].

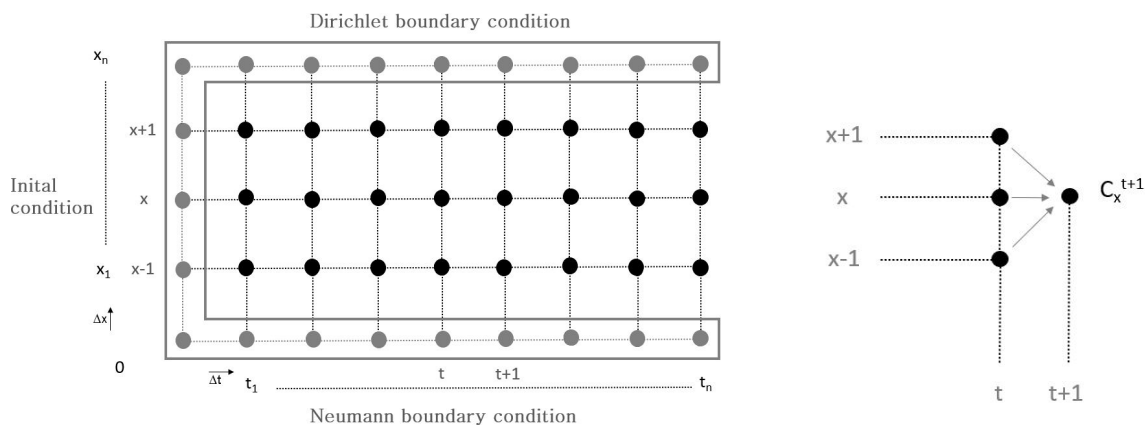
In numerical mathematics the solution is approximated by dividing the physical solution space into a mesh of small increments. The evaluated solution, at that point, is a discretized approximation of the actual solution. Therefore, the smaller the increments, the more accurate the approximated solution will be. However, more points also means that a lot of CPU speed and available memory is required from the computer to solve the problem. Figure 4.1a shows an example of a mesh, representing discretized points in a physical space. Detailed information on different methods applied for numerical mathematics can be found in appendix C.2.

Numerical solvers

MATLAB, the mathematical program deployed for the model in this research, has many different solver programs capable of numerically solving ODEs or PDEs. In appendix C.1, the equations 4.1 to 4.12 were classified as linear second order parabolic. MATLAB has a built-in solver for initial-boundary value PDEs with a time dependence and single spatial variable, called pdepe. This solver utilises the method of lines, a method which discretises into lines instead of a mesh, to convert the PDEs into ODEs, which are much easier to solve [101]. For this model, this entails assuming that the time t is the same for each segment/line of discretised x values. After all points of x for this time t are calculated, it will move up to time-step, $t = t + \Delta t$, and will calculate the next line of x values. This process is illustrated in figure 4.1b.

This discretisation and converting to ODEs is done according to the Galerkin/Petrov-Galerkin method, a finite difference method which is accurately described in the 1990 research by Skeel and Berzins [101]. The resulting ODEs are then solved with the MATLAB solver ODE15s, which utilises numerical

differentiation formulas like the backward difference method [111]. These methods apply the theory of calculating a node and using this information to calculate the subsequent node as described above.



(a) Schematic representation of an explicit finite difference calculation, where known values (grey) are used to calculate the unknown mesh-points (black).

(b) Illustration of the approach for the calculation of the concentration for the subsequent time step

Figure 4.1: Schematic representation of the iteration scheme. More detailed information on this subject can be found in section 11.3.2 of the Handbook of electrochemistry [127].

Input: pdepe

As described in sections 2.2 and 4.1 above, to solve the transport equations, sets of initial conditions and boundary conditions need to be determined. To describe the system accurately in the pdepe solver, the input is very important. Therefore, this section will describe the required input method for the MATLAB function pdepe in more detail.

The input functions and values required for the function pdepe is presented in table 4.1. To find the solution for the system, *sol*, the following statement needs to be called:

```
sol = pdepe(m,pdefun,icfun,bcfun,xmesh,tspan)
```

The function pdepe expects the transport equations to be entered in a predetermined shape. This shape is indicated in equation 4.14. To enter this information into the system in the function pdefun the c , f and s terms have to be defined separately. As an example on how to define these for the transport equations, equation 4.15, describing the transport of $[\text{OH}^-]$, is displayed below. In the pdepe function, the concentration C , is indicated with the variable u .

$$c \left(x, t, u, \frac{\partial u}{\partial x} \right) \frac{\partial u}{\partial t} = x^{-m} \frac{\partial}{\partial x} \left(x^m f \left(x, t, u, \frac{\partial u}{\partial x} \right) \right) + s \left(x, t, u, \frac{\partial u}{\partial x} \right) \quad (4.14)$$

$$\underbrace{\frac{\partial C_{\text{OH}^-}}{\partial t}}_c = \underbrace{D_{\text{OH}^-} \cdot \frac{\partial^2 C_{\text{OH}^-}}{\partial x^2} - \frac{F}{RT} D_{\text{OH}^-} C_{\text{OH}^-} \cdot \frac{\partial^2 \phi}{\partial x^2}}_f - \underbrace{r_3^f + r_3^r - r_4^f + r_4^r}_s \quad (4.15)$$

By comparing these equations, it becomes clear that the value for c , regarding equation 4.15, must be equal to one, to simulate the PDE solution is time dependent. The value for f is displayed in equation 4.15. Lastly, the value for the source term, s , is determined by the values of r , representing the interaction with the electrolyte solution as shown in equation 4.13.

The initial conditions (u_0) can either be entered in the shape of a function depending on input variable x , or as a set of values, depending on the requirements of the system. It is also possible to assign specific input values for the initial conditions, per value of spatial variable x . This becomes necessary if the input conditions are not constant in the x -direction, as is the case with having a concentration

gradient. This will be discussed in more detail in section 4.4.

```
u_0 = function(x)
u_0 = [u_1;u_2;u_3]
```

To properly enter the boundary conditions into the bcfun function, they must have the exact shape as described in equation 4.16. Here, f represents the f -functions term as defined in the pdefun function above, q is a function of the time and spatial variable only, and p is a function of the time, spatial and concentration variable. The function bcfun depends on x_L, u_L, x_R, u_R and t , where the u and x represent the left boundary condition, and the u and x represent the right boundary condition and the time variable.

$$p(x, t, u) + q(x, t) f \left(x, t, u, \frac{\partial u}{\partial x} \right) = 0 \quad (4.16)$$

Parameter	Role	Value/size
sol	System solution	(j,k,i)
m	Symmetry of the problem (slab, cylindrical, spherical)	0
pdefun	Defined partial differential equations	(ix1)
icfun	Initial conditions	(ix1)
bcfun	Boundary conditions	(ix1)
xmesh	Defined spatial coordinates	k
tspan	Defined time span	j

Table 4.1: The required parameters, their role and value/size to solve problems with the pdepe function in MATLAB.

4.2. Strategy

The last section proved that, to solve the transport equations, two boundary conditions and an initial condition are required as input for the solver program. This information will be acquired by applying known theory and formulas, in the shape of functions, to determine unknown variables. The model is organised to have one main file, containing all parameters, data and conditions. To determine variables required as input for the solver, functions are invoked in the main file. All major calculations will, therefore, be done in these functions, and the output will be added to the main file. This way, the main file remains simple and comprehensible and small parts of the model can be easily replaced or updated.

As the model was based on a pre-existing model, the model by Soeteman (2019) [102], part of the original strategy was adopted. The model in this research is based on the following premises: first, the optimal applied potential is determined to produce a maximum current efficiency towards the production of carbon monoxide. This is done by varying the overpotential while parallelly solving the transport equations with the acquired data for each individual potential. Subsequently, the subsequent concentration profile for the maximum current efficiency potential is used as an initial condition to calculate the transport equations around the second electrode. Again this calculation is done in parallel, for the entire determined overpotential range. This will provide the desired insight into the relation between the overpotential and the concentration profile after both reaction steps.

To determine the effect of pressure, both of these reduction steps are investigated again. However, in this case the transport equations, are solved for different pressures, instead of different potentials. The potentials at which the pressure behaviour is evaluated can be freely selected, or may result from the maximum current efficiency information determined in the prior two steps. Performing this pressure evaluation, will result in information on the concentration profile and the dependence on the system pressure.

Of these four described steps, only the first resembles the modelling strategy followed in the model by Soeteman [102]. The input data for this first step, however, cannot be adopted from his model, as the initial code was written to simulate different reactions on a different catalyst. Furthermore, since the data for these reactions was readily available in literature, no extra calculation was required to acquire it. This does not apply to the high pressure cascade model. Much of the required data has to be calculated, as this is not as readily available in literature. Therefore, for this first step, only the modelling strategy and not the structure is adopted from the model by Soeteman. Figure 4.5 displays which parts were based on the original code (adapted) and which parts of the structure are newly developed.

To model the cascade behaviour, the produced CO from the first step will react on the copper to form C_1 and C_{2+} products. However, as there is still CO_2 present in the system after the reduction in the first step, the left over CO_2 will also react on the copper electrode, forming C_1 and C_{2+} products. To simulate this as realistically as possible, ideally the kinetic data for CO and CO_2 reduction on copper will be taken from experimental results, performed on the same reactor set-up. Possibly the CO_2 will form more CO on the copper surface, which will subsequently react. This effect would be accounted for in this case, as the CO_2 reduction input is taken from experimental data in which this effect would be incorporated. An alternative strategy would have been utilising experimental data from cascade reactors as provided in [38]. The main advantage of using this strategy, would be that it could account for phenomena occurring inside of the cascade, which are not yet understood, and therefore, otherwise unaccounted for. However, the decision to split up the second step in a CO reduction reaction and a CO_2 reduction reaction, provides for an opportunity to see to what extent products originate from CO or CO_2 reduction. Which would be very interesting information to analyse, as the effect of pressure on the cascade system is one of the main goals to investigate in this research.

As described in section 2.2, to model an electrochemical cell, the system is often split up in different sections. The general approach identifies three different sections, as shown in figure 2.9. However, the high pressure cascade system requires a somewhat more complex scheme, as there are not one, but two working electrodes. Therefore, the three-section approach will no longer be able to cover the complexity of the system. To schematically describe the transport and show the different sections defined in the model, figure 4.2 is created. This figure demonstrates the means of transport between the characterised sections. As in figure 2.9, three different layers are identified, the bulk, the diffusion layer and the electrode surface. In addition to these sections, a second electrode surface, a gap section – between the electrodes – and an output section – after the second reduction step – are added here. The figure illustrates that in the bulk layer, the $KHCO_3$ chemically reacts with the dissolved CO_2 , after this is bubbled through the system ($CO_2(g)$ becomes $CO_2(aq)$). The reactions displayed here, show the ions and products present in the bulk layer. The diffusion layer, between 0 to δ , illustrates the transport of species between the bulk layer and the electrode surface. Note that the products produced in the first reduction step, move to the second reduction step – through the gap section – without transport to the bulk. The reasoning behind this simplification will be explained in detail in the next section. At the electrode surfaces, the electrochemical reactions taking place at each electrode are indicated. These show which products will be produced in the separate reduction steps. After each reduction step, a concentration profile consisting of the produced species is indicated. The products produced in the first reduction step will, therefore, act as input for the second reduction step. These are the schematics the model was based on.

As explained in section 2.2, 'Cascade modelling', adding these additional sections demands that, as a consequence, additional boundary/initial conditions are required as well. The way these were defined and executed, will be discussed in the following sections.

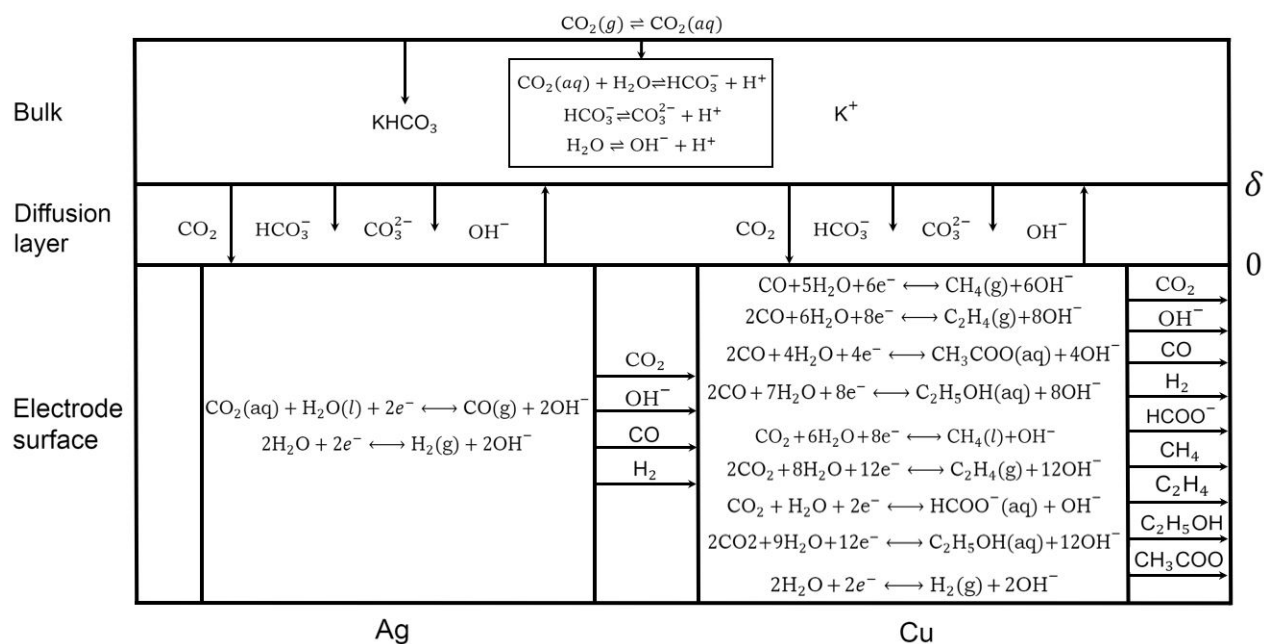


Figure 4.2: A schematic representation of the different sections and transport of species within the model.

4.3. Assumptions and limitations

Section 2.2.4 already discussed the valid assumptions originating from other models in literature. In addition to these, some simplifications were made regarding the simulation of the actual situation in the model. These will be presented in the shape of assumptions, which will be analysed on their impact on the accuracy of the results. A trade-off will be made between overcomplicating the model and the validity of the modelled results.

Input data limitations

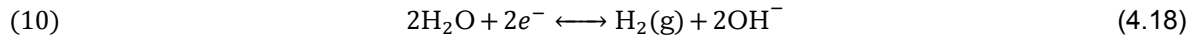
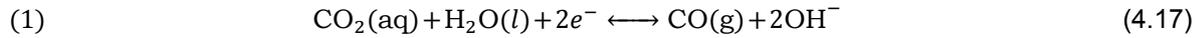
The model by Soeteman aimed to model the experimental set-up and results as described by the research of Todoroki et al. [115]. Therefore, the required input data all originated from the same representable source. For the high pressure cascade model, however, this same approach is not possible, as no experimental results exist as of yet. Hence, the data must be gathered from different sources. The source regarding the first reduction step of CO_2 on the silver electrode is the 2014 research by Hatsukade et al. [40]. For the second step, the CO_2 reduction and the CO reduction on copper, are modelled separately. This process will be described more extensively later in this section. The data regarding the CO_2 reduction on the copper electrode originates from the 2019 research by Nitopi et al. [56]. The data for the CO reduction on copper was determined from the 2018 research by Wang et al. [120]. For the CO data, a small deviation from reality is expected, as the research data originates from conducted experiments in a different electrolyte, at different pH levels than the other papers. As this research is comparing these reactions (CO_2R and COR) as if taking place in the same cell, this might result in a deviation from reality in the results. The consulted sources all originate from the same research group, where experiments were conducted in the same reactor set-up, and therefore regarded as the most representable manner to gather the required data. To validate the model, the results will be compared to the results of these individual papers in section 4.5.

Electrochemical reactions

To determine which electrochemical reaction equations to include in the reduction steps of the model, experimental product distributions are consulted. CO_2 reduction on copper alone, already has the ability to form at least sixteen different products [76]. Some of these barely account for 1% of the total

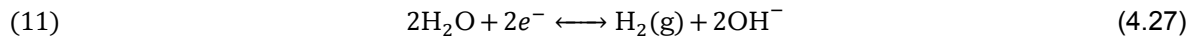
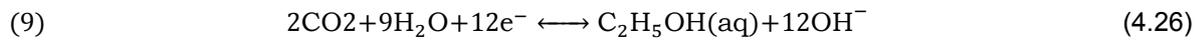
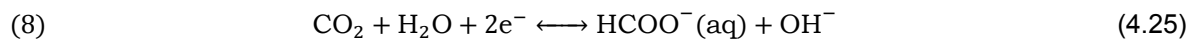
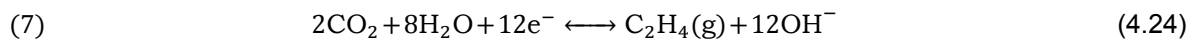
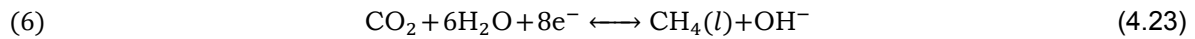
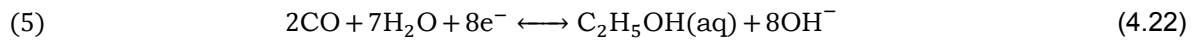
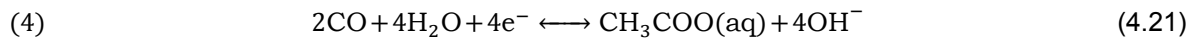
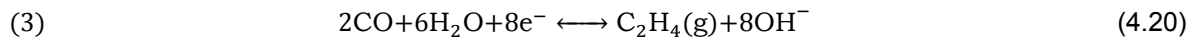
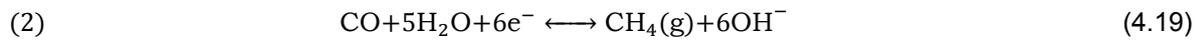
production. Therefore, a simplification has been made to only account for the following major products in the electrochemical reactions.

For the first reduction step, the following electrochemical reactions were considered:



This choice was made, based on the product distribution data published by Thevenon et al., showing that the amount of formate produced from this reaction lies far under the 5% of the total [113]. Therefore, the decision was made to assume the first reduction step only produces carbon monoxide and hydrogen. For comparison, the same assumption was made in the model by Burdyny et al. [18].

For the second reduction step, the following electrochemical reactions were considered:



These are the main CO₂ reduction reactions, based on the product distribution data published by Nitopi et al. [76]. The selected CO reduction reactions were decided on based on distributions (selectivity data) in literature [126] [57] [120]. The decision was made to include acetate and not propanol, although the selectivity for each highly depends on the source. However, since the selectivity for both is rather low, this assumption is expected to have a minimal effect on the modelling results.

Convection near the electrodes

As stated before, the assumption is made that diffusion is the dominant transport phenomena inside the diffusion layer. However, some models also assume that there is no diffusion in the sections around the diffusion layer [21]. This would be the case when the hydrodynamic boundary layer is quite large, which essentially means that there will be a near stagnant layer at the height of the diffusion layer. Inside this layer, the convective transport will be approximately zero. The hydrodynamic boundary layer is created as a result of the vorticity, or friction, on the sides of the channel. These will cause the fluid flow to stagnate at the channel wall. Each plane of fluid will, thereafter, impose friction on the next plane, effectively slowing down the flow. This will lead to a fully developed flow, where the maximum flowrate can be found in the middle of the channel. This process is indicated in figure 4.3. This is an important effect to quantify, as the cascade set-up, as shown in figure 4.2, demonstrates sections in between – before and after the sequential electrodes. For now, to decrease the models complexity, the assumption is made to adopt a constant flow profile in the gap section between the electrodes. In reality the profile will most likely be similar to figure 4.3c. This is an effect that is interesting to incorporate at a later stage.

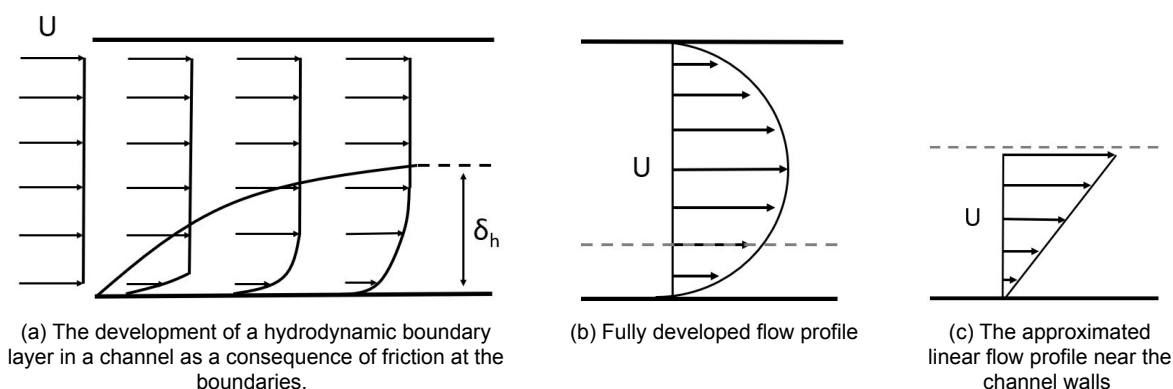


Figure 4.3: The flow profile inside the reactor. Here the dotted line indicates the height of the diffusion layer.

'Zero gap / convective dominance' assumption

As stated before, Gurudayal et al. claim to have found evidence of a CO concentration above its solubility limit when operating in cascade mode [38]. According to the preceding study by Lum and Ager, this phenomena occurs when the CO is produced locally inside the diffusion layer, this will result in a non-equilibrium state at the surface, since the CO is reduced before it can reach the bulk. Hence, when the CO does not reach the bulk phase, it will not reduce the bulk CO_2 concentration by decreasing the partial CO_2 pressure, resulting in the non-equilibrium state at the surface [63]. They continued to prove this effect by showing that the product distributions for the sequential reduction and a feed of a CO_2/CO gas mixture do not match. The tandem set-up showed a much higher oxygenates to ethylene ratio, compared to the CO_2/CO gas mixture inflow situation. This indicates that in the tandem set-up the effect of CO reduction is much larger than in the combined gas inflow situation, since CO reduction favours oxygenate production. Therefore, there must be an increased effect of CO reduction on the second electrode in cascade operation. The 2018 research by Marales-Guio et al., reports a similar effect while investigating the effect of a tandem gold-copper electrocatalyst on CO_2 reduction towards C_{2+} products [71].

However, both these studies (by Lum and Ager and by Marales-Guio et al.) regard tandem catalysts, meaning that the 'second electrode' is deposited on the 'first electrode'. For that reason, the diffusion length towards the second catalyst (10 nm) is several orders of magnitude smaller, compared to the diffusion length to the bulk section (100 μm). Hence, the time scales involved with the transport of species towards the second catalyst are indeed 3 or 4 orders of magnitude smaller than for the transport to the bulk section [71].

Moving from the first reduction step to the second, the concentration profile output from the first step functions as the input for the second step. Hence, an assumption is made that no transport within the bulk or within the diffusion layer will take place in between the steps. In other words, the assumption is made that the distance between the two electrodes is so small, that the concentration profile output from the first electrode will reach the second electrode, before being transported to the bulk section. This assumption is valid for situations where the diffusion length towards the bulk is much larger, than the diffusion length to the second electrode, as it was for the tandem electrodes.

In the sequential electrode set-up, however, the gap between the electrodes is rather large (1 mm). Therefore, the only way this same effect would occur, is when the convection term, horizontally transporting the products produced in the first reduction step, would be much larger than the vertical diffusion component, transporting these same products towards the bulk layer. This is the principle Gurudayal et al. studied in their research. Their experimental results, along with their modelled results, indicate that this is indeed possible, and can even be utilised to control the product distribution [38]. This effect, however, is strongly determined by the operating parameters. Whether these assumptions are valid or not, depend on the gap length and the flowrate. To indicate how large the impact of this assumption

will be, a scaling analysis is applied.

Figure 4.4 represents the different means of transporting *particle c* throughout the gap section between the electrodes. As stated above, the assumption that the concentrations leaving reduction step one, will enter reduction step two – practically unchanged – will be valid when the convective transport term is much larger than the diffusion transport term. To review this, we will consider the situation in figure 4.4a. Here, the transport length is taken to be equal to the gap length in between the electrodes, which is 1 mm. To compare the impact of both transport mechanisms, the following scaling relation is proposed in equation 4.28. Here the convective transport, consisting of the mass transfer coefficient k (m/s) for convective transport and the gap length, L_{gap} (m), is compared to the diffusion transport out of the gap section. The diffusion transport, as it moves in both vertical and horizontal direction, will be represented by the diffusion coefficient (m^2/s) times the diffusion lengths, L_{gap} (m). For the convective term to dominate, the resulting values must be much larger than one.

$$\frac{k_{convection} * L_{gap}}{D * L_{gap}^2} \gg 1 \quad (4.28)$$

Here, $k_{convection}$ represents the convective transport (i.e. the flowrate), L_{gap} the distance between the electrodes, and D the diffusion constant.

Generally, the order of diffusion constants for the species involved in this research is $2 * 10^{-9}$ (see appendix table C.3), the average flowrate is taken to be $u = 0.0025$ m/s and the distance between the electrodes is 1 mm. This results in a value much larger than one, therefore, it is deemed valid to assume the concentrations leaving the first reduction step will not diffuse to the bulk before entering the second reduction region.

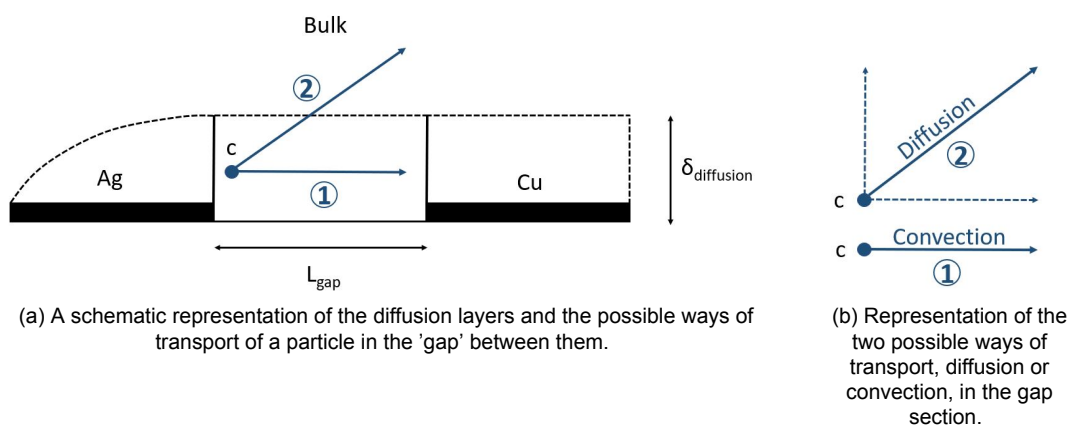


Figure 4.4: Illustration of the comparison of the transport of particle c , by convective or diffusive transport.

Approximation of the kinetic parameters

To determine the kinetic behaviour for the modelled reaction equations, a number of assumptions and simplifications have to be made. As there is no preceding research regarding a high pressure cascade system, the required information has to be derived from different sources. To make the best possible representation of the actual situation, data from the same research group, gathered in the same reactor set-up, is utilised. Not all data is readily available in literature, therefore, the lacking data is calculated where necessary. These calculations will be discussed in more detail in the next section. Ideally, all data would originate from the same experimental source, rather than calculating it or having multiple sources. At this moment in time, however, the model is limited to using this adapted approach. In a later stage, after gathering experimental data from the experimental set-up of the new reactor design, the accuracy of the model can be improved with more representable data.

One of the simplifications made, regards the determination of the charge transfer coefficients. These

are determined from the Tafel slopes originating from the experimental data regarding the first reduction step [40], the COR in the second reduction step [120] and the CO_2R in the second reduction step [56]. These values for the Tafel slopes are assumed to remain constant in the domain represented in the model, for all operating conditions. However, in reality they can change with the overpotential or system pH. The 2021 research by Li et al. illustrates this by investigating the response of the kinetics of methane on the pH and the overpotential [59]. Here, they show the Tafel slope for CH_4 changes with changing the solution pH. In addition, the Tafel slope for CH_4 formation also proved to have two different values, below, and above -0.8V vs. RHE (for an electrolyte pH of 9). This effect is also present in the Tafel plots governing the kinetics in the model for CH_4 production from CO_2 [56] and in the results by Chen et al. [21]. The changing Tafel slopes are illustrated in appendix figure C.2. This behaviour was not included in the model and constant Tafel slopes are assumed, hence, the modelling of the kinetics is simplified.

In addition, for the determination of the kinetic rate constant, k_s , the determined values have a large uncertainty. In the first place, because their values vary profoundly. This is generally the case for rate constants [11], but makes it difficult to assess their validity. Furthermore, the procedure applied for calculating the values is based on a lot of assumptions and deals with many uncertainties. For instance, to determine the rate constant, the concentration of the reactant needs to be determined. None of the consulted sources stated these, therefore, they had to be approximated. Each approximation leading up to the determination of the k_s , adds a level of uncertainty. Therefore, the expectation is that the values could deviate from reality. The complete procedure is explained in detail in section 4.4.3.

Multi-step kinetics simplification

To calculate the kinetic parameters as the current density, the charge transfer coefficient and the kinetic rate constant, Butler-Volmer kinetics are assumed. As the reaction equations deployed in the model all represent multi-step mechanisms, accurately describing the kinetic behaviour becomes a challenge. The following section will elaborate on the approach to accurately model multi-step systems, and identify the different assumptions and simplifications that have to be made in order to actually apply the Butler-Volmer equation.

As an example we will consider the following quasi-reversible / irreversible multi-step process as proposed in the textbook by Bard and Faulkner (2001) [11]:



$\text{O} + n' e^- \rightleftharpoons \text{O}'$ (net result of steps preceding RDS)

$\text{O}' + e^- \xrightleftharpoons[k_b]{k_f} \text{R}'$ (RDS)

$\text{R}' + n'' e^- \rightleftharpoons \text{R}$ (net result of steps following RDS)

Where:

$$n = n' + n'' + 1 \quad (4.30)$$

To flawlessly describe the behaviour, one has to take into account all the single steps taking place in the reaction scheme. This is often not possible, as the required data for these intermediate steps is not always available. Even for simple processes, for which this information could be known, this calculation will be very complicated and lengthy. Bard and Faulkner, therefore, simplify this approach a little, by focusing on the kinetics of the rate determining step (RDS) [11]. This step, by definition, takes much longer than the other steps, therefore, the reaction kinetics are largely dominated by it. To describe it, they adopt the following procedure.

In this example, a chemically reversible process near equilibrium, the exchange current density for the RDS can be expressed as:

$$i_{0,\text{rds}} = F A k_{\text{rds}}^0 (C_{\text{O}'})_{\text{eq}} e^{-\alpha f (E_{\text{eq}} - E_{\text{rds}}^0)} \quad (4.31)$$

$$f = \frac{F}{R * T} \quad (4.32)$$

To account for all the other electron transfer steps, before or after the RDS, this relation is taken to be n -times larger in the multi-step mechanism. This results in the following relation:

$$i_0 = nFAk_{\text{rds}}^0 (C_{O'})_{\text{eq}} e^{-\alpha f(E_{\text{eq}} - E_{\text{rds}}^0)} \quad (4.33)$$

Here, F indicates Faraday's constant, R the universal gas constant, T the temperature, A the electrode surface area, k_{rds}^0 the kinetic rate for the RDS, $C_{O'}$ the surface concentration for the intermediate reactant (at equilibrium), α the charge transfer coefficient, and E_{eq} , E_{rds}^0 are the equilibrium and standard RDS potential.

This explains the appearance of the n -term, the amount of transferred electrons, before the exponential term. The same principle can be applied to the current-potential characteristic Bard and Faulkner propose for multi-step processes with a heterogeneous electron transfer step, which is illustrated in the following equation [11]:

$$i = nFAk_{\text{rds}}^0 \left[C_{O'}(0, t) e^{-\alpha f(E - E_{\text{rds}}^0)} - C_{R'}(0, t) e^{(1-\alpha)f(E - E_{\text{rds}}^0)} \right] \quad (4.34)$$

As stated, the problem with trying to fully describe the kinetics of a multi-step process, is that the variables for the intermediates are often unknown. To apply equation 4.34, for example, one must be familiar with the intermediate surface concentrations ($C_{O'}(0, t)$ and $C_{R'}(0, t)$). These, however, are dependent on the mass transfer properties, the electron transfer kinetics, but also on the preceding and following steps [11]. Therefore, regarding the kinetics in the high pressure cascade model, the following approach is taken. To be able to use equation 4.34, the intermediate surface concentrations, $C_{O'}(0, t)$ and $C_{R'}(0, t)$, must be expressed in terms of the initial starting concentrations, $C_O(0, t)$ and $C_R(0, t)$. This can be realised with the Nernstian relations (i.e. the exponential form of the Nernst equation), which are shown below [11].

$$e^{n'f(E - E_{\text{pre}}^0)} = \frac{C_O(0, t)}{C_{O'}(0, t)} \quad (4.35)$$

and

$$e^{n''f(E - E_{\text{post}}^0)} = \frac{C_{R'}(0, t)}{C_R(0, t)} \quad (4.36)$$

With these, the current-overpotential relation for a multi-step process can be rewritten into the following equation [11].

$$i = nFAk_{\text{rds}}^0 C_O(0, t) e^{-n'f(E - E_{\text{pre}}^0)} e^{-\alpha f(E - E_{\text{rds}}^0)} - nFAk_{\text{rds}}^0 C_R(0, t) e^{n''f(E - E_{\text{post}}^0)} e^{(1-\alpha)f(E - E_{\text{rds}}^0)} \quad (4.37)$$

To solve it, however, this equation still requires knowledge of the unknown, E_{rds}^0 . Therefore, E_{rds}^0 , must be expressed into known variables, or into constants which can be approximated from experimental data. As these reactions take place at the high overpotential range (>52 mV), Tafel kinetics are assumed. Therefore, the first term in equation 4.37 is regarded dominant over the other. This simplifies equation 4.37, so it can be rewritten in order to solve it. To rewrite it from here, a procedure similar to the one described in Bard and Faulkner, section 3.5.4(d), is applied [11].

First, the equation will be multiplied with unity, in the shape of: $e^{[-(n'+\alpha)f(E_{\text{eq}} - E_{\text{eq}})]}$. This leads to the following relation:

$$i = nFAk_{\text{rds}}^0 C_O(0, t) e^{-(n'+\alpha)fE_{\text{eq}}} e^{f[n'E_{\text{pre}}^0 + \alpha E_{\text{rds}}^0]} e^{-(n'+\alpha)f(E - E_{\text{eq}})} - 0 \quad (4.38)$$

The next step is to, again, multiply equation 4.38 with unity, but this time in the shape of: $e^{[(n''+1-\alpha)f(E^0' - E^0)]}$. This results in the following relation:

$$i = nFAk_{\text{rds}}^0 C_{\text{O}}(0, t) e^{-(n'+\alpha)f(E_{\text{eq}}-E^{0'})} e^{f[n'E_{\text{pre}}^{0'} + \alpha E_{\text{rds}}^{0'} - (n'+\alpha)E^{0'}]} e^{-(n'+\alpha)f(E-E_{\text{eq}})} \quad (4.39)$$

This relation can be simplified by realising that $E - E_{\text{eq}} = \eta$. In addition, as the other exponential terms are not dependent on E , they can be regarded as constants of the system (at constant temperature). Therefore, they become constants that can be approximated from experimental data. Combining them into k_{app} , the apparent rate constant, as shown in equation 4.41, will provide a variation on the current overpotential relation which depends on the overpotential and constants of the system, instead of the standard potential of the rate determining step.

$$i = nFAk_{\text{app}}^0 C_{\text{O}}(0, t) e^{-(n'+\alpha)f\eta} \quad (4.40)$$

$$k_{\text{app}}^0 = k_{\text{rds}}^0 e^{-(n'+\alpha)f(E_{\text{eq}}-E^{0'})} e^{f[n'E_{\text{pre}}^{0'} + \alpha E_{\text{rds}}^{0'} - (n'+\alpha)E^{0'}]} \quad (4.41)$$

Following this approach, the assumption is made that the kinetic rates for multi-step process can be accurately described in a single step calculation for the entire process, by using the experimentally determined effective rate constant, k_{app} . In addition, as described above, in doing this, the assumption is made that this k_{app} is indeed a constant for the system which can be measured or determined from fitting to experimental data. However, using the relation $e^{nf(E_{\text{eq}}-E^{0'})} = \frac{C_{\text{O}}^*}{C_{\text{R}}^*}$, and taking it to the power $-(n'+\alpha)/n$, the apparent rate constant can be expressed as [11]:

$$k_{\text{app}}^0 = k_{\text{rds}}^0 e^{n'f(E_{\text{pre}}^{0'}-E^{0'})} e^{\alpha f(E_{\text{rds}}^{0'}-E^{0'})} C_{\text{O}}^* [(n'+\alpha)/n] C_{\text{R}}^* [(n'+\alpha)/n] \quad (4.42)$$

This illustrates the k_{app}^0 is only a constant for the system at constant temperatures and constant pressure, as the concentrations C_{R}^* and C_{O}^* are a function of pressure. Since the pressure will not be constant in this system, and the kinetic data will be derived from a low pressure experimental study, this relation is expected to be less representative at higher pressures.

To obtain a solvable version of the current overpotential characteristic, a final assumption is made. As the presence of n' in equation 4.40 signifies required knowledge of complicated reaction schemes, therefore, the assumption is made that the RDS for all reactions in this system would be the first step. This assumption is deemed valid, as the RDS for most of the reaction schemes for the reactions employed in the model is indeed reported to be determined by the first step [59]. In addition, two accompanying assumptions were made, 1) that the amount of electrons transferred in the RDS would always be one, and 2) that the RDS in all cases only takes place once during the reactions. According to literature, this is almost always the case, and is, therefore, fair to assume [11] [36].

This section shows the large magnitude of assumptions and simplifications that need to be made in order to express the kinetics in a way simple enough to solve them. To the best of the author's knowledge, no more elaborate forms of describing the kinetics have been proposed in models as of yet. Apart from that, other proven to be accurate modelling studies have also successfully adopted a similar approach and still found representable results [55] [21] [18] [72] [102]. Therefore, this simplification is expected to have an impact on the modelling results, but is still deemed appropriate to apply.

The final simplified version of the current overpotential characteristic, is displayed in equation 4.43. Here, k_{app} is replaced with the priorly mentioned kinetic rate constant, k_s . Its value will be determined by fitting to experimental data, as was proposed. This procedure will be described in detail in section 4.4.3. The pre-exponential factor shall from here be referred to as the exchange current density, i_0 .

$$i = FAk_s C_{\text{O}}(0, t) e^{-\alpha f\eta} = i_0 e^{-\alpha f\eta} \quad (4.43)$$

Constant diffusion layer length

The diffusion layer is identified as the layer directly above the electrodes. Here, diffusion dominates, due to the vastly changing concentrations at the electrode surface. In the model, this value is assumed to be constant and was found from the experimentally measured limiting current density in other research [12]. As expressed in equation 2.83 in section 2.2, the thickness of this layer is dependent on,

for instance, the limiting current density, the bulk concentration and the diffusion constant. Hence, it is dependent on the configuration, so adopting this value from another research is a simplification of reality. However, this approach was adopted in many previous models for CO₂ reduction, which produced accurate results [21] [85] [102] [72]. Note that in the 2006 model by Gupta et al., the boundary layer thickness is indeed assumed, but it is varied to investigate the impact on the pH [37]. However, since the diffusion layer thickness is proven to be dependent on the bulk concentration of the oxidating species, it will also be dependent on the pressure, as the solubility of a species is pressure dependent. Therefore, the diffusion layer thickness utilised in this research is adopted from the high pressure CO₂ reduction modelling studies, showing results relatively accurate to experimental situations [102] [72].

Constant temperature assumption

Temperature effects are incorporated in the modelling, for example, in calculating the standard potentials and the solubility. However, to simplify the modelling, the assumption is made that the temperature in the channel would not vary during the reactions. This simplification is regarded not to have too much impact on the model results as the temperature variation in the channel is rather small due to the flowing of the electrolyte [55].

Acidic buffer reactions

As described in section 2.1.2, the CO₂ reacts with the KHCO₃ electrolyte, according to reactions 2.17 to 2.20. Which of these reactions dominates (1–2 or 3–4), depends on the pH of the system. The system pH is highly dependent on the amount of dissolved CO₂, therefore, it will be rather acidic for the high pressures investigated in this model. Illustrating this, Morrison and co-workers, while investigating high pressure CO₂ reduction, report finding pH values that go as low as 5.4 [72]. Therefore, the assumption is made that equation 2.17 and equation 2.18 dominate in the system. This assumption is expected to hold for the bulk section, as the CO₂ concentration in this section is not largely affected by the reduction at the surface. At the electrodes however the pH becomes much higher, because of the OH⁻ produced in the electrochemical reactions. Therefore, in reality, there will be a region in between the alkaline diffusion layer and the acidic bulk layer, where the assumption for these two dominating buffer reactions will not hold. Nonetheless, this principle is not expected to impact the modelling results, as this hypothetical section of slightly alkaline bulk pH is not extensively studied in this research. The model is based on the assumption of the two different sections: the bulk, where concentrations are not impacted by electrochemical reactions, and the diffusion layer. In this model, these can, therefore, have different pH values. Complicating this further by introducing a transition section in between these sections, is regarded too complex to add to the model at this moment in time, but could be something interesting to investigate in future studies.

4.4. Modelling structure

The next section will elaborate on the structure of the high pressure cascade model. Figure 4.5 dissects the model into sections, referring to calculations and sets of functions in the code. The next sections will elaborate on the theory and relations utilised in the model, grouped per section. Only the sections regarding the solving of the transport equations (Step 1: E-dependent transport equations - Step 2: P-dependent transport equations), will entail some extra explanation regarding the format for modelling.

4.4.1. Parameters, constants and conditions

In this section of the model, the input parameters, the constants and the operating conditions are introduced. The input parameters refer to the applied pressure range and the applied potential ranges for both reduction steps to investigate. The constants listed in this section, consist of the required constants for the calculations later in the model. Examples of these are: the gas constant, Faraday constant, molar masses of species, etc. The conditions listed here, refer to the operating conditions of the simulated reactor set-up, such as the electrolyte concentration and the cell's dimensions.

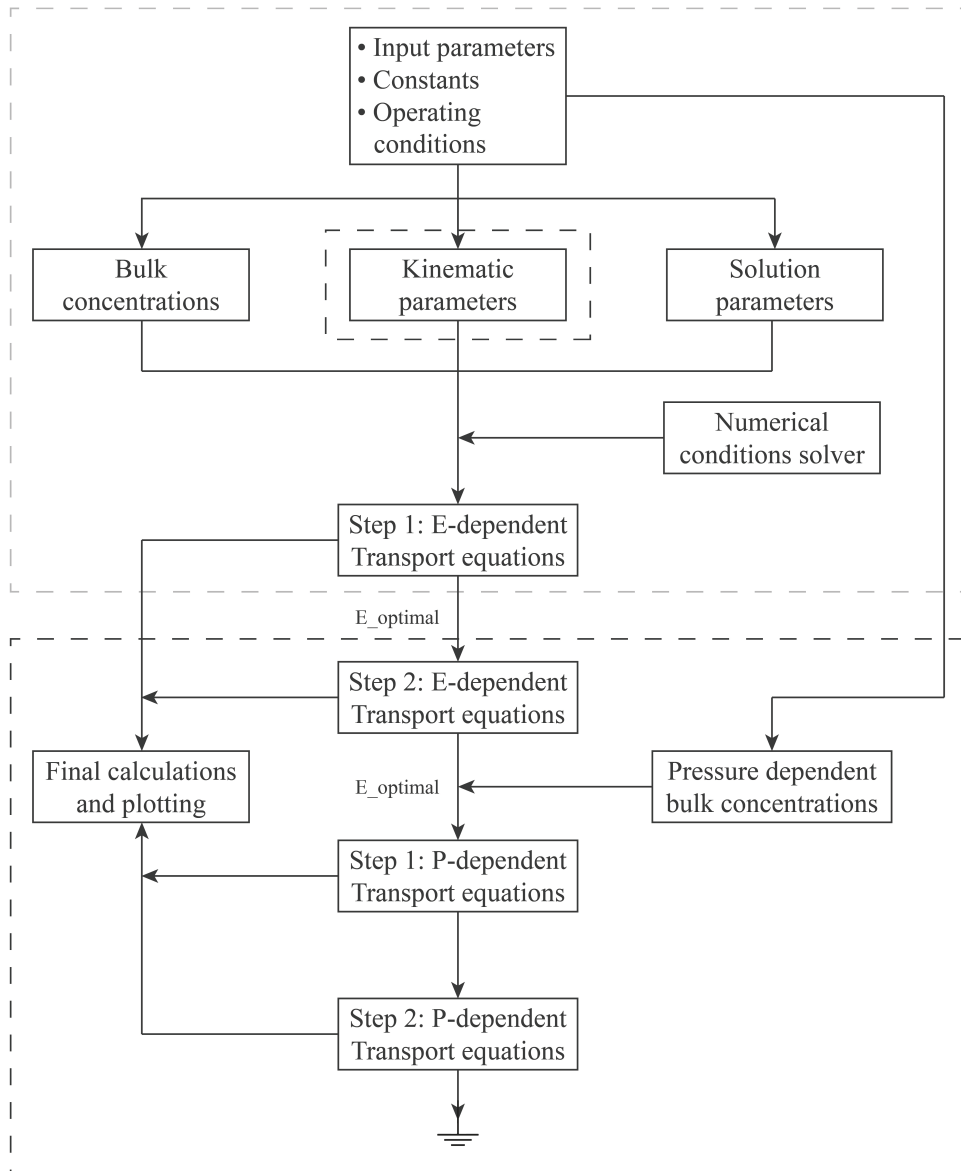


Figure 4.5: Flowchart describing the main sections of the high pressure cascade model. The grey dashed square indicates the sections where the model follows the approach of the Soeteman [102] model. The Black dashed squares indicate the sections that required a new approach.

As explained above, the modelling strategy is to keep the main file as simple and comprehensible as possible. Therefore, the parameters, constants and conditions section lists all of the data required throughout the model. The functions requiring input from the main file, will invoke the required global data, and use it locally in the function. This ensures that no mistakes can be made with assigning double values to a parameter, as it will only be defined one time. Therefore, the section lists all the information used in the model, with the exception of data which is only used once, inside of a function to make a calculation specific to the function. This comes with the additional constraint that the information in question must also be irrelevant for the rest of the model, making it acceptable that it only appears locally.

4.4.2. Bulk concentrations

This section is directed at finding the bulk concentrations of the species initially present in the solution. As described above, when CO_2 reacts with the KHCO_3 electrolyte, the following buffer reactions will dominate:



If the concentration of one of the species described in these equations is known, the concentrations of the others can be determined based on their relation. Therefore, to find the bulk concentrations, the concentration of H^+ in the system was calculated first. At this point in the calculations, there are still many unknowns, so to uncover the H^+ concentration, more equations need to be expressed. These will eventually lead to an expression with the H^+ concentration as the only unknown variable.

The procedure to find an equation with only the H^+ concentration as unknown variable, is the following. First the carbon balance equation and the zero charge requirement are set up. The carbon balance expresses that the total amount of carbon in the system, is equal to the amount dissolved into the solution. The zero charge requirement states that the combined charges of all charged species, must add up to zero. This is represented in equation 4.48. Henceforth, using mutual relations between the species involved, the variables in equation 4.47 and equation 4.48 can be expressed into $[\text{CO}_2]$ and $[\text{H}^+]$. This will result in two separate equations with only two unknowns, which can, therefore, be solved.

$$C_{\text{carbon}} = [\text{CO}_2] + [\text{HCO}_3^-] + [\text{CO}_3^{2-}] \quad (4.47)$$

$$[\text{K}^+] + [\text{H}^+] - [\text{HCO}_3^-] - 2[\text{CO}_3^{2-}] - [\text{OH}^-] = 0 \quad (4.48)$$

To express the amount of HCO_3^- and CO_3^{2-} in terms of CO_2 and H^+ concentration, the following relation will be exercised:

$$K = \frac{k_f}{k_r} \quad (4.49)$$

This leads to:

$$[\text{HCO}_3^-] = K_1 \frac{[\text{CO}_2]}{[\text{H}^+]} \quad (4.50)$$

$$[\text{CO}_3^{2-}] = K_2 \frac{[\text{HCO}_3^-]}{[\text{H}^+]} \quad (4.51)$$

Which can be rewritten to:

$$[\text{CO}_3^{2-}] = K_1 K_2 \frac{[\text{CO}_2]}{[\text{H}^+]^2} \quad (4.52)$$

After its substitution into the carbon balance and rearranging, the following relation is formed:

$$[\text{CO}_2] = \frac{C_{\text{carbon}} [\text{H}^+]^2}{[\text{H}^+]^2 + K_1 [\text{H}^+] + K_1 K_2} \quad (4.53)$$

The amount of carbon in the system, C_{carbon} , can be determined from the amount of electrolyte (C_{KHCO_3}) and the amount of CO_2 which gets dissolved into the system, S_{CO_2} . This principle is shown in equation 4.54. How the amount of dissolved CO_2 is calculated, is detailed in the next section.

$$C_{\text{carbon}} = C_{\text{electrolyte}} + S_{\text{CO}_2} \quad (4.54)$$

This same principle as was utilised above, can be deployed for the zero charge requirement equation, where $[\text{OH}^-]$ can be written as:

$$[\text{OH}^-] = \frac{K_w}{[\text{H}^+]} \quad (4.55)$$

Which leads to the following equation, by substituting in the zero charge balance:

$$[\text{K}^+] + [\text{H}^+] - K_1 \frac{[\text{CO}_2]}{[\text{H}^+]} - 2 K_1 K_2 \frac{[\text{CO}_2]}{[\text{H}^+]^2} - \frac{K_w}{[\text{H}^+]} = 0 \quad (4.56)$$

The amount of K^+ in the system, $[\text{K}^+]$, is known, as this is equal to the amount of electrolyte (C_{KHCO_3}). This leaves two equations with just two unknowns, $[\text{CO}_2]$ and $[\text{H}^+]$. To solve for $[\text{H}^+]$, as was intended, both equations are combined, resulting into equation 4.57. After solving for $[\text{H}^+]$, the other concentrations can finally be determined.

$$[C_{\text{KHCO}_3}] + [\text{H}^+] - \frac{K_1 C_{\text{carbon}} [\text{H}^+]^2}{[\text{H}^+]^3 + K_1 [\text{H}^+]^2 + K_1 K_2 [\text{H}^+]} - \frac{2 K_1 K_2 C_{\text{carbon}} [\text{H}^+]^2}{[\text{H}^+]^4 + K_1 [\text{H}^+]^3 + K_1 K_2 [\text{H}^+]^2} - \frac{K_w}{[\text{H}^+]} = 0 \quad (4.57)$$

The sections below will demonstrate how the still unknown variables, required to solve this equation, can be determined.

Reaction rates

To be able to solve equation 4.4.2, equation 4.52 and equation 4.55, the equilibrium constants, need to be determined. Section 2.1.2 explains how these can be determined, and what approach is taken for the values relating to this research. Table 2.2 portrays the origin per rate or equilibrium constant. The values for the calculations executed in table 2.2, can be found in appendix A.1.

CO₂ solubility

As explained above, to calculate the amount of carbon in the system, in order to satisfy the carbon balance equation, the solubility of CO_2 in the solution needs to be determined. Section 2.1.4 elaborates on the general theory behind finding the solubility of CO_2 and CO . This section explains the different methods for determining the solubility and their principles and limitations. Eventually this leads to the conclusion that, to calculate the S_{CO_2} , the model by Duan et al. would be the best fit, taking into account the effects of pressure, temperature and the salting-out effects of KHCO_3 [27]. The model is expected to produce accurate results in the temperature range of 0-250°C and for a pressure ranging from 1 to 1000 bar.

The formula stated by Duan et al. (2006) for the calculation of the CO_2 solubility is specified below in equation 4.58 [27].

$$\ln m_{\text{CO}_2} = \ln y_{\text{CO}_2} \phi_{\text{CO}_2} P - \mu_{\text{CO}_2}^{(0)}/RT - 2\lambda_{\text{CO}_2-\text{Na}} (m_{\text{Na}} + m_{\text{K}} + 2m_{\text{Ca}} + 2m_{\text{Mg}}) - \zeta_{\text{CO}_2-\text{Na}-\text{Cl}} m_{\text{Cl}} (m_{\text{Na}} + m_{\text{K}} + m_{\text{Mg}} + m_{\text{Ca}}) + 0.07m_{\text{SO}_4} \quad (4.58)$$

To solve this, the following parameters need to be determined: y_{CO_2} , ϕ_{CO_2} , μ_{CO_2} , λ_{CO_2} and ζ_{CO_2} . To calculate the mol fraction CO_2 in the vapor phase, y_{CO_2} , the vapor fraction of water needs to first be determined. This data is derived from the temperature dependent vapor pressure data from the NIST (National Institute of Standards and Technology) tables [75]. Here, the assumption is made that the vapor pressure of the system's solution is the same as the vapor pressure for pure water. With this information and equation 4.59, the mol fraction CO_2 in the vapor phase can, therefore, be found.

$$y_{\text{CO}_2} = \frac{p - p_{\text{H}_2\text{O}}}{p} \quad (4.59)$$

The determination of the fugacity coefficient, ϕ_{CO_2} , can be executed with equation 4.60 originating from Duan et al.(2006) [27]. This relation requires input parameters (c_1-c_n), which depend on the pressure

domain. A distinction is made between two domains: 1) $P < P_{SCO_2}$ and 2) $P_{SCO_2} < P < 1\,000$ bar, as the model is accurate up to 1 000 bar. Therefore, to determine the appropriate input parameters for the situation, the vapor pressure for CO_2 , P_{SCO_2} , needs to be established first. The vapor pressure of CO_2 is calculated in a separate function, of which the procedure will be explained in the next section.

$$\begin{aligned} \phi_{CO_2} = & c_1 + [c_2 + c_3T + c_4/T + c_5/(T - 150)]P \\ & + [c_6 + c_7T + c_8/T]P^2 \\ & + [c_9 + c_{10}T + c_{11}/T] \ln P + [c_{12} + c_{13}T]/P \\ & + c_{14}/T + c_{15}T^2 \end{aligned} \quad (4.60)$$

To acquire the standard chemical potential for CO_2 , μ_{CO_2} , relation 4.61 – originating from the research by Li and Duan (2007) – can be applied [58]. Note that the parameters (c_1 – c_n) are different from the parameters in the calculation above. Also note that λ_{CO_2-Cl} is set to zero in this case. The required parameters can be found in table 12 in the 2007 reasearch by Li and Duan, indicated by column ' $\lambda_{CO_2-CO_2}$ ' [58].

$$\begin{aligned} \mu_{CO_2} = & c_1 + c_2T + c_3/T + c_4T^2 + c_5/(630 - T) + c_6P + c_7P \ln T + \\ & c_8P/T + c_9P/(630 - T) + c_{10}P^2/(630 - T)^2 + c_{11}T \ln P \end{aligned} \quad (4.61)$$

Adjacent, the parameters describing the interaction with the salts, λ_{CO_2} and ζ_{CO_2} , are expressed. λ_{CO_2} refers to the interaction parameter between CO_2 and Na^+ . ζ_{CO_2} refers to the interaction parameter between CO_2 , Na^+ and Cl^- . Both can be calculated with equation 4.61, but require different parameters (c_1 – c_n), which can be found in table 12 in the 2007 research by Li and Duan [58].

After determining the required parameters, equation 4.58 can be applied, to find the CO_2 solubility.

Vapor pressure

In order to define the two distinct pressure domains, referred to in the calculation for the fugacity coefficient, the CO_2 vapor pressure needs to be determined. This step is conducted in a separate function, which makes use of the temperature dependent CO_2 pressure data published by the Chemical Engineering and Materials Research Information Center [22]. Here the required coefficients are published and equation 4.62, to calculate the P_{SCO_2} , is stated. The data is regarded valid for a temperature range between 154 and 304 K.

$$\ln P_{vapCO_2} = A * \log T + \frac{B}{T} + C + D * T^2 \quad (4.62)$$

$$P_{vapCO_2} = e^{\ln P_{vapCO_2}} \quad (4.63)$$

After converting this result into bar, it can be used in the calculation for the fugacity coefficient in the CO_2 solubility calculation.

4.4.3. Kinetic parameters

This section regards the determination of the kinetics of the different electrochemical reaction equations simulated in the model. The modelled equations are listed in section 4.3 in equation 4.17 to equation 4.27. This kinetic data is required to determine the electrochemical reaction rates, in other words, the partial current densities for a given applied potential. Section 4.3 provides a detailed explanation of the determination of the current-overpotential relation applied in the model and the assumptions made regarding this approach.

Current density

The aim of this section is to determine the relation between the current density and the applied overpotential. As explained in section 4.3, Tafel behaviour was assumed, because of the large overpotentials involved with CO_2 reduction [12]. Therefore, only the first term will be regarded in this calculation. This

results in the following relation:

$$i = F A k_s C_O(0, t) e^{-\alpha f \eta} \quad (4.64)$$

Where the pre-exponential factor will be referred to as the exchange current density.

$$i_0 = F A k_s C_O(0, t) \quad (4.65)$$

Therefore, to find the current densities for the electrochemical reactions in the model, the k_s , $C_O(0, t)$, α and the η need to be determined. The sections below will elaborate on the determination of these parameters, with the exception of the surface concentration of the reactant ($C_O(0, t)$), which will be explained further in the boundary conditions section below.

Overpotentials

As described in section 2.1.2, the (over)potential is always referenced to a certain scale. In this report, all potentials are referenced against Ag/AgCl scale. For a detailed explanation how to convert between different scales, refer to appendix section C.3. As explained before, the overpotential is the difference between the standard equilibrium potential (E^0) and the applied potential (E). Therefore, to acquire the overpotentials for the electrochemical reactions in the model, first their standard equilibrium potentials need to be determined. Their value depends on: the reaction equation, the reference scale, the temperature and the pH. This is illustrated in equation 4.66.

$$E_{Ag/AgCl}^0 = E_{RHE}^0 - AgAgCl_{factor} - E_n + (T - T^0) * \frac{dE}{dT} \quad (4.66)$$

Here: E_n refers to the pH deviation from standard, T^0 indicates the standard temperature (298.15 K), $AgAgCl_{factor}$ is the conversion factor with a value of 0.197 and $\frac{dE}{dT}$ represents the temperature coefficient.

There are tables available in literature listing most E^0 values for a standard temperature and pH (T=298 K and pH=7). As the reactions taking place in the diffusion layer produce a lot of $[OH^-]$, the local pH becomes alkaline. Therefore, the standard equilibrium potentials referring to alkaline reactions are considered instead of the acidic ones. However, the E^0 values regarding alkaline CO reduction are not as broadly available in literature as the other values. They are, therefore, calculated with equation 2.24. To convert the calculated values from SHE to RHE scale – to match the other values – $7 * 0.0591$ is added to their values (see equation C.11). The full calculation is shown in equation 4.67. The utilised values for the Gibbs free energy changes (ΔG) can be found in appendix table C.1.

$$E_{RHE}^0 = -\frac{\Delta G}{nF} + 7 * 0.0591 \quad (4.67)$$

The temperature coefficients, dE/dT , are derived from literature [15], or calculated from equation 4.68, assuming pressure. Their values are displayed in appendix table C.12. The derivation for this calculation, can be found in appendix section C.3. The data required for the calculation can be found in appendix table C.3.

$$\left(\frac{dE^0}{dT} \right)_p = \frac{\Delta S}{nF} \quad (4.68)$$

The pH correction factor value, E_n , can be found with equation 4.69. Its derivation can be found in appendix section C.3.

$$E_n = x_{OH^-} * \frac{2.303RT}{nF} (pH - pH_{neutral}) \quad (4.69)$$

Where x_{OH^-} denotes the stoichiometric number of the amount of OH^- in the accompanying reaction equation.

With these values and the expression for the E_0 values (equation 4.66) for the conditions (temperature and pH) in the modelled situation, the overpotentials can be determined. To investigate the response of the system in a certain potential range, the values of E are varied separately for the first and second reduction step. In the model, E , is, therefore, referred to as E_{var} or E_{var2} .

$$\eta = E - E^0 \quad (4.70)$$

Charge transfer coefficients

When assuming Tafel behaviour, the overpotential can be expressed with equation 4.71. In a Tafel plot, the overpotential is plotted against the logarithm of the magnitude of the current density. In this plot, the Tafel domain is represented by a linear straight line. Information on the kinetics of the system can be derived by measuring the slope [$m=mv/dec$] of this line, as illustrated in equation 4.72.

$$\eta = \frac{RT}{\alpha F} \ln i_0 - \frac{RT}{\alpha F} \ln i \quad (4.71)$$

$$\frac{1}{\text{Slope}} = \left| \frac{\partial E}{\partial \log i} \right| = \frac{-\alpha F}{2.3RT} \quad (4.72)$$

The slope is expressed in $mV/decade$. Note that in order to keep the units equal, either the slope must be expressed in V , or the other terms must be converted to mV .

This exact approach is taken to determine the charge transfer coefficients for the electrochemical reactions simulated in the model. With equation 4.72 and the Tafel plots originating from the sources utilised for all the kinetic data for the model [40] [56] [120], the charge transfer coefficients can be determined as shown in equation 4.73. The utilised Tafel plots can be found in appendix figure C.3.

$$\alpha = \frac{2.3RT * 1000}{\text{Slope} * F} \quad (4.73)$$

Here, the factor 1000 is included to convert the slope to volts.

Important to note is that, although some sources state this differently, the charge transfer coefficient is independent of mechanistic consideration [36]. This refers to the fact that the theoretical representation of the Tafel slope, as shown in equation 4.72 and equation 4.73, should never involve the factor n (i.e. the amount of electrons transferred). The 2014 research by Guidelli et al. explains that involving the n in the Tafel slope analysis is a common misconception, which has led to the misinterpretation of the kinetics of many systems [36].

Kinetic rate constants

The last kinetic parameter that needs to be determined in order to calculate the current densities, is the kinetic rate constant, k_s . To determine this parameter, a similar approach as for the charge transfer coefficient is applied. Accordingly, the parameters are fitted to experimental data. When the i_0 , C_o , and n are known, the rate constants can be calculated with equation 4.76. Here, the assumption is made that the kinetic rates for a multi-step process can be accurately described in a single calculation, by applying an effective rate constant, which represents the rate of all steps in the multi-step reduction. In addition, the assumption is made that the rate constant determined under experimental conditions in an experimental set-up, would still approximately have the same value under different conditions. The kinetic rate constant is, therefore, assumed a constant value, only dependent on the of electrochemical reaction.

Therefore, this is determined by deriving the other values for the parameters in equation 4.76 from experimental data. The derived k_s under the conditions as in the research the data originates from, will be utilised in the model. To acquire the data required to determine the values for k_s , the experimental research papers applied for retrieving the kinetic data, are consulted once more [40] [56] [120]. The n and F values are known from the reaction equations and from literature, but the i_0 and C_o are a lot more difficult to determine. To extract an exchange current density from the experimental data,

equation 4.74 can be employed. This equation represents the logarithmic form of the Butler-Volmer equation, where the final term can be exchanged for the experimentally determined Tafel slope [12]. To determine the values for the current density and the overpotential, a specific point in the Tafel plots illustrated in appendix figure C.3, is selected for all the products. The conditions at this point are evaluated, resulting in a value for i and E . Thereafter, the overpotential can be determined with the priorly determined standard equilibrium potentials, E^0 . Afterwards, the exchange current density can be determined with equation 4.75.

$$\log_{10}(-i) = \log_{10}(i_o) + \frac{-\alpha_c n F}{2.3RT} \eta = \log_{10}(i_o) + \frac{1}{Slope} \eta \quad (4.74)$$

$$i_o = \frac{-i}{10^{-\frac{1}{Slope} \eta}} \quad (4.75)$$

Note that to keep the units equal, either the slope must be expressed in V, or the other terms must be converted to mV.

The concentrations of the reactants are determined as follows. The concentration of CO_2 , for the CO_2 reduction, was determined by inserting the parameters of each consulted experimental study into the function calculating the bulk concentrations, as described above. Therefore, taking into account the: pressure, electrolyte type, electrolyte concentration, system pH and the temperature. For the CO concentration, Henry's law (equation 2.49), in combination with the system pressure applied in the experimental study, is exercised.

After determining the i_o , the C_o and the n values, the k_s values can be determined with equation 4.76.

$$k_s = \frac{i_o}{n * F * C_o} \quad (4.76)$$

Note that there is a large range ('more than 10 orders of magnitude') of possible values regarding the kinetic rate values [11]. Therefore, the values found with equation 4.76 are expected to have a large disparity.

4.4.4. Solution parameters

The following section will elaborate on the calculations made to determine the properties of the electrolyte solution. As KHCO_3 is added to the solvent medium, the properties will differ from pure water. Therefore, the following calculations are made.

Diffusion coefficients

As described in the previous section, the diffusion coefficient values have a large impact on the transport in the system. This was established by the conducted sensitivity analysis by Soeteman, in section 3.2 of his report [102]. Here it was demonstrated that slightly varying the diffusion constants, has a large impact on the production rates. Therefore, accurately describing these values will aid in the overall accuracy of the model.

To accurately determine the diffusion coefficients, temperature effects need to be taken into account, as their values are highly temperature dependent [102]. The diffusion coefficients can be determined with the Stokes-Einstein relation, however, this does not apply to 'ionic solutes in aqueous solution' [125]. Although, according to Zeebe et al. (2011), the temperature dependence of the diffusion coefficient in this calculation is applicable to a number of the major seawater ions [125]. They show this approximation is in line with experimental results up to a temperature of 340 K. Therefore, to determine the temperature dependent diffusion coefficients in the temperature range till 340 K, equation 4.78 can be applied. To describe the temperature dependence above this temperature, Zeebe et al. propose to use the relation as shown in equation 4.77. This relation is based on performed molecular simulations in

water, and is applicable to describe the temperature dependence of CO_2 , HCO_3^- and CO_3^{2-} from 1-100 °C [125].

$$D_i = D_i^0 \left[\frac{T}{T_i} - 1 \right]^{\gamma_i} \quad (4.77)$$

Where, D_i represents the temperature dependent diffusion coefficient, T the temperature, D_i^0 the diffusion coefficient under standard temperatures and T_i and γ_i fitted parameters, whose values are represented in table 3.2 in the 2019 report by Soeteman [102].

$$D_T = D_{298} \cdot \frac{\mu_{298}}{\mu_T} \cdot \frac{T_T}{298} \quad (4.78)$$

Where, D_{298} indicates the diffusion coefficient at standard temperature, μ_T the temperature dependent dynamic viscosity, T_T the temperature and μ_{298} the dynamic viscosity at standard temperature.

Dynamic viscosity

To determine the temperature dependent diffusion coefficients, as shown in equation 4.78, the temperature dependent dynamic viscosity of the solution is required. It can be determined with the Vogel equation, shown in equation 4.79 [10]. Here, the assumption was made that the temperature dependence of pure water would sufficiently describe the situation, as the solution consists of mostly water.

$$\mu = \exp \left(A + \frac{B}{C + T} \right) \quad (4.79)$$

To solve the equation, the following parameters can be used.

A	B	C	T_{range}
-3.7188	578.919	-137.546	273-373

Table 4.2: The parameters for equation 4.79, derived from: [10].

4.4.5. Numerical solver conditions

The eventual solution profile for the concentration, u , depends on the spatial variable x and the time variable t . As described in section 4.1, the mathematical solver applied to solve the transport equations, discretises the section to solve into a mesh. In this section of the model, the numerical conditions for this mesh are determined.

To set the conditions to create this mesh, the x and t sizes (begin and end points) and step size, need to be specified in the code prior to specifying the solver section. Next, the solver applies a second order spatial discretization method for the spatial variables, where the points should be closely spaced at the most important regions [68]. The x -values are, therefore, not evenly spaced over the entire mesh. The time step, although set, is chosen dynamically by the solver. Therefore, the defined values of t only dictate the points at which the output is returned, not the points at which the solver evaluates. The set values for x and t , determine the size of the returned solution, $\text{sol}(j,k,i)$. Here, k represents the points of x and j the points of t .

The computation time and accuracy depend more on the length of vector x than on the length of vector t [42]. Therefore, the vector for x is taken to be larger (≈ 50 steps) than the time vector. The numerical solution provides the most accurate results after the system reaches a steady state. This happens, when the changes resulting from the reactions and the mass transport are in equilibrium [72]. Therefore, to determine the input value for x_{end} and t_{end} , the system must be tested for numerical stability / convergence. The convergence values for x_{end} and t_{end} are determined in section 4.6, 'sensitivity analysis'.

4.4.6. Potential dependent: transport equations step 1

As described in sections 2.2 and 4.1, to solve the transport equations, sets of initial conditions and boundary conditions need to be determined. This section will elaborate on the input functions used in the first reduction step of the system. It aims to determine the potential dependent concentrations after the first reduction step, as, with this information, the optimal potential for producing CO with a maximum current efficiency, can be determined. This section will list the input parameters utilised to solve this problem, and will elaborate on the theory behind the calculations made.

To derive the potential dependent concentration profile after the first reduction step, the transport equations are solved in parallel for a predetermined potential range (E_{var}). This is executed with the parallel computing toolbox, by calling the MATLAB function: 'parfor'. Parfor refers to a special kind of for loop, capable of executing calculations on a parallel pool of workers [69]. The parfor loop is preferred over a regular for loop, as it reduces valuable computation time. This will result in a separate solution profile, $sol(j,k,i)$, for each applied potential in the potential range.

Initial conditions

The initial conditions for the first reduction step are taken as the bulk concentrations of all involved species, as described in section 2.2.

$$\left\{ \begin{array}{ll} [\text{CO}_2]_x^{t=0} = [\text{CO}_2]_{\text{bulk}} & \text{for } 0 \leq x \leq \delta \\ [\text{HCO}_3^-]_x^{t=0} = [\text{HCO}_3^-]_{\text{bulk}} & \text{for } 0 \leq x \leq \delta \\ [\text{CO}_3^{2-}]_x^{t=0} = [\text{CO}_3^{2-}]_{\text{bulk}} & \text{for } 0 \leq x \leq \delta \\ [\text{OH}^-]_x^{t=0} = [\text{OH}^-]_{\text{bulk}} & \text{for } 0 \leq x \leq \delta \\ [\text{K}^+]_x^{t=0} = [\text{K}^+]_{\text{bulk}} & \text{for } 0 \leq x \leq \delta \\ [\text{CO}]_x^{t=0} = 0 & \text{for } 0 \leq x \leq \delta \\ [\text{H}_2]_x^{t=0} = [\text{H}_2]_{\text{bulk}} & \text{for } 0 \leq x \leq \delta \end{array} \right. \quad (4.80)$$

$$\text{IC} = [\text{C_bulk}(1); \text{C_bulk}(2); \text{C_bulk}(3); \text{C_bulk}(4); \text{C_bulk}(6); \text{C_bulk}(7); \text{C_bulk}(8); 0];$$

Boundary conditions

The left boundary condition, the Dirichlet condition, for the first reduction step is also determined by the concentrations of the species in the bulk section (as described in section 2.2).

$$\left\{ \begin{array}{ll} [\text{CO}_2]_{x=\delta}^t = [\text{CO}_2]_{\text{bulk}} & \text{for } t > 0 \\ [\text{HCO}_3^-]_{x=\delta}^t = [\text{HCO}_3^-]_{\text{bulk}} & \text{for } t > 0 \\ [\text{CO}_3^{2-}]_{x=\delta}^t = [\text{CO}_3^{2-}]_{\text{bulk}} & \text{for } t > 0 \\ [\text{OH}^-]_{x=\delta}^t = [\text{OH}^-]_{\text{bulk}} & \text{for } t > 0 \\ [\text{K}^+]_{x=\delta}^t = [\text{K}^+]_{\text{bulk}} & \text{for } t > 0 \\ [\text{CO}]_{x=\delta}^t = 0 & \text{for } t > 0 \\ [\text{H}_2]_{x=\delta}^t = [\text{H}_2]_{\text{bulk}} & \text{for } t > 0 \\ \frac{d\phi}{dx}(x = \delta) + \phi(x = \delta) = 0 & \text{for } t > 0 \end{array} \right. \quad (4.81)$$

As explained in section 4.1, the boundary conditions need to be inserted in the shape described with equation 4.16. This results in the following expression for the left boundary condition.

$$\begin{array}{l} \text{pl} = [\text{ul}(1)\text{-C_bulk}(1); \text{ul}(2)\text{-C_bulk}(2); \text{ul}(3)\text{-C_bulk}(3); \text{ul}(4)\text{-C_bulk}(4); \text{ul}(5)\text{-C_bulk}(6); \text{ul}(6)\text{-C_bulk}(7); \\ \quad \text{ul}(7)\text{-C_bulk}(8); \text{ul}(8)]; \\ \text{ql} = [0; 0; 0; 0; 0; 0; 0; 0]; \end{array}$$

As the ql value is stated to be equal to zero, this condition programs the value of u_i to be equal to $bulk_i$.

The right boundary condition, the Neumann condition, at the electrode surface, is described by the source/sink terms resulting from the surface reactions.

$$\left\{ \begin{array}{l} D_{CO_2} \frac{d[CO_2]}{dx} \Big|_{x=0} = R_{CO_2} \\ D_{HCO_3^-} \frac{d[HCO_3^-]}{dx} \Big|_{x=0} - \frac{F}{RT} D_{HCO_3^-} C_{HCO_3^-} \cdot \frac{d\phi}{dx} \Big|_{x=0} = 0 \\ D_{CO_3^{2-}} \frac{d[CO_3^{2-}]}{dx} \Big|_{x=0} - 2 \cdot \frac{F}{RT} D_{CO_3^{2-}} C_{CO_3^{2-}} \cdot \frac{d\phi}{dx} \Big|_{x=0} = 0 \\ D_{OH^-} \frac{d[OH^-]}{dx} \Big|_{x=0} = -R_{OH^-} \\ D_{K^+} \frac{d[K^+]}{dx} \Big|_{x=0} + \frac{F}{RT} D_{K^+} C_{K^+} \cdot \frac{d\phi}{dx} \Big|_{x=0} = 0 \\ D_{CO} \frac{d[CO]}{dx} \Big|_{x=0} = -R_{CO} \\ D_{H_2} \frac{d[H_2]}{dx} \Big|_{x=0} = -R_{H_2} \\ \frac{d\phi}{dx} \Big|_{x=0} = 0 \end{array} \right. \quad (4.82)$$

The consumption (R) and formation ($-R$) rates can be determined with equation 4.83. This relation illustrates the dependence of this boundary condition on the current density. As explained in the previous section, the current density is dependent on the surface concentration, indicated in the model with: u_r . As explained in section 4.1, u_r is a variable for the function `bcfun`, describing the boundary conditions. Therefore, the boundary condition is determined in the following manner:

`Bcfun` imports the rates from the function `current_1`, for calculating the current densities. The function `current_1` uses the u_r values from the `bcfun` function, to calculate the current densities, and `bcfun` then states the boundary condition at the surface to be equal to the rates.

```
[~,~,Rate,~,ur] = current_1(n,F,k_s,alpha,eta,f,ur)
pr = [R_CO2;0;0;-R_OH-;0;-R_CO;-R_H2;0];
qr = [1;1;1;1;1;1;1;1];
```

$$R = 10^{-3} \frac{i}{nF} \quad (4.83)$$

The term 10^{-3} ensures the rates will be expressed in $mol/(cm^2 * s)$.

Equations

The equations defined for the first reduction step are defined in the shape shown in equation 4.14. Here, c is taken as a column vector of ones, f is defined with the transport equations shown in equation 4.1 to equation 4.12 in the shape of equation 4.84, and s is filled with the r -terms, listed in equation 4.13. The final term for s , relating to the electric potential to the charge density, by means of the Poisson equation, is shown below [73].

$$D_i \cdot \frac{\partial^2 C_i}{\partial x^2} - \frac{F}{RT} D_i C_i \cdot \frac{\partial^2 \phi}{\partial x^2} \quad (4.84)$$

$$\frac{\partial^2 \phi}{\partial x^2} = \frac{F}{\epsilon_s \cdot \epsilon_0} \sum_i z_i C_i \quad (4.85)$$

Here, ϵ_s represents the dielectric constant of the electrolyte, ϵ_0 the permittivity of free space, F the Faraday constant, z_i the charge of a species and C_i its concentration. This equation states that there is no charge separation in the system, therefore, electroneutrality is maintained [102].

Optimal potential: $E_{optimal}$

To determine the optimal potential, we look at the region where the overpotentials are so high, the CO_2 surface concentrations approach zero. This region is called the mass transfer controlled region [12]. Visually, this region represents the top of the Tafel plot, where the curve starts to flatten. The corresponding value for i , will therefore be the maximum partial current density the system can reach (without improving mass transfer properties). The optimal conditions will be determined by taking the point referring to the maximum value of i with the lowest potential E . These conditions will be referred to as the optimal operating conditions for the first reduction step. The resulting concentration profile will be taken as the output concentration of step one.

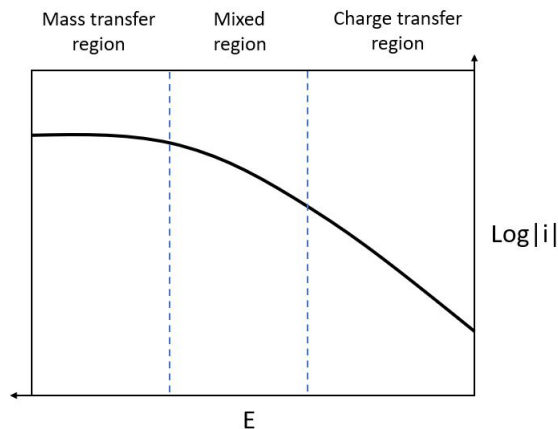


Figure 4.6: An example of the standard shape of a Tafel plot. The different regimes are indicated in the plot.

4.4.7. Potential dependent: transport equations step 2

As explained in section 4.3 'Assumptions and limitations', the assumption is made that the concentration profile leaving the first reduction step, is the concentration profile entering the second reduction step. Therefore, the initial conditions for the second step are no longer determined by the bulk concentrations, but by the first reduction step.

For the second step, again the aim will be to find the relation between a set potential range and the concentration profiles. For this reason, the approach for the second step will be similar to the first.

Initial conditions

To be able to insert the returned concentration profile from the first reduction step (C_{out}) into the second, it must be converted into the right shape. The second reduction step involves a lot more species than the first. To include these into the initial conditions, their values are set to zero, as they are yet to be produced.

```
C_out = [ sol(length(t),:,1);sol(length(t),:,2);sol(length(t),:,3);sol(length(t),:,4);sol(length(t),:,5);
          sol(length(t),:,6);sol(length(t),:,7);I_conc_hcoo;I_conc_ch4;I_conc_c2h4;I_conc_ch3oo;
          I_conc_c2h5oh;I_potential ];
```

Where the values of I_i are taken to be zero.

To ensure the values for the initial conditions can be inserted separately per step of x , they must be included differently than the first step. This issue is eventually solved by equating the variable x in

the initial conditions function, to the x -values in the defined mesh. This is composed in the following statement for calling the initial conditions function ic2.

```
ic2=@(x) C_out( : ,x==xMesh);
```

The initial condition profile for the second reduction step is, therefore, taken to be:

$$\left\{ \begin{array}{ll} [\text{CO}_2]_{x,p}^{t_2=0} = C_{\text{CO}_2}|_{x,p_i}^{t_1=t_{\text{end}}} & \text{for } 0 \leq x \leq \delta \\ [\text{HCO}_3^-]_{x,p}^{t_2=0} = C_{\text{HCO}_3^-}|_{x,p_i}^{t_1=t_{\text{end}}} & \text{for } 0 \leq x \leq \delta \\ [\text{CO}_3^{2-}]_{x,p}^{t_2=0} = C_{\text{CO}_3^{2-}}|_{x,p_i}^{t_1=t_{\text{end}}} & \text{for } 0 \leq x \leq \delta \\ [\text{OH}^-]_{x,p}^{t_2=0} = C_{\text{OH}^-}|_{x,p_i}^{t_1=t_{\text{end}}} & \text{for } 0 \leq x \leq \delta \\ [\text{K}^+]_{x,p}^{t_2=0} = C_{\text{K}^+}|_{x,p_i}^{t_1=t_{\text{end}}} & \text{for } 0 \leq x \leq \delta \\ [\text{CO}]_{x,p}^{t_2=0} = C_{\text{CO}}|_{x,p_i}^{t_1=t_{\text{end}}} & \text{for } 0 \leq x \leq \delta \\ [\text{H}_2]_{x,p}^{t_2=0} = C_{\text{H}_2}|_{x,p_i}^{t_1=t_{\text{end}}} & \text{for } 0 \leq x \leq \delta \\ [\text{HCOO}^-]_{x,p}^{t_2=0} = 0 & \text{for } 0 \leq x \leq \delta \\ [\text{CH}_4]_{x,p}^{t_2=0} = 0 & \text{for } 0 \leq x \leq \delta \\ [\text{C}_2\text{H}_4]_{x,p}^{t_2=0} = 0 & \text{for } 0 \leq x \leq \delta \\ [\text{C}_2\text{H}_5\text{OH}]_{x,p}^{t_2=0} = 0 & \text{for } 0 \leq x \leq \delta \\ [\text{CH}_3\text{COO}]_{x,p}^{t_2=0} = 0 & \text{for } 0 \leq x \leq \delta \end{array} \right. \quad (4.86)$$

Here, t_2 indicates the time variable belonging to the second reduction step and t_1 the time variable belonging to the first reduction step. p_i denotes the applied CO_2 gas pressure.

Boundary conditions

The left/Dirichlet boundary conditions for the second step are defined as follows:

$$\left\{ \begin{array}{ll} [\text{CO}_2]_{x=\delta}^t = [\text{CO}_2]_{\text{bulk}} & \text{for } t > 0 \\ [\text{HCO}_3^-]_{x=\delta}^t = [\text{HCO}_3^-]_{\text{bulk}} & \text{for } t > 0 \\ [\text{CO}_3^{2-}]_{x=\delta}^t = [\text{CO}_3^{2-}]_{\text{bulk}} & \text{for } t > 0 \\ [\text{OH}^-]_{x=\delta}^t = [\text{OH}^-]_{\text{bulk}} & \text{for } t > 0 \\ [\text{K}^+]_{x=\delta}^t = [\text{K}^+]_{\text{bulk}} & \text{for } t > 0 \\ [\text{CO}]_{x=\delta}^t = 0 & \text{for } t > 0 \\ [\text{H}_2]_{x=\delta}^t = 0 & \text{for } t > 0 \\ [\text{HCOO}^-]_{x=\delta}^t = 0 & \text{for } t > 0 \\ [\text{CH}_4]_{x=\delta}^t = 0 & \text{for } t > 0 \\ [\text{C}_2\text{H}_4]_{x=\delta}^t = 0 & \text{for } t > 0 \\ [\text{C}_2\text{H}_5\text{OH}]_{x=\delta}^t = 0 & \text{for } t > 0 \\ [\text{CH}_3\text{COO}]_{x=\delta}^t = 0 & \text{for } t > 0 \\ \frac{d\phi}{dx}(x = \delta) + \phi(x = \delta) = 0 & \text{for } t > 0 \end{array} \right. \quad (4.87)$$

Here, the concentrations for the products of the second reduction step are set to zero, as they are not yet present in the bulk section.

The right/Neumann boundary conditions for the second step are defined as follows:

$$\left\{ \begin{array}{l}
 D_{CO_2} \frac{d[CO_2]}{dx} \Big|_{x=0} = R_{CO_2} \\
 D_{HCO_3^-} \frac{d[HCO_3^-]}{dx} \Big|_{x=0} - \frac{F}{RT} D_{HCO_3^-} C_{HCO_3^-} \cdot \frac{d\phi}{dx} \Big|_{x=0} = 0 \\
 D_{CO_3^{2-}} \frac{d[CO_3^{2-}]}{dx} \Big|_{x=0} - 2 \cdot \frac{F}{RT} D_{CO_3^{2-}} C_{CO_3^{2-}} \cdot \frac{d\phi}{dx} \Big|_{x=0} = 0 \\
 D_{OH^-} \frac{d[OH^-]}{dx} \Big|_{x=0} = -R_{OH^-} \\
 D_{K^+} \frac{dC_{K^+}}{dx} \Big|_{x=0} + \frac{F}{RT} D_{K^+} C_{K^+} \cdot \frac{d\phi}{dx} \Big|_{x=0} = 0 \\
 D_{CO} \frac{d[CO]}{dx} \Big|_{x=0} = R_{CO} \\
 D_{H_2} \frac{d[H_2]}{dx} \Big|_{x=0} = -R_{H_2} \\
 D_{HCOO^-} \frac{d[H_2]}{dx} \Big|_{x=0} = -R_{HCOO^-} \\
 D_{CH_4} \frac{d[H_2]}{dx} \Big|_{x=0} = -R_{CH_4} \\
 D_{C_2H_4} \frac{d[H_2]}{dx} \Big|_{x=0} = -R_{C_2H_4} \\
 D_{C_2H_5OH} \frac{d[H_2]}{dx} \Big|_{x=0} = -R_{C_2H_5OH} \\
 D_{CH_3COO} \frac{d[H_2]}{dx} \Big|_{x=0} = -R_{CH_3COO} \\
 \frac{d\phi}{dx} \Big|_{x=0} = 0
 \end{array} \right. \quad (4.88)$$

Note that only the rates of CO and CO₂ are positive, as these are the species being consumed instead of produced.

Equations

The equations are inserted the same way as for the first reduction step, with the addition of the equations for the new products accompanying the second reduction step. The input for function f will, therefore be as shown in equation 4.84.

$$D_i \cdot \frac{\partial^2 C_i}{\partial x^2} - \frac{F}{RT} D_i C_i \cdot \frac{\partial^2 \phi}{\partial x^2} \quad (4.89)$$

The c term is again represented by a column vector filled with ones, to indicate the time dependence of the concentration. The s term is also similar to the s term from step one, with the addition of the products produced in step two, which do not react with the electrolyte (i.e. $s = 0$).

4.4.8. Pressure dependent bulk concentrations

The next sections are directed at finding the influence of pressure on the subsequent reduction steps. For that reason, henceforth, the pressures will be varied instead of the potentials.

To incorporate the effect of pressure in the model, first, the solubilities of the products in the bulk are determined as a function of pressure. Section 2.1.4 explains the effects of high pressures on the system, and section 4.4.2 elaborates on the approach taken to determine the pressure dependent bulk concentrations in the model. To incorporate the effect of the varying pressure, a for loop is created to calculate the CO₂ solubility, and subsequently the bulk concentrations, as a function of the pressure. Using these as input parameters while solving the transport equations, the pressure dependent solution profile can be determined.

4.4.9. Pressure dependent: transport equations step 1

The potential for the first reduction step will be set to the optimal potential $E_{optimal}$, as found in a previous section. The conditions (current, potential, concentration) will be evaluated at this point, so they can be used in the following calculations. To incorporate the effect of pressure in the model, the pres-

sure dependant bulk concentrations, determined in the previous section, are used as input parameters. To derive a pressure dependent solution profile for the first reduction step, another parfor loop is added, were the solution profile, $\text{sol}(i,j,k)$, is calculated for all pressures (p_{var}) in parallel.

Initial conditions

The initial conditions for the first reduction step are, as in section 4.4.6, determined by the bulk concentrations. Here, however, the bulk concentrations are dependent on the applied pressure, therefore, the resulting initial conditions are:

$$\left\{ \begin{array}{lll} [\text{CO}_2]_{x,p}^{t=0} = [\text{CO}_2]_{\text{bulk}}^i & \text{for } 0 \leq x \leq \delta & \text{and } p = p_i \\ [\text{HCO}_3^-]_{x,p}^{t=0} = [\text{HCO}_3^-]_{\text{bulk}}^i & \text{for } 0 \leq x \leq \delta & \text{and } p = p_i \\ [\text{CO}_3^{2-}]_{x,p}^{t=0} = [\text{CO}_3^{2-}]_{\text{bulk}}^i & \text{for } 0 \leq x \leq \delta & \text{and } p = p_i \\ [\text{OH}^-]_{x,p}^{t=0} = [\text{OH}^-]_{\text{bulk}}^i & \text{for } 0 \leq x \leq \delta & \text{and } p = p_i \\ [\text{K}^+]_{x,p}^{t=0} = [\text{K}^+]_{\text{bulk}}^i & \text{for } 0 \leq x \leq \delta & \text{and } p = p_i \\ [\text{CO}]_{x,p}^{t=0} = 0 & \text{for } 0 \leq x \leq \delta & \text{and } p = p_i \\ [\text{H}_2]_{x,p}^{t=0} = [\text{H}_2]_{\text{bulk}}^i & \text{for } 0 \leq x \leq \delta & \text{and } p = p_i \end{array} \right. \quad (4.90)$$

The initial condition function, IC_P1, is no longer dependent on the x , as the input concentration here does not change with x . Instead it is dependent on p , where for every evaluated p a new initial condition is inserted into the loop. This is executed the following way:

```

j=1:length(p_var)
    IC_P1=@(~) IC_1([C_bulk_new(1,j);C_bulk_new(2,j);C_bulk_new(3,j);C_bulk_new(4,j);
    C_bulk_new(5,j);C_bulk_new(6,j);C_bulk_new(7,j);C_bulk_new(8,j);C_bulk_new(9,j)]);
end

```

Here, it does not matter, that the parallel computing parfor loop does not evaluate the values of p in a set order [69], as the contributing initial conditions are called for the same pressure, indicated with index j .

Boundary conditions

The same principle as for the initial conditions, applies to the left (Dirichlet) boundary condition. Which leads to the following boundary condition:

$$\left\{ \begin{array}{lll} [\text{CO}_2]_{x=\delta,p}^t = [\text{CO}_2]_{\text{bulk}}^i & \text{for } t > 0 & \text{and } p = p_i \\ [\text{HCO}_3^-]_{x=\delta,p}^t = [\text{HCO}_3^-]_{\text{bulk}}^i & \text{for } t > 0 & \text{and } p = p_i \\ [\text{CO}_3^{2-}]_{x=\delta,p}^t = [\text{CO}_3^{2-}]_{\text{bulk}}^i & \text{for } t > 0 & \text{and } p = p_i \\ [\text{OH}^-]_{x=\delta,p}^t = [\text{OH}^-]_{\text{bulk}}^i & \text{for } t > 0 & \text{and } p = p_i \\ [\text{K}^+]_{x=\delta,p}^t = [\text{K}^+]_{\text{bulk}}^i & \text{for } t > 0 & \text{and } p = p_i \\ [\text{CO}]_{x=\delta,p}^t = 0 & \text{for } t > 0 & \text{and } p = p_i \\ [\text{H}_2]_{x=\delta,p}^t = [\text{H}_2]_{\text{bulk}}^i & \text{for } t > 0 & \text{and } p = p_i \\ \frac{d\phi}{dx}(x = \delta) + \phi(x = \delta) = 0 & \text{for } t > 0 & \text{and } p = p_i \end{array} \right. \quad (4.91)$$

The right (Neumann) boundary condition is defined as follows, to incorporate the pressure dependence.

$$\left\{ \begin{array}{l} D_{CO_2} \frac{d[CO_2]}{dx} \Big|_{x=0}^{p_i} = R_{CO_2} \\ D_{HCO_3^-} \frac{d[HCO_3^-]}{dx} \Big|_{x=0}^{p_i} - \frac{F}{RT} D_{HCO_3^-} C_{HCO_3^-} \cdot \frac{d\phi}{dx} \Big|_{x=0} = 0 \\ D_{CO_3^{2-}} \frac{d[CO_3^{2-}]}{dx} \Big|_{x=0}^{p_i} - 2 \cdot \frac{F}{RT} D_{CO_3^{2-}} C_{CO_3^{2-}} \cdot \frac{d\phi}{dx} \Big|_{x=0} = 0 \\ D_{OH^-} \frac{d[OH^-]}{dx} \Big|_{x=0}^{p_i} = -R_{OH^-} \\ D_{K^+} \frac{d[K^+]}{dx} \Big|_{x=0}^{p_i} + \frac{F}{RT} D_{K^+} C_{K^+} \cdot \frac{d\phi}{dx} \Big|_{x=0} = 0 \\ D_{CO} \frac{d[CO]}{dx} \Big|_{x=0}^{p_i} = -R_{CO} \\ D_{H_2} \frac{d[H_2]}{dx} \Big|_{x=0}^{p_i} = -R_{H_2} \\ \frac{d\phi}{dx} \Big|_{x=0} = 0 \end{array} \right. \quad (4.92)$$

Note that the boundary conditions also require the overpotentials as input, therefore, one must make sure to insert the overpotentials evaluated for the $E_{optimal}$.

Equations

The equations for the pressure dependent first reduction step are defined exactly in the same way as was done in section 4.4.6.

4.4.10. Pressure dependent: transport equations step 2

To determine the effects of pressure on the second reduction step, the pressure dependent bulk concentrations and the solution of the first step have to be taken into account. The solution of the first step is, therefore, evaluated separately for each pressure at t_{end} , so they can be inserted into the second step.

Initial conditions

The problem with using the pressure dependent solution profile from the first reduction step, is that – as opposed to before – the input would be pressure and location (x) dependent. Therefore, instead of assigning initial conditions to specific values of x as was done in the potential dependent second step, the initial conditions must now be assigned per pressure p and per location x . To solve this issue, the following approach is applied. First, the parameter x_{in} is assigned to the returned solution of the first step, for each separate pressure, evaluated at t_{end} . Afterwards, the parameter x_{in} is called in the initial conditions function IC_p , where the variable x is equated to the x -values in the mesh. This is executed for each evaluated pressure separately, by means of a loop.

```
for j=1:length(p_var)
    x_in{j}(:, :) = [CO2_x{j}; HCO3_x{j}; CO3_x{j}; OH_x{j}; K_x{j}; CO_x{j}; H2_x{j}; l_conc_hcoo; l_conc_ch4;
    l_conc_c2h4; l_conc_ch3oo; l_conc_c2h5oh; l_potential];

    IC_p=@(x) x_in{j}(:, x==xMesh);
end
```

Where l_i is taken to be zero.

The initial conditions term is shown in equation 5.7c.

$$\left\{ \begin{array}{lll} [\text{CO}_2]_{x,p}^{t_2=0} = C_{\text{CO}_2} |_{x,p_i}^{t_1=t_{\text{end}}} & \text{for } 0 \leq x \leq \delta & \text{and } p = p_i \\ [\text{HCO}_3^-]_{x,p}^{t_2=0} = C_{\text{HCO}_3^-} |_{x,p_i}^{t_1=t_{\text{end}}} & \text{for } 0 \leq x \leq \delta & \text{and } p = p_i \\ [\text{CO}_3^{2-}]_{x,p}^{t_2=0} = C_{\text{CO}_3^{2-}} |_{x,p_i}^{t_1=t_{\text{end}}} & \text{for } 0 \leq x \leq \delta & \text{and } p = p_i \\ [\text{OH}^-]_{x,p}^{t_2=0} = C_{\text{OH}^-} |_{x,p_i}^{t_1=t_{\text{end}}} & \text{for } 0 \leq x \leq \delta & \text{and } p = p_i \\ [\text{K}^+]_{x,p}^{t_2=0} = C_{\text{K}^+} |_{x,p_i}^{t_1=t_{\text{end}}} & \text{for } 0 \leq x \leq \delta & \text{and } p = p_i \\ [\text{CO}]_{x,p}^{t_2=0} = C_{\text{CO}} |_{x,p_i}^{t_1=t_{\text{end}}} & \text{for } 0 \leq x \leq \delta & \text{and } p = p_i \\ [\text{H}_2]_{x,p}^{t_2=0} = C_{\text{H}_2} |_{x,p_i}^{t_1=t_{\text{end}}} & \text{for } 0 \leq x \leq \delta & \text{and } p = p_i \\ [\text{HCOO}^-]_{x,p}^{t_2=0} = 0 & \text{for } 0 \leq x \leq \delta & \text{and } p = p_i \\ [\text{CH}_4]_{x,p}^{t_2=0} = 0 & \text{for } 0 \leq x \leq \delta & \text{and } p = p_i \\ [\text{C}_2\text{H}_4]_{x,p}^{t_2=0} = 0 & \text{for } 0 \leq x \leq \delta & \text{and } p = p_i \\ [\text{C}_2\text{H}_5\text{OH}]_{x,p}^{t_2=0} = 0 & \text{for } 0 \leq x \leq \delta & \text{and } p = p_i \\ [\text{CH}_3\text{COO}]_{x,p}^{t_2=0} = 0 & \text{for } 0 \leq x \leq \delta & \text{and } p = p_i \end{array} \right. \quad (4.93)$$

Here, t_2 indicates the time variable belonging to the second reduction step and t_1 the time variable belonging to the first reduction step.

Boundary conditions

The left (Dirichlet) boundary condition for the pressure dependent second reduction step is:

$$\left\{ \begin{array}{ll} [\text{CO}_2]_{x=\delta,p}^t = [\text{CO}_2]_{\text{bulk}}^i & \text{for } t > 0 \\ [\text{HCO}_3^-]_{x=\delta,p}^t = [\text{HCO}_3^-]_{\text{bulk}}^i & \text{for } t > 0 \\ [\text{CO}_3^{2-}]_{x=\delta,p}^t = [\text{CO}_3^{2-}]_{\text{bulk}}^i & \text{for } t > 0 \\ [\text{OH}^-]_{x=\delta,p}^t = [\text{OH}^-]_{\text{bulk}}^i & \text{for } t > 0 \\ [\text{K}^+]_{x=\delta,p}^t = [\text{K}^+]_{\text{bulk}}^i & \text{for } t > 0 \\ [\text{CO}]_{x=\delta,p}^t = 0 & \text{for } t > 0 \\ [\text{H}_2]_{x=\delta,p}^t = [\text{H}_2]_{\text{bulk}}^i & \text{for } t > 0 \\ [\text{HCOO}^-]_{x=\delta,p}^t = 0 & \text{for } t > 0 \\ [\text{CH}_4]_{x=\delta,p}^t = 0 & \text{for } t > 0 \\ [\text{C}_2\text{H}_4]_{x=\delta,p}^t = 0 & \text{for } t > 0 \\ [\text{C}_2\text{H}_5\text{OH}]_{x=\delta,p}^t = 0 & \text{for } t > 0 \\ [\text{CH}_3\text{COO}]_{x=\delta,p}^t = 0 & \text{for } t > 0 \\ \frac{d\phi}{dx}(x = \delta) + \phi(x = \delta) = 0 & \text{for } t > 0 \end{array} \right. \quad (4.94)$$

Here, the concentrations for the products of the second reduction step are set to zero, as they are not yet present in the bulk section.

The right/Neumann boundary condition for the second step is:

$$\left\{ \begin{array}{l}
 D_{CO_2} \frac{d[CO_2]}{dx} \Big|_{x=0}^{p_i} = R_{CO_2} \\
 D_{HCO_3^-} \frac{d[HCO_3^-]}{dx} \Big|_{x=0}^{p_i} - \frac{F}{RT} D_{HCO_3^-} C_{HCO_3^-} \cdot \frac{d\phi}{dx} \Big|_{x=0}^{p_i} = 0 \\
 D_{CO_3^{2-}} \frac{d[CO_3^{2-}]}{dx} \Big|_{x=0}^{p_i} - 2 \cdot \frac{F}{RT} D_{CO_3^{2-}} C_{CO_3^{2-}} \cdot \frac{d\phi}{dx} \Big|_{x=0}^{p_i} = 0 \\
 D_{OH^-} \frac{d[OH^-]}{dx} \Big|_{x=0}^{p_i} = -R_{OH^-} \\
 D_{K^+} \frac{d[K^+]}{dx} \Big|_{x=0}^{p_i} + \frac{F}{RT} D_{K^+} C_{K^+} \cdot \frac{d\phi}{dx} \Big|_{x=0}^{p_i} = 0 \\
 D_{CO} \frac{d[CO]}{dx} \Big|_{x=0}^{p_i} = R_{CO} \\
 D_{H_2} \frac{d[H_2]}{dx} \Big|_{x=0}^{p_i} = -R_{H_2} \\
 D_{HCOO^-} \frac{d[H_2]}{dx} \Big|_{x=0}^{p_i} = -R_{HCOO^-} \\
 D_{CH_4} \frac{d[H_2]}{dx} \Big|_{x=0}^{p_i} = -R_{CH_4} \\
 D_{C_2H_4} \frac{d[H_2]}{dx} \Big|_{x=0}^{p_i} = -R_{C_2H_4} \\
 D_{C_2H_5OH} \frac{d[H_2]}{dx} \Big|_{x=0}^{p_i} = -R_{C_2H_5OH} \\
 D_{CH_3COO} \frac{d[H_2]}{dx} \Big|_{x=0}^{p_i} = -R_{CH_3COO} \\
 \frac{d\phi}{dx} \Big|_{x=0} = 0
 \end{array} \right. \quad (4.95)$$

Note that only the rates of CO and CO₂ are positive, as these are the species being consumed instead of produced.

Equations

The equations for the pressure dependent second reduction step are defined exactly in the same way as was done in section 4.4.7.

4.4.11. Plotting

Current efficiency

For the current efficiency versus potential plot, the current efficiency needs to be determined. To calculate the current efficiency, first the total currents are calculated by adding all partial current densities. Note that for the second reduction step, both the CO₂R and the COR reactions are assumed to have a hydrogen evolution reaction. Therefore, the current density value for the HER is included twice. The numbers in the equation refer to the numbered electrochemical reactions in equation 4.17 to 4.27.

$$i_{tot}^{step1} = i_1 + i_{10} \quad (4.96)$$

$$i_{tot}^{step2} = i_2 + i_3 + i_4 + i_5 + i_6 + i_7 + i_8 + i_9 + 2 * i_{11} \quad (4.97)$$

Next, with the total currents and equation 4.98, the current efficiencies can be determined. Note that for the cases where products are produced from two separate reactions, such as CH₄, the currents are added. An example of this procedure for CH₄ is shown in equation 4.99. CH₄ is produced from COR in reaction number 2 and from CO₂R in reaction number 6.

$$CE = \frac{i_i}{i_{tot}} * 100\% \quad (4.98)$$

$$CE_{CH_4} = \frac{i_2 + i_6}{i_{tot}} * 100\% \quad (4.99)$$

4.5. Model validation

Most models simulate an existing situation or a performed experiment in a research. In those cases, the modelled results can properly be judged on validity, by comparing them to the original situation. For the high pressure cascade model, however, this is not possible yet. Therefore, an indication of the validation of the model will be provided by comparing the separate steps to the research on the kinetic data originating from [40] [56] [120]. The high pressure aspect, also simulated in the model, will be validated with separate high pressure research, indicating if the model provides a reasonable pressure response [115]. To compare a part of the model to research results, the input conditions will be taken to resemble the input conditions of the research in question as closely as possible. Whether or not the results approximate the actual situation, will signify the validity of the modelled results.

4.5.1. First reduction step

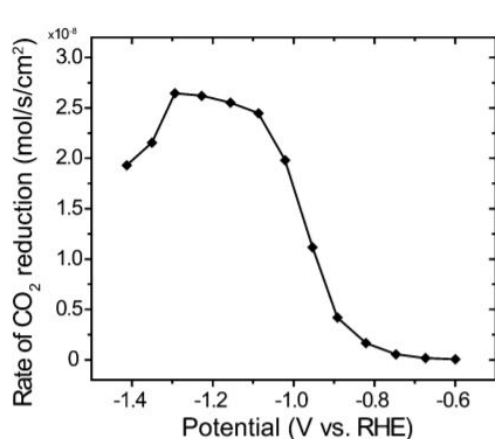
To compare the model's results to the experimental results by Hatsukade et al., the following input parameters are adopted [40]:

Parameter	Value
Pressure	1 atm
T	298.15 K
Electrolyte	0.1 KHCO ₃
Potential range	-1.4 to -0.6
Cell volume	8 cm ³
Cell surface area	4.5 cm ²

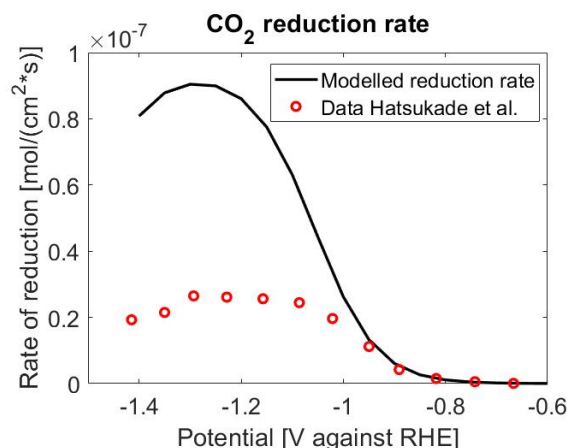
Table 4.3: Input data originating from the research by Hatsukade et al. [40].

Comparing the reduction rate profiles for CO₂ reduction, can provide a good analysis of the described solubility behaviour and salting out effects for the CO₂ in the system. Figure 4.7 shows the reduction rate profiles originating from the experimental data in the research by Hatsukade et al. [40] (figure 4.7a) and the modelled results generated with the high pressure cascade model (figure 4.7b). Apparent from this comparison is the similar trend both graphs show. Initially the reduction rate increases with the applied potential, until the process enters the mass transport limited regime (see figure 4.6 for the different regimes). From this point on the mass transport of CO₂ to the electrode surface is limiting the reaction. The hydrogen supply, on the other hand, is not mass transport limited in this regime, as the H₂O supply is assumed to be unlimited. Therefore, in this domain, only the hydrogen evolution reaction is active, resulting in high OH⁻ concentrations at the surface. These, in turn, drive the CO₂ to participate in the chemical reactions as shown in equation 4.44 to equation 4.46, effectively increasing the salting out effects [41].

This effect is demonstrated in the graphs in figure 4.7, as the reduction rate drops after entering the mass transport regime, instead of retaining a constant value. This, therefore, shows the model accurately captures the salting out effects. In addition, it also estimates the mass transport section at similar potentials to the experimental results. This shows the model's representation to be rather accurate. However, as illustrated in figure 4.7b, the modelled results overestimate the results compared to the experimental results. But since, as the overestimation is only $6 * 10^{-8}$ mol/(s cm²), this overestimation does not have a major impact on the validity of the results. This is most likely the result of a deviation from reality in the assumed values for the diffusion coefficients of the reactants. Section 4.6 will investigate the sensitivity of the model towards the diffusion coefficient values, illustrating this dependence. Section 4.4.3 demonstrates how the current density and rates are determined. It indicates the dependence of the current density, and therefore the rates, on the surface concentration of the reactant. Hence, if the described transport of the reactant slightly deviates from reality, this will result in a deviation of modelled results, such as the rate and current density. However, these small deviations are expected, as a model always will be an approximation of reality.



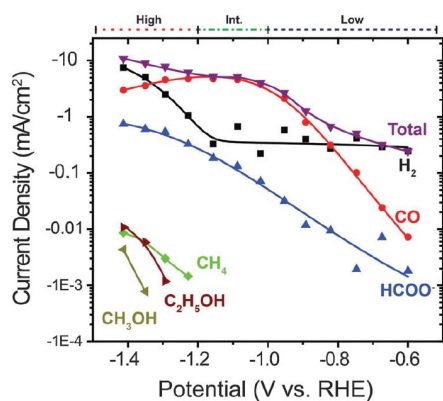
(a) CO₂ reduction rate profile from experimental results by Hatsukade et al. [40].



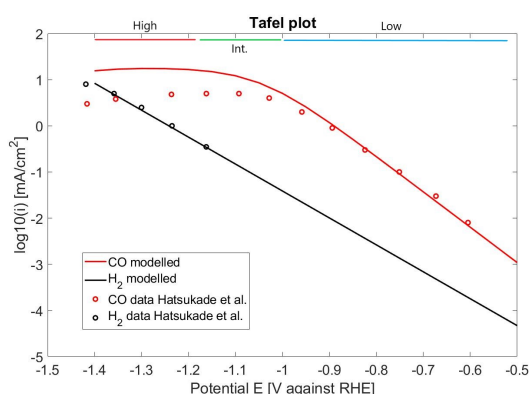
(b) CO₂ reduction rate profile returned by the model, compared to the experimental results [40].

Figure 4.7: Comparison of the CO₂ reduction rate on the Ag electrode, between the experimental results (left) and the modelled outcome (right).

Comparing the Tafel plots will show the accordance of the kinetics as they are modelled in the high pressure cascade model to the experimental results. As the kinetic parameters are derived from figure 4.8a, similar trends should be visible in figure 4.8b. From analysing figure 4.8, it becomes clear the modelled results show the same trend as the experimental results. The graphs both show an intersection around $E = -1.4$, and a decline starting around $E = -1$. Note that the assumption is made that slopes in the charge transfer domain retain a constant value (see section 4.3, 'Assumptions and limitations'). Accordingly, the slope for the hydrogen evolution reaction – indicated in black – is evaluated between $-1.4 < E < -1.2$. Therefore, the modelled trend, logically, simulates this same slope in the lower potential regions. This results in a deviation from the experimental data, however, this is an expected consequence from making this assumption. Apart from showing the same trends, the graphs also demonstrate to obtain approximately the same maximum current density ($\approx 10 \text{ mA/cm}^2$). The modelled results, however, again indicate a small overestimation of the current density. Most likely this originates from the same dependence on the deviating diffusion parameters, as with the reduction rates.



(a) Tafel plot originating from Hatsukade et al. [40].



(b) Tafel plot returned by the model, compared to the experimental results by [40]. The low, intermediate and high potential ranges are indicated at the top of the figure.

Figure 4.8: Tafel plots, demonstrating the logarithmic partial current densities of the involved species against the applied potential.

To show the accordance of the model and the experimental results with respect to product distribution, a Faradaic Efficiency (i.e. Current Efficiency) plot is formulated. Figure 4.9 shows both CE plots,

which show a similar trend, but also some differences. First of all, the modelled graph only demonstrates one intersection between the current efficiencies of hydrogen and carbon monoxide. This can be explained by the assumption regarding the constant hydrogen evolution reaction slope in the charge transfer domain, as explained before. Figure 4.8a shows a deviation in the slope of the HER, resulting in an intersection between the two curves around $E = -0.8$. This same intersection is shown in figure 4.11a at $E = -0.8$. In the model, as the slope is taken to be constant, this second intersection will only be visible at much lower potentials. A second deviation between figure 4.11a and figure 4.9b is the intersection at high potentials; in the modelled plot it is shifted slightly to the left. The same shift can be observed in figures 4.7 and 4.8, and is likely due to an overestimation of the mass transport properties in the model, such as the diffusion coefficients.

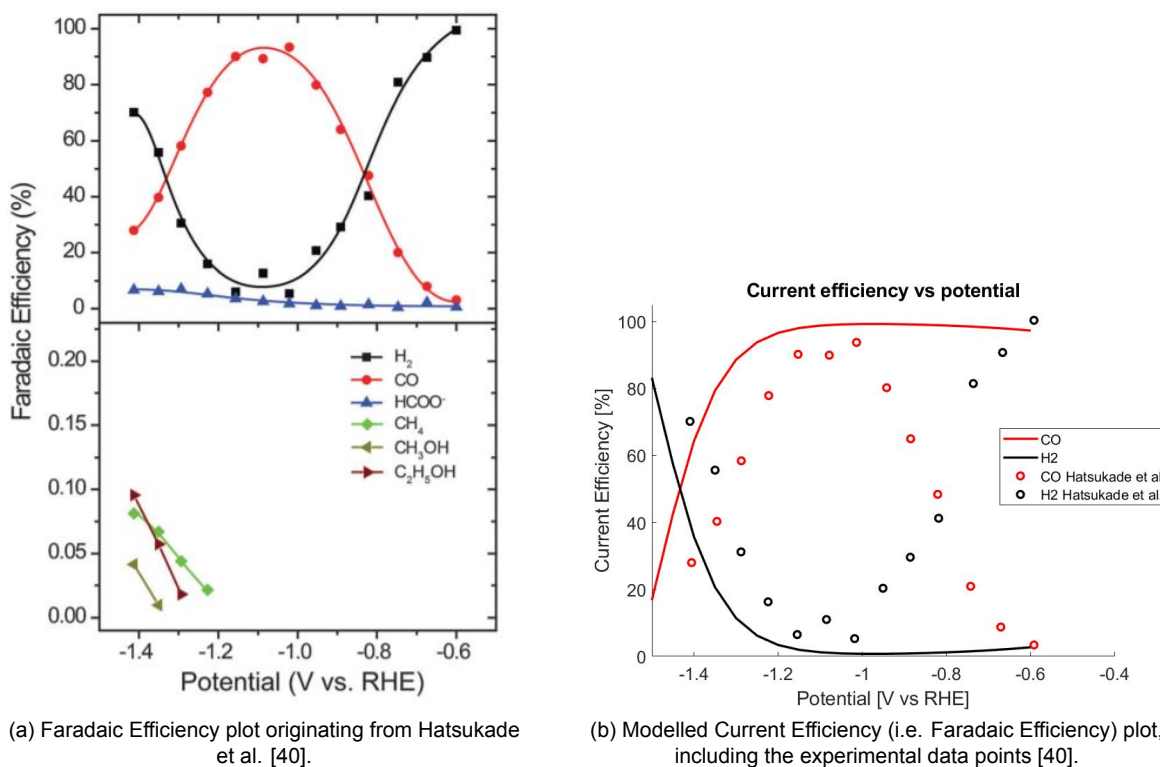


Figure 4.9: Faradaic efficiency plots, showing the selectivity for a product for a specific potential.

From the comparison between the modelled results and the experimental results, the model accuracy for the first reduction step is assessed to be fairly good. Apart from some small deviations, which are explainable by the required approximations made for modelling, the curves all show similar trends and values.

As the data for the second reduction step originates from two different sources, the validation will be carried out separately as well. First, the CO_2 reduction on the Cu model results will be analysed with the data originating from the research by Kuhl et al. [56]. Subsequently, the CO reduction model results will be compared with the experimental data originating from the research by Wang et al. [120].

4.5.2. Second reduction step CO_2R

To compare the model's results to the experimental results by Kuhl et al., the following input parameters were adopted [56]:

Figure 4.10 displays both the modelled and the experimentally derived Tafel plots. As demonstrated in figure 4.10a, the slopes of the species in this research are less clearly defined than the slopes in figure 4.8a. Most display multiple different slopes, depending on the section under review. As explained

Parameter	Value
Pressure	1 atm
T	298.15 K
Electrolyte	0.1 KHCO ₃
Potential range	-1.2 to -0.6
Cell volume	8 cm ³
Cell surface area	4.5 cm ²

Table 4.4: Input data originating from the research by Kuhl et al.[56].

in section 4.4.3, the charge transfer coefficients are determined from the slopes originating from the graphs. The slopes were assumed to remain constant, therefore, they can only perfectly describe the kinetics at the section they were evaluated in. For figure 4.8 this assumption has less impact, compared to figure 4.10, as the slopes are not as constant in this case. This effect is, therefore, represented in figure 4.10b, where the trends demonstrate they equal the experimental results only for a certain section. In addition to this, not all the species shown in figure 4.10a are represented in the model, as described in section 4.3. Therefore, the model is likely to overestimate the results to some degree compared to the experimental results. An explanation for this could be that in the model the same amount of reactant, CO₂, will be simulated to produce less different products. As the assumption was made that the products with low selectivity will not be present in the model at all (CO for example). Therefore, the total amount of available reactant will be reduced to form more of the products that are incorporated. This effect is clearly represented in figure 4.10b, as was expected.

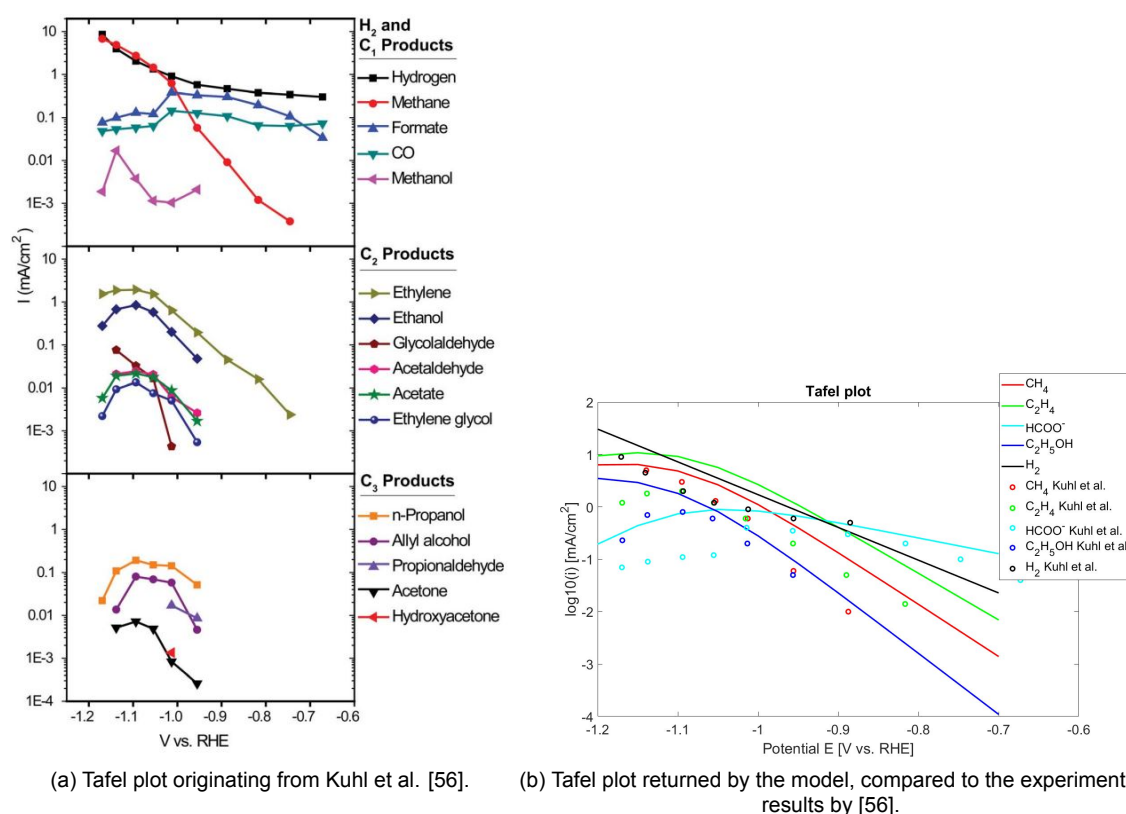
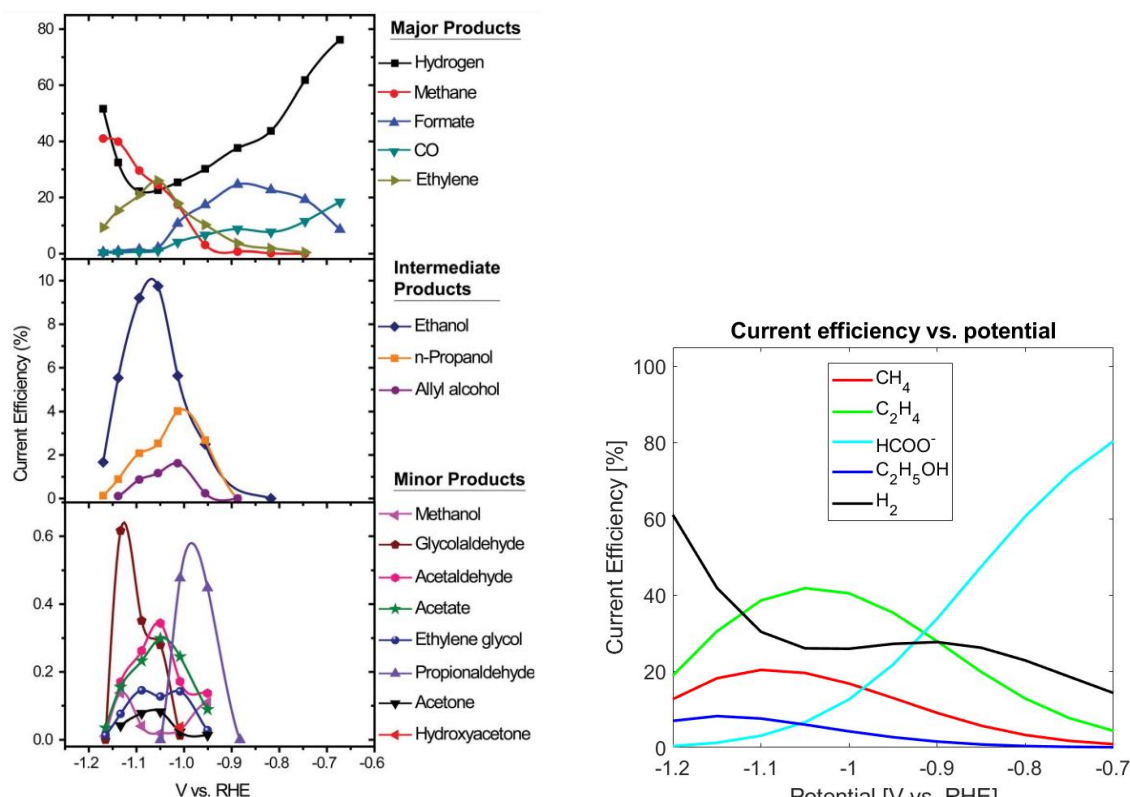


Figure 4.10: Tafel plots, demonstrating the logarithmic partial current densities of the involved species against the applied potential.

Overall, the modelled results do show roughly the same trends and kinetic behaviour as dictated by the experimental data. The only inaccuracy regarding the mutual current density distribution, is that the model returns a higher maximum current density for ethylene than for methane, which is not in accor-

dance with the experimental data. This is most likely due to a deviation in the input data compared to reality, resulting from the changing slope behaviour displayed by methane. This effect will be visible in the selectivity of the system as well, and is something to take into account when analysing the results of the high pressure cascade model.



(a) Faradaic Efficiency plot originating from Kuhl et al. [56].

(b) Modelled Current Efficiency (i.e. Faradaic Efficiency) plot.

Figure 4.11: Faradaic efficiency plots, showing the selectivity for a product for a specific potential.

To evaluate the accordance of the modelled results regarding the selectivity, the Faradaic Efficiency (i.e. Current Efficiency) results are displayed in figure 4.11. This comparison shows the ethylene selectivity to be overestimated at the expense of the methane selectivity, as was expected from the Tafel plot results. Moreover, something else is going on; at low overpotentials the selectivity for formate drastically increases in the modelled results (figure 4.11b). From reviewing figure 4.10, it becomes clear this is due to the constant slope assumption for the hydrogen slope. Figure 4.10a shows the slope to flatten in the range $E = -0.9$ to $E = -0.6$; this is not accounted for in the model. Instead, the partial current density for hydrogen is simulated to decrease with the slope evaluated at $E = -1.2$ to $E = -0.9$. Therefore, the simulated value in the $E = -0.9$ to $E = -0.6$ domain will be much lower than the actual value. This effect persists in the Faradaic Efficiency plot, as only hydrogen and formate are active at the low potential values (around $E = -0.7$). Therefore, figure 4.11b misrepresents the behaviour in this range. Instead of a selectivity spike for hydrogen, it displays a selectivity peak for formate around $E = -0.9$ to $E = -0.6$.

In the region from $E = -1.2$ to $E = -0.9$, the modelled Faradaic Efficiency results compare better to the experimental results. Here the hydrogen, ethanol, ethylene, and methane FE values compare relatively accurately to the experimental results, showing peaks at roughly the same potentials and with comparable values (taking the methane/ethylene under/over-estimation in mind).

To conclude this validation, the modelled results are most accurate in the $E = -1.2$ to $E = -0.9$ range. However, even in this range it shows some deviations from reality regarding the methane and ethylene

distributions. Therefore, the Current Efficiency analysis for the high pressure cascade model can be used to acquire insight in the possible product distributions under varying conditions, but these need to be validated experimentally as there is a known level of uncertainty in these values.

4.5.3. Second reduction step COR

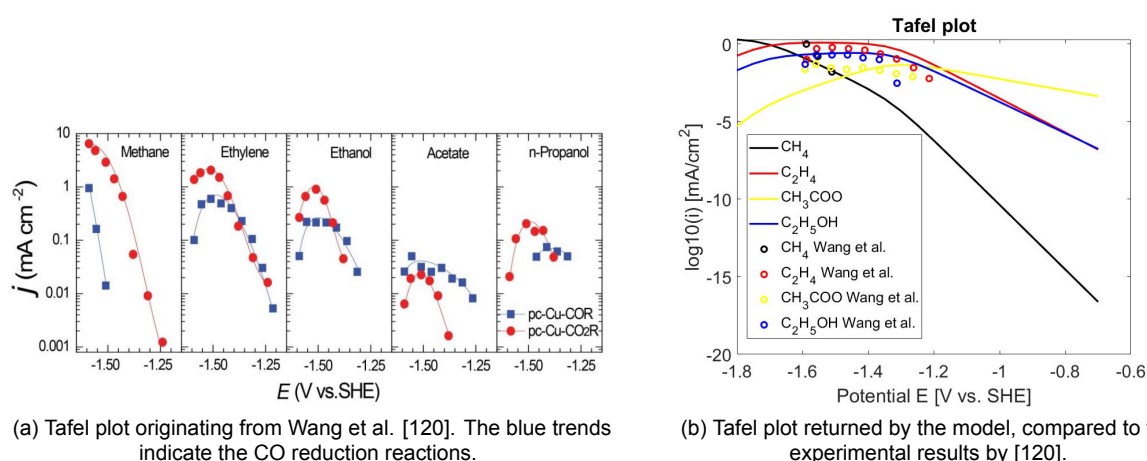
To compare the model's results to the experimental results by Wang et al., the following input parameters are adopted [120]:

Parameter	Value
Pressure	1 atm
T	298.15 K
Electrolyte	0.1 M KOH
Potential range	-1.4 to -0.6
Cell volume	8 cm ³
Cell surface area	4.5 cm ²

Table 4.5: Input data originating from the research by Wang et al.[120].

Note that in this version of the model the solubility of CO₂ is set to zero, so only CO would be present as reactant. In addition, the electrolyte for this research is different than the other studies, resulting in a high system pH level of 13, instead of 6.8. Therefore, to clearly show the trends in the graphs, they will be represented in – pH independent – SHE scale. To convert the SHE values to RHE values, equation C.11 can be utilised. Furthermore, since the research by Wang et al. does not disclose the kinetic information on the hydrogen evolution reaction, except for in the FE plot, this information is derived from another similar research [59].

Figure 4.12 demonstrates the experimental and modelled Tafel plots for the CO reduction reactions taking place in the model. Figure 4.12b shows the modelled results match the experimental results rather accurately with respect to the maximum current density and potential range. The model does predict the onset of mass transfer for the production of methane and acetate to be earlier compared to the experimental results in figure 4.12a. However, it has a reasonably accurate fit with the experimental results, taking into account the complexity of the system. The product distribution is evaluated to be similar to figure 4.12a; therefore, the Faradaic Efficiencies are expected to be a good match as well.



(a) Tafel plot originating from Wang et al. [120]. The blue trends indicate the CO reduction reactions.

(b) Tafel plot returned by the model, compared to the experimental results by [120].

Figure 4.12: Tafel plots, demonstrating the logarithmic partial current densities of the involved species against the applied potential.

The Faradaic Efficiencies for the CO reduction on copper are represented in figure 4.13. Note that

figure 4.13a is expressed in RHE scale, whereas figure 4.13b is expressed in SHE scale. To convert between the two scales, equation C.11 can be utilised, which, at a pH of 13, leads to a divergence of ≈ 0.77 V. This factor is approximately in accordance with the apparent difference between the potentials accompanying the maxima of the curves in figure 4.13a and figure 4.13b. The peaks in the modelled results, as was the case in the first reduction step, have shifted slightly in potential, compared to the experimental results. This effect could result from a discrepancy in the mass transport properties in the model, such as the diffusion coefficient values.

The graphs, however, do display very similar trends, even though the hydrogen evolution reaction kinetics utilised in the model originates from a different study [59]. This could also explain why the selectivity for hydrogen production is overestimated in the modelled results. As a result, the ethylene selectivity is underestimated, compared to figure 4.13a. The selectivity for the other three products, on the other hand, does compare well to the experimental results. This results in a rather accurate modelled selectivity representation in terms of product distribution. However, these deviations from reality, especially the overestimation for hydrogen, must be taken into account in the sequential analyses of the high pressure cascade model in section 5.1.

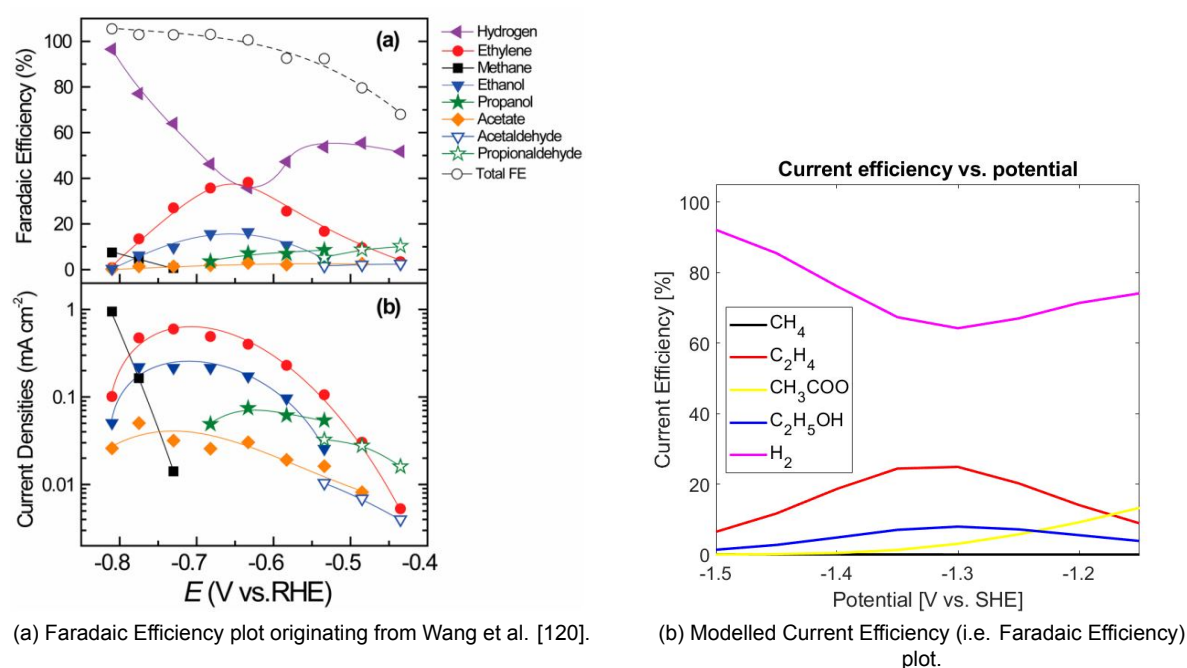


Figure 4.13: Faradaic efficiency plots, showing the selectivity for a product for a specific potential.

4.5.4. High pressure effects

To validate the modelled behaviour at higher pressures, trends shown in experimental studies regarding high pressure experiments, will be compared with the modelled results. This will provide insight into the expected behaviour under high pressure. The conditions in other high pressure research will not explicitly match the input data utilised for the three modelled sections (first reduction step, CO₂R in second reduction step and COR in second reduction step). Therefore, their results will not be directly compared in value to the modelled results, as this would not be a valid comparison. Instead, we will look at the trends and displayed behaviour under pressure, and compare this to expected occurrences in the modelled trends. As stated before, increasing the pressure will increase the solubility of the reactants, which will increase their mass transfer to the electrode surface. This effect will be represented by an increase in partial current density for the desired products. Therefore, to indicate whether the model captures this effect, Tafel plots are produced at different gas pressures.

The pressure behaviour for the first reduction step, CO_2 reduction on Ag to form CO, is demonstrated in figure 4.14b. The trends of the modelled Tafel plots are compared with the trends shown in figure 4.14a. They distinctly show the increase in current density with increasing pressure, as anticipated. Note that figure 4.14a displays the experimental results measured at an In electrode, instead of an Ag electrode. Therefore, the experimental data points, as shown in figure 4.14a, are not indicated in figure 4.14b, as these cannot be compared. These results are only combined to show the correlation in system response to the increasing pressure.

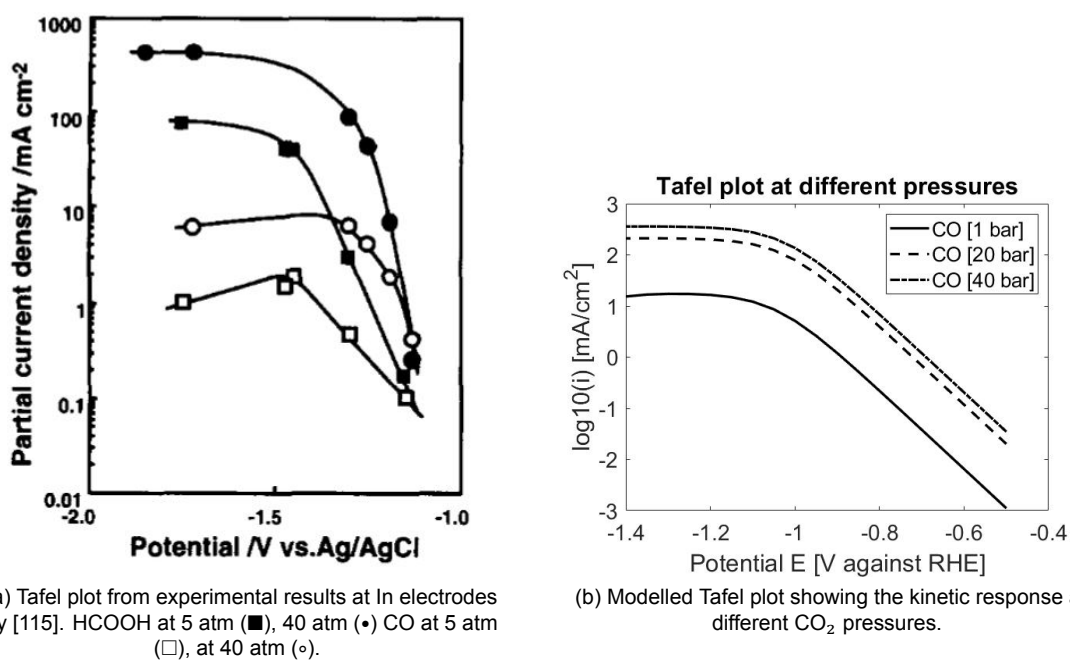
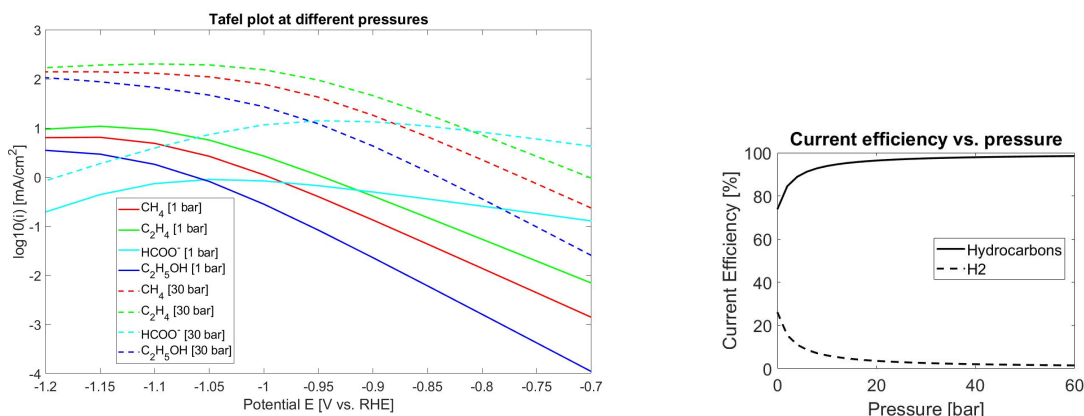


Figure 4.14: Comparison of the kinetic trends at different gas pressures.

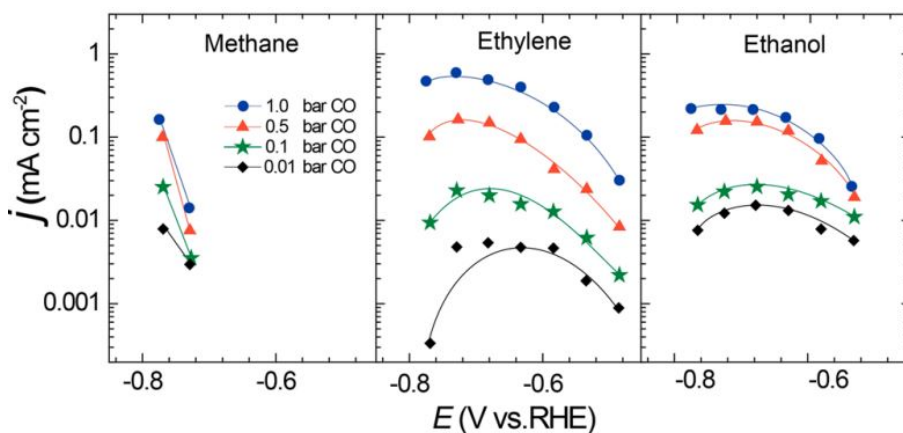
The modelled results for the second reduction step, regarding the CO_2 reduction reactions, demonstrate the same behaviour under increasing pressures. Figure 4.15a; illustrates this as the current densities are shown to increase with the applied pressure. As explained in section 2.1, applying high pressures will increase the selectivity towards hydrocarbon products, as the HER is not affected by the pressure. To validate if this effect is captured by the model as well, the Current Efficiency for hydrocarbons and hydrogen are plotted against the CO_2 gas pressure. Figure 4.15b indicates this behaviour is indeed captured by the model, as it shows the selectivity towards hydrogen to decrease with increasing pressure.

To further validate the ability of the model to capture the effect of pressure, the pressure dependent Tafel plots for the CO reduction reactions are compared to experimental data [120]. As explained in the introduction section, research focusing on the relation between high pressures and CO reduction is yet to be conducted. Therefore, to indicate the validity of the pressure dependent behaviour for the COR in the second step, the effects of pressure on the kinetics in the range of 0.01-1 bar will be investigated. Figure 4.16 indicates the behaviour of the modelled and experimental results to be similar in trend and approximate maximum current density. The modelled results in figure 4.16d do deviate slightly from the experimental results in the value for the maximum ethanol current density at low pressures of 0.001 bar. The most likely cause is the approximated solubility behaviour for CO, as this is modelled using Henry's law, which does not have the highest accuracy. Table 2.3 demonstrates the Henry's coefficient is not actually constant; its value declines slightly with declining pressure. Hence, the solubility behaviour at the low pressure region could be misrepresented, which could provide the explanation for the deviation in the described behaviour in the low pressure region.

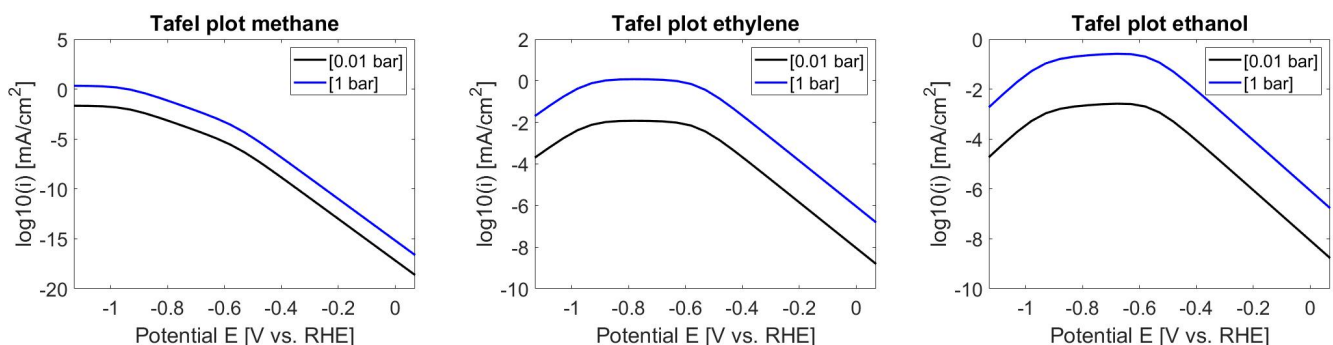


(a) A Tafel plot, comparing the kinetic behaviour for the CO₂ reduction on Cu at 1 and 30 bar. (b) Current Efficiency as a function of the CO₂ pressure for the different types of products at E=-1.1 vs RHE.

Figure 4.15: Indication of the pressure behaviour for the CO₂ reduction on Cu as returned by the model.



(a) Experimental plots demonstrating the effect of changing partial pressures on the Tafel plots for different products. Derived from [120]



(b) Modelled Tafel plot showing the kinetic response at different CO₂ pressures. (c) Modelled Tafel plot showing the kinetic response at different CO₂ pressures. (d) Modelled Tafel plot showing the kinetic response at different CO₂ pressures.

Figure 4.16: Comparison of the modelled and experimental effects of pressure on the kinetics regarding COR on Cu electrodes.

Overall, the model's response to pressure aligns well with the trends in the available experimental studies and the expected behaviour indicated by the theory section. The further validation of the high pressure response for the model, is contingent up on the availability of future experimental research.

4.6. Sensitivity and conversion analysis

To determine the magnitude of the effect of the adopted parameters on the modelled results, a sensitivity analysis is carried out. In the previous sections, slightly deviating diffusion coefficients was offered as possible explanation for the shift in mass transfer onset. The 2019 research by Soeteman also investigated the response in their model to changing diffusion coefficient values, reporting a distinguishable effect on the production rates of the products [102]. To indicate the sensitivity of this model on the diffusion constants, the maximum CO₂ reduction rate will be analysed after varying the diffusion coefficient values between 0.8 - 1.2 times the real value, in the first reduction step section.

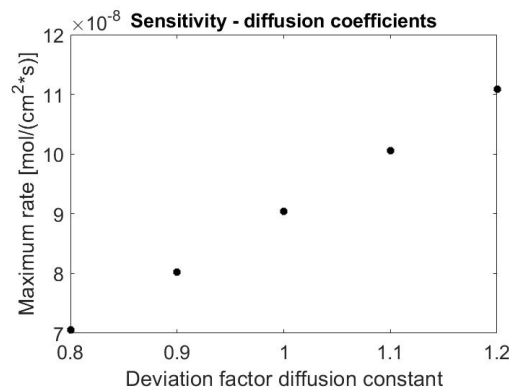


Figure 4.17: Sensitivity analysis of the reduction rate of CO₂ on Ag on the variation in diffusion coefficient values.

Figure 4.17 demonstrates a linear relation between the change in diffusion coefficient and the maximum reduction rate of CO₂. This relation is foreseeable, looking at the Neumann boundary conditions stated in section 4.4, where Fick's second law of diffusion is equated to the sources/sinks (i.e. the rates). Nonetheless, as anticipated in the previous sections, a slight deviation in the diffusion coefficient has a large impact on the reduction rate, maximum current density and the selectivity profile. Therefore, this explanation can, to a certain extent, effectively account for the deviations seen in the validation sections above.

To assure the model converges, a maximum value for the spatial and time variable has to be selected. To determine at what time and spatial variable the model has reached convergence, the following analysis is carried out. Again the rates will be selected as the validation variable, while the x_{end} and t_{end} values will be varied until the modelled value for the rate does no longer change with the varying x_{end} and t_{end} values. This will provide the value for x_{end} and t_{end} for which the model reaches convergence. As stated before in section 4.4.5, the accuracy and computation time for the model depend more strongly on the x variable compared to the t variable. This is validated by figure 4.18, showing the minimum required amount of t and x points for convergence. Note that both the first and second CO₂ reduction step show a peak of the same magnitude before 20 spatial points, where the COR step predicts constant rate values from the minimal onset value for x .

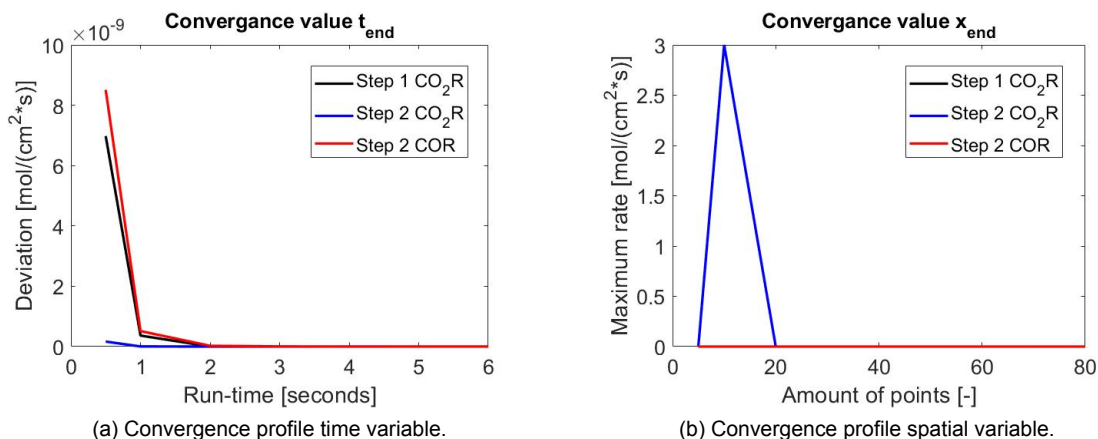


Figure 4.18: Showing the convergence profiles for the discretised and time variables.

4.7. Conclusion validity model

The validation of the first reduction step demonstrates that the model can predict the kinetics, salting-out effect and the product selectivity very well, when the number of reactions taking place is low, along with rather constant kinetic behaviour. The validation of the second step shows some noteworthy deviations, as it proves to be hard to accurately simulate such a complicated system. The sections regarding the second reduction step demonstrate that the quality of the input parameters has a large influence on the accuracy of the modelled results. Figure 4.10a is lacking the required detail for a high quality representation of the system for this modelling approach, whereas figure 4.12a is less complex, which leads to more accurate modelling results. In addition, the assumption adopted in the modelling approach, regarding constant slope behaviour, has also demonstrated to lead to deviations in modelling behaviour regarding complicated systems showing multiple changes in slopes for multiple products. Consequently, the simulated CO₂ reduction on copper contains some evaluation limitations, whereas the CO reduction and the CO₂ reduction in the first step do present accurate model results.

The kinetic parameters adopted from other sources than the validation researches [40] [56] [120], may explain some of the slight deviations between the modelled results and the experimental data. This, however, can be expected, as a model is a system based on consecutive approximations from reality. Additionally, the goal of the model is to provide insight into a new research direction, to finding relations between operating parameters and to determine the parameters for experimental research. Therefore, small deviations from reality are acceptable, as these do not impact the ability of the system to reach these goals.

Even though there is no experimental or modelled research available regarding the high pressure cascade system, this validation provides valuable information regarding the performance of the model. It shows the limitations of the model, but also shows which sections and reactions it can accurately describe. This information is key in the analysis of the eventual results returned by the high pressure cascade model. It also indicates the need for experimental data for this research direction, emphasising the need for the experimental set-up.

5

Results & Discussion

5.1. Modelling results

This section will elaborate on the modelled results produced by the high pressure cascade model. An analysis will be made regarding the demonstrated effects and the expected behaviour as predicted by literature. Special focus will be applied to the investigation regarding the benefit of pressure on the cascade system. Both technologies pose individual benefits regarding CO₂ electrocatalysis, however, their combined effect had not yet been researched. Therefore, the following section will indicate their combined effects on the efficiency of the CO₂ reduction reaction.

In addition, this section will provide a recommendation on the direction and nature of the experimental follow-up study. By providing information on the relations with respect to the parameters and operating conditions regarding the high pressure cascade system, the experimental work can be applied more effectively. These recommendations will eventually lead to an overall conclusion, regarding the potential for this new system. This will be discussed in detail in the following chapter. It is important to note that all the demonstrated results were generated based on the operating conditions from the experimental set-up as proposed in chapter 3. This way the results can be accurately compared when conducting further experimental research. Over the course of all simulations, the electrolyte concentration in the model was kept constant at 0.1 M KHCO₃ to simulate the operating conditions in the experimental set-up.

This section will be divided into subsections, discussing the important system parameters contributing to the overall efficiency of the system, the reaction rate, the selectivity and the onset potential.

5.1.1. Reaction rates

As discussed in the introduction section, the current density is a good measure for the reaction rate and, therefore, for the efficiency of the system. It signifies the rate of charge transfer on the electrode area; hence, the larger the current density, the higher the rate of reaction [127]. Therefore, a lot of research has been dedicated to finding ways to increase the current density, while retaining a low applied potential. Currently, the reaction rate has been identified as one of the most important factors governing the efficiency of electrochemical CO₂ reduction [107] [23]. It is limited by the following principles:

1. the low solubility characteristics of the main reactants (CO₂ and CO) [98]
2. the competition for surface sites with the hydrogen evolution reaction [71]
3. the participation of CO₂ in the electrolyte buffer reactions [14]

Splitting up the overall reduction reaction in two sequential reduction steps, has shown it can increase the transport of CO to the catalyst surface, resulting in an increased reaction rate [71]. As the cascade commences with both CO₂ and CO reduction in the second reduction step, the salting-out effect stemming from the buffer reactions will be reduced, since CO does not take part in these chemical reactions. Another applied solution for increasing the reactant transport is the application of high system pressures. This also increases the reactant solubility, while simultaneously suppressing the competition with the hydrogen evolution reaction, as this reaction is not affected by the pressure, since it is not mass transfer limited. Based on these findings and the literature study conclusions, the high pressure cascade set-up will, consequently, increase the reaction rates on these accounts. To test if these phenomena do occur in the high pressure cascade model, the modelled results regarding these will be investigated and analysed in this section.

As explained above, by operating in tandem with two sequential reduction reactions, the CO solubility at the Cu electrode can be increased, effectively bypassing its low solubility behaviour. Since CO reduction has a higher activity and selectivity for oxygenates [38], it is desirable to increase its participation in the overall reaction. When the convective transport to the second reduction electrode is much larger than the diffusion to the bulk section, the transport of the produced CO to the second electrode will dominate. This will result in a higher local CO concentration reaching the Cu electrode, compared to directly dissolving the CO. This effect is illustrated in figure 5.1a, where the CO concentration entering the second reduction section is plotted against the CO concentration resulting from directly dissolving CO gas in the electrolyte. This comparison was made at ambient pressures and temperatures. The graph shows the increased concentration; however – as explained in section 4.3, 'Assumptions and limitations' – to model this effect, the assumption was made that all produced CO will reach the second reduction section. For this to be accurate, the flow-rate will have to be very high; therefore, the model is limited to describing systems adopting high flow-rates. This graph illustrates the positive effect the cascade system can have on the CO solubility and, therefore, the reaction rate.

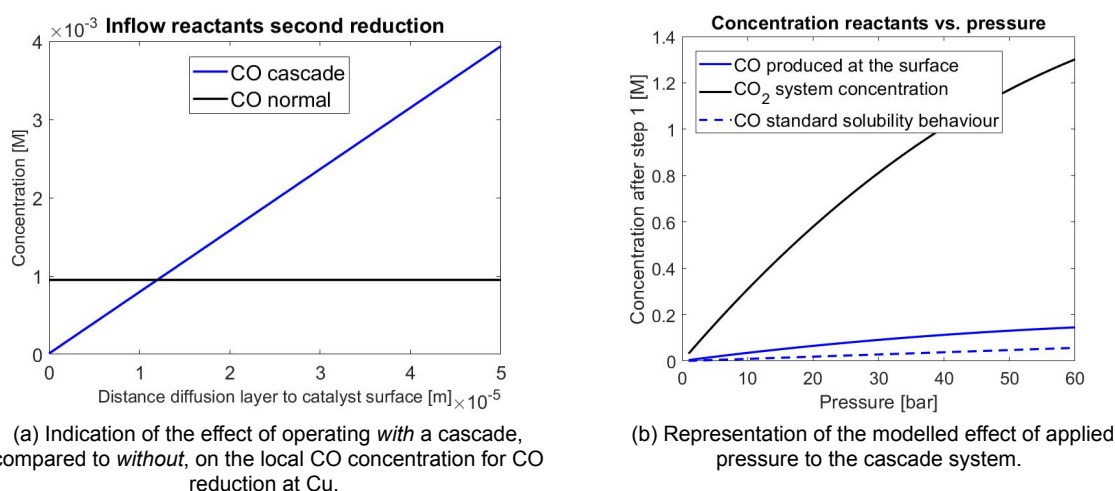


Figure 5.1: Analysis of the effects of a cascade system and pressure on the solubility of the reactants, CO and CO₂.

To increase the reactant solubility even more, high pressures were applied to the cascade system. Figure 5.1b shows the CO₂ solubility calculated as described in section 4.4.2 and the CO concentration at the surface produced in the first reduction step. Both are positively affected by the applied pressure, showing the applied pressure increases the effect of the cascade, as more CO is produced when more CO₂ can be converted in the first reduction step. In order to compare this with a situation without the cascade, the graph also presents the standard pressure dependent solubility behaviour of CO, modelled with Henry's law. The figure indicates the combined effect of the cascade and that the high pressure could result in a higher CO surface concentration than can be achieved by applying these techniques separately. However, as explained, the accuracy of this figure depends on the flow-rate in

the system. This can be taken as a preliminary indication of the positive effect of the combined system on the reactant solubility and therefore the reaction rate. Figure 5.2 shows the effect of pressure on the reduction rates in the cascade system. These are all shown to severely increase with the pressure, indicating the potential benefits of the combined system regarding an increase in the reaction rate as simulated by the model.

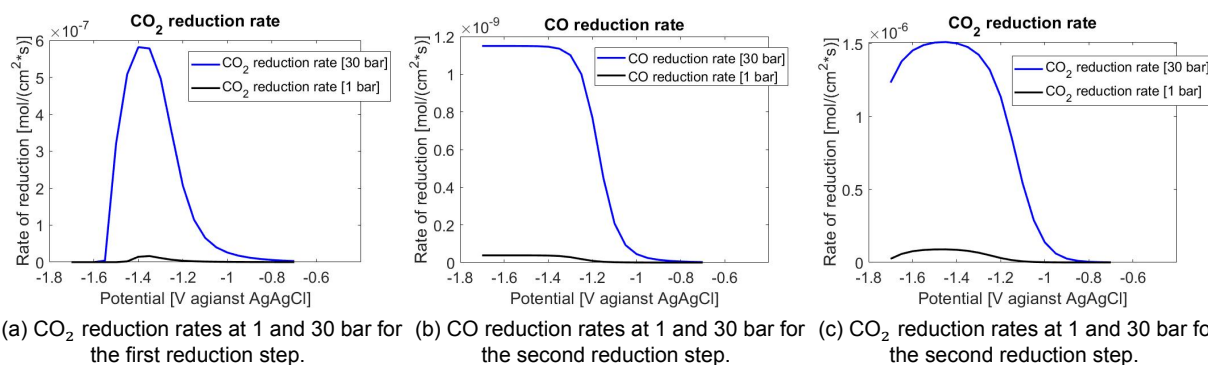


Figure 5.2: Comparison between the modelled reduction rates at low pressure (1 bar) and high pressure (30 bar).

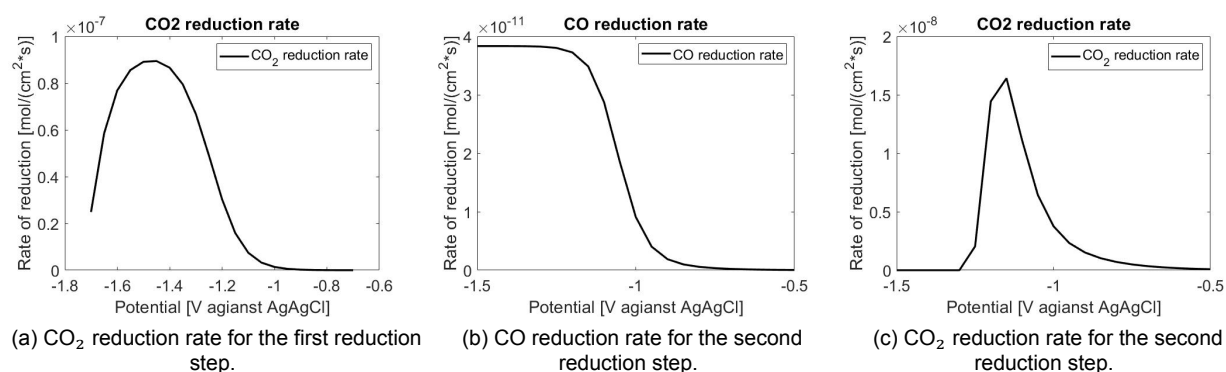
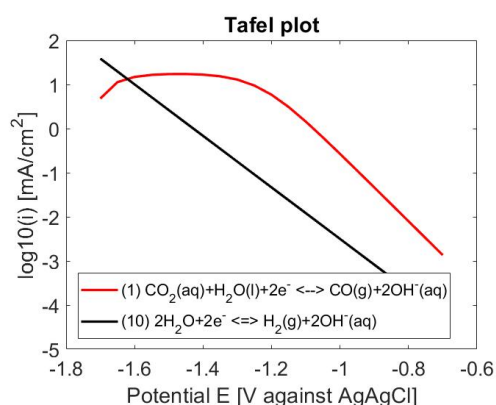


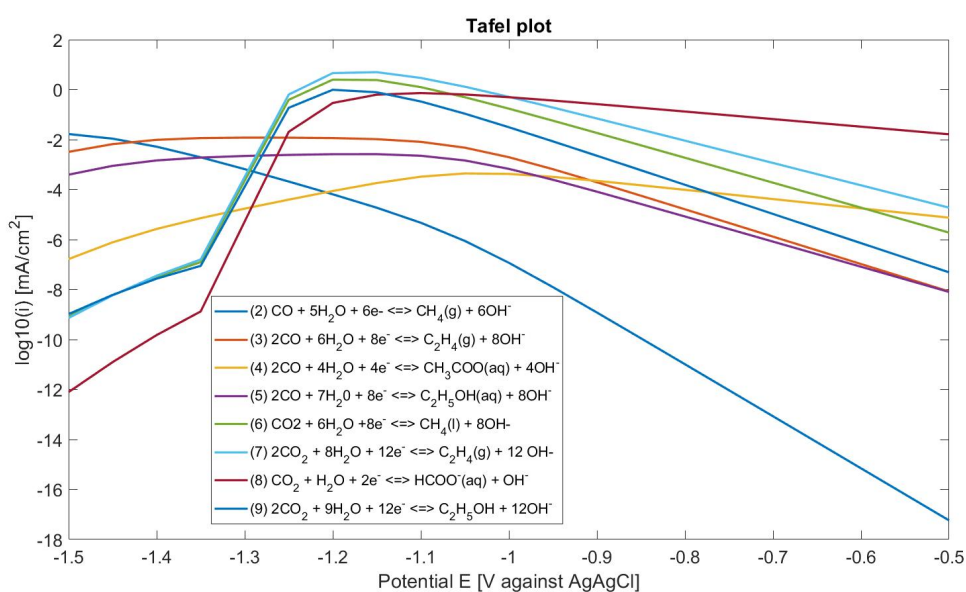
Figure 5.3: The modelled reduction rates, illustrating the maximum reduction and the accompanying potential.

However, the solubility of the reactants is not the only factor directly influencing the reaction rates. The hydrogen evolution reaction also has an impact on the reduction rates of CO₂, as it can crowd and occupy the available sites at the catalyst surface. Additionally, it also increases the surface pH at higher overpotentials, causing more mass transfer limitations, as the leftover CO₂ will be pushed to participate in the buffer reactions [71]. This effect also appears in the high pressure cascade set-up, as demonstrated in figure 5.3. At sufficiently high potentials, the reaction products deplete, indicating onset of the mass transfer limited zone. Figure 5.3 demonstrates this effect, which commences as the reduction rate is no longer increasing. The same effect can be seen in the Tafel plots in figure 5.4, advancing in the same potential region. The hydrogen evolution reaction, conversely, is not mass transfer limited, therefore, even at the high potential range, OH⁻ will continuously be produced. This will result in a high local pH level, which drives the leftover CO₂ to participate in the buffer reactions with the electrolyte [14]. This effect is distinctly shown in figure 5.3, as the rates in figures 5.3a and 5.3c display a decline after reaching their maximum value. This also explains the difference in the rate profiles between figure 5.3b and figures 5.3a and 5.3c, as CO does not participate in the buffer reactions, resulting in a constant profile after the peak. As a result, the CO reduction reactions, together with the hydrogen evolution reactions, will determine the production profile at the higher potential range (E ≈ -1.5). This effect is represented in figure 5.4b, where the CO reduction reactions are shown to participate at high potentials while the CO₂ reductions show a step decline after E = -1.2, as a result of the high OH⁻ concentration at the surface. A more detailed discussion regarding this principle and its effects on the

product selectivity will be represented in the next section.



(a) Tafel plot of the first reduction step.

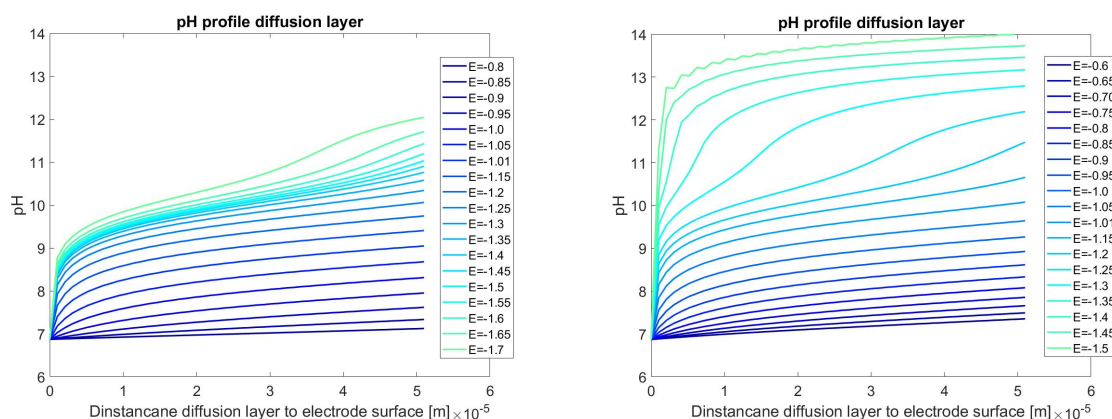


(b) Tafel plot of the second reduction step.

Figure 5.4: Tafel plots, displaying the relation between the reaction rate (i.e the current density) and the applied potential.

To validate whether the decreasing slopes are a direct result of the increased salting-out effect, caused by the high local OH^- concentration, the surface pH profiles in the diffusion layer are presented in figure 5.5. This figure shows the pH inside the diffusion layer increases with the applied potential, as predicted. It also shows the pH values for the second reduction step are much higher – at lower potentials – than for the first reduction step. This is consistent with the steep drop in figure 5.3c compared to the shape of the curve in figure 5.3a. This is, therefore, taken as proof of the model's capability of describing the salting-out effect.

Consequently, the modelled results demonstrate, that applying high pressures to a cascade set-up will increase the reaction rates, and therefore, the efficiency of the system.



(a) pH profile in the diffusion layer of the first reduction step. Here the distance is indicated to start from the diffusion layer (0 m) to the electrode surface ($5\mu\text{m}$).

(b) pH profile in the diffusion layer of the second reduction step. Here the distance is indicated to start from the diffusion layer (0 m) to the electrode surface ($5\mu\text{m}$).

Figure 5.5: pH profiles in the diffusion layer, showing low pH values at low absolute potentials and high values at high absolute potentials.

5.1.2. Product selectivity

Another main factor determining the system's efficiency is the selectivity. Having a high selectivity for a single product will reduce the need for complicated post-separation processes, while increasing the overall system efficiency. As explained in the introduction section, an interesting product group to focus on, are C_{2+} products. These are valuable and have a high energy density, which makes them very interesting for energy storage and transport. At the moment, the only catalysts capable of producing significant amounts of C_{2+} products are copper based [57] [119] [92]. Unfortunately, copper based catalyst usually do not possess a high selectivity for a single product. Therefore, the challenge is to tune the operating conditions, to maximally increase the selectivity for a single product. This research focuses on producing a high selectivity towards C_{2+} products; so far we have seen that C_1 and C_{2+} products have a different mechanistic reaction pathway (section 2.1.4). Consequently, their ratio can be influenced by changing the operating conditions. Based on the principles found in the literature study, the high pressure cascade could influence the selectivity by varying the following parameters:

1. the reactant type
2. the system pH
3. the system pressure
4. the applied potential
5. the competition with the HER

This section will be dedicated to evaluating these effects by analysing the modelled results. First of all, the Current Efficiency will be evaluated against the applied potential and pressure, to gain insight in the resulting selectivity. Literature has provided indications regarding changing kinetic behaviour for different potentials. The effect of this has already been encountered in the shape of the changing Tafel slopes for different potential regions. In addition, the pressure will increase the surface concentrations of the reactants, resulting in an increased amount of CO^* at the surface. The literature study has indicated the C_{2+} products have a second order CO^* dependence, whereas the C_1 products only have a first order dependence [60]; therefore, the increase in pressure may show a change in selectivity between C_{2+} and C_1 products. In addition, the competition with the hydrogen evolution reaction for surface sites also has an influence on the selectivity. Although when the pressure in the system is increased, the relative effect on the product selectivity caused by competition with the HER will decrease, as the pressure does not affect the H_2O concentration. This will, therefore, result in a decrease of hydrogen selectivity

and an increase for the selectivity for the other products. A last factor influencing the selectivity which might occur in the high pressure cascade system, is the reactant type. From literature it is known, CO reduction has a higher selectivity for oxygenates [38], therefore, the selectivity at a certain potential will be influenced by the reduction reactions that are dominant in that section. Hence, analysing at what potential and pressure regions the products originate from CO reduction or CO₂ reduction, will provide insight in how to instate more control on the selectivity.

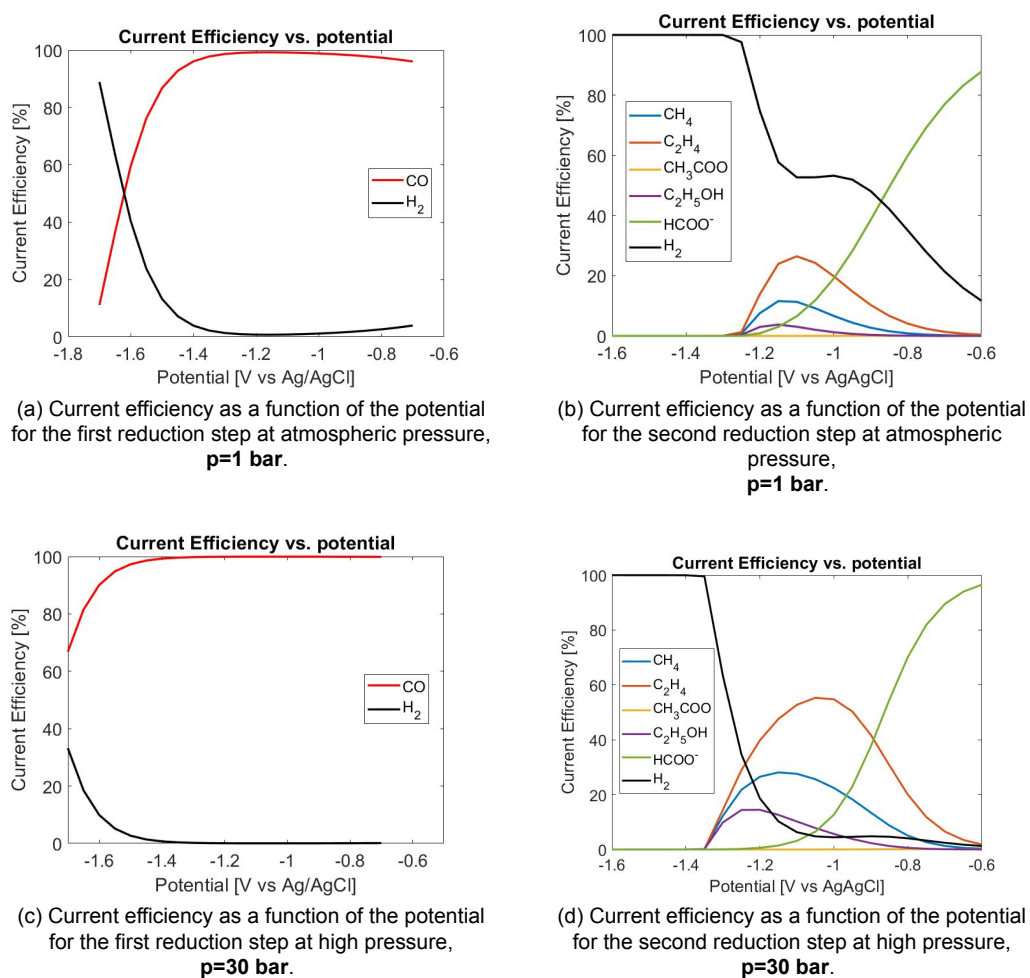


Figure 5.6: Comparison regarding the profiles for the Current Efficiency to the applied potential.

To determine the effect of the potential on the high pressure cascade system's selectivity, in order to determine which potential ranges are interesting to investigate further, a Current Efficiency plot against the potential was produced. Figure 5.6 shows the results generated by the high pressure cascade model. Here, figure 5.6a shows the current efficiency for CO production to be really high at potentials below $E=-1.4$. From the validation section, however, we know that due to the assumptions made, this representation has its limitations. First of all, the assumption was made that no formate would be produced in the first reduction reaction. In reality, the Current Efficiency for the CO will not be a 100%. Also due to the deviating hydrogen Tafel-slope and the constant slope assumption as described in section 4.3, the hydrogen Current Efficiency is underestimated at lower overpotentials (see: section 4.5). The same goes for the second reduction step, shown in figures 5.6b and 5.6d. Section 4.5 has shown the deviating hydrogen slope to result in an underestimation of the hydrogen production and an overestimation of formate production at low overpotentials. This effect is demonstrated in the graphs, and should be taken into account during the analysis. Therefore, any further analysis will be done at sufficiently high potential ranges, so this deviation is not expected to influence the results.

To indicate if the competition for selectivity with the hydrogen evolution reaction will indeed decrease with increasing pressure, figure 5.6d will be analysed in more detail. This figure demonstrates the selectivity for hydrogen indeed decreases while the selectivity for the other products increase. This solidifies the expectation regarding the hydrogen evolution reactions dependence on the pressure, showing its Current Efficiency to decrease as a result.

Another interesting effect demonstrated by the graphs in figure 5.6 is the slight change in the figure shape when increasing the pressure. This is especially noticeable in the ethylene plot. This could indicate the ethylene produced originates from different sources (CO and CO_2) which have different optimal potentials for a high ethylene selectivity. It could also indicate the share of CO reduction and CO_2 reduction changes with the operating pressure. To study this effect, however, the contributions from CO_2 and CO reduction for the separate products must be investigated in more detail. This analysis will be made below.

As intended, this figure provides valuable insight into the interesting potential regions to investigate when aiming for a high C_{2+} selectivity. Based on this knowledge, the potentials $E=-1.2$, $E=-1.3$ and $E=-1.4$ are selected to evaluate in more detail.

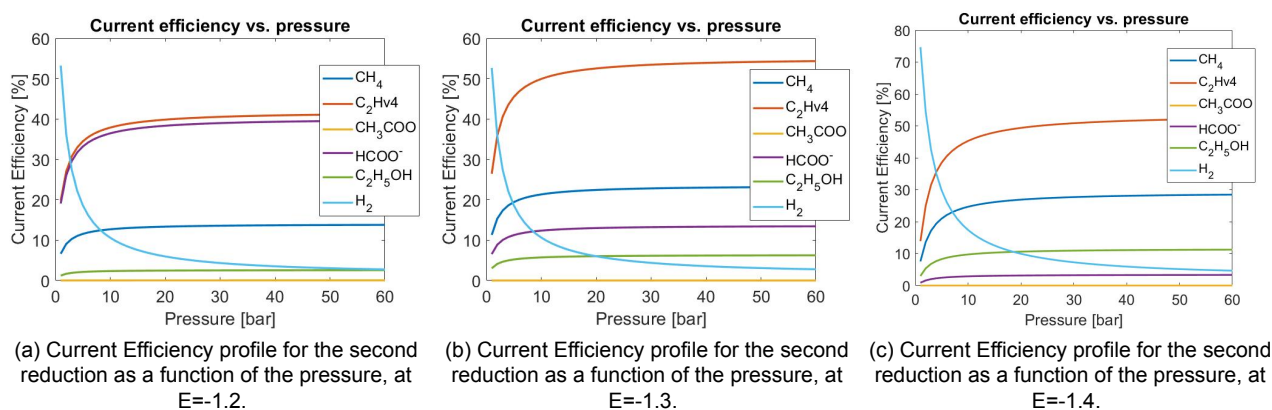
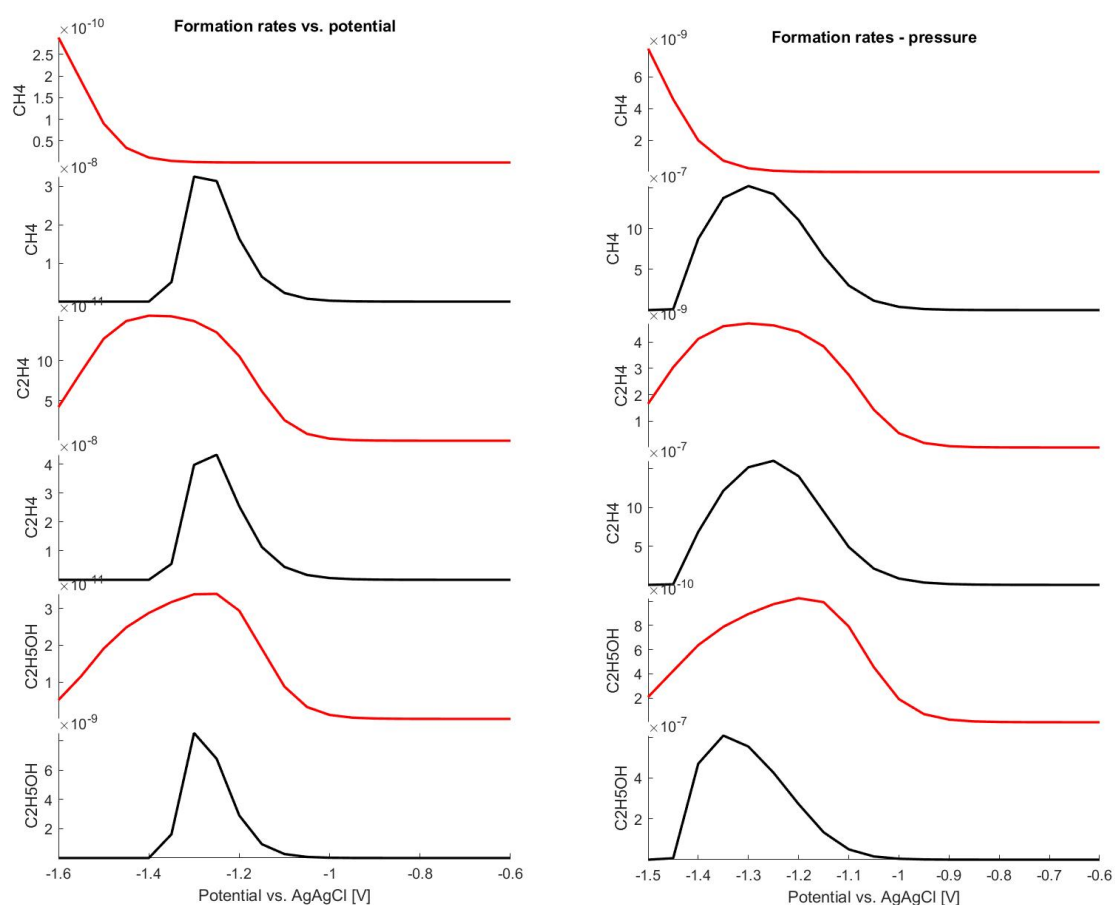


Figure 5.7: Comparison between the pressure Current Efficiency profiles and their relation with pressure at different potentials.

To acquire insight into the relation between the pressure and the selectivity, figure 5.7 was evaluated in the high pressure cascade model. The figure demonstrates the Current Efficiencies against the pressure at the three interesting potentials, selected based on figure 5.6. Interestingly, the product distribution is shown to change considerably with the applied potential. Additionally, the pressure is shown to have a positive effect, decreasing the hydrogen contribution and increasing the formate, methane, ethylene and ethanol selectivity. When reviewing the effect of pressure, it appears that the contribution initially increases strongly, after which it flattens out. This is an interesting detail, as it provides an estimate regarding the trade-off between applying extra pressure (i.e. energy) and its added benefit on the product distribution for these operating conditions.

So far, the modelled results have shown indications of the effects of the pressure, potential and HER competition to indeed affect the system's selectivity. Another interesting parameter to investigate regarding this effect, is the dependence on the reactant. First of all, because of the cascade electrode set-up, the generated products will originate from both CO and CO_2 reduction. To indicate the origin of a generated product, Gurudayal et al. compare the oxygenates to ethylene ratio, as CO_2 is known to produce a lot of ethylene compared to CO [38]. Conversely, for this research, the model was structured to separately model CO and CO_2 reduction on copper. Therefore, it becomes possible to examine the share of a specific reactant for the production of a single product at specific potentials and pressures. The resulting analysis for the high pressure cascade system is shown in figure 5.8.



(a) The CO reduction rates are shown in red and the CO₂ reduction rates are shown in black.
p=1 bar.

(b) The CO reduction rates are shown in red and the CO₂ reduction rates are shown in black.
p=30 bar.

Figure 5.8: Formation rates for products originating from CO and CO₂ reduction shown separately, at p=1 and p=30 bar.

This figure corroborates the theory posed in the previous section, regarding the CO reduction reactions being active in the region where the CO₂ is inhibited by the salting-out effects. The figure distinctly shows the CO reduction reactions to partake at higher overpotentials compared to the CO₂ reduction reactions. Especially the production of methane from CO is evaluated to have a really high onset potential. This is consistent with the findings in literature, showing increased rates for CH₄ production at high overpotentials and high pH levels [120] [59]. This behaviour is described to originate from the increase of available H* at the surface, as CH₄ production is believed to result from a Langmuir-Hinshelwood (LH) surface mechanism, requiring a reaction between a surface bound species and a surface bound H* (see section 2.1.4 for a more detailed description) [96]. Therefore, at high overpotentials mainly CH₄ will be produced, as its production rates only have a first order dependence on the reactant surface concentration, making them less dependent on the mass transfer limitations. Additionally, at high pH levels, the H* coverage will be increased, which has shown to also increase the CH₄ reaction kinetics [59].

Therefore, the formation rate behaviour, as shown in figure 5.8, indicates the model accurately describes these effects taking place in the high pressure cascade set-up. However, before accepting this, it is interesting to analyse how the model is structured, to determine to what extent the model is capable of incorporating this behaviour. The pH dependent behaviour, for example, is incorporated in

the model by including the OH^- concentration in the transport equations. The kinetics are derived from experimental data evaluated at set operating conditions. These operating conditions are, therefore, assumed to be constant even for changing system pressures. Therefore, it is interesting to discuss to what extent the model actually captures this complicated surface mechanism behaviour. The pH effects on the reactions are incorporated in the model by including the local amount of OH^- in the transport equations. Therefore, the decrease in C^* at the electrode surface at high overpotentials would be represented in the model. The changing selectivity based on the applied potential and pH is also partially incorporated, as the reduction reactions for CO and CO_2 reduction are modelled separately. Assuming the evaluated CO and CO_2 kinetic behaviour accurately captures the accompanying surface mechanism behaviour, the effect of the surface mechanisms for changing operating conditions (pH and potential) is partially included in the model, as the share of CO and CO_2 reduction is allowed to vary. Therefore, these effects will essentially capture the principles described in literature. This would not have been the case if the model's kinetic behaviour was based on the experimental results regarding a cascade system, as the decoupled effects of the share of CO and CO_2 reduction would be more complicated to capture and analyse. However, the extent to which the high pressure cascade model accurately describes this effect has to be evaluated with the experimental set-up, as the reaction kinetics of some species present really complex behaviour, which is hard to capture in the model. An example of this would be the changing pH dependence of the CH_4 kinetics, which have been indicated to change with pressure [59].

Another insight gained from analysing figure 5.8, is the knowledge on the contribution of CO and CO_2 reduction in a certain potential section. This makes it possible to further analyse the Current Efficiency potential graphs shown in figure 5.6 and determine the dominant reactant type contributing to the formation of specific products. With this knowledge, even more control can be instated on the selectivity of the system, as it was shown that both reactants respond differently to operating conditions. To put this information into practice, the C_{2+}/C_1 product ratio was determined at different potentials in the cascade set-up at ambient conditions; the results are displayed in figure 5.9a.

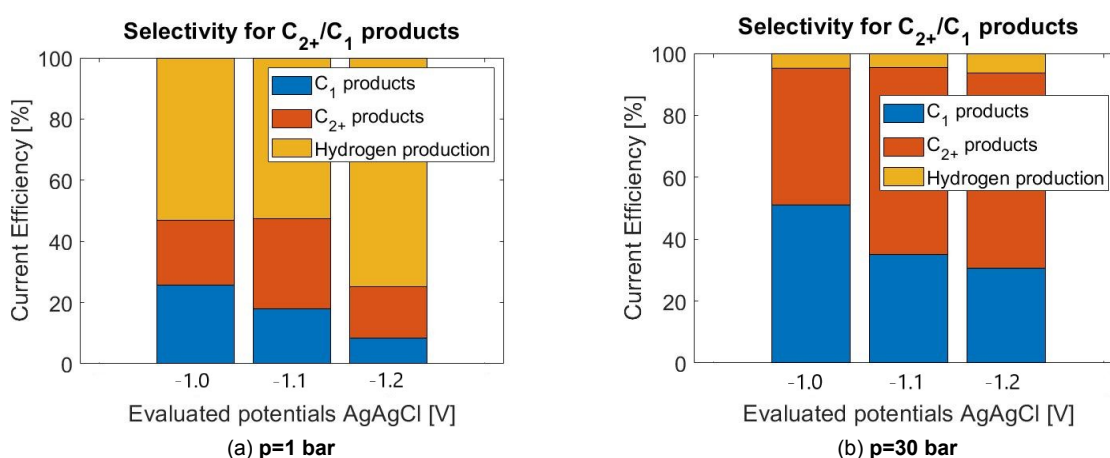


Figure 5.9: A comparison of the different C_{2+} , C_2 and hydrogen distributions for three different potentials, evaluated at two different pressures.

These results show that for the investigated potential range, the potential with the highest selectivity towards C_{2+} products is $E=-1.1$ vs. Ag/AgCl. This result can be expected when reviewing figure 5.6b, as at higher potentials the share of produced hydrogen starts to increase, while at lower potentials the formate production is overestimated on the account of the hydrogen evolution reaction (as explained in section 4.5). To investigate the effect of pressure on this optimal onset potential for high C_{2+} product generation, figure 5.9b was evaluated at a pressure of 30 bar, for the same potentials. The graph demonstrates the selectivity for C_{2+} products massively increases at high pressures. This result can be expected after reviewing figure 5.6d, as this illustrates the hydrogen selectivity to be suppressed in this region as a result of the high pressure. Most interesting, when comparing figures 5.9a and 5.9b, is that the optimal onset potential for a high C_{2+} product selectivity at high pressure, still presents around

$E=-1.2$ and $E=-1.1$ vs. Ag/AgCl. At higher potentials the hydrogen evolution reaction starts to dominate again, as predicted by figure 5.6d. This indicates, this region is an interesting topic for future investigation, regardless of the pressure in the system.

This section has shown there are a lot of factors incorporated in the high pressure cascade set-up which affect the selectivity of the system. Therefore, the information generated by the model is especially useful for interpreting the complex selectivity behaviour. By showing the contribution of the reactants to the product formation, considerable insight is created in the mechanisms taking place in the model and their dependence on system parameters. With this knowledge an adequate comparison with the theory describing the systems could be made, which further validates the model behaviour. These identified potential and pressure ranges will make a good starting point for further research aimed at optimising for a C_{2+} selectivity.

5.1.3. Onset potential

The onset potential of the system is a value regarding the required applied potential for a reduction reaction, and is directly related to the overpotential. Therefore, it represents a measure of the system efficiency. An efficient system will have a current density as high as possible for an as low as possible onset potential. So far literature has provided an indication that the onset potential for the cascade high pressure system could be affected by:

- The reactant type

Literature research regarding the onset potentials for tandem electrode configurations has shown that by applying a tandem catalyst, the onset potential of the system decreases, as demonstrated in figure 5.10. This effect has been investigated in the study regarding a tandem Au-Cu catalyst at ambient conditions by Morales-Guio et al., [71]. In this research they claim the tandem set-up has a 100 times higher product selectivity for C-C coupled products, while simultaneously showing that the onset potential for the reduction rates drops when applying a tandem electrode compared to normal reduction on Cu surfaces. The decrease in onset potential is proposed to originate from the share of CO reduction in the tandem system, instated by the sequential reduction steps. CO supposedly has a higher activity at lower overpotentials compared to CO_2 reduction, therefore, decreasing the overall onset potential.

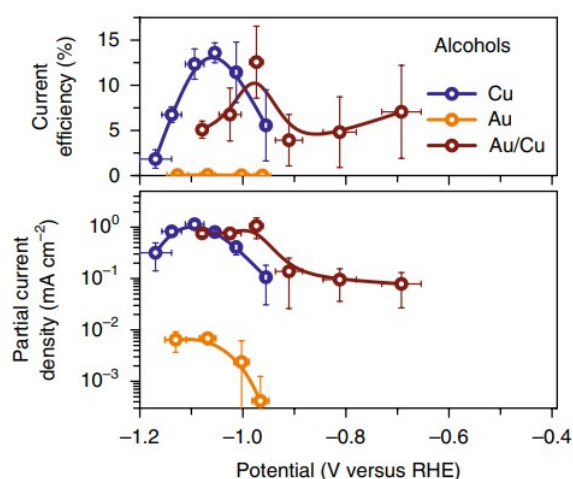


Figure 5.10: Comparison of the changing onset potentials when operating with a tandem electrode instead of direct CO_2 reduction on a Cu catalyst. Derived from [71].

This development could also be present in the high pressure cascade set-up. However, the research reporting significantly lower onset potentials for CO reduction reactions, evaluate its conditions at a high

pH level [119] [120] [59]. As stated before, a high pH will result in low overpotentials and a high selectivity for oxygenates. Therefore, in the high pressure cascade system, which operates at a system pH of around 6.8 (even lower after saturating with CO₂ at high pressures), this effect will be less defined. Wang et al. investigate the onset potential ranges for CO reduction in 0.1 KOH and the CO₂ reduction in 0.1 KHCO₃ [120]. In this research it is shown that the recorded initial shift in onset potential can be explained by the difference in pH. They continue to demonstrate that CO and CO₂ reduction operate in the same potential range (excluding acetate), when plotted independent of pH. This indicates the reported effect in onset potential shift for a cascade or tandem electrode, could be mainly the result of the high system pH. This is in accordance with the evaluated Tafel plot produced by the high pressure cascade model, shown in figure 5.4b. Here the CO reduction reactions are shown to have similar onset potentials to the CO₂ reduction reactions.

Therefore, from evaluating the modelled results, in combination with the collected data from other research, there is no reason to assume a large change in onset potential as a direct effect of the high pressure cascade system. To determine what onset potential ranges are interesting for a high selectivity for C₂₊ products, figure 5.9 can be reviewed.

This chapter was dedicated to investigating the effects of pressure on the cascade system. As mentioned in the introduction section, the combination of both high pressures and the cascade system is essential, as systems separately – although showing promising results – are not sufficiently efficient to be commercially interesting. Therefore, the preceding chapter has focused on indicating the combined effect of both technologies. Section 5.1.1 has demonstrated the reaction rate can be enhanced as the result of the combined effect of the cascade and the high pressure on the solubilities of the reactants. Section 5.1.2 subsequently shows a number of different ways to increase the selectivity for a single product, for which the effects are largely incorporated in the model. These consist of tuning the conditions for a specific reactant type which shows the desired behaviour (as displayed in figure 5.8). Additionally, the model demonstrates that the selectivity for this system can be tuned by applying a certain pH level, pressure or potential, eventually evaluating an optimal range for selectively producing C₂₊ products. Consequently, the model results imply the overall system efficiency largely benefits from the combination of high pressure and cascade operation.

Conclusion & Recommendations

6.1. Conclusion

At the start of this research, the conducted literature study has indicated that within the electricity driven conversion methods, electrocatalysis is the closest to commercialisation. However, in order to achieve this, the system efficiency needs to be increased in terms of reaction rate, onset potential and selectivity.

This research was based on the premise that a combination of a cascade electrode system and high operating pressures, can effectively increase the efficiency of these three aspects. The main objective for this research was, therefore, to answer the following main research question.

How can high pressure influence the efficiency (reaction rate, selectivity and onset potential) towards C_{2+} products in a cascade system?

This was approached by first identifying the possible effects of the combined system, based on published information in literature regarding these separate technologies and extrapolating this knowledge to fit the combined system. This was executed in order to determine the structure and allowable assumptions for the mathematical model, in order to accurately describe the main effects of the system as proposed by literature. Afterwards, the modelled results were evaluated and analysed based on these same principles. This resulted in a definite overview regarding the interesting phenomena taking place in the high pressure cascade system, and their relation to the operating conditions. After indicating the potential for this new combined system with the newfound modelled results and insights, it can be validated further by means of experimental research, as this study also includes a design study, resulting in an intricate preliminary design for a high pressure cascade reactor. The novel reactor set-up and the insights gained regarding this new system, combine all the conditions necessary to enable a further detailed study into this promising new research direction.

To identify the most important research conclusions, the following section will provide concluding statements regarding the predetermined research questions.

What is the effect of pressure on each individual electrochemical step (CO_2 to CO and CO to C_{2+} products)?

In order to determine the effects of pressure on the cascade electrode system, both reduction steps were evaluated separately. Evaluating this by use of the model, shows that the pressure drastically increases the CO_2 solubility. This high reactant concentration at the first electrode, results in a high CO production. At sufficient flow-rates or small mutual catalyst distances, this leads to a non equilibrium state of dissolved CO close to the electrode surfaces. This creates a high reactant concentration, consisting of the produced CO and leftover CO_2 at the second sequential electrode surface, which results in an increased reaction rate and selectivity for C_{2+} products for the second reduction step. The model

indicates that the CO solubility, which is generally really low, will benefit more from the combined system, than from both technologies separately.

How can the selectivity towards specific C_{2+} products be controlled by regulating the CO_2/CO ratio in the feed of the high pressure cascade reactor?

To provide an indication of the operating conditions which will ensure a high selectivity for C_{2+} products, the effects of the influence of CO and CO_2 reductions on the product distribution were investigated by use of the model. As the structuring of the model allows for the separate evaluation for the CO and CO_2 reductions, this effect and its consequences and relations can be presented distinctively. This shows that the CO reduction reaction remains active at higher overpotential levels, when the CO_2 reduction reactions suffer from reactant depleting due to the buffer reactions taking place in the electrolyte. At this potential, CO is shown to mainly produce methane, as the surface conditions (low amount of CO^* and a high amount of H^*) favour the methane production. This analysis, along with other produced results showing the selectivity of the system as a function of different operating conditions, has aided in providing a detailed understanding of the selectivity behaviour in the high pressure cascade system. To indicate relevant operating conditions for in-depth experimental research for the creation of data regarding a high selectivity for C_{2+} products, an analysis regarding the optimal applied potential was carried out. This way this potential region was identified to be in-between the low overpotential region, where generally formate and hydrogen production dominate, and the high overpotential region, where the (not mass transport limited) hydrogen production dominates. This section was identified to be around $E=-1.2$ vs. Ag/AgCl. Interestingly this range does not drastically change with pressure, which leads to the conclusion that the potential for optimal C_{2+} products selectivity and high reduction rates, was evaluated to be around $E=-1.2$ vs. Ag/AgCl for the high pressure cascade combination. In experimental research, control on the CO and CO_2 ratio can be instated by tuning the flow-rate and electrode sizes to match the conditions predicted by the model, in order to create even more optimal configurations. However, as a consequence of the assumption made regarding the transport between the first and second electrode, this effect cannot be simulated by the model at this moment in time.

How do the modelled results regarding the high pressure cascade electrochemical reduction relate to the literature and the experimental results?

To determine the accuracy of the high pressure cascade model and to indicate its reliability, the model was validated with experimental results. As no experiments had been conducted yet regarding the combination of the increased pressures and the cascade system, the model could not directly be verified by way of experimental data. Therefore, the three separate reduction reactions were modelled as separate systems, and evaluated with separate experimental research describing these systems. To make an estimation of the accuracy of the model, the operating conditions of the papers were added to the model; this way, an exact match between the modelled and experimental results will indicate the validity of the modelled results. This analysis has demonstrated the model's approach and adopted assumptions do indeed result in accurate representations of reality for straightforward systems with comprehensible high quality kinetic data. In rather complex processes, deviations from the experimental results do occur. For example the data regarding the reduction of CO_2 on copper, which has proven to be difficult to model, as the system is complex, fast changing and the provided kinetic data does not present a high enough quality (amount of data points). This results in a deviation from the experimental results in some sections of the process (mainly low overpotentials). Therefore, the model is, for now, limited to investigating outside of these identified regions. This underlines the demand for good experimental studies regarding this subject and therefore the need for the novel high pressure cascade reactor.

How to design an adaptable electrochemical cell capable of safely executing multiple experiments with the option for high pressures and cascade electrocatalysis?

In order to produce more relevant results regarding this new technology combination, a design for a new reactor design was researched and developed. The design process was based on determining the required system criteria, which formed the basis for the design. Hereafter, based on the desired

operating conditions, a set of design parameters was defined, in order to verify the proper operation of the designed system. Based on these conditions, a design was developed where both cathodes are placed in a flexible holder and fitted into the reaction chamber, so the electrodes will be located closely to the flow, in order to increase the conversion properties. Apart from that, the cathodes had to be electrically connected separately, so they can be controlled separately. This was realised by a combination of small bolts and nuts connecting the electrode surfaces to mechanically engineered rods, to which an electrical source can be attached. One of the design considerations is to make the design as simple and adaptable as possible; this was realised by using as many readily available parts as possible. Eventually the body was machined by the author at the university workshop, to save valuable time. However, advanced 3D printing companies could be considered as an alternative solution. The reactor design was validated by a series of experimental tests, conducted in the laboratory at the university. These tests indicated the reactor can operate at pressures up to 35 bar, is easy to construct/adopt and the separate electrical connections have shown to work without issue. Therefore, the resulting design is deemed suitable for a multitude of high pressure cascade experiments.

Overall, the developed model and reactor design, have both led to promising results regarding the new high pressure cascade system. Combining these technologies in this research has proven relevant, as the model provides essential insights required for experimental research. In addition, the designed reactor can validate the model, while also providing relevant input data to improve its accuracy in the future. The combination of both technologies will aid in the interpretation of results, as a model is a means to connect physical occurrences taking place to the known theoretical concepts.

Consequently, this research indicates the combined benefits on the system efficiency in terms of reaction rate, selectivity and onset potential regarding the production of C_{2+} products of the applied pressure to the cascade system. The mathematical model in this research shows the high potential for this technology. Simultaneously, this research has provided the means to continue the research in this promising new direction, by the creation of the reactor design. This way, it contributes to the overall objective for the commercialisation of electrocatalysis.

6.2. Recommendations

6.2.1. General

As described in the introduction section, the other possible research directions for increasing the system efficiency entail, for example, catalyst development. Since a lot of research is already dedicated to finding better catalysts and electrode surface structures, for this research it was decided to place the focus on tuning the operating conditions in order to increase the overall system efficiency, rather than instigating catalyst types. Therefore, the proposed system in this research applies normal planar Ag and Cu electrodes. However, the advantages of deploying better catalysts or more efficient electrode configurations, could also increase the properties of the high pressure cascade system. After the full experimental quantification of the effects of the high pressure cascade system, additional research can be directed at combining the system with other ways for increasing the efficiency, such as better catalysts or GDEs.

6.2.2. The model

As explained in the 'Assumptions and limitations' section, the diffusion layer length is assumed to be constant with operating conditions in this research. In reality, this is not the case, as it is affected by bubbles and operating conditions in the cell. Therefore, to provide a more accurate representation, the diffusion layer thickness needs to be determined as a function of the operating parameters, so it can vary with the current density. In addition, to include the effect of bubbles, Burdyny et al. propose to use the following formula, which describes the thickness of the diffusion layer in a 1-D planar system [18]:

$$\delta_i = \frac{D_i}{k_m} \quad (6.1)$$

Here, D_i denotes the diffusion coefficient and k_m the mass transfer coefficient. In our case the mass transfer is largely determined by convection. Burdyny et al. propose to also include the momentum induced by the gas bubbles at the surface. This results in the following expression for k_m , where the convective contribution is approximated with a relation between dimensionless numbers describing the different flow contributions, as represented in equation 6.3.

$$k_m = k_{\text{conv}} + k_{\text{bubble}} \quad (6.2)$$

$$k_{\text{conv}} = \frac{\overline{Sh}D_i}{L} = \frac{0.664D_i}{L} \text{Re}_L^{0.5} \text{Sc}^{0.333} \quad (6.3)$$

Applying this relation in the model, might result in a more accurate representation of the diffusion layer length.

To investigate the effect of the sequential electrode position, as opposed to a tandem system, for the modelling it is assumed the flow rate in the system is high enough for the convective term to dominate over the diffusion term. This effectively means the assumption is made there is no gap between the electrodes. This also imposes a limitation regarding the investigation of the effect of changing the electrode distance. Rather than assuming a zero gap, the model could be improved by modelling the transport in the gap section. Section 4.3 described the development of the flow profile at the reactor wall, and the diffusion layer section. An iterating approach would be to model the transport in the gap section, for example, based on the flow profile shown in figure 4.3c. Modelling the effect this way would allow for analysing the effect of controlling the electrode distance.

One of the most impactful simplifications made in the modelling regards the assumption for constant Tafel slopes. This has resulted in a lot of deviations in the modelling results in the lower overpotential region. A proposed solution for this problem could be to add all the different slope data to the model, and call the slopes per overpotential section. However, in this case the assumption is made that the change in slope is not dependent on the system or the operating conditions. In reality, this would also provide questionable results. In addition, the previous section has described the slope behaviour for CH_4 is not only potential dependent, it is also pH dependent. Besides, the slope's dependence on the pressure of the reactant (CO) also depends on the pH in the system. Therefore, this slope behaviour becomes too complicated to accurately describe, as this will result in many different pH and potential dependent slope values, for which not even all data will be available, as the CO reduction becomes too mass transfer limited for measurements at low pH. Therefore, the author recommends to add the changing Tafel slopes for the hydrogen evolution reaction, as this has a large impact on the system's selectivity profile at low overpotentials. For the methane slope (and possibly the slope of other desired new products), the best course is to take an average and evaluate how and where this assumption has a large impact on the system, as was done in section 4.5. With this knowledge, valid analysis of modelled results can still be provided.

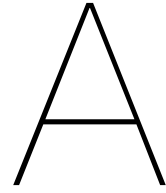
Section 4.3 describes all the required assumptions and simplifications made to find a simplified equation, which can be utilised to describe the system kinetics. One of these simplifications regards the assumption that the kinetic behaviour does not change with pressure, even though section 4.3 has shown this is not accurate. Thus far, to the best of the author's knowledge, literature has not yet provided a more accurate way of describing the kinetics in such a system. However, as it is known this relation will not describe the system as well at different pressures, one might consider approximating k_{app} values in different pressure ranges, to supplement this deviating behaviour.

The literature study has provided a detailed description regarding the solubility behaviours for CO_2 and CO. However, the CO solubility data and its effect on the CO_2 (and other products) was not adopted in this version of the model. It would be interesting to investigate the dissolving effects presenting as a consequence of the changing partial pressures in the system, as described in section 2.1.4. To model this effect, the equation by Dufek et al. can be applied [28]. The required information to solve this

relation is already available in the present model. An interesting analysis would involve the magnitude of this dissolving effect, in addition to its effect on the inflow ratio of CO to CO₂ entering the second reduction step. With this analysis a decision can be made regarding the effect of the assumption to keep the solubilities at 100% independent of the partial pressures.

6.2.3. The design

As explained in chapter 3, the accuracy of the research results depends on the performance (resistance) of the reference electrode. Figure 3.10 has shown the reference electrode applied is not high pressure resistant, as its resistance has been shown to increase after experiments. However, at present there are no suitable high pressure resistant alternative reference electrodes available. Hopefully in the near future this will change, as this could increase the stability in the reference electrode and therefore the future experimental research results.



Theory

A.1. Equilibrium and reaction rate constants

As described in the Theory chapter (section 'Kinetics'), there are different methods to approach the equilibrium (K) and reaction rate constants (k). The following section will elaborate on how these values were determined for the reactions taking place in the 2019 study by Soeteman, as this study was used as a basis for the first step of the model in this research [102].

Constant	Equation (T,p) or constant value	Source
PK_1, K_1	$\ln(K) = a_1 + a_2 * T + a_3/T + a_4/T^2 + a_5 * \log(T) + (a_6/T + a_7/T^2 + a_8/T * \log(T)) * (p - p_s) + (a_9/T + a_{10}/T^2 + a_{11}/T * \log(T) * (p - p_s)^2)$ $K_1 = e^{PK_1}$	[58]
PK_2, K_2	$\ln(K) = a_1 + a_2 * T + a_3/T + a_4/T^2 + a_5 * \log(T) + (a_6/T + a_7/T^2 + a_8/T * \log(T)) * (p - p_s) + (a_9/T + a_{10}/T^2 + a_{11}/T * \log(T) * (p - p_s)^2)$ $K_2 = e^{PK_2}$	[58]
PK_w, K_w	$PK_w = \log K_w = A + B/T + C/T^2 + D/T^3 + (E + F/T + G/T^2) \log \rho_w$ $K_w = e^{PK_w}$	[67]
K_3	K_1/K_w	-
K_4	K_2/K_w	-
k_{1f}	$\ln k = A + BS^{0.5} + D/T + E \ln T$	[50]
k_{1r}	K_{1f}/K_1	-
k_{2f}	value: $5.0 * 10^{10} \text{ Kg mol}^{-1} \text{ s}^{-1}$	[97]
k_{2r}	k_{1f}/K_1	-
k_{3f}	$k_{3f} = Ae^{-E_A/RT}$	[91]
k_{3r}	k_{f3}/K_3	-
k_{4f}	value: $6.0 * 10^9 \text{ Kg mol}^{-1} \text{ s}^{-1}$	[30],[97]
k_{4r}	k_{4f}/K_4	-

Table A.1: Equations used in the 2019 study bij Soeteman for the calculation of the required equilibrium and rate constants [102].

The parameters used in the different equations can be found in the tables below. The corresponding sources are indicated in the captions below the table.

For the calculation of PK_1 and PK_2 the following parameters can be used:

Parameter	Values for: $\ln K_1$	Values for: $\ln K_2$
a1	233.5159304	-151.1815202
a2	0.0	-0.088695577
a3	-11974.38348	-1362.259146
a4	0.0	0.0
a5	-36.50633536	27.79798156
a6	-450.8004597	-295.1448102
a7	21313.18848	13890.15354
a8	67.14256299	44.19625804
a9	83.93915212	32.19993525
a10	-4015.441404	-1644.471261
a11	-12.40187350	-4.736672395

Table A.2: Parameters derived from [58].

For the calculation of PK_w the following parameters can be used:

Parameter	Value
A	-4.098
B	-3245.2 K
C	$2.2362 \times 10^5 K^2$
D	$-3.981 \times 10^7 K^3$
E	13.957
F	-1262.3 K
G	$8.5641 \times 10^5 K^2$

Table A.3: Parameters derived from [67].

For the calculation of k_{1f} the following parameters can be used:

Parameter	Value
A	1246.98
B	0
D	-6.19×10^4
E	-183.0

Table A.4: Parameters derived from [50].

For the calculation of k_{3f} the following parameters can be used:

Parameter	Value
A	$4.2 \times 10^{13} L/(mol \cdot s)$
E_A	55.439 kJ/mol
R	8.314 J/(K * mol)

Table A.5: Parameters derived from [90].

nr.	Reaction	dE/dT [$\cdot 10^{-3}V/K$]	Source
1	$CO_2(aq) + H_2O(l) + 2e^- \rightleftharpoons CO(g) + 2OH^-$	-0.3977	[15]
2	$CO + 5H_2O + 6e^- \rightleftharpoons CH_4(g) + 6OH^-$	-0.7327	$\frac{dE}{dT} = \frac{\Delta S}{nF}$
3	$2CO + 6H_2O + 8e^- \rightleftharpoons C_2H_4(g) + 8OH^-$	-0.8815	$\frac{dE}{dT} = \frac{\Delta S}{nF}$
4	$2CO + 4H_2O + 4e^- \rightleftharpoons CH_3COO^-(aq) + 4OH^-$	-1.4429	$\frac{dE}{dT} = \frac{\Delta S}{nF}$
5	$2CO + 7H_2O + 8e^- \rightleftharpoons C_2H_5OH(aq) + 8OH^-$	-0.1682	$\frac{dE}{dT} = \frac{\Delta S}{nF}$
6	$CO_2 + 6H_2O + 8e^- \rightleftharpoons CH_4(l) + OH^-$	-0.5311	[15]
7	$2CO_2 + 8H_2O + 12e^- \rightleftharpoons C_2H_4(g) + 12OH^-$	-0.7728	$\frac{dE}{dT} = \frac{\Delta S}{nF}$
8	$CO_2 + H_2O + 2e^- \rightleftharpoons HCOO^-(aq) + 12OH^-$	-0.4400	$\frac{dE}{dT} = \frac{\Delta S}{nF}$
9	$2CO_2 + 9H_2O + 12e^- \rightleftharpoons C_2H_5OH + 12OH^-$	-0.8834	$\frac{dE}{dT} = \frac{\Delta S}{nF}$
HER	$2H_2O + 2e^- \rightleftharpoons H_2(g) + 2OH^-$	-0.8360	[15]

Table A.6: The temperature coefficient values utilised in the model and their origin.

B

Design

B.1. Illustrations of the design

The illustrations of the mechanical clamp (heavy pressure rod pusher 6842) and the correction bolt as used in the 2020 high pressure design are shown below.

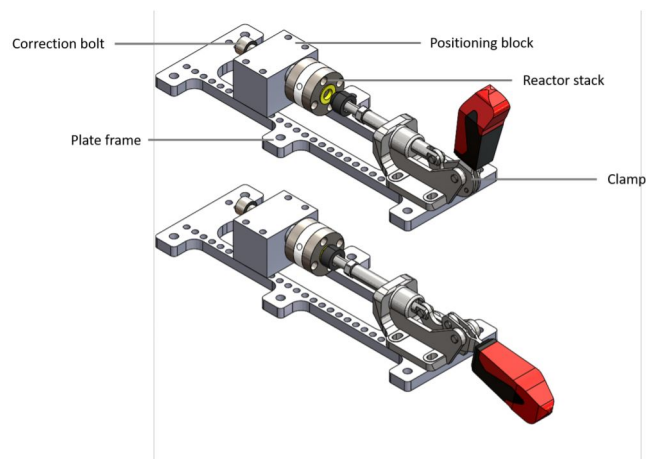


Figure B.1: An illustration of the clamp pressurising the reactor stack. Derived from: [123].

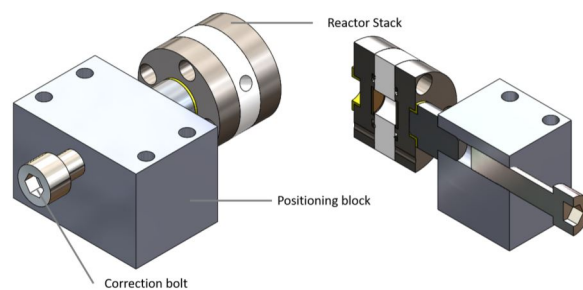


Figure B.2: An illustration of the correction bolt pressurising the reactor stack. Derived from: [123].

A preview showcasing the shape and measurements of the female fittings utilised in the reactor design.

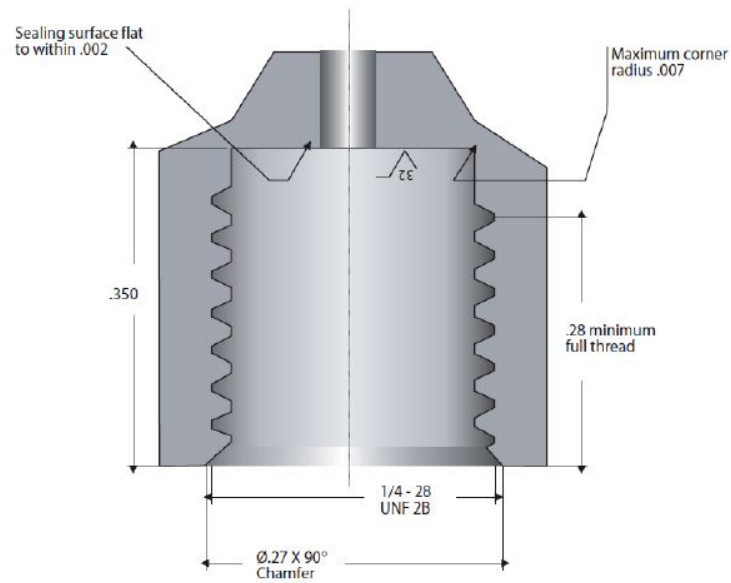


Figure B.3: An illustration of the female fittings used to connect the tubing to the reactor stack. Derived from: [123].

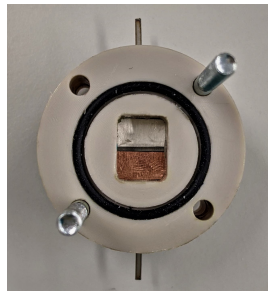


Figure B.4: An illustration of the design being built up with the longitudinal placement bolts.

The following images show the adapted reactor design for the new BASI reference electrode and the reference electrode itself.

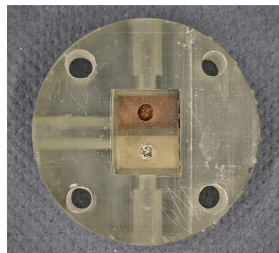
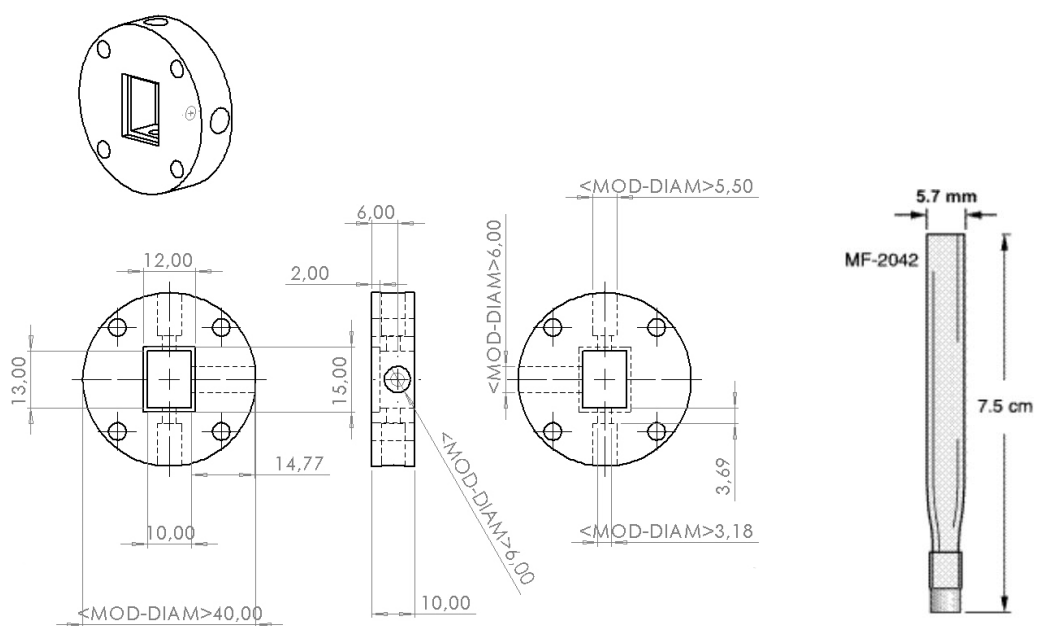


Figure B.5: The 3D printed cathode reaction chamber part, to fit the new BASI reference electrode.



(a) The construction drawing from the adapted cathode reaction chamber for the new BASI reference electrode

(b) BASI reference electrode

B.2. Strength calculations in MATLAB

Listing B.1: Strength calculations

```

1 clear all
2 close all
3
4
5 %% Parameters:
6
7 F = 4000; %N
8 b = 0.015/2; %m
9 a = 0.02-b; %m
10 h = 0.003; %m
11 v = 0.39; %Poisson ratio
12 factor = a/b;
13 k = 0.105+((factor-1.25)/(1.5-1.25))*(0.259-0.105);
14 k1 = 0.00199+((factor-1.25)/(1.5-1.25))*(0.0139-0.00199);
15 E_p = 3850*10^6; %Pa, young's modulus PEEK
16 E_s = 215*10^9; %Pa, young's modulus steel
17
18 Pi = 100*10^5; %Pa
19 Po = 1*10^5; %Pa
20 Pc = F/(pi*0.02^2); %N/m^2 Pressue axial from clamp
21 ri = 0.0075; %m
22 ro = 0.02; %m
23 r = ri:0.0001:ro; %m, radius
24 q = F/(Pi*0.02^2-Pi*b^2); %N/m^2, load
25 Sig_y = 65*10^6; %Pa, minimal yield strength PEEK
26
27 %% Stress originating from clamp force:
28
29 w_max = k1*q*a^4/(E_p*h^3); %m
30 Sig_max = k*q*a^2/(h^2); %Pa
31
32 %% Stress inside the reaction chamber:
33
34 Sig_z = (Pi*ri^2-Pc*ro^2)/(ro^2-ri^2); %Pa
35 Sig_r = (Pi*ri^2-Po*ro^2)/(ro^2-ri^2)-((Pi-Po)*(ri^2*ro^2))./(r.^2*(ro^2-ri^2)); %Pa
36 Sig_circ = (Pi*ri^2-Po*ro^2)/(ro^2-ri^2)+((Pi-Po)*(ri^2*ro^2))./(r.^2*(ro^2-ri^2)); %Pa
37
38 SCF = (4*(a/b)^2+1)/((a/b)^2+1); %Ratio max stress and sig_circ at hole
39 Sig_hole = SCF*(Pi*ri^2-Po*ro^2)/(ro^2-ri^2)+((Pi-Po)*(ri^2*ro^2))./(r.^2*(ro^2-ri^2)); %Pa, local stress around the holes (inflow/outflow)
40
41 %%Von Misses stress criteria:
42 Sig_1 = Sig_circ;
43 Sig_2 = Sig_r;
44 Sig_3 = Sig_z;
45 Sig_v = sqrt(0.5*((Sig_1-Sig_2).^2+(Sig_2-Sig_3).^2+(Sig_3-Sig_1).^2));
46 Sig_v_hole = sqrt(0.5*((Sig_hole-Sig_2).^2+(Sig_2-Sig_3).^2+(Sig_3-Sig_hole).^2));
47
48 %%Figures: stress throughout cylinder:
49 figure

```

```

50 xlabel('Radius [m]')
51 ylabel('Stress [Pa]')
52 yline(Sig_z, 'm');
53 hold on
54 plot(r, Sig_r, 'b')
55 hold on
56 plot(r, Sig_circ, 'r')
57 hold on
58 plot(r, Sig_v)
59 hold on
60 %plot(r, Sig_v_hole)
61 hold on
62 %yline(Sig_y);
63 legend('Axial stress', 'Radial stress', 'Cirumferential stress', 'Von Mises
        Yield criterion')

```

B.3. Construction drawings

This section will showcase the different construction drawings for the production of the reactor stack. The measurements for each part are included in the drawings.

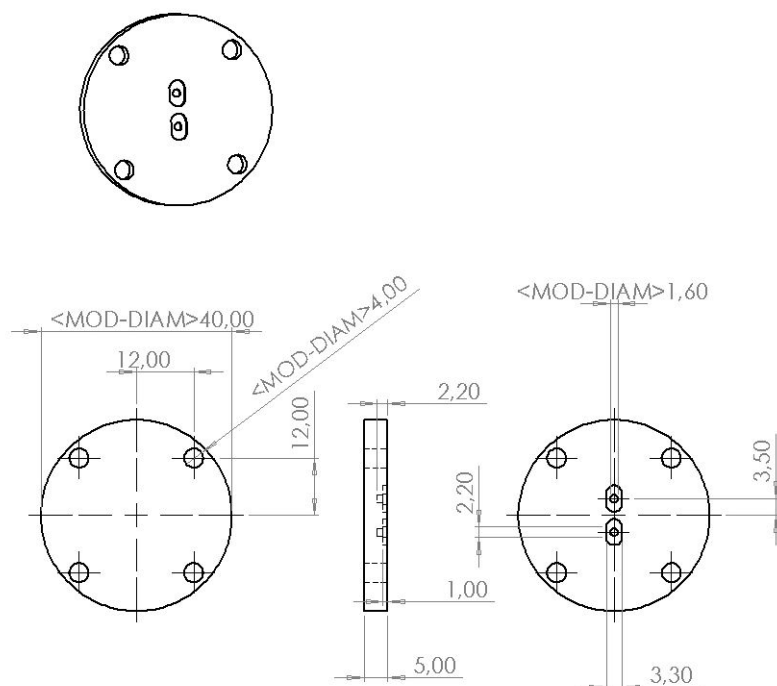


Figure B.6: The construction drawing featuring the back cathode endplate.

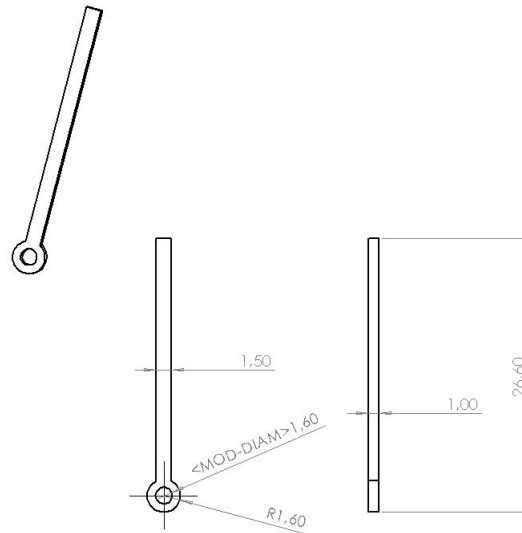


Figure B.7: The construction drawing featuring the connection rod.

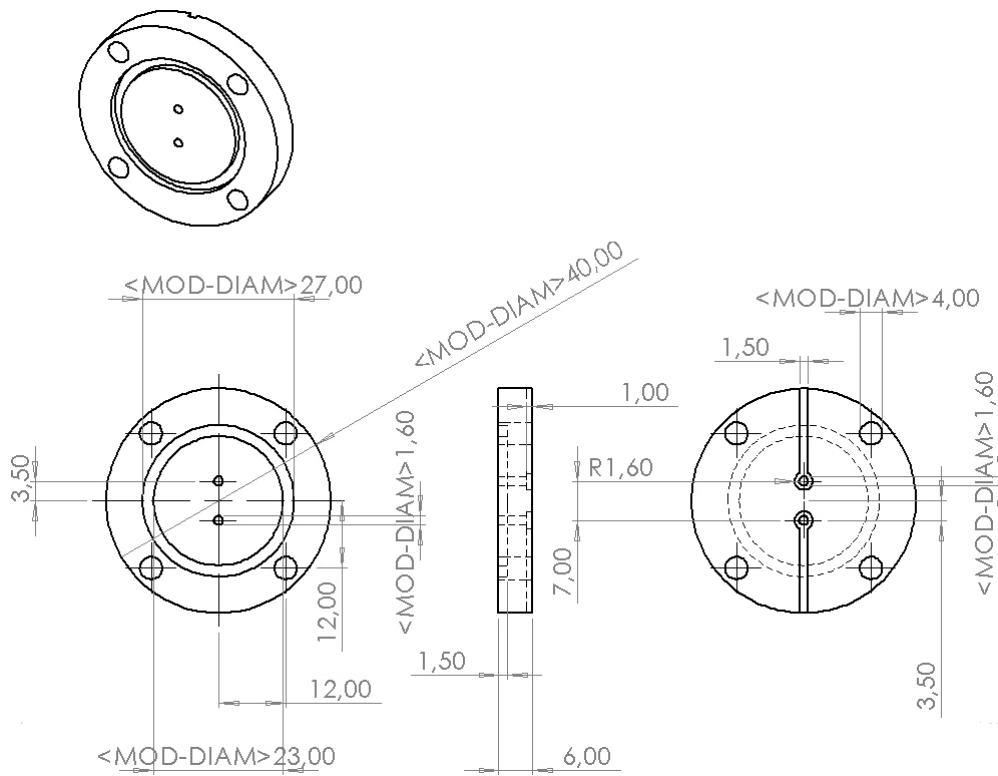


Figure B.8: The construction drawing featuring the cathode front endplate.

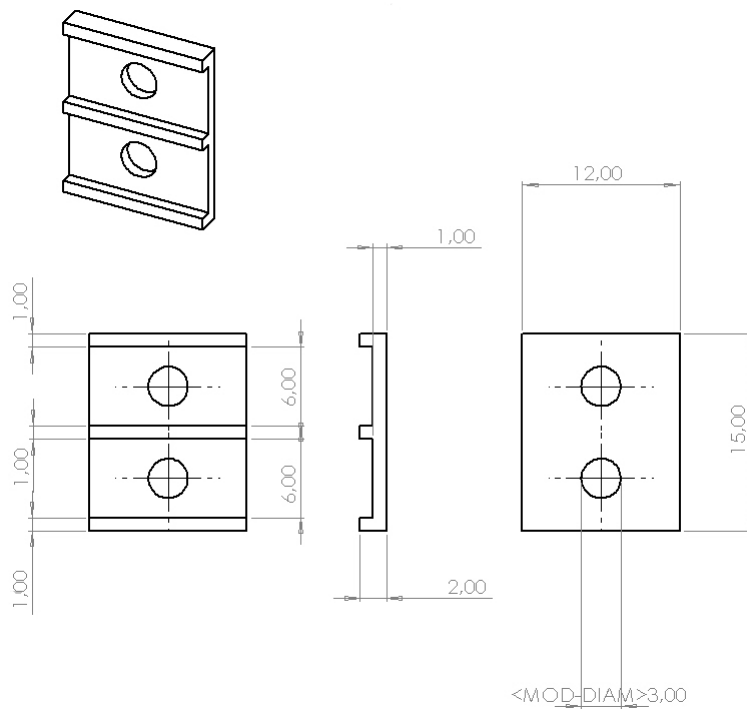


Figure B.9: The construction drawing featuring the electrode holder.

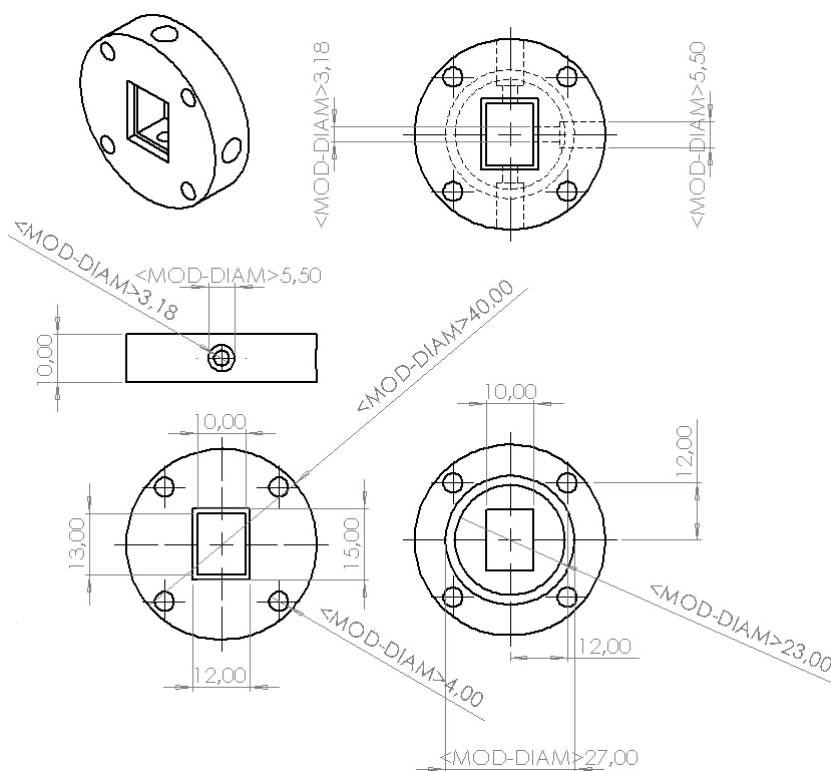


Figure B.10: The construction drawing featuring the cathode reaction chamber.

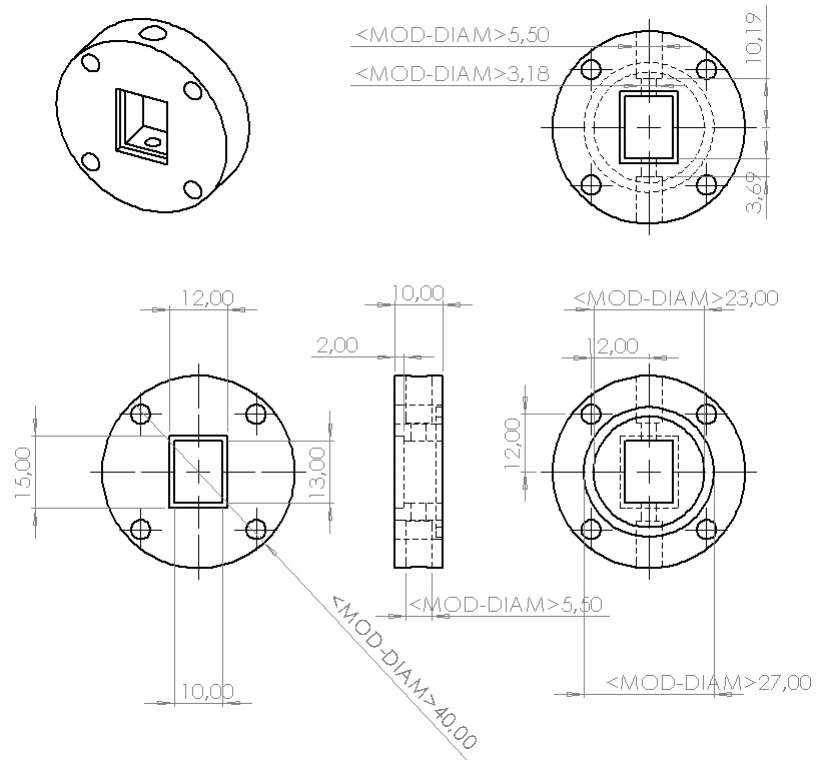


Figure B.11: The construction drawing featuring the anode reaction chamber.

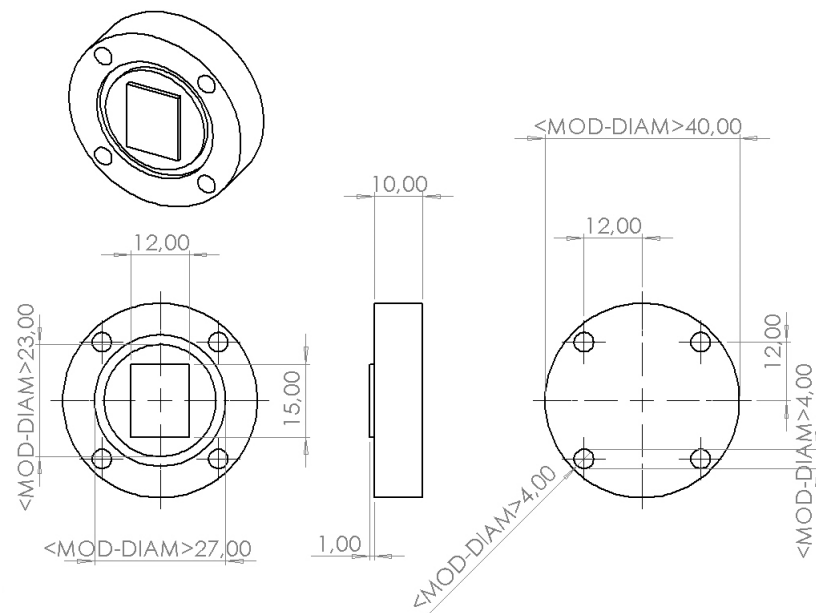


Figure B.12: The construction drawing featuring the conductive endplate

B.4. Production

B.4.1. 3D printing

To make a 3D printed part from a SolidWorks model, the model first has to be converted into Standard Tessellation Language (.STL). This signifies that the 3D model surface needs to be dissected into a set of triangles, making up a polyhedron shape. The reason for this is, that it needs to be translated into a shape that can be made from a series of 2D consecutive layers, as this is how a 3D printer will construct a part. The printers used in the construction of the electrode holder, are Formlabs printers. An example of the result can be found in figure B.13a and figure B.13c.

B.4.2. Laser cutting

To produce the designed stainless steel connection rods, a (1 mm thick) steel plate needs to be laser-cut. In order for this to happen, the modelled part in SolidWorks, need to be transferred into Drawing eXchange Format (.DXF). This transforms the 3D modelled part into a 2D drawing, so it can be cut out from the plate in this exact shape. The construction drawing for the connector rods can be found in appendix B.3. The resulting parts are displayed below, in figure B.13a and figure B.13b.

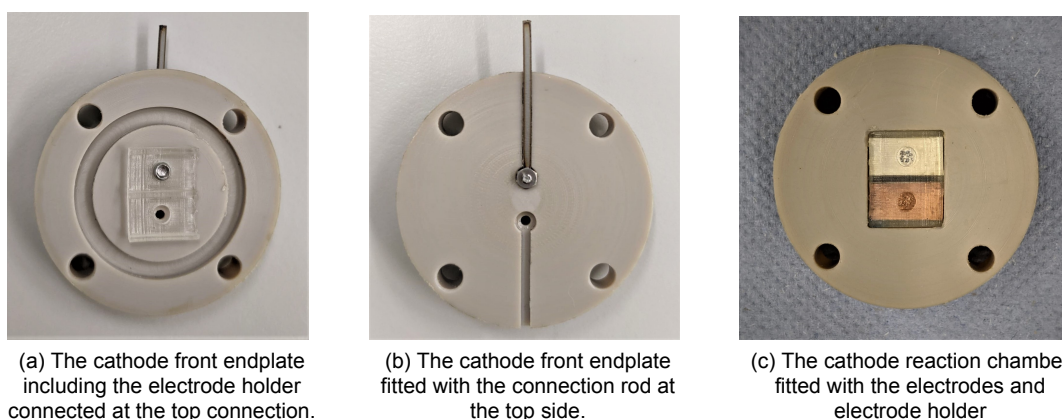


Figure B.13: Images of the produced parts of the reactor stack including the lasercut and 3D printed parts.

B.4.3. Machining processes

To produce the reactor stack parts as, such as, the reaction chambers and endplates, different machining processes are required. These machining processes are carried out at the university workshop. All parts are manufactured from a 40 mm diameter PEEK or a 40 mm diameter stainless steel rod. The machine components discussed below are indicated with numbers in figure B.14a and figure B.14b. Tables indicating the milling or lathing speeds based on the work-piece material can be found in the book by Virasaks (n.d) [117].

Lathing

To produce the cylindrical slabs from the long rods, a lathe, or turning, machine can be used. This machine rotates the work-piece in axial direction, while a cutting tool is operated to remove the undesired material. For the lathe the work-piece is stagnant, it only rotates, while the cutting tool can be actuated to move in three directions, the x, the y and the z axis. Before cutting, the work-piece needs to be aligned with the cutting tool, to be able to determine the positioning and how much material to cut away later. Aligning can be done by moving the cutting tool over its axis, by turning the corresponding turning levers and keeping track of the movement on the lever dials or a digital readout, if the machine is included with one. To initialise the axis in the centre, the cutting tool must be aligned properly after being placed and secured in the lathe tool holder (number 2). This can be executed by referencing

the position of the tip of the tool to the centre of the tailstock, a peaked centring tool, which should exactly meet the tip of the tool with the peaked end (number 3). This process is further illustrated in Virasaks book explaining manufacturing processes [117]. After initialising, the turning levers can be used to move the cutting tool and the digital readout (or lever dials) can be used to keep track of the positioning over the axis while removing material. A schematic representation of the milling machine is illustrated in figure B.14a.

The first step in the production of the cylindrical slabs is to cut the rod into smaller parts of roughly the sizes of the slabs. For this operation a parting tool bit, or, cutoff tool bit, can be utilised. This tool consists of a square cutting edge, which is to be inserted into the work-piece from the side, so small pieces can be cut off when the work-piece is rotated [7]. This operation is not as precise as often desired, therefore, a certain clearance on both sides must be accounted for. The execution of this process is illustrated in figure 3.7a. The next step in the process, is to remove this extra clearance material with more precise tools. This is done by separately securing the cylindrical slabs in the lathe, after which a facing tool can be used to remove the access material. After this operation is carried out successfully the general shapes of the cylindrical slabs are produced and ready for the next operation.

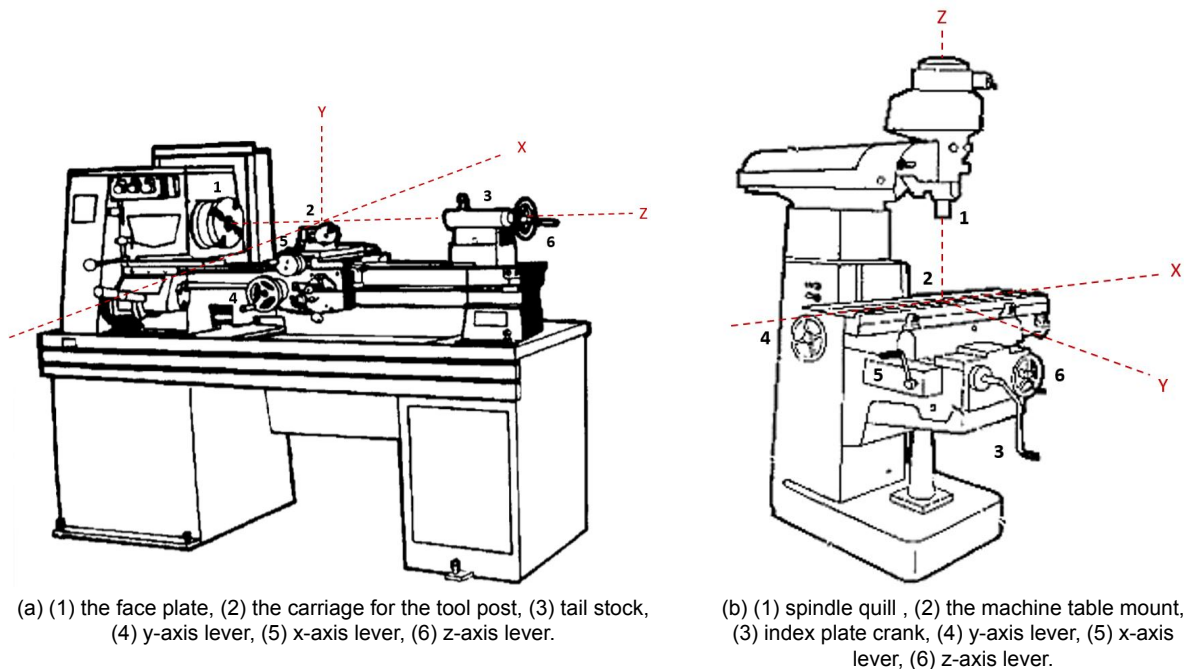


Figure B.14: Schematic representation of a: (a). lathe, (b). milling machine. The axis are indicated in red in the figure. Original image derived from [7]

Milling

The next step in the production of the stack parts is the construction of the holes, slots, grooves and cutouts. For these operations a milling machine can be deployed. As opposed to the lathe, with milling, the work-piece is stagnant, while the spindle rotates. Milling machines are very versatile machines. The work-piece is anchored to a table, which has the option to not only move over the x-axis, y-axis, or z-axis, but also to turn and rotate. Therefore, in addition to planar grooves and holes, this machine can also, for example, produce round grooves or tilted cutouts. The x, y and z motion is initiated by the accompanying levers for each axis, and can be monitored on the lever dials or a digital readout machine. To turn the table, to expose the sides of the work-piece to the spindle, a crank is situated at the side of the machine. To rotate the table, so circular grooves can be made in the work-piece face, the index plate crank can be rotated (number 3). To keep track of the degrees of rotation, a sector at the plate indicates the rotation. A schematic representation of the milling machine is illustrated in figure B.14 b.

In this case, the work-piece will be mounted parallel to the milling machine table. For the initial operations for producing the reactor stack, the table will remain in horizontal position, while only the x-, y- and z-axis will be adjusted in order to remove material. Before cutting, the machine needs to be initialised to properly align the axis with the centre of the work-piece. This process has various approaches, of which only one will be described in detail. To find the true centre of the work-piece, a centring microscope can be inserted into the quill. This tool allows the user to accurately locate the edges or contours of the work-piece [110]. With this knowledge and some simple calculation, the centre of the product can be determined and instated in the digital readout machine (see appendix figure B.16).

After initialising, the next step is to make a plan for the milling operation and to write it out on the construction drawing. This entails deciding what size cutter to use, deciding the cutting path and writing out the accompanying points on the axis. The milling cutter choice needs to be based on the type of material, its size and its shape [7]. Making such a slot too deep with a small diameter cutter, could result in damaging the cutter. However, the softer the material, the lower these chances are. For this reason, all these variables are taken into account when determining a plan of action.

To cut out the reaction chamber and the frame for the electrode holder, for example, multiple traverses will be required, as this hole is quite deep. After cutting out the hole, the frame can be created, requiring a very small cutter size and many careful traverses following the square shape. This process is shown in figure 3.7b. To fashion the grooves into the cathode endplates, shown in figure B.15, several different cutters need to be used. The circular and oval shaped holes can be produced with larger diameter cutters, while the small connection rod grooves require smaller, more precise cutters (figure 3.7a). Manufacturing the grooves for the o-rings, requires the machine table to be rotated. This operation can be performed by rotating the index plate as mentioned above. This operation must be carried out slowly, with a smaller cutter making multiple traverses (figure 3.7b). Adding some oil to the work-piece during the milling would be preferable, so the heat can dissipate, to keep the cutter edges in good shape [7].

Apart from creating the slots, grooves and cutouts, the milling machine is also capable of drilling holes. All cylindrical slabs require four small holes near the edges, so they can be placed around the alignment bolts while assembling. In addition to this, the cathode and anode reaction chambers also require holes for the female fittings in order to connect the tubing in assembly.

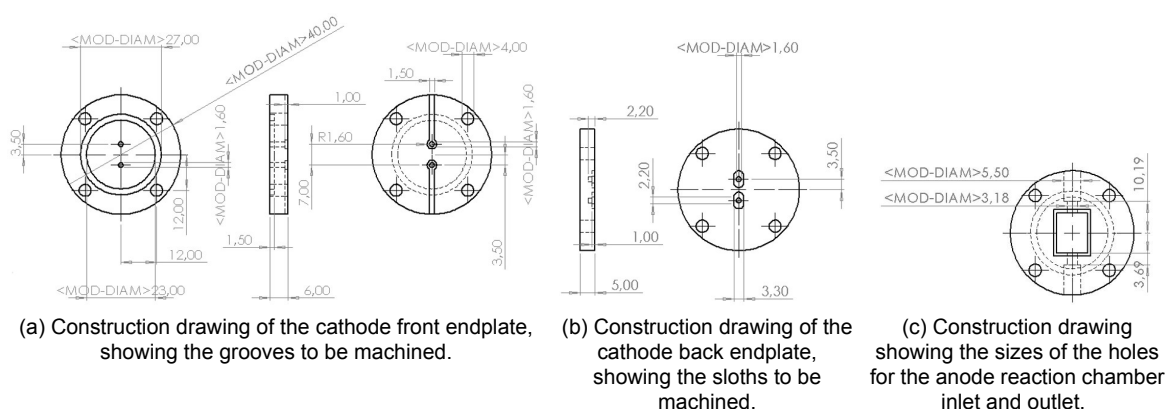


Figure B.15: Construction drawings from the endplates and a reaction chamber.

Drilling

The four small holes (4 mm diameter) at the edges of the slabs, can be produced with the work-piece mounted to the table, parallel to the spindle. To drill, using the milling machine, a drill chuck can be secured into the spindle quill or adapt [7]. The appropriate drill bits can be fastened into the drill chuck and the z-axis can be operated to drive the turning drill into the work-piece. The initialisation of the

centre with the scope, along with the construction drawings, will dictate the location of the holes, to guarantee that all holes in all slabs will align perfectly.

The holes in the reaction chamber are slightly more complex, as the table needs to be rotated into vertical position in order to make them. This process is documented in figure 3.7b. These holes also require a very specific depth and two different diameters as shown in appendix figure B.10. This all needs to be carried out very precise, to make sure the fittings – for the inlet, outlet and reaction chamber – will fit the holes. Therefore, this operation was conducted on the milling machine instead of the regular drilling machine, as the movement is displayed up to 0.001 mm accurately on the digital readout machine.

Tapping

After the holes for the fittings are manufactured, a thread needs to be inserted to enable the fittings to be locked into the holes. To insert a thread into an existing hole, a tapping tool can be used. The tapping tool can be employed manually or it can be inserted into a drilling machine. For this operation the motor of the drilling machine should not be turned on, to avoid breaking taps. Instead, the drilling machine is slowly turned by hand [7]. It is, therefore, mainly used to align the tap with the hole. Figure B.17 in appendix B.5 illustrates this process. To select the proper size tap for the desired thread, drill size charts should be consulted [117].

Of course there are many different ways to produce these parts and to execute the required operations. The procedure described, is the procedure that was followed in the manufacturing of the reactor stack for this project. Other manufacturing methods could, evidently, be applied for this process as well.

B.5. Production supplementary

Some figures to better represent the process of the production of the reactor stack.

B.5.1. Milling machine parts

B.5.2. Design validation set-up and results

The red wire is connected to the working electrode, which could be Ag (right) or Cu (left) in this case. The blue wire is connected to the counter electrode and the white wire is connected to the reference electrode.

The set-up for the reference electrode OCP testing.



Figure B.16: A visual representation of the digital readout machine on the milling machine.

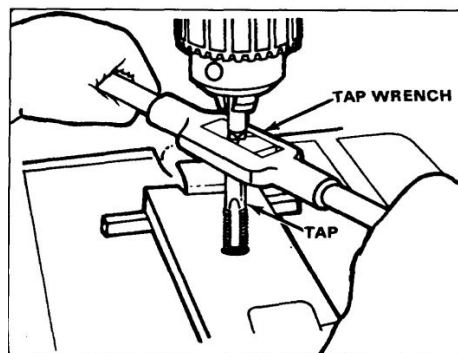


Figure B.17: A visual representation of the process of tapping a thread into a hole. Derived from: [7].

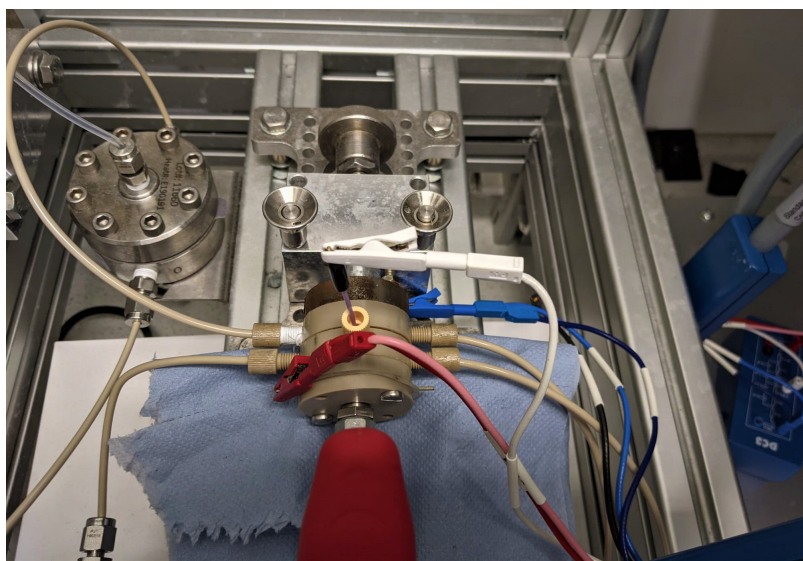


Figure B.18: An illustration of the connection of the stack to the potentiostat.



Figure B.19: An illustration of the connections and set-up of the OCP testing of the reference electrode (right) against the master reference electrode (left).

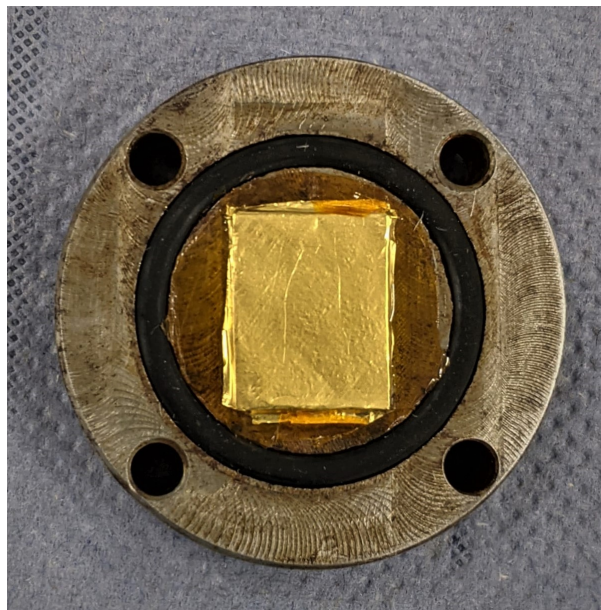
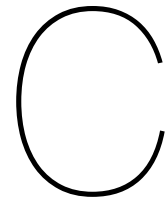


Figure B.20: The gold layer on the protrusion of the steel endplate to prevent corrosion as a result of the connection between the Nickel anode and the steel endplate.



Model

C.1. Classification of PDEs

There are a lot of different types of PDEs. To determine the most suitable solution strategy, the PDE first has to be classified into a certain type. The first distinction to make between PDEs, is the order of the equation. The order of a PDE refers to the order of the highest partial derivative present in the equation [53]. A second important distinction to make is the linearity of the equation. The equation is classified linear, when the function of the unknown variable is stated in linear form [24]. This is the case when the functions consist only of independent variables. A nonlinear PDE can be easily identified by the presence of roots or squares in the equation. Nonlinear equations require different solution strategies than linear problems, therefore, it is important to make this distinction beforehand.

An example of a linear first order PDE [53]:

$$a \frac{\partial u}{\partial x} + b \frac{\partial u}{\partial y} = c \quad (C.1)$$

An example of a nonlinear first order PDE [53]:

$$(x + 3) \frac{\partial u}{\partial x} + xy^2 \frac{\partial u}{\partial y} = u^3 \quad (C.2)$$

Linear second order PDEs, in turn, can be classified into three different types: elliptic, parabolic and hyperbolic. Identifying the type of PDE can provide information on, for example, the smoothness of the solution and suitable solution approaches. To identify the type, the nature of the discriminant of the equation needs to be evaluated.

As example, we use a second-order PDE of standard form [24]:

$$A \frac{\partial^2 u}{\partial x^2} + B \frac{\partial^2 u}{\partial x \partial y} + C \frac{\partial^2 u}{\partial y^2} + D \frac{\partial u}{\partial x} + E \frac{\partial u}{\partial y} + Fu = G \quad (C.3)$$

This can be rewritten in the following way:

$$Ax^2 + Bxy + Cy^2 + Dx + Ey + F = 0 \quad (C.4)$$

In matrix form, this comes down to:

$$\begin{bmatrix} x & y \end{bmatrix} \begin{bmatrix} A & \frac{B}{2} \\ \frac{B}{2} & C \end{bmatrix} \begin{bmatrix} x \\ y \end{bmatrix} + \begin{bmatrix} D & E \end{bmatrix} \begin{bmatrix} x \\ y \end{bmatrix} + F = 0 \quad (C.5)$$

The discriminant, Δ , is defined as the negative determinant of the matrix of the quadratic part of the equation; this results in the following expression:

$$\Delta = B^2 - 4AC \quad (C.6)$$

If the discriminant is found negative, the equation is regarded elliptic. If the discriminant is found to be equal to zero, the equation is regarded parabolic. When the discriminant is found to be positive, the equation is regarded hyperbolic [53] [35]. The solutions of elliptic equations are generally very smooth, although, the level of smoothness is largely determined by the coefficients in the system. Parabolic equations are not only dependent on space, but also include a time derivative, $\frac{\partial u}{\partial t}$. When the transformed time variable increases, the solution is known to smooth out. Lastly, the smoothness of hyperbolic equations is largely determined by the smoothness of the initial/boundary conditions of the system. When there are discontinuities in the boundary conditions, these propagate into the solution of the hyperbolic PDE [89].

The system of PDEs for the model (equation 4.1 to 4.12) can, therefore, be classified as second order linear parabolic partial differential equations. This information will help in determining the best way to solve the system.

C.2. Examples of methods for numerical mathematics

The specifics for solving the points in the mesh depend on the numerical strategy applied. An example of a widely applied strategy is, the finite difference method. In this method the time is divided into a set of discrete points with a set time step, Δt , in between. The space is divided into increments following the same approach. To evaluate for each point in the mesh, an approximation function is set up to calculate the approximate solution for the next point in the mesh, based on the answer for the previous point and the time step. An example of what this function can look like for spacial variable, y , and time, t , is provided below:

$$y_{n+1} = y_n + (t_{n+1} - t_n) * f(t_n, y_n) \quad (\text{C.7})$$

This example is known as the forward Euler method [118]. Demonstrated here, is that the solution, y_{n+1} , depends on the previous solution, y_n , the time step $(t_{n+1} - t_n)$ and the function, f .

As explained above, the problem to solve for the model in this research is a initial/boundary value problem of a set of linear second order PDEs. To approximate the function required to solve the problem, a numerical approximation of the derivatives of the function needs to be set up. With the finite difference method, the numerical approximation is determined as follows. To find the function for a point located a distance h away from known point x_0 , Taylor expansion is utilised [118]:

$$f(x_0 + h) = f(x_0) + \frac{f'(x_0)}{1!} * h + \frac{f''(x_0)}{2!} * h^2 + \frac{f^{(n)}(x_0)}{n!} * h^n \quad (\text{C.8})$$

After dividing and rearranging, this leaves the following expression for the derivative $f'(x_0)$:

$$f'(x_0) = \frac{f(x_0 + h) - f(x_0)}{h} - R_n(x) \quad (\text{C.9})$$

Where R_n indicates the remainder term.

This shows how the function f/f' can be found, using the finite difference method as an example. In addition, the equation also demonstrates, that the smaller the step h , the better the evaluated solution will approximate the actual solution.

C.3. Standard equilibrium potentials

As explained in the chapter 'Literature study', the overpotential is defined as the difference between the theoretical potential the system should have and the actual potential of the system. The value of the overpotential is essential for determining the current density, as illustrated in equation 2.11. To determine the overpotential, first the theoretical potential will need to be determined. It's value originates from three important variables: the reaction equation, the temperature and the pH of the system.

Additionally, the standard potential (i.e. theoretical potential), E^0 , is referenced against a certain scale. The initial E^0 values used as input for the model are either referenced to SHE (Standard Hydrogen Electrode) or against RHE (Reversible Hydrogen Electrode) scale. The SHE scale assumes the E^0 for hydrogen to be zero volts at all temperatures and pH. This is then used as a reference for standard potentials of other reactions. E^0 values on the RHE scale, on the other hand, do change with changing pH and temperature. Therefore, it is important to incorporate the potential temperature and pH deviations when referencing to RHE scale.

C.3.1. Convert between scales

When the standard electrode potentials are referenced against a different scale, it is necessary to convert them.

The SHE scale is determined by placing a Pt electrode in an aqueous solution, where H_2 gas and H^+ protons are supplied at a fugacity of 1.00 bar with an activity of 1.00 [49]. In this case the hydrogen reference electrode used represents the SHE. However, when these values deviate from standard, in other words, if the fugacity and activity are not equal to one, the hydrogen reference electrode represents the RHE [49]. For the RHE, the concentration of hydrogen ions resembles that of the electrolyte concentration employed. Where the SHE has a constant value for all temperatures and pH, the potential against RHE varies with changing the pH or temperature of the system. This principle is shown in figure C.1.

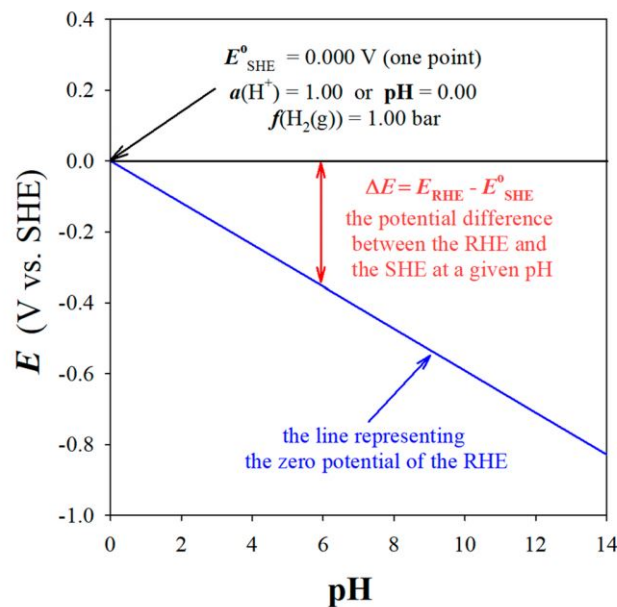


Figure C.1: Showing the difference between the SHE and RHE scales over different system pH for a temperature of 298 K. Derived from [49].

At a temperature of $25^\circ C$ the factor RT/F in the Nernst equation shown in equation C.10, will be approximately 0.0592. This corresponds to the slope of the graph in figure C.1, identifying the decrease in potential E per unit pH.

$$E = E_0 - \frac{RT}{nF} \ln Q \quad (C.10)$$

Where:

- $Q = K$, (i.e. equilibrium constant) in equilibrium conditions

- $Q = a_{red}/a_{ox}$, when not in equilibrium, where a denotes the activity
- $Q = C_{red}/C_{ox}$, for low concentrations, since the activity often approaches unity in this case

Hence, to convert from SHE to RHE scale the following formula can be used [16]:

$$E_{RHE} = E_{SHE} + 0.0592 * pH \quad (C.11)$$

The E^0 values applied in the model are converted to the RHE scale, using equation C.11.

There are tables available displaying the standard E^0 values for reactions at standard conditions, $T = 298.15$ K and $pH = 7$ for SHE and RHE scale. However, since the reactions taking place often deviate from these standard conditions, corrections factors need to be included on top of the standard E^0 values.

C.3.2. Temperature correction factor

A temperature variation, will cause the E^0 values to deviate from standard (i.e. 298 K). In this case a correction factor for this temperature deviation needs to be implemented. Equation C.12, describes the effect of a temperature deviation on the standard electrode potential [15].

$$E_T^0 = E_{298}^0 + (T - 298.15) \cdot \left(\frac{dE^0}{dT} \right)_{298} \quad (C.12)$$

Where, E_T^0 denotes the standard potential at the non-standard temperature, E_{298}^0 denotes the standard potential at standard temperature, T denotes the temperature and dE^0/dT denotes the temperature coefficient expressed in mV/K .

In this equation, the assumption is made that E^0 is a linear function of temperature. Some temperature coefficient values are listed in the 1989 research by Bratsch [15]. The values for the remaining reactions need to be calculated. Table ?? portrays the temperature coefficient values used in this research and their origin.

nr.	Reaction	dE/dT [$\cdot 10^{-3}V/K$]	Source
1	$CO_2(aq) + H_2O(l) + 2e^- \rightleftharpoons CO(g) + 2OH^-$	-0.3977	[15]
2	$CO + 5H_2O + 6e^- \rightleftharpoons CH_4(g) + 6OH^-$	-0.7327	$\frac{dE}{dT} = \frac{\Delta S}{nF}$
3	$2CO + 6H_2O + 8e^- \rightleftharpoons C_2H_4(g) + 8OH^-$	-0.8815	$\frac{dE}{dT} = \frac{\Delta S}{nF}$
4	$2CO + 4H_2O + 4e^- \rightleftharpoons CH_3COO^-(aq) + 4OH^-$	-1.4429	$\frac{dE}{dT} = \frac{\Delta S}{nF}$
5	$2CO + 7H_2O + 8e^- \rightleftharpoons C_2H_5OH(aq) + 8OH^-$	-0.1682	$\frac{dE}{dT} = \frac{\Delta S}{nF}$
6	$CO_2 + 6H_2O + 8e^- \rightleftharpoons CH_4(l) + OH^-$	-0.5311	[15]
7	$2CO_2 + 8H_2O + 12e^- \rightleftharpoons C_2H_4(g) + 12OH^-$	-0.7728	$\frac{dE}{dT} = \frac{\Delta S}{nF}$
8	$CO_2 + H_2O + 2e^- \rightleftharpoons HCOO^-(aq) + 12OH^-$	-0.4400	$\frac{dE}{dT} = \frac{\Delta S}{nF}$
9	$2CO_2 + 9H_2O + 12e^- \rightleftharpoons C_2H_5OH + 12OH^-$	-0.8834	$\frac{dE}{dT} = \frac{\Delta S}{nF}$
HER	$2H_2O + 2e^- \rightleftharpoons H_2(g) + 2OH^-$	-0.8360	[15]

To calculate the temperature coefficients, we again look at equation 2.24, relating the Gibbs free energy to the standard potential. After rearranging, we get the standard potential as a function of the Gibbs free energy, as illustrated below:

$$E_0 = -\frac{\Delta G}{nF} \quad (C.13)$$

For a constant pressure, the Gibbs free energy can be expressed in terms of: enthalpy, H , entropy, S , and temperature, T . This relation is portrayed in the following expression:

$$(G)_p = H - TS \quad (\text{C.14})$$

The change in Gibbs free energy, dG , or, ΔG , can therefore be expressed in the following way:

$$(dG)_p = dH - d(T \cdot S) \quad (\text{C.15})$$

Where dH can be substituted for:

$$dH = TdS + Vdp \quad (\text{C.16})$$

As a constant pressure was assumed, the term Vdp will be neglected, leaving us with the following equation:

$$dG = TdS - SdT - TdS = -SdT \quad (\text{C.17})$$

After inserting this result into the equation relating the standard potential to the Gibbs free energy, the equation for the temperature coefficients becomes:

$$\left(\frac{dE^\circ}{dT}\right)_p = -\frac{d}{dT} \left(-\frac{SdT}{nF}\right) = \frac{dS}{nF} = \frac{\Delta S}{nF} \quad (\text{C.18})$$

The change in entropy can be expressed as the sum of the entropy of the products subtracted by the sum of the entropy of the reactants, as shown below:

$$\Delta S^\circ = S^\circ_{products} - S^\circ_{reactants} \quad (\text{C.19})$$

Note that in this calculation the stoichiometric factors of the products and reactants need to be taken into account. An example of this procedure is provided in the supplementary info of the 2019 research by Nitopi et al. [76]. Entropy values for the reactants and products involved were extracted from this research and the Table of thermodynamic values published by the University of Wisconsin-Madison [20]. Table C.1 presents the species, accompanying entropy values and their sources.

Species	Formula	$S^\circ [JK^{-1}mol^{-1}]$	Source
Hydrogen	H_2	130.7	[76]
Water	H_2O	70.0	[76]
Hydroxide	OH^-	-10.54	[20]
Carbon Dioxide	CO_2	213.8	[76]
Carbon Monoxide	CO	197.7	[76]
Formate	$HCOO^-$	21.9	[95]
Methane	CH_4	186.7	[76]
Ethanol	C_2H_5OH	160.7	[20]
Ethylene	C_2H_4	219.3	[76]
Acetate	CH_3COO^-	282.8	[76]

Table C.1: Listed entropy values for the species involved in the reactions taking place.

C.3.3. pH correction factor

As the pH of the system increases, the activity, and therefore the E, will decrease [49]. Consequently, the pH deviation from standard has a large impact on the potential.

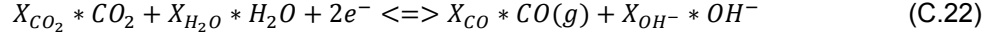
As explained in the theory chapter, the equilibrium constant K can be calculated from the concentrations of the reactants and products. The electrochemical reactions taking place at the surface all produce OH^- , therefore, the concentration of OH^- is an important factor in determining the equilibrium constants. The concentration OH^- is related to the pH of the system, according to:

$$pH = -\log [H^+] = 14 + \log [OH^-] \quad (\text{C.20})$$

The Nernst equation, displayed above in equation C.10, illustrates how the potential depends on the logarithm of the equilibrium constant. In equilibrium, the system potential is zero, as the $E_{oxidation}$ is equal to $E_{reduction}$ in this case. Therefore, the Nernst equation in this instance, simplifies to the following equation:

$$E_{pH}^0 = \frac{RT}{nF} \ln K = \frac{2.303RT}{nF} \log_{10} K \quad (C.21)$$

An example of how the equilibrium constant can be calculated is provided below. This illustrates the dependence of the equilibrium constant, K , on the concentration of OH^- .



$$K = \frac{[CO]^{X_{CO}} [OH^-]^{X_{OH^-}}}{[CO_2]^{X_{CO_2}} [H_2O]^{X_{H_2O}}} \quad (C.23)$$

When the pH deviates from standard (i.e 7), the $\log[OH^-]^{X_{OH^-}}$ deviates, which has an effect on the E^0 , as shown above in equation C.21. This effect can be expressed in the following formula, taking into account the pH correction factor for deviating from standard.

$$E^0 = X_{OH^-} * \frac{2.303RT}{nF} (pH - pH_{neutral}) \quad (C.24)$$

Where X_{OH^-} denotes the stoichiometric number of OH^- in the accompanying reaction equation.

C.3.4. Reference electrode correction factor

In practice other electrodes than the hydrogen electrode are often used as reference. In the experiments for this research the applied reference electrode is an Ag/AgCl (silver-silver chloride) electrode. Since this electrode has different properties from the hydrogen electrode, a correction factor needs to be incorporated for using a different electrode. To convert the potentials measured with the Ag/AgCl to the SHE scale, the following formula can be applied [49]:

$$E_{SHE}^0 = E_{m,RE}^0 + E_{RE}^0 \quad (C.25)$$

Where, E_{SHE}^0 represents the potential verses SHE scale, $E_{m,RE}^0$ represents the measured potential verses the reference electrode and E_{RE}^0 represents the standard potential of the reference electrode verses SHE.

The factor for the standard potential of the reference electrode is taken to be 0.197. Therefore, to convert to SHE scale, this factor needs to be subtracted from the total to find the real E^0 for the reaction.

Accordingly, to express all values in the model in the Ag/AgCl scale, so they can be easily compared with the experimental results, the following formula was used:

$$E_{Ag/AgCl}^0 = E_{SHE}^0 - 0.197 \quad (C.26)$$

where values expressed in RHE scale first need to be converted to SHE according to:

$$E_{SHE}^0 = E_{RHE}^0 - pH_{deviation} + T_{deviation} = E_{standard}^0 - X_{OH^-} * \frac{2.303RT}{nF} (pH - pH_{neutral}) + (T - 298.15) \cdot \left(\frac{dE^0}{dT} \right)_{298} \quad (C.27)$$

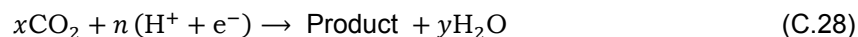
C.3.5. Supplementing the available information

Since CO reduction is not as widely studied as CO_2 reduction, information on the E^0 values for the CO reduction reactions can be unavailable in some cases. To solve this, E^0 values need to be calculated from the reaction equations and their thermodynamics. This segment will explain how this was conducted for the data used in the model.

Calculating RHE values

When the RHE equilibrium potential values are not reported, they can be calculated from the available thermodynamic data, as illustrated in the supplementary information of the 2019 research by Nitopi et al. [76]. Explained here, is how the equilibrium potentials of the CO reduction equations can be calculated from the known values for the CO₂ reduction equations. This is conducted in the following way.

A standard CO₂ reduction equation has the following shape:



CO can be produced from CO₂ reduction according to:



Therefore, to produce the same product from CO reduction, the CO₂ to CO reaction needs to be subtracted x times from the CO₂ reduction reaction. This leads to the following equation:



Subsequently, for this reaction, the equilibrium potential can be calculated with:

$$E_{\text{COR}}^\circ = \frac{(n_{\text{COR}} + 2x) E_{\text{CO}_2\text{R}}^\circ - 2xE_{\text{CO}_2\text{R}}^\circ(\text{CO})}{n_{\text{COR}}} \quad (\text{C.31})$$

With:

$$n_{\text{COR}} = n - 2x \quad (\text{C.32})$$

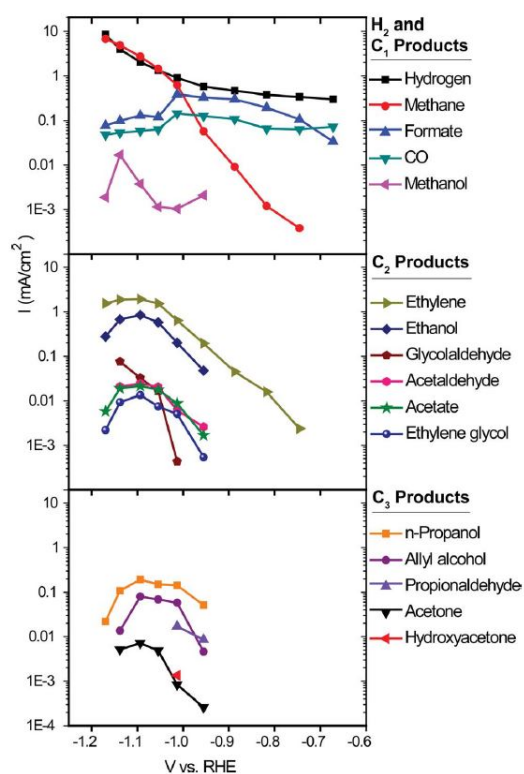
Where $E_{\text{CO}_2\text{R}}^\circ(\text{CO})$ indicates the standard equilibrium potential for the CO₂ reduction to CO and $E_{\text{CO}_2\text{R}}^\circ$ indicates the standard equilibrium potential for the CO₂ reduction reaction for making the same product.

Utilising these equations, the following standard equilibrium potential values were calculated:

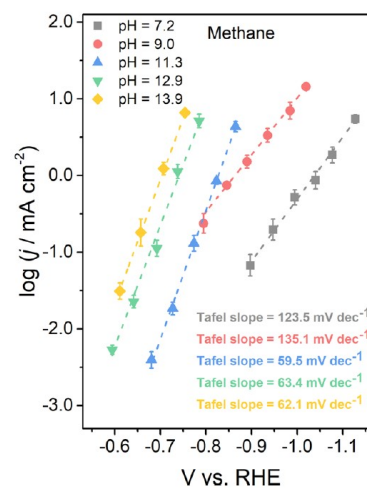
nr.	Reaction	E_{RHE}^0 [V]
4	$2\text{CO} + 4\text{H}_2\text{O} + 4\text{e}^- \rightleftharpoons \text{CH}_3\text{COO}(\text{aq}) + 4\text{OH}^-$	0.324
5	$2\text{CO} + 7\text{H}_2\text{O} + 8\text{e}^- \rightleftharpoons \text{C}_2\text{H}_5\text{OH}(\text{aq}) + 8\text{OH}^-$	0.187

Table C.2: Calculated standard equilibrium potential values against RHE for the CO reduction equations for which no values were listed in literature.

C.4. Experimental input-data



(a) Tafel slopes for CO₂R on Cu, showing changing slopes for CH₄ production. Derived from: [56].



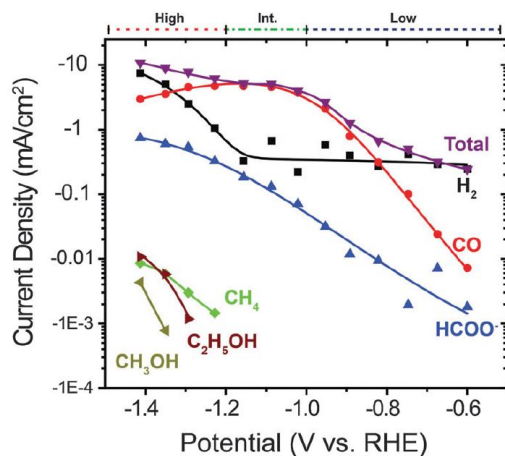
(b) Tafel slopes for COR on Cu, showing changing slopes for CH₄ production. Derived from: [59].

Figure C.2: Representing the changing Tafel slope behaviour.

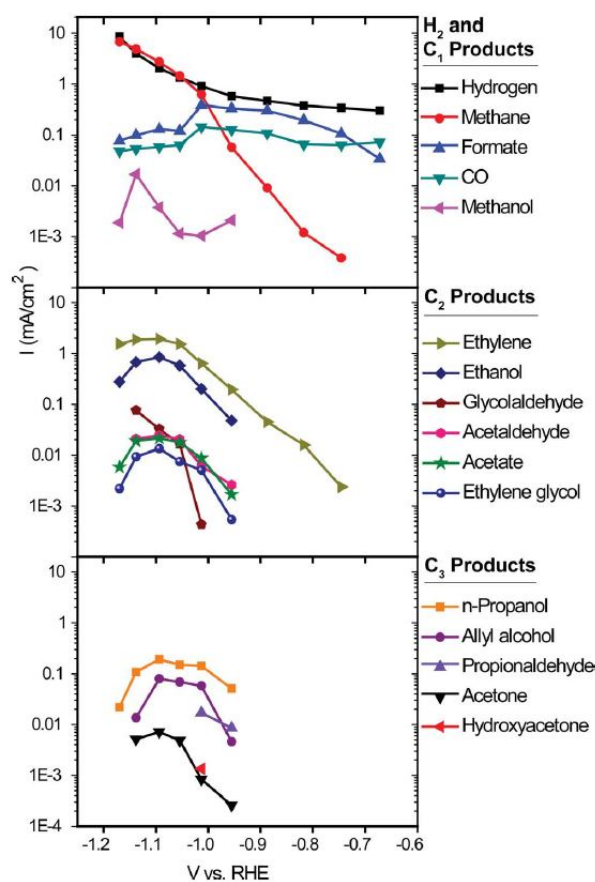
C.5. Input data for the model

Species	Diffusion constant D [m ² /s]
CO ₂	1.92*10 ⁻⁹
HCO ₃ ⁻	1.18*10 ⁻⁹
CO ₃ ²⁻	9.20*10 ⁻¹⁰
OH ⁻	5.3*10 ⁻⁹
H ⁺	9.21*10 ⁻⁹
HCOO ⁻	1.5*10 ⁻⁹
CH ₃ COO	1.1*10 ⁻⁹
C ₂ H ₅ OH	1.22*10 ⁻⁹
CO	2.03*10 ⁻⁹
H ₂	4.5*10 ⁻⁹
K ⁺	1.96*10 ⁻⁹
CH ₄	1.64*10 ⁻⁹
C ₂ H ₄	1.09*10 ⁻⁹

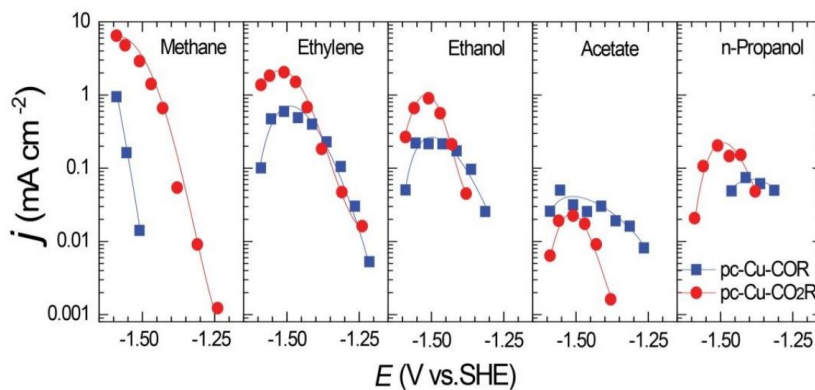
Table C.3: The values of the diffusion constants for the species investigated in this research.



(a) Tafel slopes for CO₂R on Ag. Derived from: [40].



(b) Tafel slopes for CO₂R on Cu. Derived from: [56].



(c) Tafel slopes for COR on Cu. Derived from [120].

Figure C.3: The Tafel slopes that were used as input for the modelling of the kinetic behaviour.

Bibliography

- [1] 2015. URL: <https://www.comsol.com/multiphysics/what-is-ionic-migration>.
- [2] URL: <https://www.beswick.com/resources/the-basics-of-compression-fittings/>.
- [3] International Energy Agency (IEA). *CCUS in Clean Energy Transitions*. 2020. URL: <https://www.iea.org/reports/ccus-in-clean-energy-transitions>.
- [4] International Energy Agency (IEA). *Renewable Power*. 2020. URL: <https://www.iea.org/reports/renewable-power>.
- [5] International energy agency. *Tracking the decoupling of electricity demand and associated CO2 emissions*. 2019. URL: <https://www.iea.org/commentaries/tracking-the-decoupling-of-electricity-demand-and-associated-co2-emissions>.
- [6] Muhammad Alfath and Chan Woo Lee. "Recent Advances in the Catalyst Design and Mass Transport Control for the Electrochemical Reduction of Carbon Dioxide to Formate". In: *Catalysts* 10.8 (2020), p. 859. DOI: 10.3390/catal10080859.
- [7] Us Army. "FUNDAMENTALS OF MACHINE TOOLS". In: *US Army Training Circulation 9-524* (1996). URL: https://armypubs.army.mil/epubs/DR_pubs/DR_a/pdf/web/tc9_524.pdf.
- [8] Allen Bradley Jr. Atkinson. *A Model for the PTX Properties of H2O-NaCl*. 2002. URL: <http://hdl.handle.net/10919/34376>.
- [9] Prof. Dinsahw S. Balsara. *Numerical PDE Techniques for Scientists and Engineers. Chapter 2: Finite Difference Approximations*. URL: <https://www3.nd.edu/~dbalsara/Numerical-PDE-Course/ch2/abstract.shtml>.
- [10] Dortmund Data Bank. *Liquid Dynamic Viscosity Calculation by Vogel Equation (Water)*. URL: <http://ddbonline.ddbst.de/VogelCalculation/VogelCalculationCGI.exe?component=Water>.
- [11] Allen J. Bard and Larry R. Faulkner. *ELECTROCHEMICAL METHODS Fundamentals and Applications*. 2nd ed. John Wiley Sons, Inc, 2001, pp. 1–850.
- [12] Vincent van Beusekom. *Electrochemical Reduction of Carbon Dioxide: Modeling the electrochemical conversion of CO₂ to Formic Acid under high pressure*. 2020. URL: <http://resolver.tudelft.nl/uuid:b8e40171-619e-4fcb-9175-734484291999>.
- [13] BioLogic. *Checking and validating reference electrodes*. 2020. URL: <https://www.biologic.net/topics/checking-and-validating-reference-electrodes/>.
- [14] J.W. Blake, J.T. Padding, and J.W. Haverkort. "Analytical modelling of CO2 reduction in gas-diffusion electrode catalyst layers". In: *Electrochimica Acta* 393 (2021), p. 138987. DOI: 10.1016/j.electacta.2021.138987.
- [15] Steven G. Bratsch. "Standard Electrode Potentials and Temperature Coefficients in Water at 298.15 K". In: *Journal of Physical and Chemical Reference Data* 18.1 (1989), pp. 1–21. DOI: 10.1063/1.555839.
- [16] Vanessa J. Bukas et al. "Combining Experiment and Theory To Unravel the Mechanism of Two-Electron Oxygen Reduction at a Selective and Active Co-catalyst". In: *ACS Catalysis* 8.12 (2018), p. 11940. DOI: 10.1021/acscatal.8b02813.
- [17] P. Bumroongsakulsawat and G.H. Kelsall. "Tinned graphite felt cathodes for scale-up of electrochemical reduction of aqueous CO₂". In: *Electrochimica Acta* 159 (2015), pp. 242–251. DOI: <http://dx.doi.org/10.1016/j.electacta.2015.01.209>.

- [18] Thomas Burdyny et al. "Nanomorphology-Enhanced Gas-Evolution Intensifies CO₂ Reduction Electrochemistry". In: *ACS Sustainable Chemistry Engineering* 5.5 (2017), pp. 4031–4040. DOI: 10.1021/acssuschemeng.7b00023.
- [19] Oleksandr S. Bushuyev et al. "What Should We Make with CO₂ and How Can We Make It?" In: *Joule* 2.5 (2018), pp. 825–832. DOI: 10.1016/j.joule.2017.09.003.
- [20] Department of Chemistry University of Wisconsin-Madison. *Table of Thermodynamic Values*. URL: <https://www2.chem.wisc.edu/deptfiles/genchem/netorial/modules/thermodynamics/table.htm>.
- [21] Yikai Chen, Nathan S. Lewis, and Chengxiang Xiang. "Modeling the Performance of A Flow-Through Gas Diffusion Electrode for Electrochemical Reduction of CO or CO₂". In: *Journal of The Electrochemical Society* 167.11 (2020), p. 114503. DOI: 10.1149/1945-7111/ab987a.
- [22] ChERIC. *Temperature Dependent Properties: Vapor pressure of CARBON DIOXIDE*. URL: <https://www.cheric.org/research/kdb/hcprop/showcoef.php?cmpid=1943&prop=PVP>.
- [23] Phil De Luna et al. "What would it take for renewably powered electrosynthesis to displace petrochemical processes?" In: *Science* 364.6438 (2019), eaav3506. DOI: 10.1126/science.aav3506.
- [24] Lokenath Debnath. *Linear Partial Differential Equations for Scientists and Engineers*. 4th ed. Birkhäuser, 2007, pp. 90–100.
- [25] GRANTA DESIGN. *GRANTA DESIGN CES EDUPACK 2021 R2*. Granta Design, 2021.
- [26] Zhenhao Duan, Nancy Moler, and John H Weare. "An equation of state for the CH₄-CO₂-H₂O system: I. Pure systems from 0 to 1000⁰C and 0 to 8000 bar". In: *Geochimica et Cosmochimica Acta* 56.7 (1992), pp. 2605–2617. DOI: 10.1016/0016-7037(92)90347-1.
- [27] Zhenhao Duan et al. "An improved model for the calculation of CO₂ solubility in aqueous solutions containing Na⁺, K⁺, Ca²⁺, Mg²⁺, Cl⁻, and SO₄²⁻". In: *Marine Chemistry* 98.2-4 (2006), pp. 131–139. DOI: 10.1016/j.marchem.2005.09.001.
- [28] Eric J. Dufek, Tedd E. Lister, and Simon G. Stone. "Sampling dynamics for pressurized electrochemical cells". In: *Journal of Applied Electrochemistry* 44.7 (2014), pp. 849–855. DOI: 10.1007/s10800-014-0693-z.
- [29] Eric J. Dufek et al. "Operation of a Pressurized System for Continuous Reduction of CO₂". In: *Journal of The Electrochemical Society* 159.9 (2012), F514–F517. DOI: 10.1149/2.011209jes.
- [30] M. Eigen. "Proton Transfer, Acid-Base Catalysis, and Enzymatic Hydrolysis. Part I: ELEMENTARY PROCESSES". In: *Angewandte Chemie International Edition in English* 3.1 (1964), pp. 1–19. DOI: 10.1002/anie.196400011.
- [31] Formlabs. *Introducing Elastic Resin: A Soft, Resilient 3D Printing Material*. 2019. URL: <https://formlabs.com/blog/elastic-resin-soft-resilient-3d-printing/>.
- [32] Xianbiao Fu, Jiahao Zhang, and Yijin Kang. "Electrochemical reduction of CO₂ towards multi-carbon products via a two-step process". In: *Reaction Chemistry Engineering* (2021). DOI: 10.1039/d1re00001b.
- [33] Christine M. Gabardo et al. "Combined high alkalinity and pressurization enable efficient CO₂ electroreduction to CO". In: *Energy Environmental Science* 11.9 (2018), pp. 2531–2539. DOI: 10.1039/c8ee01684d.
- [34] Nitish Gadgil. *Modeling a Flow-Cell for Electrochemical Reduction of Carbon Dioxide to Formate*. 2018. URL: <http://resolver.tudelft.nl/uuid:885c941e-f98a-4761-9e09-c62071773af5>.
- [35] Viktor Grigoryan. *PARTIAL DIFFERENTIAL EQUATIONS*. 2010. URL: <http://www.math.ucsb.edu/~grigoryan/124A.pdf>.
- [36] Rolando Guidelli et al. "Defining the transfer coefficient in electrochemistry: An assessment (IUPAC Technical Report)". In: *Pure and Applied Chemistry* 86.2 (2014). DOI: 10.1515/pac-2014-5026.

- [37] N. Gupta, M. Gattrell, and B. MacDougall. "Calculation for the cathode surface concentrations in the electrochemical reduction of CO₂ in KHCO₃ solutions". In: *Journal of Applied Electrochemistry* 36.2 (2005), pp. 161–172. DOI: 10.1007/s10800-005-9058-y.
- [38] Gurudayal et al. "Sequential Cascade Electrocatalytic Conversion of Carbon Dioxide to C-C Coupled Products". In: *ACS Applied Energy Materials* 2.6 (2019), pp. 4551–4559. DOI: 10.1021/acsaem.9b00791.
- [39] Kohjiro Hara, Akihiko Kudo, and Tadayoshi Sakata. "Electrochemical reduction of carbon dioxide under high pressure on various electrodes in an aqueous electrolyte". In: *Journal of Electroanalytical Chemistry* 391.1-2 (1995), pp. 141–147. DOI: 10.1016/0022-0728(95)03935-a.
- [40] Toru Hatsukade et al. "Insights into the electrocatalytic reduction of CO₂ on metallic silver surfaces". In: *Phys. Chem. Chem. Phys.* 16.27 (2014), pp. 13814–13819. DOI: 10.1039/c4cp00692e.
- [41] J.W. Haverkort. "A theoretical analysis of the optimal electrode thickness and porosity". In: *Electrochimica Acta* 295 (2019), pp. 846–860. DOI: 10.1016/j.electacta.2018.10.065.
- [42] P. Howard. "Partial Differential Equations in MATLAB 7.0". In: (2010). URL: <https://www.math.tamu.edu/~phoward/m401/pdemat.pdf>.
- [43] Marie-José Huron and Jean Vidal. "New mixing rules in simple equations of state for representing vapour-liquid equilibria of strongly non-ideal mixtures". In: *Fluid Phase Equilibria* 3.4 (1979), pp. 255–271. DOI: 10.1016/0378-3812(79)80001-1.
- [44] H IBRAHIM, A ILINCA, and J PERRON. "Energy storage systems - Characteristics and comparisons". In: *Renewable and Sustainable Energy Reviews* 12.5 (2008), pp. 1221–1250. DOI: 10.1016/j.rser.2007.01.023.
- [45] BioLogic Science Instruments. "EC-Lab Software: Techniques and Applications". In: 10.38 (2014). URL: <https://mmrc.caltech.edu/BioLogic%20Echem/EC%20Manuals/EC-Lab%20software%20Techniques%20and%20Applications%20manual.pdf%20%7D>.
- [46] Gamry Instruments. *Reference Electrodes Influence Electrochemical Measurements*. URL: <https://www.gamry.com/application-notes/instrumentation/reference-electrodes/>.
- [47] Gyorgy Inzelt. "Chronoamperometry, Chronocoulometry, and Chronopotentiometry". In: *Encyclopedia of Applied Electrochemistry* (2014), pp. 207–213. DOI: 10.1007/978-1-4419-6996-5.
- [48] IPEX. *EPDM FKM Chemical Resistance Guide*. 2nd ed. IPEX by Aliaxis, 2020, pp. 1–36.
- [49] Gregory Jerkiewicz. "Standard and Reversible Hydrogen Electrodes: Theory, Design, Operation, and Applications". In: *ACS Catalysis* 10.15 (2020), pp. 8409–8417. DOI: 10.1021/acscatal.0c02046.
- [50] Kenneth S. Johnson. "Carbon dioxide hydration and dehydration kinetics in seawater¹". In: *Limnology and Oceanography* 27.5 (1982), pp. 849–855. DOI: 10.4319/lo.1982.27.5.0849.
- [51] Matthew Jouny, Wesley Luc, and Feng Jiao. "High-rate electroreduction of carbon monoxide to multi-carbon products". In: *Nature Catalysis* 1.10 (2018), pp. 748–755. DOI: 10.1038/s41929-018-0133-2.
- [52] Matthew Jouny, Wesley Luc, and Feng Jiao. "High-rate electroreduction of carbon monoxide to multi-carbon products". In: *Nature Catalysis* 1.10 (2018), pp. 748–755. DOI: 10.1038/s41929-018-0133-2.
- [53] Evy Kersalé. *Analytic Solutions of Partial Differential Equations*. 2003. URL: http://www1.maths.leeds.ac.uk/~kersale/Teach/M3414/Notes/m3414_1.pdf.
- [54] Ruud Kortlever et al. "Catalysts and Reaction Pathways for the Electrochemical Reduction of Carbon Dioxide". In: *The Journal of Physical Chemistry Letters* 6.20 (2015), pp. 4073–4082. DOI: 10.1021/acs.jpcllett.5b01559.
- [55] Yosra Kotb et al. "Modeling of a Microfluidic Electrochemical Cell for the Electro-Reduction of CO₂ to CH₃OH". In: *Journal of The Electrochemical Society* 164.13 (2017), E391–E400. DOI: 10.1149/2.0741713jes.

- [56] Kendra P. Kuhl et al. "New insights into the electrochemical reduction of carbon dioxide on metallic copper surfaces". In: *Energy Environmental Science* 5.5 (2012), p. 7050. DOI: 10.1039/c2ee21234j.
- [57] Christina W. Li, Jim Ciston, and Matthew W. Kanan. "Electroreduction of carbon monoxide to liquid fuel on oxide-derived nanocrystalline copper". In: *Nature* 508.7497 (2014), pp. 504–507. DOI: 10.1038/nature13249.
- [58] Dedong Li and Zhenhao Duan. "The speciation equilibrium coupling with phase equilibrium in the H₂O-CO₂-NaCl system from 0 to 250°C, from 0 to 1000 bar, and from 0 to 5 molality of NaCl". In: *Chemical Geology* 244.3-4 (2007), pp. 730–751. DOI: 10.1016/j.chemgeo.2007.07.023.
- [59] Jing Li et al. "Electrokinetic and in situ spectroscopic investigations of CO electrochemical reduction on copper". In: *Nature Communications* 12.1 (2021). DOI: 10.1038/s41467-021-23582-2.
- [60] Xinyan Liu et al. "pH effects on the electrochemical reduction of CO(2) towards C2 products on stepped copper". In: *Nature Communications* 10.1 (2019). DOI: 10.1038/s41467-018-07970-9.
- [61] F. A. Long and W. F. McDevit. "Activity Coefficients of Nonelectrolyte Solutes in Aqueous Salt Solutions." In: *Chemical Reviews* 51.1 (1952), pp. 119–169. DOI: 10.1021/cr60158a004.
- [62] Qi Lu et al. "A selective and efficient electrocatalyst for carbon dioxide reduction". In: *Nature Communications* 5.1 (2014). DOI: 10.1038/ncomms4242.
- [63] Yanwei Lum and Joel W. Ager. "Sequential catalysis controls selectivity in electrochemical CO₂ reduction on Cu". In: *Energy Environmental Science* 11.10 (2018), pp. 2935–2944. DOI: 10.1039/c8ee01501e.
- [64] Ming Ma et al. "Selective and Efficient Reduction of Carbon Dioxide to Carbon Monoxide on Oxide-Derived Nanostructured Silver Electrocatalysts". In: *Angewandte Chemie International Edition* 55.33 (2016), pp. 9748–9752. DOI: 10.1002/anie.201604654.
- [65] P Makulsawatudom, D Mackenzie, and R Hamilton. "Stress concentration at crossholes in thick cylindrical vessels". In: *The Journal of Strain Analysis for Engineering Design* 39.5 (2004), pp. 471–481. DOI: 10.1243/0309324041896506.
- [66] Shide Mao et al. "An improved model for calculating CO₂ solubility in aqueous NaCl solutions and the application to CO₂-H₂O-NaCl fluid inclusions". In: *Chemical Geology* 347 (2013), pp. 43–58. DOI: 10.1016/j.chemgeo.2013.03.010.
- [67] William L. Marshall and E. U. Franck. "Ion product of water substance, 0-1000°C, 1–10,000 bars". In: *Journal of Physical and Chemical Reference Data* 10.2 (1981), pp. 295–304. DOI: 10.1063/1.555643.
- [68] MathWorks. "MATLAB Math For Use with MATLAB". In: *Mathematics* Version 7 (.).
- [69] Mathworks. *parfor*. URL: <https://nl.mathworks.com/help/parallel-computing/parfor.html>.
- [70] Morgan M Monroe et al. "Membraneless laminar flow cell for electrocatalytic CO₂ reduction with liquid product separation". In: *Journal of Physics D: Applied Physics* 50.15 (2017), p. 154006. DOI: 10.1088/1361-6463/aa6359.
- [71] Carlos G. Morales-Guio et al. "Improved CO₂ reduction activity towards C₂+ alcohols on a tandem gold on copper electrocatalyst". In: *Nature Catalysis* 1.10 (2018), pp. 764–771. DOI: 10.1038/s41929-018-0139-9.
- [72] Andrew R. T. Morrison et al. "Modeling the Electrochemical Conversion of Carbon Dioxide to Formic Acid or Formate at Elevated Pressures". In: *Journal of The Electrochemical Society* 166.4 (2019), E77–E86. DOI: 10.1149/2.0121904jes.
- [73] John Newman and Karen E. Thomas-Alyea. *Electrochemical Systems*. 3rd ed. John Wiley Sons, Incorporated, 2012, p. 286.

- [74] Gérard C. Nihous, Christopher K. Kinoshita, and Stephen M. Masutani. "Stress Concentration Factors for Oblique Holes in Pressurized Thick-Walled Cylinders". In: *Journal of Pressure Vessel Technology* 130.2 (2008). DOI: 10.1115/1.2891915.
- [75] SRD 69 NIST Chemistry WebBook. *Water*. 2021. URL: <https://webbook.nist.gov/cgi/cbook.cgi?ID=C7732185&Units=SI&Mask=4#Thermo-Phase>.
- [76] Stephanie Nitopi et al. "Progress and Perspectives of Electrochemical CO₂ Reduction on Copper in Aqueous Electrolyte". In: *Chemical Reviews* 119.12 (2019), pp. 7610–7672. DOI: 10.1021/acs.chemrev.8b00705.
- [77] Ding-Yu Peng and Donald B. Robinson. "A New Two-Constant Equation of State". In: *Industrial Engineering Chemistry Fundamentals* 15.1 (1976), pp. 59–64. DOI: 10.1021/i160057a011.
- [78] Robert H Perry, Don W Green, and James O Maloney. *Perry's chemical engineers' handbook*. 7th ed. McGraw-Hill, 1997, pp. 2–125.
- [79] Samuel C. Perry, Carlos Ponce de León, and Frank C. Walsh. "Review - The Design, Performance and Continuing Development of Electrochemical Reactors for Clean Electrosynthesis". In: *ECS The Electrochemical Society* 167.155525 (2020). DOI: 10.1149/1945-7111/abc58e.
- [80] Slobodan Petrovic. *Electrochemistry crash course for engineers*. 1st ed. Springer, Cham, 2021, pp. 1–108.
- [81] B.N. Phalguna. "Stress and Failure Analysis of Thick Walled Cylinder with Oblique Hole". In: *International Journal of Engineering Research and V6.08* (2017). DOI: 10.17577/ijertv6is080017.
- [82] Kenneth S. Pitzer. "Thermodynamics of electrolytes. I. Theoretical basis and general equations". In: *The Journal of Physical Chemistry* 77.2 (1973), pp. 268–277. DOI: 10.1021/j100621a026.
- [83] Kenneth S. Pitzer, J. Christopher Peiper, and R. H. Busey. "Thermodynamic Properties of Aqueous Sodium Chloride Solutions". In: *Journal of Physical and Chemical Reference Data* 13.1 (1984), pp. 1–102. DOI: 10.1063/1.555709.
- [84] Federica Proietto et al. "Electrochemical conversion of pressurized CO₂ at simple silver-based cathodes in undivided cells: study of the effect of pressure and other operative parameters". In: *Journal of Applied Electrochemistry* 51.2 (2020), pp. 267–282. DOI: 10.1007/s10800-020-01505-1.
- [85] David Raciti, Mark Mao, and Chao Wang. "Mass transport modelling for the electroreduction of CO₂ on Cu nanowires". In: *Nanotechnology* 29.4 (2017), p. 044001. DOI: 10.1088/1361-6528/aa9bd7.
- [86] G. Raju and K. Hari Babu. "Design and analysis of Stress on Thick Walled Cylinder with and with out Holes". In: *International Journal of Engineering Research and Applications* 5.1 (2015), pp. 75–83. URL: http://www.ijera.com/papers/Vol5_issue1/Part%5C%20-%5C%201/J501017583.pdf.
- [87] Mahinder Ramdin et al. "High-Pressure Electrochemical Reduction of CO₂ to Formic Acid/Formate: Effect of pH on the Downstream Separation Process and Economics". In: *Industrial Engineering Chemistry Research* 58.51 (2019), pp. 22718–22740. DOI: 10.1021/acs.iecr.9b03970.
- [88] Edward P. Randviir and Craig E. Banks. "Electrochemical impedance spectroscopy: an overview of bioanalytical applications". In: *Analytical Methods* 5.5 (2013), p. 1098. DOI: 10.1039/c3ay26476a.
- [89] Arash Rastegar. "EPH-classifications in Geometry, Algebra, Analysis and Arithmetic". In: (2015). URL: <https://arxiv.org/pdf/1503.07859.pdf>.
- [90] Aiman Eid Al-Rawajfeh. *Modelling and Simulation of CO₂ Release in Multiple-Effect Distillers for Seawater Desalination*. 2004, p. 34. URL: <http://d-nb.info/972520511/34>.
- [91] Aiman Eid Al-Rawajfeh. "Modelling and simulation of CO₂ release in multiple-effect distillers for seawater desalination". In: (2004). DOI: <http://dx.doi.org/10.25673/3764>.

- [92] Shaoxuan Ren et al. "Electrocatalysts derived from copper complexes transform CO into C₂+ products effectively in a flow cell". In: *Research Square* (2021). DOI: 10.21203/rs.3.rs-83176/v2.
- [93] Princeton Applied Research. *Application Note E-4 Subject: A Review of Techniques for Electrochemical Analysis*. URL: https://nanobioelectronics.weebly.com/uploads/3/8/8/6/38862535/review_of_techniques_for_electrochemical_analysis.pdf.
- [94] B. A. Rosen et al. "Ionic Liquid-Mediated Selective Conversion of CO₂ to CO at Low Overpotentials". In: *Science* 334.6056 (2011), pp. 643–644. DOI: 10.1126/science.1209786.
- [95] Frederick Dominic Rossini. *Selected values of chemical thermodynamic properties*. U.S. Department of Commerce, National Bureau of Standards, 1961, p. 101.
- [96] Marcel Schreier et al. "Competition between H and CO for Active Sites Governs Copper-Mediated Electrosynthesis of Hydrocarbon Fuels". In: *Angewandte Chemie International Edition* 57.32 (2018), pp. 10221–10225. DOI: 10.1002/anie.201806051.
- [97] K.G. Schulz et al. "Determination of the rate constants for the carbon dioxide to bicarbonate interconversion in pH-buffered seawater systems". In: *Marine Chemistry* 100.1-2 (2006), pp. 53–65. DOI: 10.1016/j.marchem.2005.11.001.
- [98] Charles I. Shaughnessy et al. "Insights into pressure tunable reaction rates for electrochemical reduction of CO₂ in organic electrolytes". In: *Green Chemistry* 22.8 (2020), pp. 2434–2442. DOI: 10.1039/d0gc00013b.
- [99] Wei Shi and Edward J. Maginn. "Molecular Simulation and Regular Solution Theory Modeling of Pure and Mixed Gas Absorption in the Ionic Liquid 1-n-Hexyl-3-methylimidazolium Bis(Trifluoromethylsulfonyl) ([hmim][Tf₂N])". In: *The Journal of Physical Chemistry B* 112.51 (2008), pp. 16710–16720. DOI: 10.1021/jp8075782.
- [100] Xunli Shi and Shide Mao. "An improved model for CO₂ solubility in aqueous electrolyte solution containing Na⁺, K⁺, Mg²⁺, Ca²⁺, Cl⁻ and SO₄²⁻ under conditions of CO₂ capture and sequestration". In: *Chemical Geology* 463 (2017), pp. 12–28. DOI: 10.1016/j.chemgeo.2017.05.005.
- [101] Robert D. Skeel and Martin Berzins. "A Method for the Spatial Discretization of Parabolic Equations in One Space Variable". In: *SIAM Journal on Scientific and Statistical Computing* 11.1 (1990), pp. 1–32. DOI: 10.1137/0911001.
- [102] T.A. Soeteman. "Reduction of CO₂ to formate/formic acid under high pressure: Exploration of design parameters". In: (2019).
- [103] Hakhyeon Song et al. "Activation of C₂H₄ reaction pathways in electrochemical CO₂ reduction under low CO₂ partial pressure". In: *Applied Catalysis B: Environmental* 272 (2020), p. 119049. DOI: 10.1016/j.apcatb.2020.119049.
- [104] Roland Span and Wolfgang Wagner. "A New Equation of State for Carbon Dioxide Covering the Fluid Region from the Triple-Point Temperature to 1100 K at Pressures up to 800 MPa". In: *Journal of Physical and Chemical Reference Data* 25.6 (1996), pp. 1509–1596. DOI: 10.1063/1.555991.
- [105] Neil Spinner. *Reference Electrode Storage and Master Reference Electrodes*. 2019. URL: <https://pineresearch.com/shop/wp-content/uploads/sites/2/2016/12/DRP10031-Reference-Electrode-Storage-and-Master-Reference-Electrodes-REV001.pdf>.
- [106] Joshua M. Spurgeon and Bijandra Kumar. "A comparative technoeconomic analysis of pathways for commercial electrochemical CO₂ reduction to liquid products". In: *Energy Environmental Science* 11.6 (2018), pp. 1536–1551. DOI: 10.1039/c8ee00097b.
- [107] Zhenyu Sun et al. "Fundamentals and Challenges of Electrochemical CO₂ Reduction Using Two-Dimensional Materials". In: *Chem* 3.4 (2017), pp. 560–587. DOI: 10.1016/j.chempr.2017.09.009.
- [108] Peter Swidersky and Yong Guo. "The solubility of gases and gas-mixtures in rape seed oil". In: *Rivista Italiana delle Sostanze Grasse* 85 (Mar. 2008), pp. 33–38.

- [109] Yong Tang et al. "Measurement and prediction model of carbon dioxide solubility in aqueous solutions containing bicarbonate anion". In: *Fluid Phase Equilibria* 386 (2015), pp. 56–64. DOI: 10.1016/j.fluid.2014.11.025.
- [110] Ken Thayer. *Using a centering microscope for precise workpiece location*. 2019. URL: <https://insights.globalspec.com/article/11822/using-a-centering-microscope-for-precise-workpiece-location>.
- [111] "The MATLAB ODE Suite". In: *SIAM: Society for Industrial and Applied Mathematics* 18.1 (1997), pp. 1–22. DOI: 10.1137/s1064827594276424.
- [112] Nolan Theaker et al. "Heterogeneously catalyzed two-step cascade electrochemical reduction of CO₂ to ethanol". In: *Electrochimica Acta* 274 (2018), pp. 1–8. DOI: 10.1016/j.electacta.2018.04.072.
- [113] Arnaud Thevenon et al. "Dramatic HER Suppression on Ag Electrodes via Molecular Films for Highly Selective CO₂ to CO Reduction". In: *ACS Catalysis* 11.8 (2021), pp. 4530–4537. DOI: 10.1021/acscatal.1c00338.
- [114] S. Timoshenko and S. Woinowsky-Krieger. *Theory of plates and shells*. 2nd ed. McGraw-Hill Book Company, 1989, pp. 51–72.
- [115] Makoto Todoroki et al. "Electrochemical reduction of high pressure CO₂ at Pb, Hg and In electrodes in an aqueous KHCO₃ solution". In: *Journal of Electroanalytical Chemistry* 394.1-2 (1995). DOI: 10.1016/0022-0728(95)04010-1.
- [116] Arnau Verdaguer-Casadevall et al. "Probing the Active Surface Sites for CO Reduction on Oxide-Derived Copper Electrocatalysts". In: *Journal of the American Chemical Society* 137.31 (2015), pp. 9808–9811. DOI: 10.1021/jacs.5b06227.
- [117] LamNgeun Virasak. *Manufacturing Processes 4-5*. Open Oregon Educational Resources. URL: <https://openoregon.pressbooks.pub/manufacturingprocesses45/>.
- [118] C. Vuik et al. *Numerical Methods for Ordinary Differential Equations*. 2nd ed. Delft Academic Press, 2016.
- [119] Lei Wang et al. "Electrochemical Carbon Monoxide Reduction on Polycrystalline Copper: Effects of Potential, Pressure, and pH on Selectivity toward Multicarbon and Oxygenated Products". In: *ACS Catalysis* 8.8 (2018), pp. 7445–7454. DOI: 10.1021/acscatal.8b01200.
- [120] Lei Wang et al. "Electrochemical Carbon Monoxide Reduction on Polycrystalline Copper: Effects of Potential, Pressure, and pH on Selectivity toward Multicarbon and Oxygenated Products". In: *ACS Catalysis* 8.8 (2018), pp. 7445–7454. DOI: 10.1021/acscatal.8b01200.
- [121] Xingli Wang et al. "Mechanistic reaction pathways of enhanced ethylene yields during electroreduction of CO₂-CO co-feeds on Cu and Cu-tandem electrocatalysts". In: *Nature Nanotechnology* 14.11 (2019), pp. 1063–1070. DOI: 10.1038/s41565-019-0551-6.
- [122] University of Washington. *Thick Walled Cylinders - University of Washington*. URL: <https://pdf4pro.com/amp/view/thick-walled-cylinders-university-of-washington-516aa8.html>.
- [123] Quincy Wols. "Design of a High-Pressure CO₂ Reduction Reactor System". In: 2020. URL: <http://resolver.tudelft.nl/uuid:d56cca3d-33e9-4b95-84e8-3735c627037e>.
- [124] Chenlu Xie et al. "Tandem Catalysis for CO₂ Hydrogenation to C₂-C₄ Hydrocarbons". In: *Nano Letters* 17.6 (2017), pp. 3798–3802. DOI: 10.1021/acs.nanolett.7b01139.
- [125] Richard E. Zeebe. "On the molecular diffusion coefficients of dissolved , and and their dependence on isotopic mass". In: *Geochimica et Cosmochimica Acta* 75.9 (2011), pp. 2483–2498. DOI: 10.1016/j.gca.2011.02.010.
- [126] Peng Zhu et al. "Direct and continuous generation of pure acetic acid solutions via electrocatalytic carbon monoxide reduction". In: *Proceedings of the National Academy of Sciences* 118.2 (2021), e2010868118. DOI: 10.1073/pnas.2010868118.
- [127] Cynthia G Zoski. *Handbook of electrochemistry*. Elsevier, 2007.